ABSTRACT

FIELD-TEST DATA FROM SOIL-STRUCTURE INTERACTION OF SHALLOW AND DEEP FOUNDATIONS

By

Peter D. Fourtounis

May 2015

This thesis presents an analysis of data from two soil-structure interaction field tests, one involving a deep foundation and the other a shallow foundation. The objective of this research is to use the field data to validate and inform models used by engineers. Soil-structure interaction fundamentals and background are first discussed. Field-test data was used in conjunction with a soil-structure system model to develop equations that can be used to determine stiffness and damping of a rigid pile foundation system subjected to forced vibration loading. The stiffness and damping characteristics are presented through complex-valued impedance functions. The equations were applied to field data; however the results were inconclusive due in part to the limited frequency range of the data used. Additionally, soil-foundation interface pressures are analyzed for a shallow foundation system. Analysis of the shallow foundation behavior indicated resonance of the field test structure and the corresponding pressure generation.

FIELD-TEST DATA FROM SOIL-STRUCTURE INTERACTION OF SHALLOW AND DEEP FOUNDATIONS

A THESIS

Presented to the Department of Civil Engineering and

Construction Engineering Management

California State University, Long Beach

In Partial Fulfillment

of the Requirements for the Degree

Masters of Science in Civil Engineering

Committee Members:

Lisa M. Star, Ph.D. (Chair)
Yu-Fu Ko, Ph.D.
Emelinda M. Parentela, Ph.D.

College Designee:

Antonella Sciortino, Ph.D.

By Peter D. Fourtounis

B.S., 2011 California State University, Long Beach

May 2015

ACKNOWLEDGEMENTS

I would like to thank my advisor Dr. Lisa M. Star, for her patience, understanding, and guidance during this process. Her optimism, positive approach and ability to make the topic interesting and easy to understand motivated me. I would like to thank all the professors that influenced me throughout my undergraduate and graduate career at California State University, Long Beach, which include those on my committee. I would like to also thank my graduate committee for reviewing this thesis and providing feedback. I would like to acknowledge Dr. Asli Kurtulus with the University of Texas at Austin and Dr. Lisa M. Star with the University of California, Los Angeles, with respect to their postgraduate work and their contributions in the form of raw data that allowed me to produce this thesis. I would also like to acknowledge my employer, NMG Geotechnical, Inc., for their constant support and understanding throughout my graduate coursework and thesis. Finally, I would like to express my sincere thanks to my family and the Demos family for the support and positive reinforcement they have provided throughout my life and pertaining to this work.

Dedication

I dedicate this thesis to my late mother, Asimina Jasmine Tavernakis, for being the best thing that ever happened to me, my champion and the driving force of all my accomplishments in life.

TABLE OF CONTENTS

Page

ACKNOWLEDGEMENTS iii

LIST OF TABLES vi

LIST OF FIGURES... vii

CHAPTER

1. INTRODUCTION.. 1

1.1 Limitations of Current Practice and Need for SSI Awareness 1
1.2 Background on Soil-Structure Interaction 2
1.2.1 Inertial Interaction 2
1.2.2 Kinematic Interaction 8
1.3 Stiffness and Damping Equations for Shallow Foundations 9
1.4 Objective.. 12
1.5 Scope and Organization 12

2. DYNAMIC STIFFNESS AND DAMPING OF A RIGID PILE FOUNDATION FROM FORCED VIBRATION LOADING..................... 14

2.1 Introduction 14
2.2 Background.. 15
2.3 Deriving Impedance Functions for Deep Foundations.......................... 17
2.4 Objective.. 20
2.5 Method of Deriving Impedance Functions for a Deep Foundation........ 21
2.6 Data from Forced Vibration Field Testing of Pile Foundations............. 24
2.7 Analysis of Impedance Functions from Field-Test Data........................ 26
2.8 Conclusions 29

3. SHALLOW FOUNDATION PRESSURE DISTRIBUTION DURING FORCED VIBRATION LOADING 30

3.1 Introduction 30
3.2 Background.. 31
3.2.1 Experimental Design and Field Test Setup 31

CHAPTER Page

3.3 Pressure Cell Sensor Set-up 40
3.4 Analysis of Pressure Cell Data 42
3.5 Conclusions 48

4. CONCLUSIONS AND SUGGESTIONS FOR FUTURE WORK 50

4.1 Summary of Research Findings 50
4.2 Suggestions for Future Work 51

APPENDICES 53

A. GRAPHICAL RESULTS FROM 21 PRESSURE CELL TESTS AT WLA SITE 54

B. MATLAB CODES 181

REFERENCES 193

LIST OF TABLES

TABLE Page

2.1. (From Table 5.2 Kurtulus 2006) Table Depicting Sequence of Loading of the Test Drilled Shaft 27

3.1. Functioning Pressure Cell Data Recorded at WLA with Mighty Mouse Shaker 44

LIST OF FIGURES

FIGURE Page

1.1. (From NIST 2012) Figure depicting deflections resulting from forces applied to: (a) fixed-base model denoting force and displacement; and (b) model with horizontal, vertical and rotational movement located at its base 5

1.2. (From NIST 2012) Spectral acceleration (base shear) graphs depicting period lengthening combined with a change in damping as a result of inertial SSI effects 7

1.3. (From Kramer 1996) Illustration depicting the concept of base-slab averaging with and without the presence of a foundation.. 9

2.1. (From NIST 2012) Plot of dynamic stiffness modifier and damping ratio for lateral and vertical loading of a single pile foundation 17

2.2. Schematic of a) simple structure with instrumentation and b) model of soil, foundation and a single degree-of-freedom structure used to derive impedance functions (adapted fromTileylioglu et al. (2011)).................... 18

2.3. Free-body diagram illustrating given variables involved with a deepened foundation under forced vibration loading................................. 22

2.4. (From Kurtulus 2006) Illustration with generalized locations depicting the testing arrangement for measuring shear wave propagation in situ using a deep foundation system 25

2.5. (From Figure 5.8 Kurtulus 2006) Graphical representation of forced vibration acting on drilled shaft illustrating 15 cycles with embedded sensor G2 noted by the blue line 28

3.1. (From Star 2011) Schematic of portable UCLA SSI test structure.................. 32

3.2. (From Star 2011) Triaxial accelerometer locations on the test structure 33

FIGURE Page

3.3. (From Star 2011) Location of installed triaxial accelerometer on the test structure 34

3.4. (From Star 2001) Picture of LVDT installed on corner of foundation slab........ 35

3.5. (From Star 2011) Picture of Atom Ant used for loading of SSI test structure 36

3.6. (From Star 2011) Mighty Mouse Eccentric Mass Shaker used for loading of test structure 37

3.7. (From Star 2011) Tri-axial vibroseis shaker truck 39

3.8. Pressure cells similar to those used in UCLA field test (Photo: A. Lemnitzer)........ 40

3.9. (From Star 2011) Pressure cells located on foundation subgrade prior to concrete pour 41

3.10. (From Star 2011) Locations of eight pressure cells on foundation slab........ 42

3.11. Pressure versus time graphs from test 2.2.20; (a) indicates non-functioning pressure cell while (b) indicates functioning pressure cell........ 46

3.12. FFT amplitude versus frequency graphs from test 2.2.20; (a) indicates non-functioning pressure cell while (b) indicates functioning pressure cell 47

CHAPTER 1

INTRODUCTION

1.1 Limitations of Current Practice and Need for SSI Awareness

Soil-structure interaction (SSI) is the study of the relationship between three major engineering components found in most civil structures: the superstructure, the foundation that supports it, and the adjacent soil. When we refer to a SSI system, we refer to all three components and their interconnected behavior. When the SSI system is subjected to dynamic loading, such as during an earthquake, the three components behave in a complex manner, where each component heavily influences the behavior of the others. When a structure is present at the time of ground motion there will be a dynamic relationship between the soil and structure. The combination of the soil influencing the motion of the structure and the reaction of the structure to the soil is the subject of ongoing research by geotechnical and structural engineers.

Conventional engineering design practice relies on code-based prescriptive requirements for demand specification and structural detailing. SSI effects have typically been ignored in this practice, because of the misguided perception that this omission will always result in a conservative error. As will be discussed later in this thesis, this is not always true. Furthermore, since some analysis schemes, such as performance-based design, depend not on conservatism, but on accurately evaluating building response, any deliberate error would be counterproductive. Many of these issues can be attributed to a poor understanding of the fundamentals and principles of SSI. It is not taught in most graduate programs and the literature that has been published pertaining to SSI is often difficult to understand and involves complicated mathematical equations and derivations. However, as more practitioners become aware of the problems associated with the omission of key details, there has been an increasing push to consider SSI effects in design.

There are still technical hurdles related to the understanding of SSI to be addressed by researchers. Although the theoretical understandings of SSI effects have improved, the availability of field-test data and the analysis of that data has not kept up. There are gaps in the understanding of soil stiffness and damping, as well as soil-foundation pressure behavior as a result of forced vibration. In this thesis I analyze data from several field performance tests with the goal of providing insights into SSI effects for systems with deep and shallow foundations.

1.2 Background on Soil-Structure Interaction

The complex behavior of a SSI system is a challenge for engineers to describe and model. In order to better understand SSI, it is useful to consider the overall phenomena as consisting of two primary effects: inertial and kinematic interaction effects, as suggested by Whitman in 1975 (Kausel 2010).

1.2.1 Inertial Interaction

Inertial interaction effects arise from the inertia that develops in massive systems undergoing dynamic loading. When structures and foundations are subjected to dynamic loading, the inertia of the system imposes forces on the structure including base shear, moment, and torsion. These forces have the potential to cause damage to the structure and disrupt the foundation. As engineers, we want to avoid adverse effects due to inertial interaction and do our best to predict possible complications with reasonable certainty.

We know that inertial loads must be transferred from the structure, into the supporting soil. Soils and foundations are not rigid, so when the loads are imposed, the soil displaces. The flexibility of the soil-foundation interface significantly contributes to the overall flexibility of the structure.

In addition to the flexibility contributed by the soil, the soil deformations also provide an important source of energy damping. Chopra (1995) describes damping force as a process by which free vibration steadily diminishes in amplitude. In structures, damping comes from friction between the structural components and material damping from cyclic loading of structural materials such as steel and concrete. It is generally impractical to model the details of the damping in structures explicitly. Instead damping is often accounted for using a general damping ratio for the structural system, usually taken to be about 5% according to the National Institute of Standards and Technology (NIST 2012).

When a structure experiences inertial interaction effects, the loading causes straining of the soil, which dissipates energy through hysteretic material damping. This damping is similar to the material damping that the structure contributes, which is well known to engineers. In terms of material damping, soil damping ratios are often higher than other materials such as concrete. Another substantial source of damping comes from geometric or radiation damping. As the foundation displaces, energy waves are transmitted into the soil and radiate away from the foundation. Since the soil is effectively infinitely large, as the energy wave spreads away from the structure, the energy is lost. This behavior occurs even in elastic media and is typically much greater than structural material damping as well.

Figure 1.1 shows a schematic of the effect that soil flexibility has on structure behavior, versus a structure founded on a rigid base (no soil spring). Figure 1.1(a) illustrates a rigid base system, not allowing foundation movement. As a force (F) is applied, the structure will bend, generating a moment, and there will be a corresponding displacement (Δ) at the top of the structure. The displacement depends on the stiffness of the structure (k), and can be calculated using the well-known equation ($\Delta = F/k$).

Figure 1.1(b) depicts a flexible base system. The flexibility of the soil is often modeled as viscoelastic behavior. Springs and dashpots are used to illustrate the soil response to inertial effects. A dashpot acts as a damper that resists motion using viscous friction and the spring resists motion elastically. Springs and dashpots are attached to the foundation in Figure 1.1(b) to depict the response of the soil to translational, rotational and vertical modes of movement. The foundation can translate in the x direction (u_f), and rotate (θ). This figure does not depict possible out of plane movements or a third possible in-plane movement, vertical translation (u_z). When a force (F) acts on the mass in the x direction, the structure will still deform by an amount (Δ). There will also be additional displacement from the foundation translation (u_f) and the effect of rotation (θ). Foundation displacement will depend on both the translational, vertical and rotational stiffness k_x, k_z and k_{yy}.

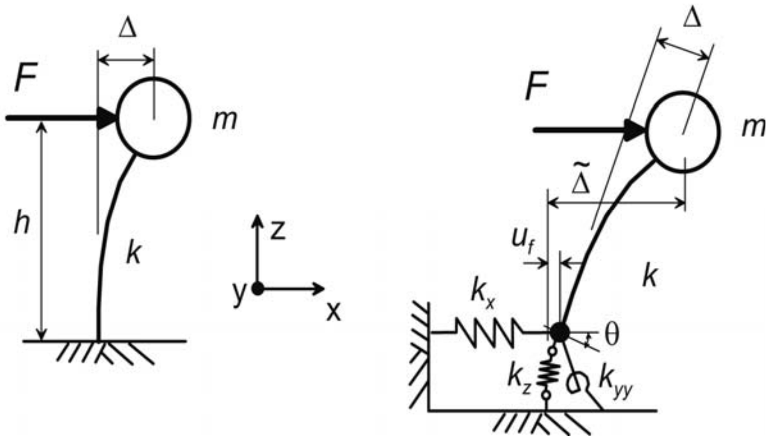

(a) (b)

FIGURE 1.1. (From NIST 2012) Figure depicting deflections resulting from forces applied to: (a) fixed-base model denoting force and displacement; and (b) model with horizontal, vertical and rotational springs located at its base.

As depicted in Figure 1.1(b), the total deflection of the flexible base system ($\tilde{\Delta}$) can be represented as:

$$\tilde{\Delta} = \frac{F}{k} + u_f + \theta * h \tag{1-1 a}$$

or

$$\tilde{\Delta} = \frac{F}{k} + \frac{F}{k_x} + \left(\frac{F * h}{k_{yy}}\right) h \tag{1-1 b}$$

Inertial interaction effects alter the behavior of the SSI system in key ways, some of which are easy to predict and others that are not. The rigid base condition is often considered the default condition, and the effect of SSI is measured as the difference between the theoretical rigid base condition and the true response of the structure. In addition to the increase in damping for the SSI system relative to the rigid base system, the flexibility of the soil will lengthen the response period of the structure. This can be intuitively understood, but has been shown mathematically by Veletsos and Meek (1974).

The square root of the period can be expressed by relating period (T), mass (m) and stiffness (k).

$$T = \frac{2\pi}{\omega} = 2\pi\sqrt{\frac{m}{k}} \tag{1-2}$$

Taking the square and substituting ($\Delta = F/k$) gives:

$$T^2 = (2\pi)^2\frac{m}{k} = (2\pi)^2\frac{m}{(F/\Delta)} = (2\pi)^2\frac{m\Delta}{F} \tag{1-3}$$

Substituting Equation (1-1 b) into Equation (1-3) yields the flexible base period ($\tilde{T}$):

$$\tilde{T}^2 = (2\pi)^2 m\left[\frac{1}{k} + \frac{1}{k_x} + \frac{h^2}{k_{yy}}\right] \tag{1-4}$$

If Equation 1-4 is combined with Equation 1-2, it will result in:

$$\left(\frac{\tilde{T}}{T}\right)^2 = \frac{k}{(2\pi)^2 m} * (2\pi)^2 m * \left[\frac{1}{k} + \frac{1}{k_x} + \frac{h^2}{k_{yy}}\right] \tag{1-5}$$

Simplifying Equation 1-5 we can see the period lengthening equation expressed as (Veletsos and Meek 1974):

$$\frac{\tilde{T}}{T} = \sqrt{1 + \frac{k}{k_x} + \frac{kh^2}{k_{yy}}} \tag{1-6}$$

Veletsos and Meeks' equation can be used for both single-degree of freedom (SDOF) and multi-degree of freedom (MDOF) applications. When a MDOF structure is analyzed, the first-mode shape is used, since it typically dominates the behavior. Therefore the height (h) is measured up to the first-mode center of mass. Another name for this dimension is the effective modal height and can be approximated through multiplying the total height of the structure by two-thirds according to ASCE/SEI 7-10 (ASCE 2010).

We can examine a spectral acceleration diagram in order to investigate some of the effects that these changes may have on the structure performance. Figure 1.2 shows a schematic of the spectral acceleration (S_a) on the y-axis of a structure with a first mode period of T in a linear and log scale on the x-axis. We start by examining the effect of SSI on a structure with a long period, such as a tall, slender building. Using the figure, we can find the corresponding S_a value for a structure with a large fixed-base period (T) and a structural damping ratio of (β_i). We can compare this value of S_a to that of the same structure, when accounting for a flexible base. The increased flexibility causes the period to elongate to ($\tilde{T}$). The flexible foundation also increased the damping ratio to (β_0), due to soil material and radiation damping. When both the increase in period and damping are considered, the spectral acceleration will be lower. We can also consider the case of a relatively stiff structure, such a low-rise, reinforced concrete structure. In this case, the fixed-base period would be short. The increase in period caused by period elongation for the flexible-base case may cause an increase in the predicted spectral acceleration.

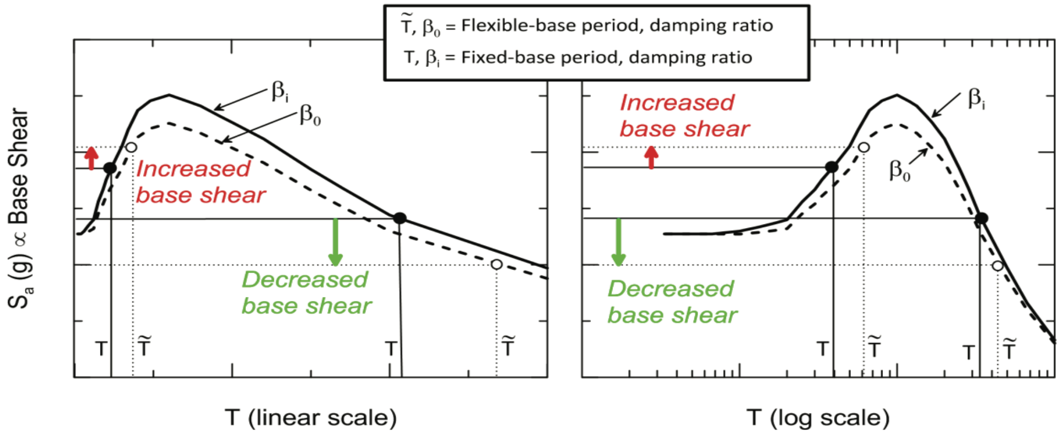

FIGURE 1.2. (From NIST 2012) Spectral acceleration (base shear) graphs depicting period lengthening combined with a change in damping as a result of inertial SSI effects.

Unfortunately, the most frequent scenario when engineers examine SSI effects is when designing a large project, such as a tall building. In that case SSI effects are potentially beneficial, due to the lower spectral acceleration predicted. Because of this some engineers have the mistaken impression that SSI is always beneficial, and may be safely ignored. However, the more critical case may be for the short period buildings where SSI effects will tend to increase the predicted spectral acceleration. If SSI effects are ignored, this may result in an unconservative error.

1.2.2 Kinematic Interaction

Kinematic interaction effects impact the ground motions that the structure will experience during an earthquake. There are two types of ground motions that can be measured: free-field motions and foundation motions. Specifically, free-field motions are measured in the field, outside of the influence of any structures or foundations. Foundation motions are measured at the site of a foundation, and include the effects that the foundation has on the recorded motion.

There are certain phenomena to which we can attribute the deviation of the foundation motion relative to the free-field motion. As earthquake waves pass through the soil on their way to the ground surface, they create soil displacements. Therefore, a relatively rigid foundation near or at the soil surface subjected to such movement cannot behave in a manner similar to the soil. Kinematic interaction describes the movement experienced by the foundation relative to the movement that the soil alone, would experience. Figure 1.3 shows the variations in free field ground motion as dashed lines. The foundation structure, being much more rigid than the soil, is unable to respond in a similar manner. For example, the flexural stiffness prevents a foundation from following the variation in vertical soil displacements (Figure 1.3(a)), or horizontal soil displacement (Figure 1.3(b)), and the axial stiffness prevents large shortening or elongation of the foundation (Figure 1.3(c)). The result is that the soil motions must be averaged over the foundation area, as a function of the foundation's size and stiffness, in a phenomenon known as base-slab averaging. Embedded foundations are also subject to embedment effects, where input motions tend to be reduced, because ground motions are smaller at depth, compared to the soil surface.

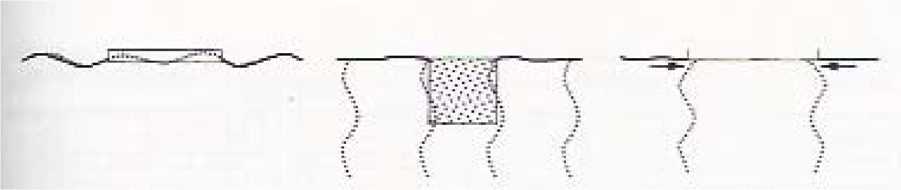

(a) (b) (c)

FIGURE 1.3. (From Kramer 1996) Illustration depicting the concept of base-slab averaging with and without the presence of a foundation.

1.3 Stiffness and Damping Equations for Shallow Foundations

When we mathematically describe the dynamic behavior of any system, we can use the equation of motion. We can write it for a simple SDOF system as:

$$F = ma + cv + kd \tag{1-7}$$

Where m is the mass, *c* is the damping, *k* is stiffness, *a* is acceleration, *v* is velocity, *d* is displacement, and *F* is the force driving the dynamic behavior.

Parameters *a*, *v* and *d* are all functions of time. We can apply the Fourier transform to the equation of motion, to investigate the relationship as a function of frequency instead. In the Fourier domain, acceleration, velocity and damping are related by the following relationship:

$$\frac{a}{-\omega^2} = \frac{v}{i\omega} = d$$

Where ω is the angular frequency measured in radians per second. In the Fourier domain the equations of motion, can thus be written as:

$$F = -m\omega^2 d + ci\omega d + kd$$

or rewritten as:

$$F = -m\omega^2 d + (ci\omega + k)d$$

The stiffness and damping terms are now combined into a single term, known in SSI research as an impedance function. The term has both a real and an imaginary part, making it complex-valued. It is expressed in classical solutions (Luco and Westman 1971; Veletsos and Wei 1971) as:

$$\bar{k}_j = k_j + i\omega c_j \tag{1-8a}$$

Where $\bar{k}_j$ is the complex-valued impedance function, k_j and c_j are frequency-dependent foundation stiffness and damping variables. Subscript j is used here to denote that in a MDOF system, this complex stiffness would apply to a particular mode of translational displacement or rotation. An alternative form for Equation 1-8a is written as (NIST 2012):

$$\bar{k}_j = k_j(1 + 2i\beta_j) \tag{1-8b}$$

Where;

$$\beta_j = \frac{\omega c_j}{2k_j} \text{ (defined for } k_j>0) \tag{1-9}$$

At resonance β_j is equal to the critical damping ratio (Clough and Penzian 1993).

When studying inertial interaction effects, the stiffness and damping of the soil play a key role in the behavior of the soil-structure system. There have been many studies that proposed mathematically derived stiffness and damping equations. The proposed solutions to these equations generally assume uniform soil conditions and a rigid foundation. Impedance functions are presented in this complex-valued formulation as shown in equations 1-8a and 1-8b, because it allows for frequency-dependent values of stiffness and damping.

For a rigid rectangular foundation, which is reviewed in Chapter 3, resting on a surface of half-space with shear wave velocity (V_s), Pais and Kausel (1988), Gazetas (1991), and Mylonakis et al. (2006) reviewed impedance solutions. They produced equations for stiffness and damping terms in Equation 1-8. The solutions describe translational stiffness and damping in the x, y and z axes. Rotational stiffness and damping about those axes are denoted using xx, yy, and zz.

$$k_j = K_j \times \alpha_j \tag{1-10a}$$

Where;

$$K_j = GB^m f(B/L, \nu),\ \alpha_j = \alpha_j(\mathrm{B/L}, \alpha_0) \tag{1-10b}$$

Stiffness (k_j) is proportional to the static foundation stiffness at zero frequency for mode j, and the dynamic stiffness modifiers (α_j). K_j depends on the soil shear modulus (G), foundation dimensions, and soil Poisson ratio (ν). For translation and rotation, $m = 1$ and $m = 3$ respectively. Shear modulus is related to modulus reduction and should change with increasing shear strain amplitude. Maximum shear modulus (G_{max}) is equal to $V_s^2\rho_s$, where V_s is the shear wave velocity of the soil, and ρ_s is the soil mass density. The dynamic stiffness modifiers are dependent on dimensionless frequency (α_0):

$$\alpha_0 = \frac{\omega B}{V_s} \tag{1-11}$$

1.4 Objective

Impedance function solutions exist for simplified cases for shallow and deep foundations. One objective of this thesis is to develop a better understanding of deepened foundations and how dynamic loading affects stiffness and damping of the soil in the system. The goal is to measure the soil stiffness and damping behavior in a deep foundation installed in the field. By measuring the behavior in the field we can compare and validate impedance function solutions. Because stiffness and damping cannot be directly measured, we develop methods in order to back calculate the values.

It is known that soil stiffness and damping will affect the behavior of the structure, altering the loads that structural members will experience. Another objective of this thesis is to measure pressures beneath shallow foundations given an array of dynamic inputs.

1.5 Scope and Organization

In this paper I will discuss two relevant topics related to SSI. In Chapter 2 I will discuss the dynamic stiffness and damping of a rigid pile foundation during forced vibration loading. Chapter 3 discusses the foundation pressure distribution of a shallow foundation during forced vibration loading. This work spans two very important areas of study of SSI; one analyzes a deep foundation while the other explores the behavior of a shallow foundation where both are experiencing seismic type loading.

In the second chapter of this thesis I focus on deep foundation systems. Field testing was performed to evaluate in situ nonlinear shear modulus of soils using long drilled shafts in a University of Texas at Austin study. Data that was collected included shaker force inputs, drilled shaft displacements, shear wave velocities, and shear strains. I will provide background on the field testing and data that was collected. I present the development of a method of determining impedance functions for deep foundations from field data, including the method for deriving the equations. Finally, I will present the results of the analysis of the field test data and discuss the limitations.

In the third chapter I discuss pressures beneath shallow foundations and provide a brief introduction with respect to SSI. I will provide background information regarding the field test sites, experimental design, field test setup, and the data collected. Finally, I will interpret the data and discuss the findings.

In the fourth and final chapter I will present conclusions, including suggestions for future work pertaining to these studies and the field of SSI.

CHAPTER 2

DYNAMIC STIFFNESS AND DAMPING OF A RIGID PILE FOUNDATION FROM FORCED VIBRATION

2.1 Introduction

The engineering community is increasingly using advanced modeling to better predict the behavior of structures subjected to earthquake or other dynamic loads with the purpose to improve the safety and economy of design. As described in Chapter 1 of this thesis, during the dynamic loading of a deep foundation one will find the flexibility and damping of the soils brought on as a result of SSI, which may have a large impact on the behavior of the entire system. Accurate models of the soil behavior are needed by engineering practitioners today but are scarce. Researchers have developed methods to derive analytical models to describe soil stiffness and damping properties in the form of frequency-dependent impedance functions, for simplified conditions. There are past studies validating models of dynamic loading of shallow foundations using field scale test data (Tileylioglu et al. 2011; Star 2011; Givens 2012). However, there have been no studies using high quality field test data under realistic field conditions in an effort to validate analytical models for dynamic loading of deep foundations. This limitation in model validation has contributed to reluctance and uncertainty in the application of the models in engineering practice.

In this study I seek to analyze data in order to allow the validation of existing analytical models of SSI effects. A procedure for deriving impedance functions from field data gathered during the dynamic loading of pile foundations is developed and the procedure is then applied using existing data from past field investigations.

This chapter begins with a review of commonly used analytical models of frequency-dependent stiffness and damping, which is represented mathematically as a complex-valued impedance function. An inversion procedure for deriving impedance functions, from forced vibration loading of a pile foundation, is then presented. Finally, I focus on the derivation of impedance functions, using data collected during forced vibration field tests by researchers at the University of Texas, Austin (Kurtulus 2006).

2.2 Background

The stiffness and damping associated with inertial interaction effects of soil-foundation behavior is commonly represented by impedance functions. As described in Chapter 1, impedance functions commonly are represented in the Fourier domain, in order to represent the frequency dependence of the stiffness and damping functions.

In the literature, impedance functions are often represented as complex-valued (Crouse and McGuire 2001; Gazetas 1991; Veletsos and Wei 1971). The functions are often written in the form:

$$\bar{k}_j = k_j + i\omega c_j \tag{1-8a}$$

Where $\bar{k}_j$ is the complex-valued impedance function, k_j and c_j are frequency-dependent foundation stiffness and damping variables, and ω is the angular frequency measured in radians per second. In the equation, i indicates an imaginary number. Subscript j is used here to denote the fact that in a MDOF system, complex stiffness would apply to a particular mode of translational displacement or rotation. Impedances may also be presented in an alternative form through the foundation damping ratio, β:

$$\bar{k}_j = k_j(1 + 2i\beta_j) \tag{1-8b}$$

Where;

$$\beta_j = \frac{\omega c_j}{2k_j}$$

Several researchers have developed equations describing the stiffness and damping terms for both shallow and deep foundation based on elastic solutions for rigid foundations on a homogeneous viscoelastic soil half-space. The stiffness of a pile is commonly represented as the product of the static stiffness and a dynamic modifier:

$$k_j = K_j \times \alpha_j \tag{1-10a}$$

Where;

$$K_j = \chi_j E_s d, \ \ \alpha_j = f(E_p/E_s, \rho_p/\rho_s, w_{sj}, v, a_0) \tag{1-10b}$$

Where χ_j is a dimensionless constant for vibration mode j; d is the pile diameter; E_s and E_p are the Young's moduli for soil and pile materials, respectively; ρ_s and ρ_p are the mass densities for soil and pile materials, respectively; v is the Poisson's ratio of the soil; w_{sj} represents a weight factor for soil stiffness contribution for the vibration mode and a_0 is a dimensionless frequency for piles calculated as:

$$\alpha_0 = \frac{\omega d}{V_s} \tag{1-11}$$

Where V_S is the shear wave velocity of the soil.

Figure 2.1 summarizes the equations for dynamic modifier α_j and radiation damping β_j for a rigid surface foundation presented by Pais and Kausel (1988).

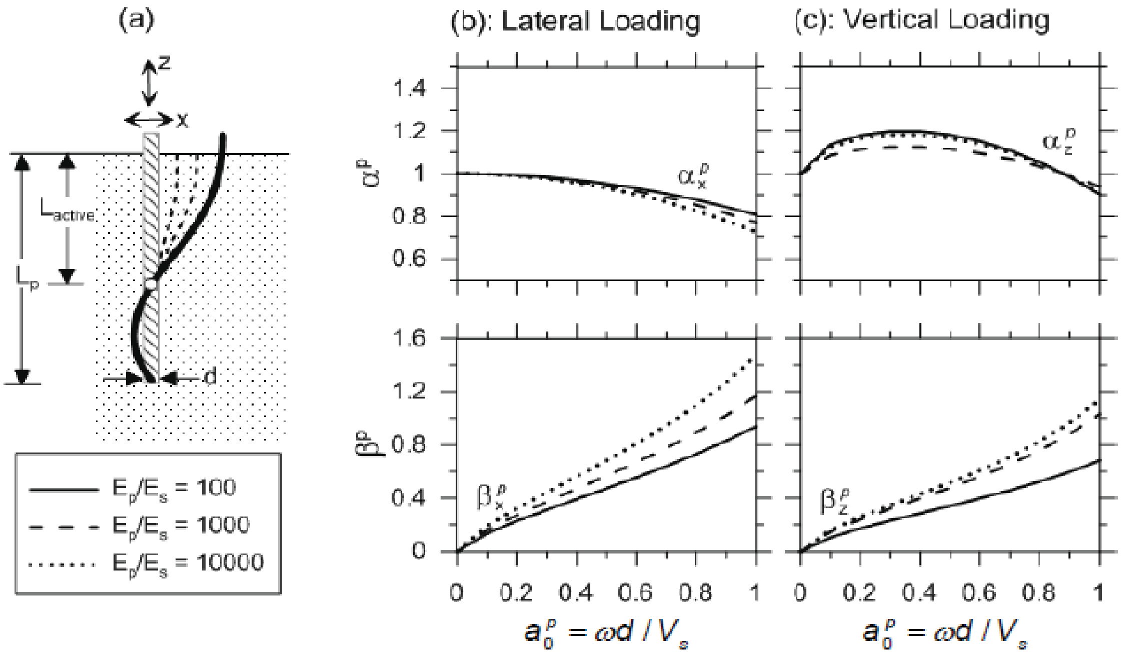

FIGURE 2.1. (From NIST 2012) Plot of dynamic stiffness modifier and damping ratio for lateral and vertical loading of a single pile foundation.

2.3 Deriving Impedance Functions for Deep Foundations

The objective of this study is to determine the stiffness and damping of the soil adjacent and below a deep foundation while it is experiencing vibration loading. A relevant journal article discussing dynamic stiffness and damping of a shallow foundation subjected to forced vibration loading is referenced in this thesis (Tileylioglu et al. 2011). The researchers evaluated impedance functions using data from forced vibration testing of a structure in the field. A theoretical model for evaluating the frequency-dependent impedance function using field data was proposed. By exploring stiffness and damping in the frequency-dependent domain the authors were able to simplify the experiment and obtain information that they can compare to published analytical models.

Tileylioglu et al. (2011) developed equations for calculating impedance functions based on acceleration recordings from a field structure. Roof translation, and foundation-level translation, and rotation as well as the force being applied must be measured. Figure 2.2 shows a schematic of a structure and instrumentation that could be deployed to determine impedance functions. The proposed equations are based on a simplified model of the structure system, which allows foundation translation and rotation, and a translational degree of freedom at the top of the structure. The model structure has a roof mass (m_s) and foundation slab (m_f) and the structure system is modeled as a single massless cantilevered beam with a stiffness and damping (k_s and c_s). Translational and rotational springs and dampers represent the soil flexibility and damping.

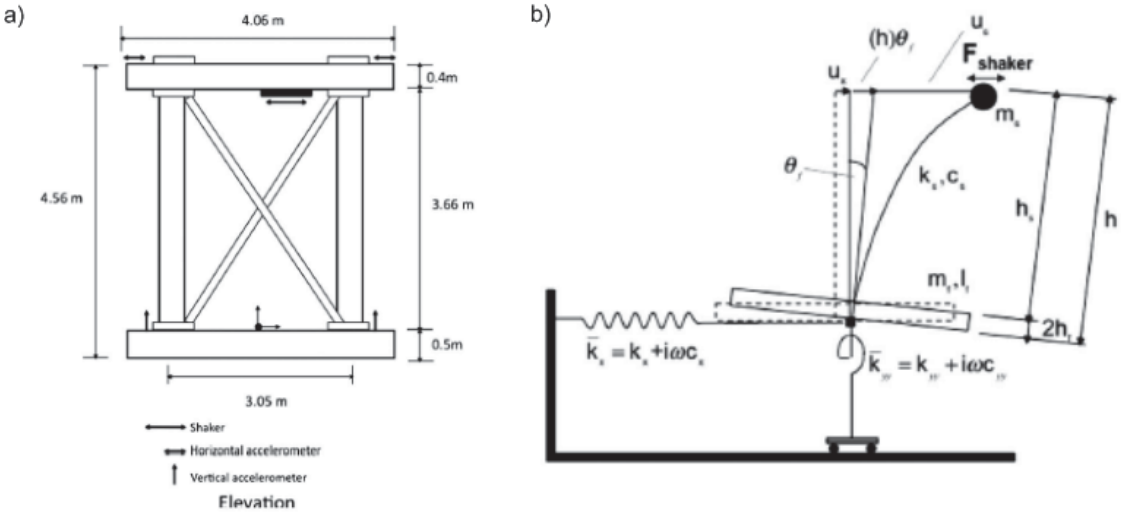

FIGURE 2.2. Schematic of a) simple structure with instrumentation and b) model of soil, foundation and a single degree-of-freedom structure used to derive impedance functions (adapted from Tileylioglu et al. (2011)).

Tileylioglu et al. (2011) set up equations of motion for the model structure as:

$$F_{sh} = M\ddot{U} + C\dot{U} + KU$$

Where **M** is the mass matrix, **C** is the damping matrix, and **K** is the stiffness matrix of the system. $\mathbf{F}_{sh}$ is the shaker force vector and U represents displacements and rotations for each degree of freedom within the system; $\ddot{U}$ = acceleration, $\dot{U}$ = velocity. Written in matrix form U is equal to:

$$U = [u_f \quad \theta_f \quad u_s]^T$$

Where u_f is the foundation translation, θ_f is the foundation rotation, u_s is the structure drift and T indicates matrix transposition.

The matrices can be multiplied and separated into three equations, which can be transformed into the frequency domain through the Fourier transform. In the Fourier domain displacement, velocity and acceleration are related through the equations:

$$\frac{\ddot{u}}{-\omega^2} = \frac{\dot{u}}{i\omega} = u$$

allowing the equations to be written in terms of displacements. Finally the equations can be rearranged to solve for the complex impedances for foundation rocking and translation:

$$\bar{k}_x = \frac{F_{sh} + \omega^2 m_s\left(u_f + h\theta_f + u_s\right) + \omega^2 m_f\left(u_f + h\theta_f\right)}{u_f}$$

$$\bar{k}_{yy} = \frac{hF_{sh} + \omega^2 m_s h\left(u_f + h\theta_f + u_s\right) + \omega^2 I_f\theta_f + \omega^2 m_f h_f\left(u_f + h\theta_f\right)}{\theta_f}$$

As shown in equation 1-8b, the real parts of $\bar{k}$ gives the stiffness coefficient and the complex parts can be related to damping. Further information on the validation of this method can be found in Tileylioglu et al. (2011).

Using similar reasoning to this method I will develop a simple model for a SDOF deep foundation system. The Fourier transform will be employed to represent the equations in the frequency domain lumping stiffness and damping together into the complex stiffness that I will be solving for. The fundamentals of this particular model are based on the equations given below.

2.4 Objective

The primary objective of this study is to develop a model of the behavior of a rigid deep foundation mathematically in the same method as the work by Tileylioglu et al. (2011). Using MATLAB, and the field test data, we will calculate impedance functions. The field data is provided by others from the University of Texas at Austin. The variables that were measured include the force of the vibration source, the mass of the SSI structure, and the acceleration, velocity or displacement of the SSI structure. Once impedance functions are generated from the data, graphs of stiffness versus frequency and damping versus frequency can be used to compare the results from analytical models.

Theoretical predictions derived by mathematical equations provide us with a baseline to compare our results. There are limitations in the analytical models in that they do not account for many real life complications including excessively deep foundations, different ranges of frequencies, large strain variations, and stratified soils. The method of calculating impedance functions developed in this chapter will provide a way for more complicated field conditions to be evaluated and compared to simplified analytical models.

2.5 Method of Deriving Impedance Functions for a Deep Foundation

As mentioned above, there are analytical solutions available to calculate the frequency dependent, complex valued impedance functions for vertical vibration of a deep foundation. There has not, however, been very much data available to validate the solutions. Past researchers have developed methods to analyze field data to validate impedance functions for shallow foundations. In this section I will develop a similar analysis method to analyze field data for vertical loading of a deep foundation.

The equation of motion for a deep foundation subjected to vertical loading can be written as:

$$F_{sh} = ma + cv + kd \tag{2-1}$$

Where;

$$\begin{gathered} F_{sh} = \text{ Vertical Shaker Force, } m = \text{mass of the foundation,} \\ a = \text{vertical acceleration of the foundation, } c = \text{vertical soil damping} \\ \\ v = \text{vertical velocity of the foundation, } k = \text{vertical soil stiffness,} \\ d = \text{vertical displacement of the foundation} \end{gathered} \tag{2-2}$$

Figure 2.3 below illustrates the model of a deepened foundation and indicates where each parameter is located. The soil spring in this case represents both the stiffness and damping in the vertical or Y direction (k_{y}, c_{y}), at that location. The mass of the pile (m_s) is located at the centroid. Displacement is measured in the vertical direction. Finally, the vertical shaker force is encountered at the exposed top portion of the pile. The upward Y direction is taken as the positive direction in analyzing this problem.

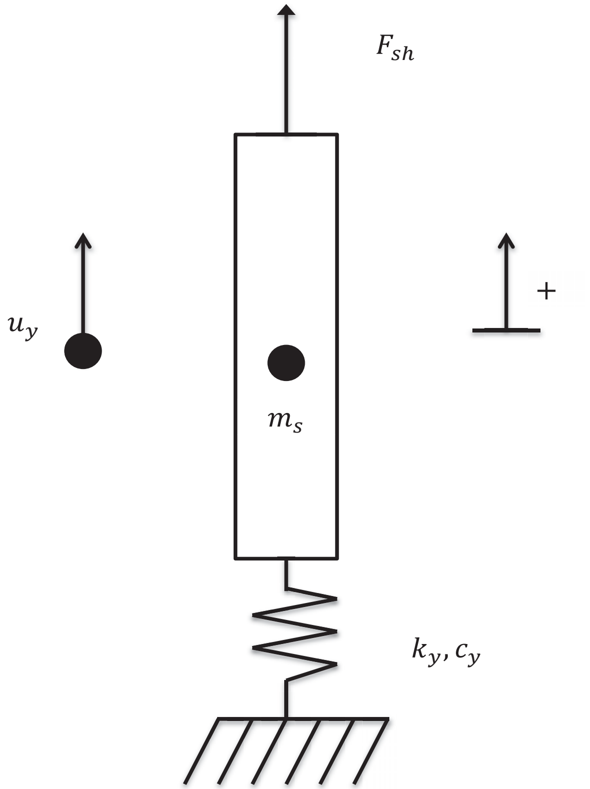

FIGURE 2.3. Free-body diagram illustrating given variables involved with a deepened foundation under forced vibration loading.

For convenience, we will write displacement as $u =$ displacement. Acceleration, and velocity can then be expressed in derivative form as:

$$\ddot{u} = \text{Acceleration}, \qquad \dot{u} = \text{Velocity} \tag{2-3}$$

Substituting into equation (2-1) it can be written as follows:

$$F_{sh} = m\ddot{u}_y + c\dot{u}_y + ku_y \tag{2-4}$$

Where;

$u_y =$ Pile movement in vertical direction

The Fourier transform is used to translate the given function into an easily solvable equation represented in the frequency domain. In general, the Fourier Transform is a method involving the decomposition of a generic function using the superposition principle creating an easier to solve symmetric function. In executing this function, we convert the time dependence of the displacement, velocity and acceleration, into a frequency dependent function.

In the frequency domain the acceleration, velocity and displacement are easily related to each other as:

$$\begin{gathered} \ddot{\bar{u}} = -\omega^2\bar{u} \\ \dot{\bar{u}} = \omega i\bar{u} \\ \bar{u} = \bar{u} \end{gathered} \tag{2-5}$$

Where i represents an imaginary number, ω is the rotational frequency, and the over bar indicates that the variables are frequency dependent. Substituting the equations from 2-5 into equation 2-4 we achieve an equation as follows;

$$F_{sh} = m(-\omega^2\bar{u}) + c_y\omega i\bar{u} + k_y\bar{u} \tag{2-6}$$

Combining stiffness and damping together we can simplify equation 2-6 further creating a term known as the complex stiffness denoted by $\bar{k}$.

$$\begin{aligned} F_{sh} &= -m_s\omega^2\bar{u}_y + \left(k_y + c_y\omega i\right)\bar{u}_y \\ &= -m\omega^2\bar{u}_y + \bar{k}_y\bar{u}_y \end{aligned} \tag{2-7}$$

Where $\bar{k}$ is equal to;

$$\bar{k}_y = k_y(1 - 2i\beta_y) \tag{2-8}$$

and damping, β is equal to;

$$\beta_y = \frac{\omega c_y}{2k_y} \tag{2-9}$$

Isolating complex stiffness;

$$\bar{k}_y = \frac{\bar{F}_{sh}+\omega^2 m_s \bar{u}_y}{\bar{u}_y} = \frac{\bar{F}_{sh}}{\bar{u}_y} + \omega^2 m_s \tag{2-10}$$

Solving for complex stiffness;

$$\bar{k}_y = \frac{\bar{F}_{sh}}{\bar{u}_y} + \omega^2 m_s \tag{2-11}$$

Equation 2-11 provides us with a method to solve for the complex, frequency dependent impedance function as a function of the shaker force, the mass of the foundation and the vertical displacement of the foundation.

2.6 Data from Forced Vibration Field Testing of Pile Foundations

A field study was performed at the University of Texas at Austin utilizing drilled shafts acting as deepened foundation systems. Testing involved the application of vertical dynamic loading at the top of the drilled shafts. Embedded sensors and geophones were installed within the drilled shaft and soil adjacent to the drilled shafts to collect data and record shear wave propagation generated from the dynamic loading. A general schematic is shown in Figure 2.4 with approximate locations of sensors and the location of loading. The dynamic loading ranged from small hand-held impact loads to large vibroseis loading with heavy equipment. The goal of the field testing was to measure the linear and non-linear shear moduli and associated shearing strain amplitudes.

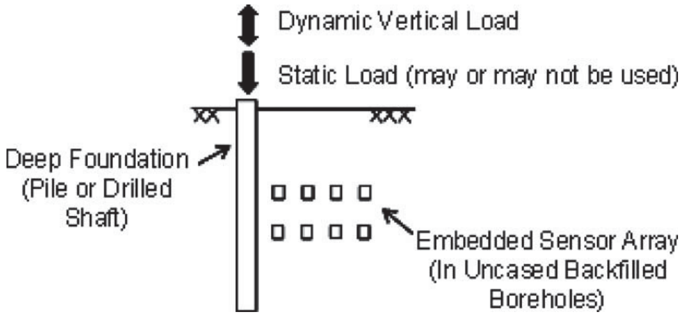

FIGURE 2.4. (From Kurtulus 2006) Illustration with generalized locations depicting the testing arrangement for measuring shear wave propagation in situ using a deep foundation system.

The study was performed using small-scale, prototype experiments at a well sampled and studied field site located in Austin, Texas. Many in situ and laboratory tests were performed to aid in classification and identification of the soil at the test site. Some of the tests performed included Standard Penetration Tests (SPT), Penetration Tests (CPT), and Resonant Column Torsional Shear Tests (RCTS). The study was conducted on two deep foundations: a 30 cm (12 in) diameter, 1.8 m (6 ft) long reinforced drilled shaft, and a 38 cm (15 in) diameter, 3.7 m (12 ft) long reinforced drilled shaft. Dynamic loads over were applied using a large shaker truck. Mass, displacement, velocity, acceleration, and shaker force data were collected. Geophones were used to measure shear wave velocities within the soil. The sensors were backfilled in uncased boreholes and installed in a one-dimensional array. Two geophones were also installed within the reinforced concrete drilled shaft. This allowed for a measurement of shear wave velocity passing through the deep foundation. At the field site in Austin, Texas the groundwater was found to be at a depth of 6.6 m (21.5 ft). The piles were embedded in nonplastic silt (ML) with silty sand (SM) layers. Shale was also encountered at a depth of 11.0 m (36 ft). The CPT results indicated that the upper 5 feet was predominantly sandy, with fines content increasing at depth. A small-strain shear wave velocity (V_S) profile determined an approximate velocity of 183 m/sec (600 fps) inclusive of the upper 3.7 m (12 ft) of soil. During the field experiment, moisture contents were approximately 9%, total unit weights were around 17 kN/m^3 (110 pcf), and the degree of saturation at depth was approximately 36%.

After analyzing Kurtulus's data, certain parameters were uncovered along with recorded data output. The masses of the caissons were estimated to be approximately 1105 (501 kg) and 2210 (1002 kg) pounds for the six and twelve foot caisson. Seismic loading measured in pounds was generated by heavy dynamic load inducing equipment called Thumper and T-rex. Also, loading order also played a factor in the testing of the caissons. Vertical displacements of the caissons were represented graphically and the load-settlement behavior varied. Static loading and reloading ranged from 20 to 40-kips. Settlement at the time of loading ranged from 0.006 (0.015 cm) to 0.055 (0.14 cm) inches. Maximum vertical displacements ranged from 0.02 (0.05 cm) to 0.09 (0.22 cm) inches. Permanent settlement of the deep foundation after the completion of the testing, including loading and reloading, came out to be approximately 0.82 inches (2.08 cm).

The sensors that were studied meticulously were G1 and G2 because they were embedded within the caisson. Kurtulus presents and illustrate in her dissertation the displacements of the drilled shafts throughout cycles of loading and reloading.

2.7 Analysis of Impedance Functions from Field-Test Data

I examined 9 sets of data from the field tests performed at the University of Texas at Austin. Each test had multiple sensor outputs including geophones measuring velocity, and external loading information. Table 2.1 shows the sequence of loading applied to the test drilled shaft. Of particular interest to us is the variation of the dynamic loads applied. In this test sequence the dynamic load amplitude varied from 180 lbs up to 2880 lbs. The loading frequency was consistent across the test sequence with 15 cycles at 55 Hz.

TABLE 2.1. Table Depicting Sequence of Loading of the Test Drilled Shaft.
Note: From table 5.2 Kurtulus 2006.

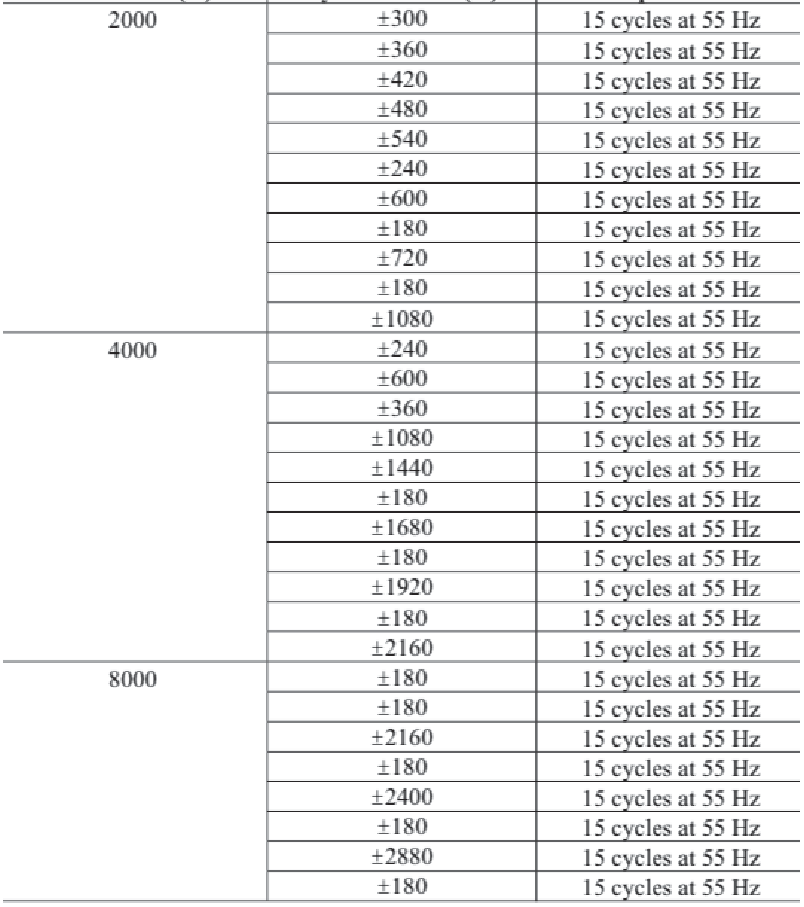

Static Load (lb)	Dynamic Load (lb)	Description of Test
2000	±300	15 cycles at 55 Hz
	±360	15 cycles at 55 Hz
	±420	15 cycles at 55 Hz
	±480	15 cycles at 55 Hz
	±540	15 cycles at 55 Hz
	±240	15 cycles at 55 Hz
	±600	15 cycles at 55 Hz
	±180	15 cycles at 55 Hz
	±720	15 cycles at 55 Hz
	±180	15 cycles at 55 Hz
	±1080	15 cycles at 55 Hz
4000	±240	15 cycles at 55 Hz
	±600	15 cycles at 55 Hz
	±360	15 cycles at 55 Hz
	±1080	15 cycles at 55 Hz
	±1440	15 cycles at 55 Hz
	±180	15 cycles at 55 Hz
	±1680	15 cycles at 55 Hz
	±180	15 cycles at 55 Hz
	±1920	15 cycles at 55 Hz
	±180	15 cycles at 55 Hz
	±2160	15 cycles at 55 Hz
8000	±180	15 cycles at 55 Hz
	±180	15 cycles at 55 Hz
	±2160	15 cycles at 55 Hz
	±180	15 cycles at 55 Hz
	±2400	15 cycles at 55 Hz
	±180	15 cycles at 55 Hz
	±2880	15 cycles at 55 Hz
	±180	15 cycles at 55 Hz

In order to apply equation 2-11 using the field test data, we need to determine the shaker loading function, the mass of the foundation structure and the displacement characteristics of the foundation.

In order to determine the displacement characteristics of the foundation I focused on sensors G1 and G2 because of their location embedded within the drilled shaft. Figure 2.5 below shows velocities measured within the shaft and of adjacent geophones within the soil. Geophone output is represented using velocity and is displayed on the y-axis and time shown in milliseconds on the x-axis. As expected, sensor G2 will experience the highest velocities because of its close proximity (within the shaft) to the loading source while the other sensors show decreasing velocities since they are installed within the soil and at staggered distances away from the drilled shaft. Figure 2.5 depicts sensor G2 which was embedded within the drilled shaft and one can see the 15 cycles at a loading frequency of 55 Hz experienced by the sensor.

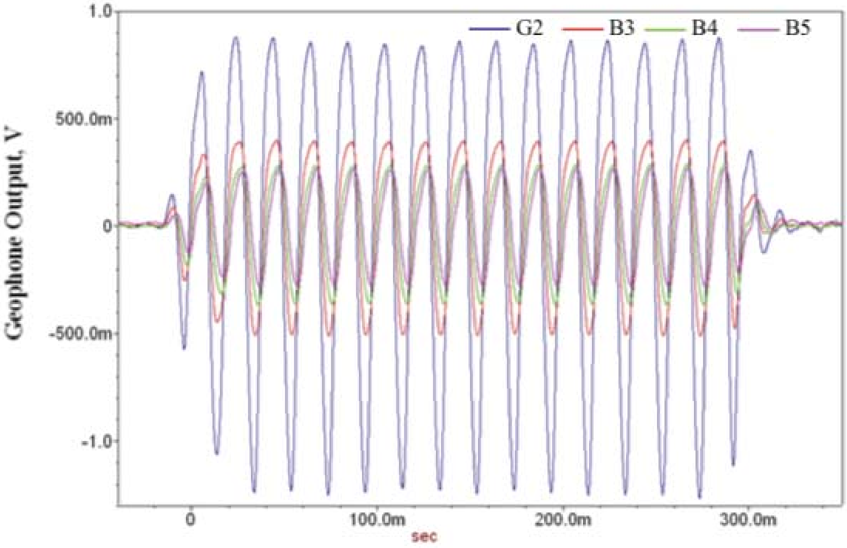

FIGURE 2.5. (From Figure 5.8 Kurtulus 2006) Graphical representation of forced vibration acting on drilled shaft illustrating 15 cycles with embedded sensor G2 noted by the blue line.

Equation 2-11 is formulated in the frequency domain in order to resolve the variation of the impedance functions over the range of frequencies. Unfortunately, since the field data from the University of Texas at Austin field site is dominated by loading at a single frequency, 55 Hz, it is impossible to determine the impedance functions.

2.8 Conclusions

Geotechnical modeling of deep foundations and predicting behavior from seismic loading is a challenging task. Researchers continue to work to validate analytical models for dynamic loading of deep foundations. I used classical impedance function equations combined with a model I developed to break down and analyze a deep foundation system. I used data collected by researchers at the University of Texas at Austin to aid in validating my model. In deriving impedance functions for a deep foundation I was able to begin with an equilibrium equation and conclude by solving for complex stiffness. The complex stiffness describes together the stiffness and damping of surrounding soil as a function of the shaker force, foundation displacement, and mass of the deep foundation. I described the applicable details, methodologies and procedures as I understood them from Dr. Kurtulus's dissertation which aided in this thesis.

After analyzing data received from Dr. Kurtulus I was able to determine it did not provide broadband frequency data. Unfortunately, constant frequencies were encountered. Since this formulation for determining impedance functions relies on frequency-dependent values, without broad spectrum data, it is not possible to use this method.

I would urge additional data be collected similar to that presented in Chapter 3 of this thesis representing a wide range of frequencies and loading scenarios of deep foundations to aid in validating the equations presented in this thesis.

CHAPTER 3

SHALLOW FOUNDATION PRESSURE DISTRIBUTIONS DURING FORCED VIBRATION LOADING

3.1 Introduction

This section focuses on foundation-soil pressure for shallow foundations subjected to SSI effects. This work involved data from a field test of a shallow foundation system consisting of a slab on grade with 4 steel columns and a top slab. The field testing I discuss in this chapter was performed by the University of California, Los Angeles (UCLA) in an effort to better understand the behavior of a shallow foundation subject to forced-vibration loading. I will be focusing on the foundation pressures and their relationship with the surrounding soils.

Field test data provides many advantages in the analysis of complex SSI problems. There are two issues that distinguish field tests versus other analysis methods. The first is a function of scaling; because stiffness and damping occurs due to the interaction between the foundation and the surrounding soil, if one is using a small-scale laboratory or field model then it will be difficult to accurately represent the interaction. The data set used in this study is a high quality set, with a wide dynamic range. The data is available for highly nonlinear soil response. A wide range of frequencies and loading amplitudes were used to allow for more variation within the study.

This chapter will begin with an introduction to the field test set-up and the testing protocols. Then I will present the recorded pressure data and an analysis of the results.

3.2 Background

The field test work used in this study was performed as part of a multi-institutional project involving the National Science Foundation (NSF) study on the "Mitigation of Collapse Risk in Vulnerable Concrete Buildings." There are three locations where the field tests were performed; University of California, Los Angeles Structural Engineering Laboratory (LAB); field testing at the Wildlife Liquefaction Array (WLA) site; and field testing at the Garner Valley Downhole Array (GVDA) site. Instrumentation associated with the experiment included accelerometers, pressure cells, and uplift displacement. These sensors worked together to enable real time recording of the foundation response. Shaker systems were used to induce forced vibration to mimic seismic forces of varying strains accompanied by systems of monitoring the input and output. The test included multiple experiment trials at each site, with varying test conditions. The full data set is accessible online at https://nees.org/warehouse/project/637. More details about the tests are available from Star 2011, Givens 2013 and Star et al. 2015.

3.2.1 Experimental Design and Field Test Setup

The three test locations were chosen to allow experimentation on three types of subgrade and underlying soils. The LAB location mimics a fixed-base condition. The WLA site soils consist of soft clays overlying loose, liquefiable coarse grained materials, and the GVD site is founded on firm lake-bed alluvium. Alluvium is characterized as a water deposited soil over time. The lake-bed alluvium represents a flexible-base condition having different levels of soil stiffness. The intent of the study was to have a variety of SSI effects take place for better evaluation and comparison between sites.

The test structure foundations are simple spread rectangular footings that were formed and poured as a conventional slab-on-grade. There are no footing excavations or embedment in the design to allow for optimal foundation-soil contact. The foundation slab is adequately thick to withstand the forced vibration and perform as a rigid foundation. The structures design includes a top slab with supporting braces and sufficient strength to not fail if and when foundation bearing failures occur. The test structure can best be described as a single, portable structure that was used at all three experiment locations. Figure 3.1 provides a drawing of the test structure. The top slab consists of reinforced concrete that is 0.61 m thick, 4.28 m long and 2.31 m wide. Four steel columns, HSS 12” x 12” x 1/2” (30.5 cm x 30.5 cm x 1.3 cm), support the top slab and are 2.13 m tall with approximate masses of 250 kg each. The support bracing or cross-bracing can be added or removed to allow for variable stiffness. The braces are also steel sections, HSS 4” x 4” x 1/2” (10.2 cm x 10.2 cm x 1.3 cm), with an approximate total mass of 800 kg.

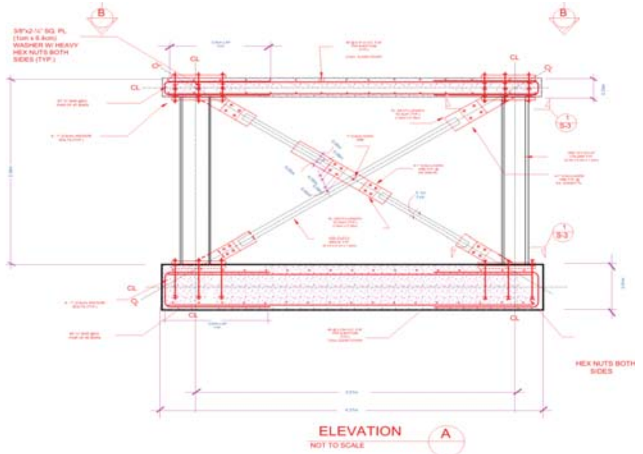

FIGURE 3.1. (From Star 2011) Schematic of portable UCLA SSI test structure.

The reinforced concrete foundation slab was cast-in-place and has the same plan dimensions as the top slab, but is 0.25 m thick. Again the goal is to have the foundation slab behave as a rigid bod for the purposes of analysis. The concrete was allowed to cure for longer than the standard 28 days prior to testing. The foundation has an approximate mass of 13,340 kg. Threaded rods were used to connect the base plates of the four columns to the foundation and top slab. The approximate total height of the structure and foundation is 3 m tall.

The experiment performed by UCLA involved instrumentation throughout the experimental structure. Figure 3.2 displays the locations of the accelerometers on the portable SSI test structure.

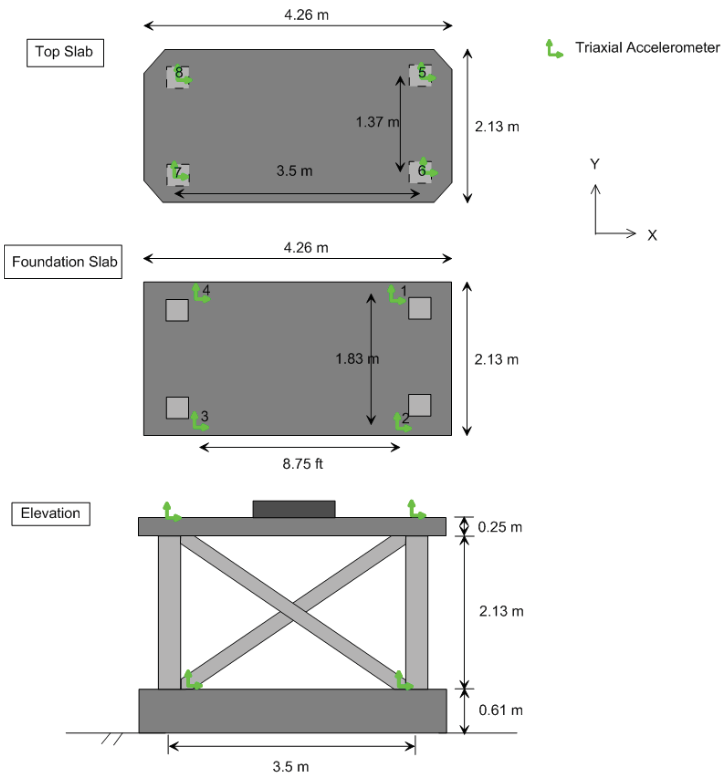

FIGURE 3.2. (From Star 2011) Triaxial accelerometer locations on the test structure.

Eight Kinemetrics EpiSensor ES-T triaxial accelerometers were instrumented to the structures top and foundation slab. Measurements for translation and rotation were represented by x, y, z, and xx, yy, zz, respectively. The accelerometers were mounted using screw connectors and shown attached to foundation in Figure 3.3.

FIGURE 3.3. (From Star 2011) Location of installed triaxial accelerometer on the test structure.

The accelerometers are cylindrical in shape with a height of 6.2 cm and a diameter of 13.3 cm. The output range of the accelerometers is ± 20 V, for an amplitude range of ± 40 g with a bandwidth up to 200 Hz using a direct current (DC). The calibrated accelerometers have sensitivities within a tolerance of 5.00 ± 0.02 volts per g. One triaxial accelerometer was secured at each corner of the top and foundation slab. When high amplitude shaking was scheduled, two extra accelerometers were buried in the soil adjacent to the structure. Both were placed at the same elevation as the base of the foundation but were orientated differently. One was longitudinally placed relative to the structure in the positive x-direction and the other was in the positive y-direction.

Three key components were required in making this experiment successful; digital data from sensors, data acquisition equipment, and data processing. Care was taken to avoid errors in the data due to time delay and phasing issues.

Displacements between the foundation and surrounding soils were measured using four Trans-Tek Inc. model 0244-0000 DC LVDTs (linear variable differential transformers). These displacement sensors were installed in the areas with the most anticipated displacement, which would be the corners of the foundation slab. The sensors were utilized when high levels of forced vibration were induced on the test structure. The LVDTs are able to measure a range of 5 cm at up to 300 Hz. Figure 3.4 shows the location of a LVDT with respect to the structure concrete foundation slab.

FIGURE 3.4. (From Star 2011) Picture of LVDT installed on corner of foundation slab.

The test structure experienced forced vibration testing from two types of shakers. The linear shaker is the smaller of the two and creates small-amplitude forces. The eccentric mass shaker provides larger-amplitude forces on the test structure. Additional testing was performed utilizing a large Tri-Axial Vibroseis vehicle similar to the ones mentioned in Chapter 2. Coincidentally, naturally occurring earthquake data was also captured. The forced vibration testing for this study took place between September 2009, and August 2011.

The linear mass shaker, referred to as “Atom Ant” (AA), was a portable Acoustic Power System “ELECTROSEIS” model 400 Long Stroke Shaker and can be seen in Figure 3.5.

FIGURE 3.5. (From Star 2011) Picture of Atom Ant used for loading of SSI test structure.

The mass of the shaker is approximately 73.0 kg and can generate forces up to 440 N. The equipment used to control the shaker was an APS Dynamic Inc. dual mode power amplifier, model 144 and a HP Agilent 33220A, 2 MHz function / arbitrary waveform generator. Variations of waveforms were used including continuous linear frequency sweeps and step frequency sweeps. Linear sweep loading involved an almost constant amplitude force combined with variable frequencies ranging from 4 to 54 Hz. Frequency step loading consisted of similar applied forces and constant frequency loading in short intervals. An increment 0.5 Hz steps were implemented to increase the frequencies to achieve the same range as the sweep loading. The linear mass shaker affected movement in the x- and y- directions along with torsional (zz) forces being applied at both the top and bottom slab.

The larger eccentric mass shaker shown in Figure 3.6 was an AFB Engineered Test Systems Model 4600A referred to as "Mighty Mouse" (MM).

FIGURE 3.6. (From Star 2011) Mighty Mouse Eccentric Mass Shaker used for loading of test structure.

MM has the ability to adjust the eccentricity of the attached weights generating moments ranging from 0 to 110 N-m. MM also has a range in operating loading frequency from 0 to 20 Hz. The eccentric mass shaker operates by means of two internal masses that spin in opposite directions of one another. Therefore the forces will be amplified in the shaking direction and cancel out in the perpendicular direction. Since we know the way in which the shaker force (F) is generated, it can be calculated as:

$$F = m_r r \omega^2 \cos\theta + (m_r + m_b)\ddot{u} \tag{3-1}$$

Where m_r represents the rotating mass, m_b is the mass of the non-rotating portion of the shaker, r represents radius and is the distance from the center of rotation to the centroid of the rotating mass, ω is the angular frequency, θ is the angular position of the rotating mass and $\ddot{u}$ is the translation acceleration of the shaker base (after Reinert et al. 2012). Equation 3-1 represents the sum of the shaker force due to rotation of the eccentric mass and force from translation of the total shaker mass. The frequency of the generated forces were controlled using a National Instruments-based controller to monitor and maintain consistency. Continuous sweeps and frequency steps similar to the forced vibration testing with the linear mass shakers were performed. The sweep and step loading frequencies ranged went as high as 20 Hz while the step loading used applied in 0.2 Hz steps.

The test structure also experienced seismic type loading from a large triaxial vibroseis vehicle called “T-Rex” shown in Figure 3.7.

T-Rex can generate a peak force of 267 kN in the vertical direction and 134 kN in horizontal directions. The subject forces can be experienced over a frequency range of 12 – 180 Hz in the vertical direction and 5 – 180 Hz in the horizontal directions. T-Rex is from the George E. Brown Network for Earthquake Engineering Research group located at the University of Texas at Austin (NEES@UTexas). The vibroseis vehicle was used approximately 20 m away from the test structure and was utilized at the WLA test site. Ground motions reaching 0.15 g were encountered and measured at the site adjacent to the test structure.


FIGURE 3.7. (From Star 2011) Tri-axial vibroseis shaker truck.

Finally, naturally occurring earthquake shaking was recorded at the WLA site. Data of the encountered earthquakes were retrieved from the United States Geologic Survey website (earthquake.usgs.gov). The magnitudes and epicenters were located near the California and Mexico border approximately 50 km south of the WLA test site. The earthquakes occurred in the late morning on 8 May 2010 and were most likely a result of aftershocks of the 4 April 2010 **M** 7.2 El Mayor Cucapah earthquake.

An X, Y, Z coordinate system was used in order to represent the structure as seen in Figure 3.5 and orientate the structure with respect to the instrumentation. The positive X direction is represented as moving longitudinally across the longer side of the slab relative to the test structure. The positive Y direction can be described as the direction moving across the shorter side of the slab and the positive Z direction is directly upward from the structure. Acronyms were used to distinguish between the type of forced vibration used, braced or unbraced, location of the shaker (top or bottom), and loading direction (X or Y). Regarding the shaker loading, mainly two types were performed which included fast sign sweeps and slow step sweeps. The sign sweeps ranged from 4 to 44 Hz, over 40 to 160 seconds with near constant amplitude over the frequency range when AA was used. A limitation of 20% of the maximum force was implemented for the braced direction of shaking to avoid potentially unwanted soil movement that could jeopardize the test results.

3.3 Pressure Cell Sensor Set-up

At the WLA site, pressure cells were used in order to measure foundation-soil interface pressure. The data collected from the pressure cells will be the main focus of the remainder of this thesis. Figure 3.8 shows a typical pressure cell sensor used in this test. The sensors were custom built for the test. The pressure cells had steel casing and were approximately 2 cm thick and 10 cm in in diameter.

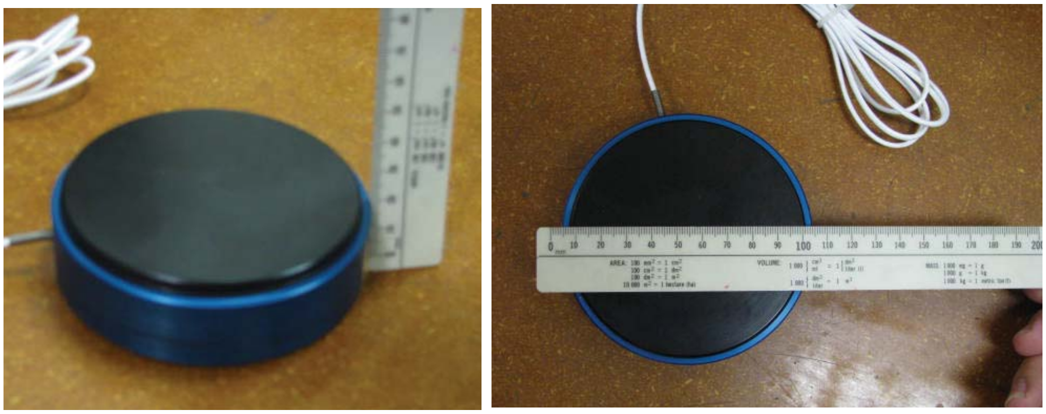

FIGURE 3.8. Pressure cells similar to those used in UCLA field test (Photo: A. Lemnitzer).

Eight pressure cells were installed after the rebar cage and formwork was constructed, but prior to pouring the concrete foundation slab. Figure 3.9 a) shows one pressure cell being located. The cells were situated with good contact between the cell facing and the cleared soil surface. The pressure cells had a washer and bolt projecting from the upper surface, which was embedded in the concrete once it was poured into place, as shown in Figure 3.9 b). This prevented the pressure cells from being misaligned in the event of foundation uplift. The sensors were orientated to measure pressure in the vertical direction, in order to capture contact pressure between the base of the foundation and the soil surface.

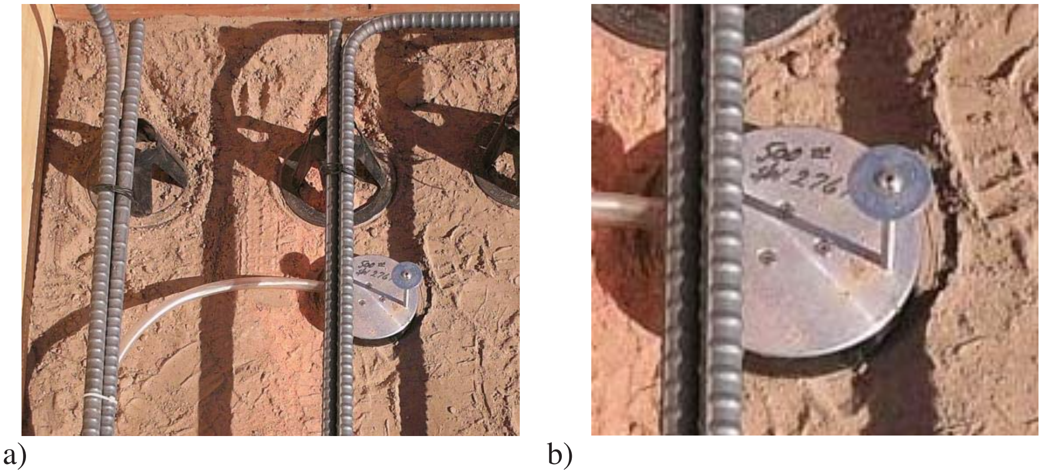
a) b)

FIGURE 3.9. (From Star 2011) Pressure cells located on foundation subgrade prior to concrete pour.

The eight pressure cells were installed in two concentric rectangles as shown in Figure 3.10. The interior and exterior pressure cells have a max capacity, which are 137 and 274 kPa respectively. The distribution of pressure cells makes it possible to measure the pressure distribution under the foundation slab.

During forced vibration loading of the test system, dynamic rocking as well as translational sliding of the foundation was induced. The pressure cells were installed in order to capture the change in vertical pressure that occurred due to foundation rocking.

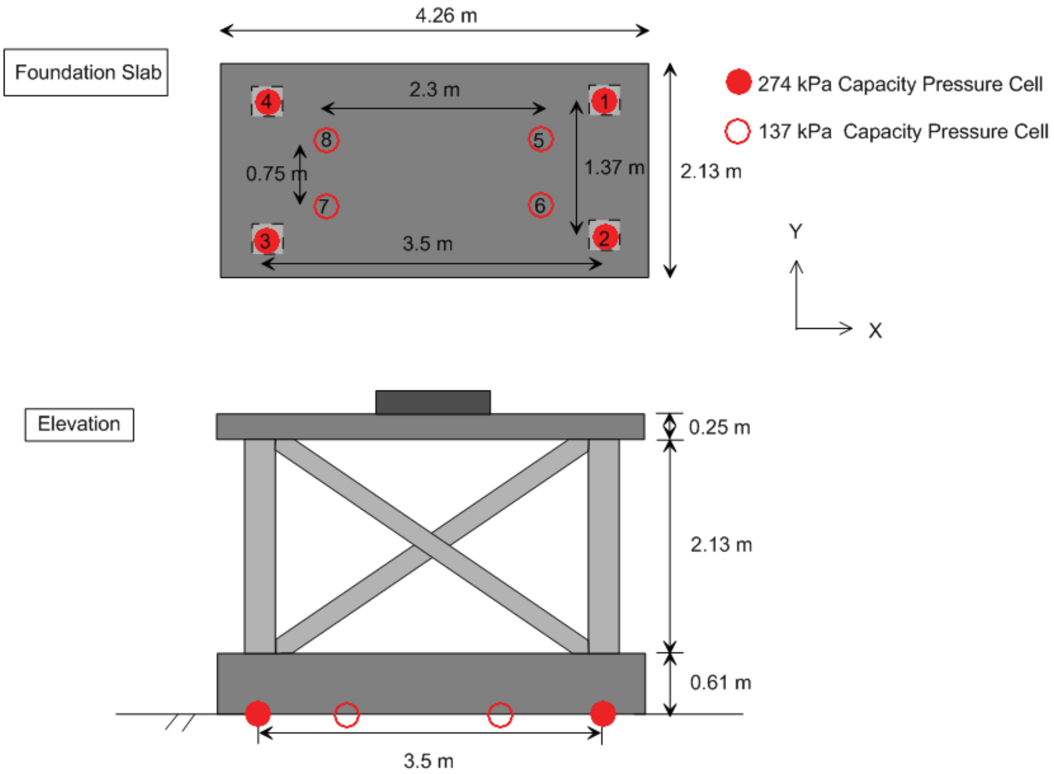

FIGURE 3.10. (From Star 2011) Locations of eight pressure cells on foundation slab.

Data from the pressure cells was recorded at a frequency of 200 Hz, allowing the resolution of data up to a frequency of 100 Hz.

3.4 Analysis of Pressure Cell Data

I will be focusing on the WLA site for the purposes of this thesis. The WLA experiment consisted of several trials and each trial consisted of multiple repetitions of loading in multiple directions (*x*, *y*, and torsion). Each subevent was assigned an identification string based on the test location, trial number, subevent number, and repetition. The first number in the string refers to the test location. The WLA location has been given the number 2. At the WLA test location, the second number in the string refers to the trial number minus one (so trial 3 is listed as 2). The third number in the string is the subevent number, based on the chronology of testing. If the subevent number has a letter following the order number, this letter represents the redundancy of the test. For example, Exp.2.0.1b represents experiment at WLA, trial 1, first forced vibration test of the trial, and 'b' represents this test being the second of its type.

Data was collected for the 21 test trials performed at WLA and the data was recorded and made available online. Unprocessed data, converted data, and corrected data files, are available online for each trial repetition. In this study we used the converted data. We examined the data recorded for the eight pressure cells and the shaker force for each test trial. MATLAB was used to decompose the data.

Each subevent had a particular location, vibration force, duration, and frequency range. The information about each trial is summarized in the description column in Table 3.1. The description consists of the location (WLA), a description of the shaker vibration source (MM), whether the structure was braced (Br) or unbraced (UB) and the direction or shaking (X or Y). The loading column of Table 3.1 describes the force that was applied for each trial. In some trials the loading frequency was rapidly changed from low to high and back down again (known as a frequency sweep), in others a step function was used to step up the frequency from low to high and back down again (step). Mighty-mouse shaker has a maximum eccentric of 110 N-m. The percent eccentricity describes the percentage of the maximum applied during each trial.

TABLE 3.1. Functioning Pressure Cell Data Recorded at WLA with Mighty Mouse Shaker.

				Pressure Cells							
Test #	Date	Description	Loading	1	2	3	4	5	6	7	8
2.2.1a	5/24/2010	WLA-MMBrX	Fast Sweep, 5%	✓	x	✓	x	✓	✓	✓	✓
2.2.1b	5/24/2010	WLA-MMBrX	Fast Sweep, 5%	✓	x	✓	x	✓	✓	✓	✓
2.2.2a	5/24/2010	WLA-MMBrX	Fast Sweep, 5%	✓	x	✓	x	✓	✓	✓	✓
2.2.2b	5/24/2010	WLA-MMBrX	Fast Sweep, 5%	✓	x	✓	x	✓	✓	✓	✓
2.2.4	5/24/2010	WLA-MMBrX	Fast Sweep, 10%	✓	x	✓	x	x	x	✓	✓
2.2.5	5/24/2010	WLA-MMBrX	0.2 Hz Step, 10%	✓	x	✓	✓	✓	✓	✓	✓
2.2.6	5/24/2010	WLA-MMBrX	Fast Sweep, 20% ecc	✓	✓	✓	x	✓	✓	✓	✓
2.2.7	5/24/2010	WLA-MMBrX	0.2 Hz Step, 20%	✓	x	✓	x	✓	✓	✓	✓
2.2.8	5/24/2010	WLA-MMBrY	Fast Sweep, 5% ecc	✓	✓	✓	✓	x	x	✓	✓
2.2.9	5/24/2010	WLA-MMBrY	0.2 Hz Step, 5% ecc	✓	✓	✓	x	✓	x	✓	✓
2.2.10	5/24/2010	WLA-MMBrY	Fast Sweep, 10% ecc	✓	✓	✓	✓	✓	✓	✓	✓
2.2.11	5/24/2010	WLA-MMBrY	0.2 Hz Step, 10% ecc	✓	✓	✓	x	✓	x	✓	✓
2.2.12	5/24/2010	WLA-MMBrY	Fast Sweep, 20% ecc	✓	✓	✓	x	✓	✓	✓	✓

TABLE 3.1. Continued

				Pressure Cells							
Test #	Date	Description	Loading	1	2	3	4	5	6	7	8
2.2.13	5/24/2010	WLA-MMBrY	0.1 Hz Step, 20% ecc	✓	✓	✓	x	✓	✓	✓	✓
2.2.14	5/25/2010	WLA-MMUbY	Fast Sweep, 5% ecc	✓	✓	✓	✓	✓	x	✓	✓
2.2.15	5/25/2010	WLA-MMUbY	0.2 Hz Step, 5% ecc	✓	✓	✓	✓	✓	x	✓	✓
2.2.16	5/25/2010	WLA-MMUbY	Fast Sweep, 20% ecc	✓	✓	✓	✓	✓	✓	✓	✓
2.2.19	5/25/2010	WLA-MMUbX	0.2 Hz Step, 5% ecc	x	✓	✓	✓	✓	✓	✓	✓
2.2.20	5/25/2010	WLA-MMUbX	Fast Sweep, 20% ecc	✓	✓	✓	✓	✓	✓	✓	✓
2.2.22	5/25/2010	WLA-MMUbX	Fast Sweep, 100% ecc	✓	✓	✓	✓	✓	✓	✓	✓
2.2.24b	5/25/2010	WLA-MMUbY	Fast Sweep, 100% ecc	✓	✓	✓	✓	✓	✓	✓	✓

Graphs showing the time history recording of each pressure cell for each trial can be found in Appendix A of this thesis. It was crucial the behavior of the shaker force was recorded along with the reaction of the pressure cells beneath the foundation in order for us to relate the pressure and the imposed dynamic force. The shaker force time history recording for each trial is also presented in Appendix A.

Two types of graphs are shown for each pressure cell for each trial: (1) log-log graphs showing the Fourier amplitude of the pressure cell data measured in kPa-s on the y-axis and frequency measured in Hertz (Hz) shown on the x-axis; and (2) pressure versus time where pressure is measured in kPa on the y-axis and time in seconds is on the x axis. The shaker force for the log-log Fourier transform shows the FFT amplitude measured in N-s versus frequency and the pressure versus time graphs show newtons (N) versus time in seconds.

Two types of loading were applied during this testing sequence: sweep and step loading. The sweep loading can be easily identified by symmetric somewhat diamond shaped graph illustrating a constant increase with and equivalent decrease in loading amplitude. The step loading can be identified by a gradual increase in loading amplitude with a peak occurring near the end of the testing cycle.

A major component of this study was to determine which of the pressure cells were functioning properly at the time of the test. In order to evaluate this, we examined the time history of the data, as well as the Fourier domain amplitude of the data. Figure 3.11 shows two example time histories from pressure cells 2 and 3 for trial 2.2.20.

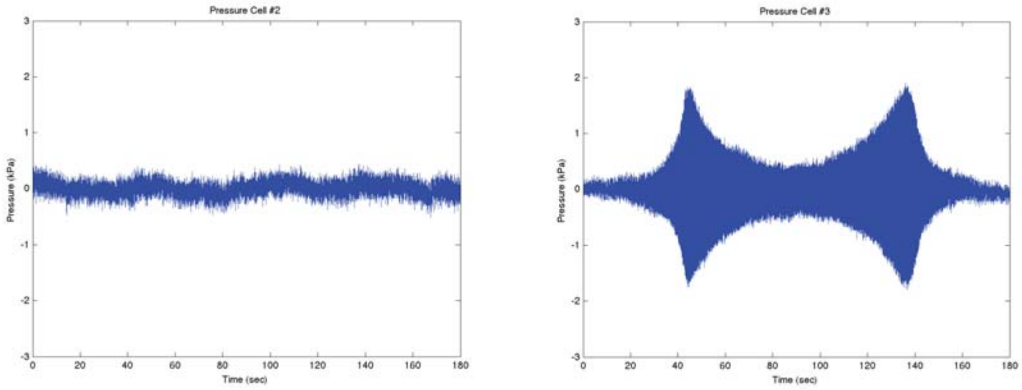

(a) (b)

FIGURE 3.11. Pressure versus time graphs from test 2.2.20; (a) indicates non-functioning pressure cell while (b) indicates functioning pressure cells.

In the time Figure 3.11 (a) the change in amplitude is harder to identify observationally. In the same figure (b) the variation in the data that results from the foundation loading can easily be seen at time.

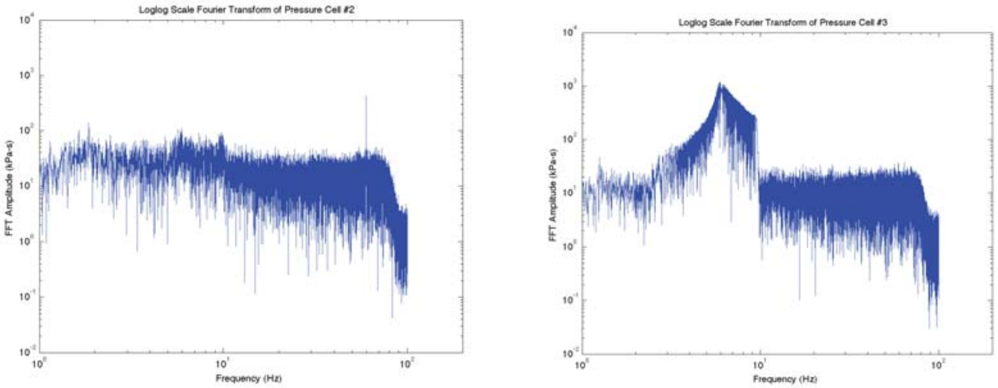

(a) (b)

FIGURE 3.12. FFT amplitude versus frequency graphs from test 2.2.20; (a) indicates non-functioning pressure cell while (b) indicates functioning pressure cells.

Similarly in the Fourier domain amplitude Figure 3.12 (a) the FFT amplitude is difficult to differentiate. In the same figure (b) we can clearly see the increase in FFT pressure cell amplitude with frequency. Table 3.1 summarizes which pressure cells were functioning properly during the data recording process.

After graphing all the data it became apparent that a few pressure cells were potentially not providing clear readings and mainly included pressure cells 2 and 4. A few of the actual tests indicated a movement or shift in the graph, some minor and some major. The particular cause is not clear, but I can hypothesize a possible movement of the actual test structure or maybe an electrical aberration involving a voltage fluctuation that was the source used in collecting the pressure data. Tests indicating shifting included 2.2.4, 2.2.10 and 2.2.11. The remainder of the graphs appeared to show coherent data through spikes in the pressures versus time.

When examining the graphs we can see consistent high amplitudes among the independent pressure cells near the structure's resonant frequency. At resonant frequency the test structure began rocking, generating the soil-foundation pressures seen in the graphs. Resonance was commonly encountered twice during each trial because the shaker force was applied with a sweep up through the frequencies and then a sweep back down to zero.

3.5 Conclusions

I analyzed data from the forced vibration loading of a shallow foundation test structure consisting of a slab on grade foundation with steel columns, a connected top slab, and removable bracing. Field testing data was provided by UCLA. My goal was to focus on the behavior of the shallow foundation pressure distributions during forced vibration loading. The WLA site was the selected site of analysis which consists of soft clays overlying loose, liquefiable coarse-grained soils. The foundation was not embedded or keyed into the soil subgrade. Instrumentation was used in the form of accelerometers, pressure cells and uplift displacement sensors. Applicable experimental design and field test set up measures were described including test structure dimensions, instrumentation locations and force vibration mechanisms. Equation 3-1 describes the force that will be generated specifically by the two shaker forces analyzed in this study.

After analyzing the pressure cells of the 21 tests collected, I determined which cells were functioned properly in each test and then proceeded to evaluate their behavior graphically. Two types of graphs were generated to represent the time domain and frequency domain. Graphical data was also collected for the shaker force which aided in interpreting the pressure cell graphs. In magnifying portions of the pressure cell graphs that indicated an increase in foundation pressures we were able to see resonance of the test structure. Based on this information we can conclude at that point the test structure began effectively rocking which caused the noticeable pressure generations. We were also able to see with an increase in the shaker force strength, larger pressures were observed.

CHAPTER 4

CONCLUSIONS AND SUGGESTIONS FOR FUTURE WORK

4.1 Summary of Research Findings

SSI is the overarching topic of this thesis and the foundation by which the summary of the research findings can be made. This thesis begins with some limitations of current practice and need for SSI awareness followed by background of the topic. Most importantly, the introduction ends with an objective to develop a better understanding of deep and shallow foundations and how dynamic loading affects their behavior.

In this study, geotechnical modeling of shallow and deep foundations subject to forced vibration were evaluated. Field experimental test data provided by others allowed for the model generation and analysis to be made possible. Drilled shafts represented deep foundations in Chapter 2 and a slab on grade foundation as part of a test structure represented a shallow foundation in Chapter 3.

The details, configurations, equipment and instrumentation used for the field testing of each individual study is described in their respective chapters. Multiple figures and pictures help illustrate the procedures that took place. Multiple equations are presented to provide the foundation and framework of this study and to develop a better understanding of the derived work.

In Chapter 2 I derived the complex stiffness which describes the stiffness and damping together of the soil being affected by the deep foundation. Unfortunately after analyzing the vibration force from the field data, it became evident that the constant frequency of that force would prevent adequate graphical analysis in the frequency domain. This is based upon the fact that impedance functions are frequency-dependent and we rely on changes in frequency to decompose the results.

In Chapter 3, 378 graphs were collected and are represented in Appendix A. The purpose of the graphs is to help illustrate pressures beneath shallow foundations experiencing dynamic loading. After careful analysis of the time domain and frequency domain graphs we were able to see obvious response from the pressure cells. The increase in the amplitude of the shaker force based on the type of loading gave rise to increased pressures beneath the shallow foundation at specific times. Based on these results we feel confident that the test structures resonant frequency matched the shaker forces frequency intern causing the structure to rock therefore creating noticeable pressure spikes. Upon closer inspection of the areas of increased pressure it was common to find equal distances of time between amplitude fluctuations which is an indicator of resonance.

4.2 Suggestions for Future Work

The work described and performed in this thesis represents two small-scale studies intended to better evaluate and understand shallow and deep foundations as they relate to SSI. I believe the data collected at the time of the two experiments was considerable for their respective studies and purpose. However, additional data from more test foundations would greatly contribute to the knowledge base of SSI. A wider variety of structures and loading combinations would be beneficial to consider. Potentially structures with different types of foundations with practical applications in areas where engineers have seen distress as a result of SSI. Some examples include foundations for bridge abutments and piers. I evaluated the performance of drilled shafts and examining the behavior of driven piles should also be looked at with respect to stiffness and damping of the surrounding soil.

Related specifically to Chapter 2, more extensive data is needed to complete the validation of the model.

Related to Chapter 3, a larger area foundation, possibly with partial embedment would add to the knowledge of behavior and pressures encountered beneath the foundation. Also, adding additional stories to the test structure to examine how the effects of doubling the height could alter the pressures beneath the shallow foundation.

APPENDICES

APPENDIX A

GRAPHICAL RESULTS FROM 21 PRESSURE CELL TESTS AT WLA SITE

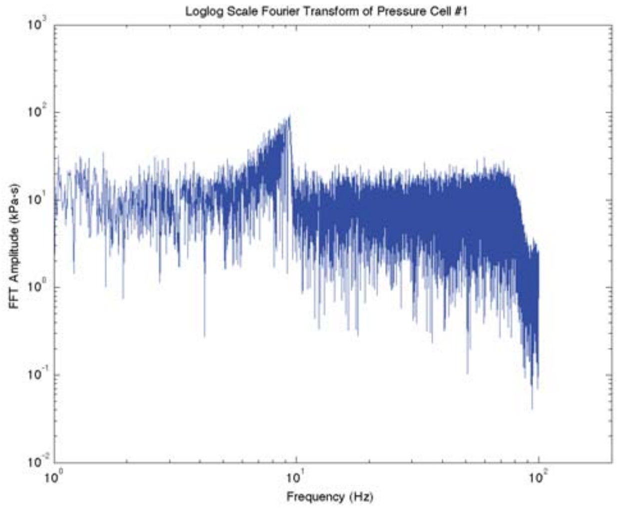

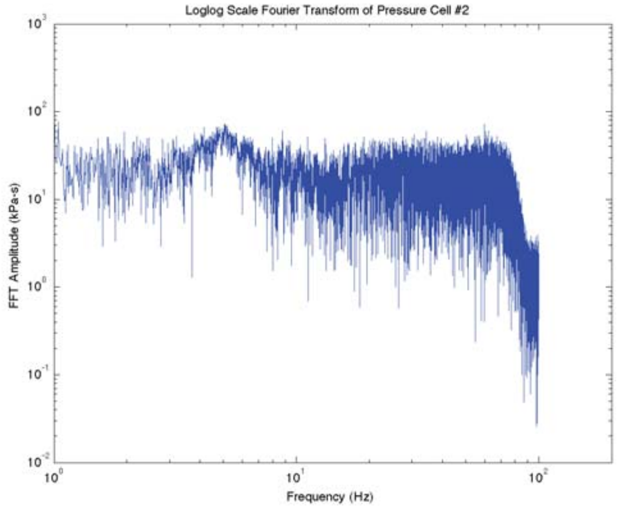

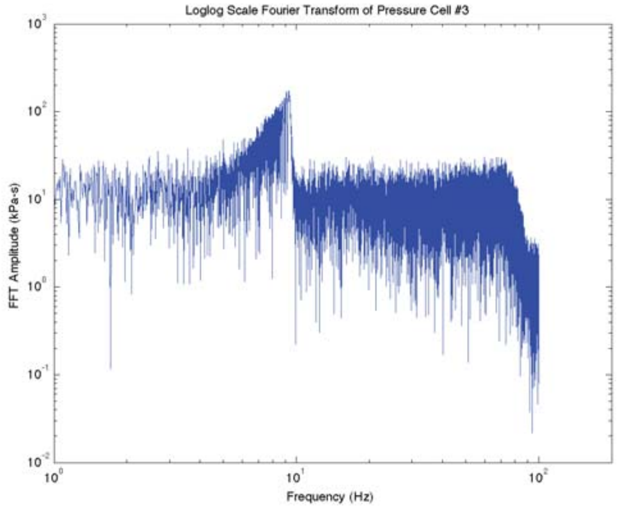

Frequency domain pressure cell graphs from test 2.2.1a

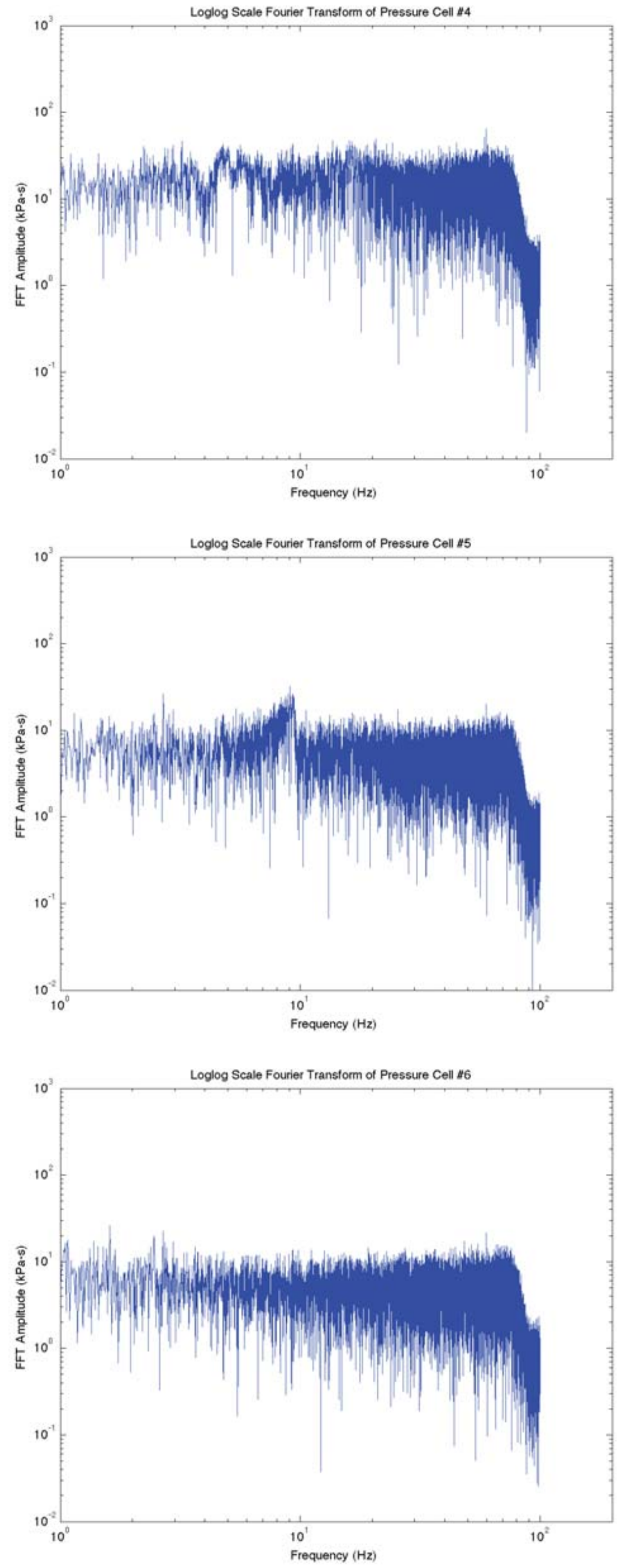

Frequency domain pressure cell graphs from test 2.2.1a (continued)

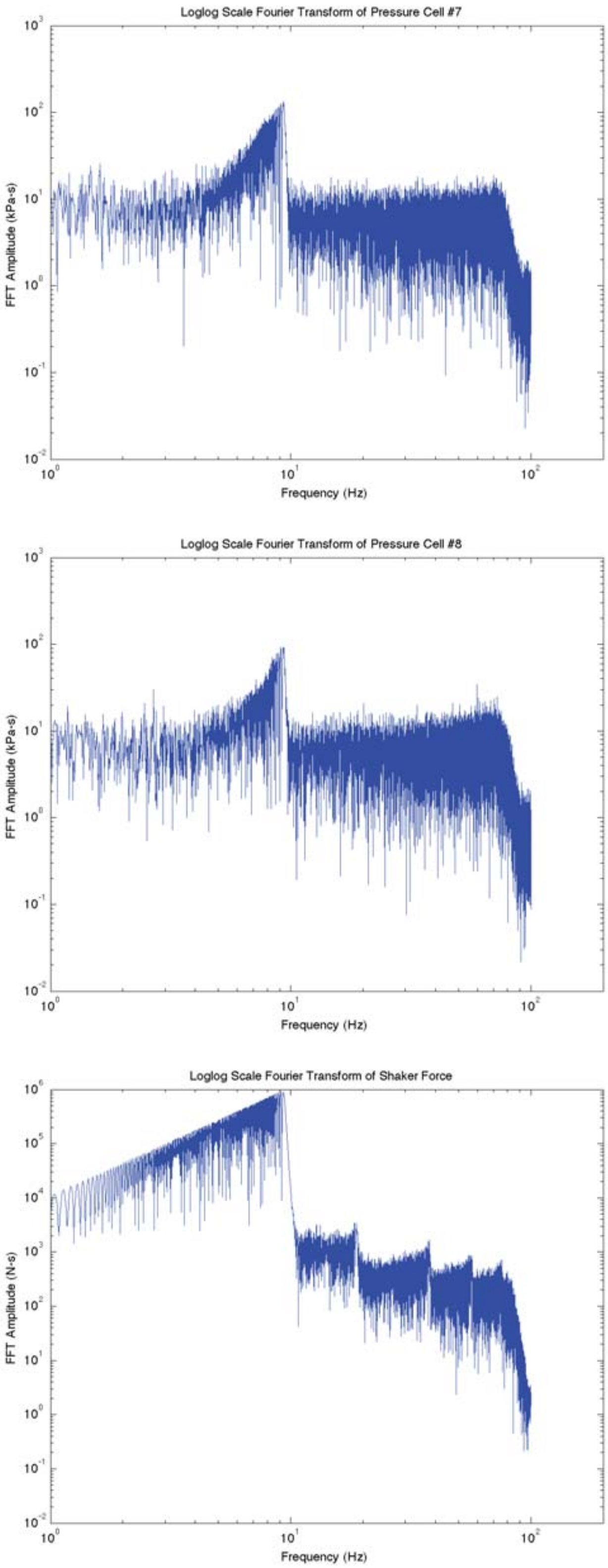

Frequency domain pressure cell graphs from test 2.2.1a (continued)

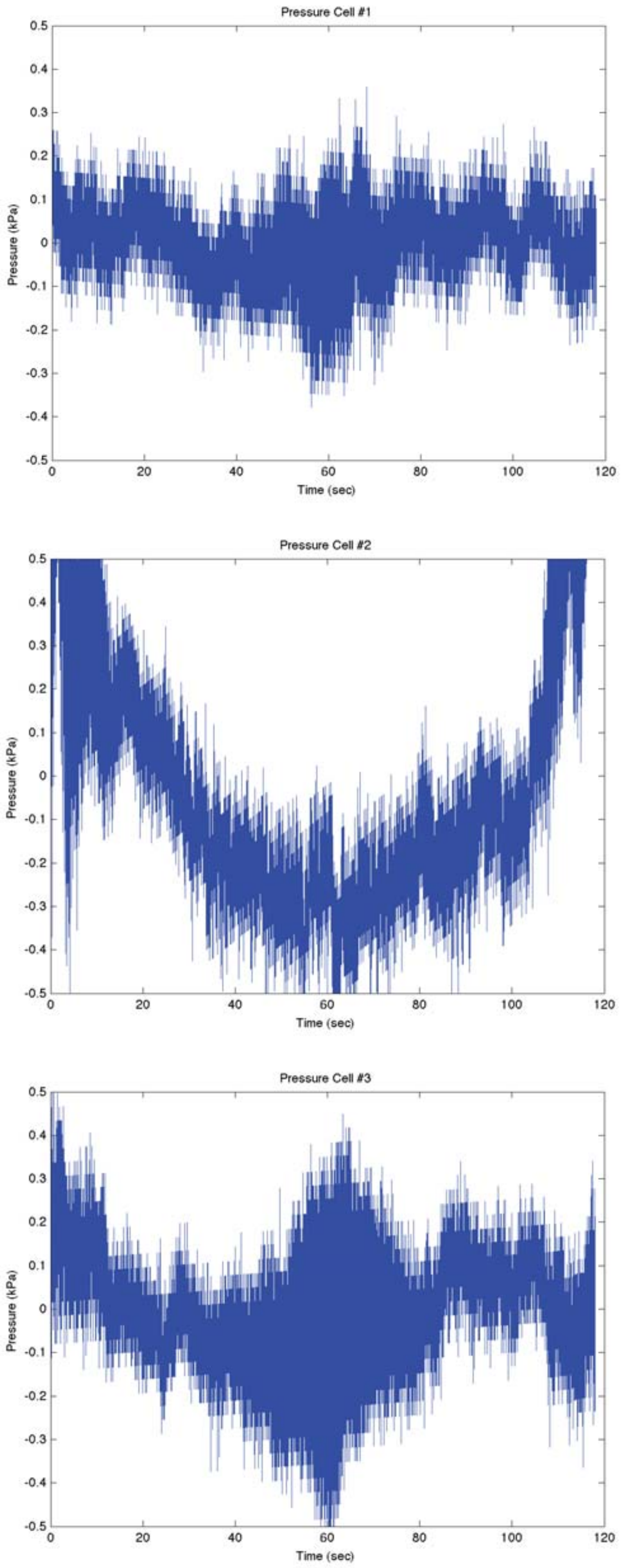

Time domain pressure cell graphs from test 2.2.1a

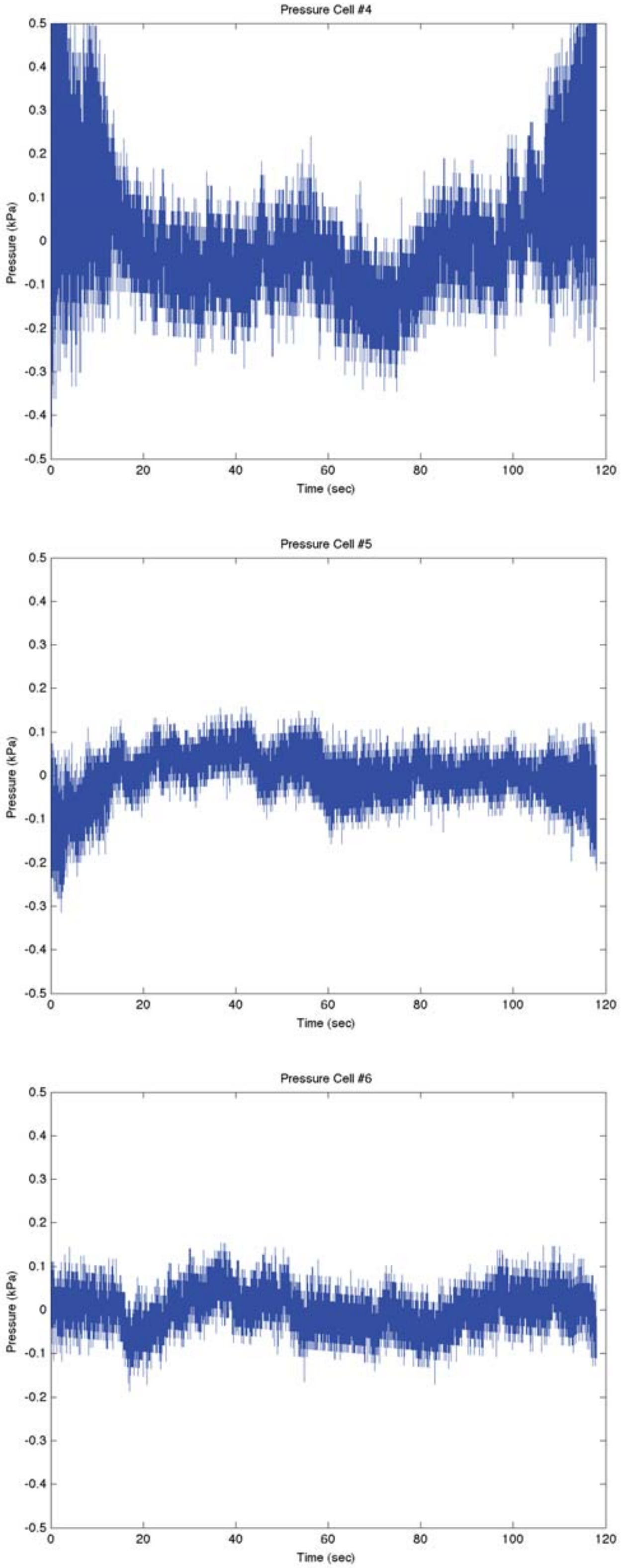

Time domain pressure cell graphs from test 2.2.1a (continued)

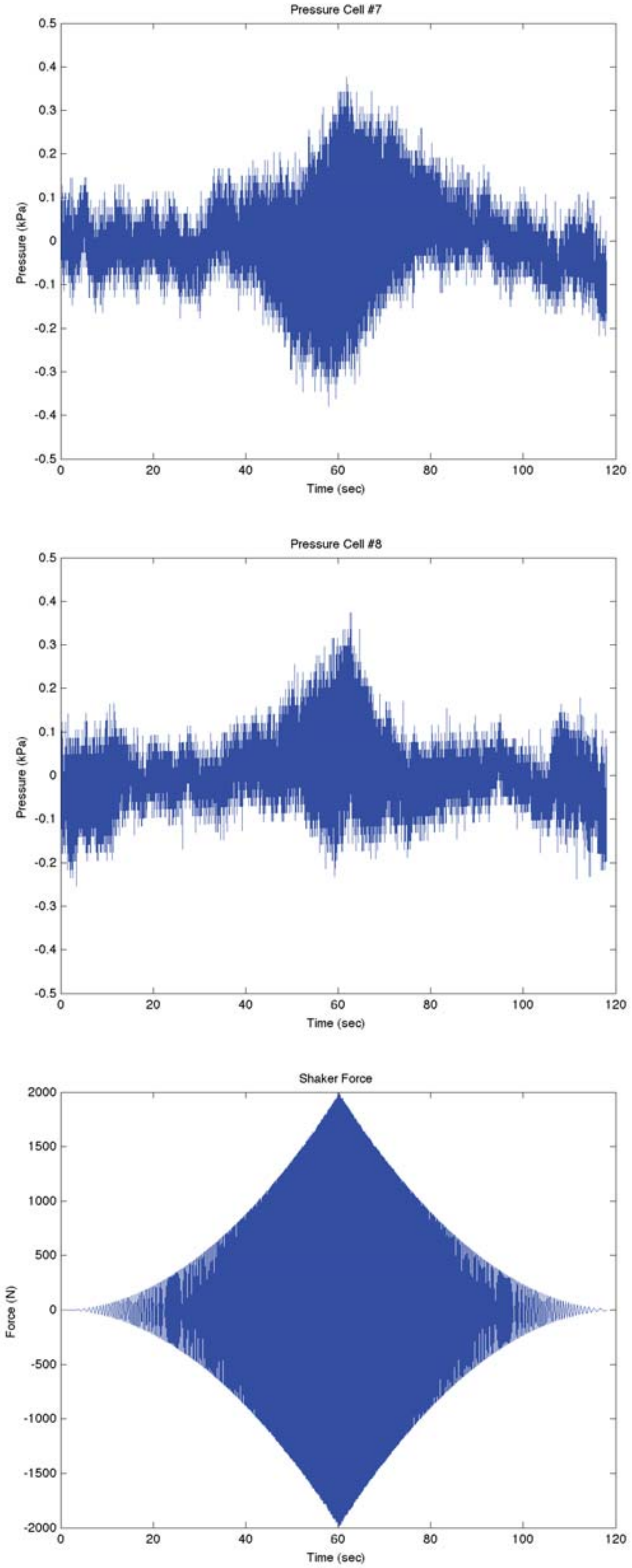

Time domain pressure cell graphs from test 2.2.1a (continued)

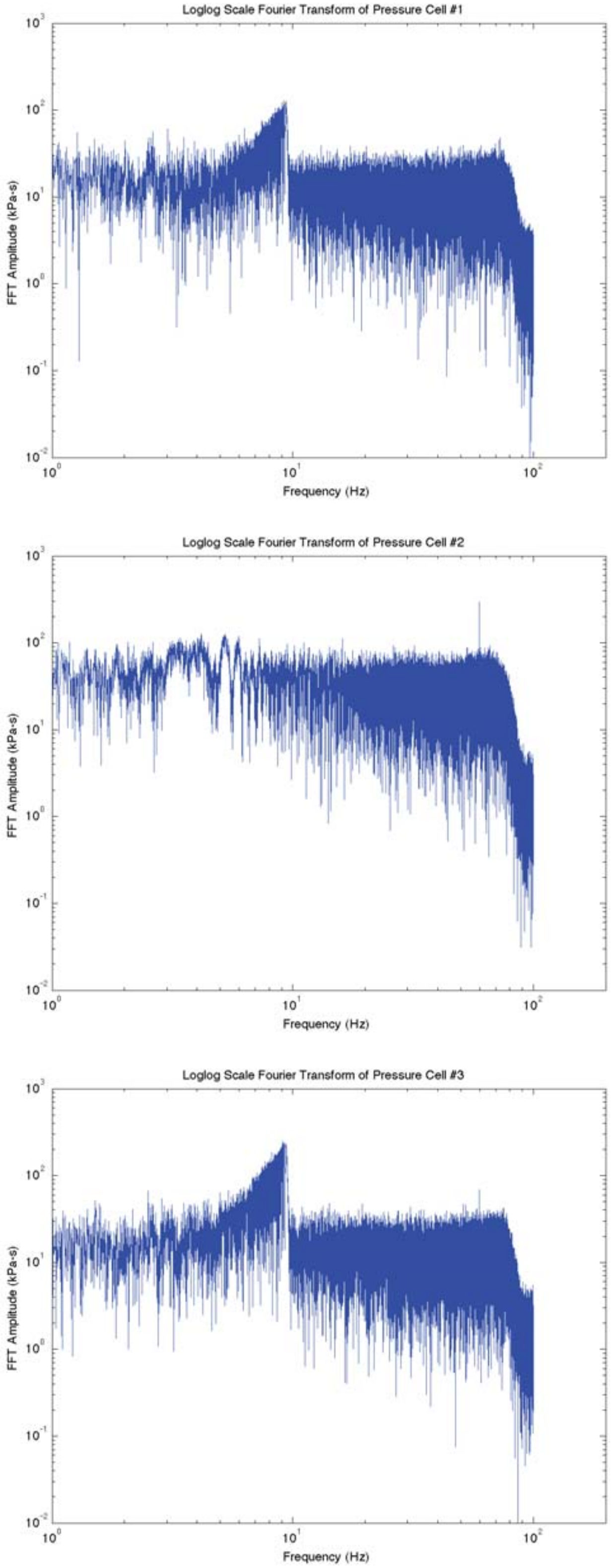

Frequency domain pressure cell graphs from test 2.2.1b

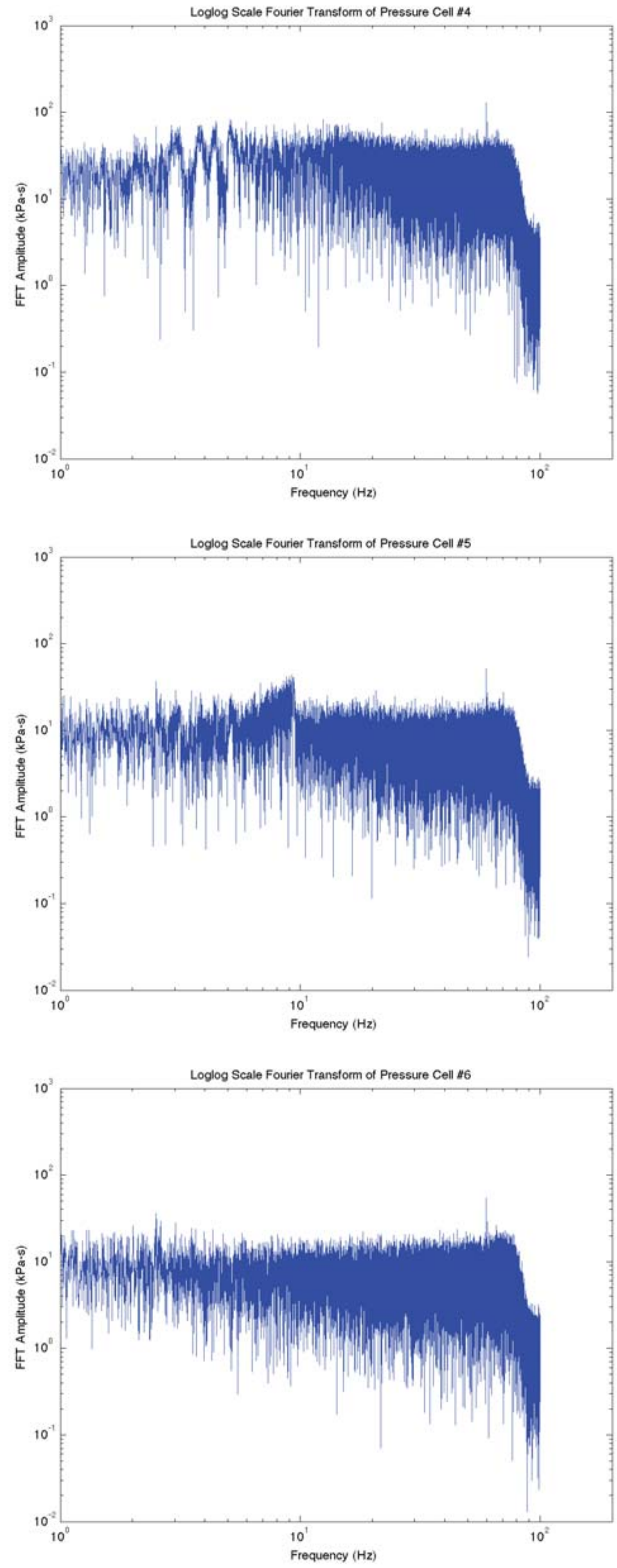

Frequency domain pressure cell graphs from test 2.2.1b (continued)

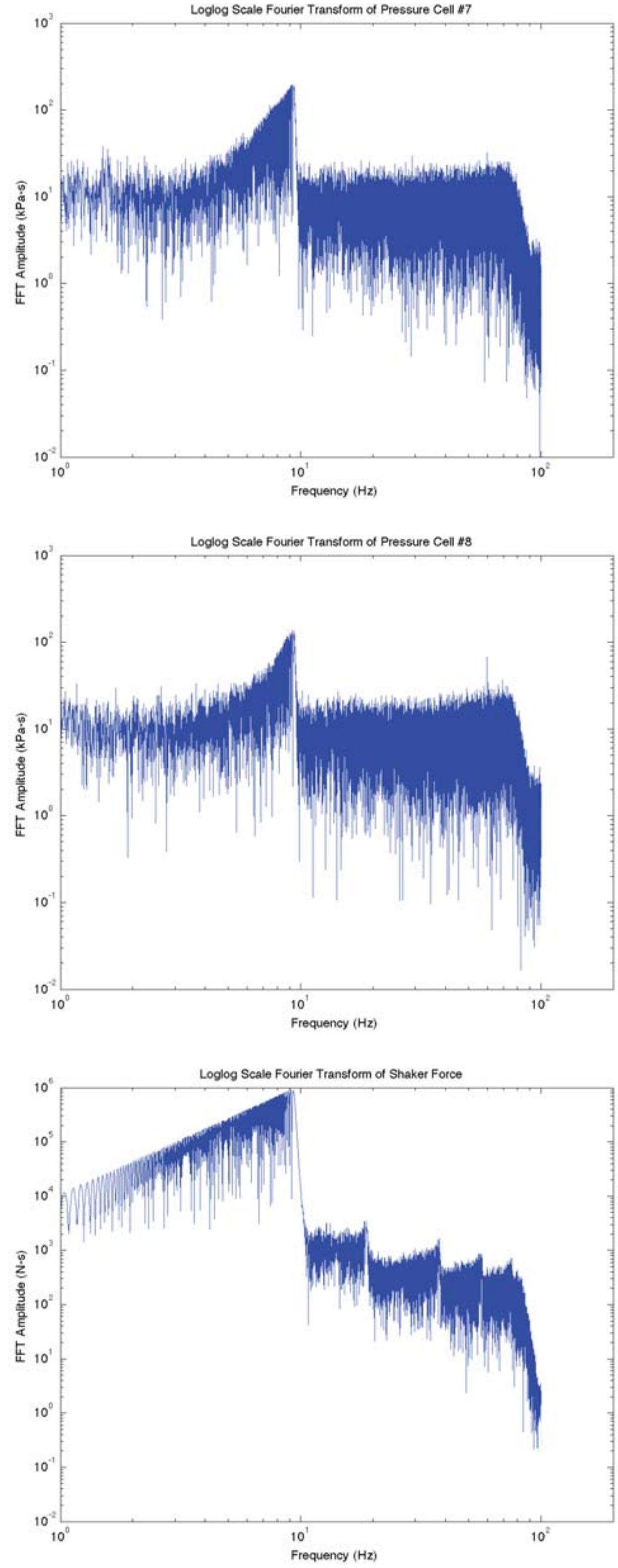

Frequency domain pressure cell graphs from test 2.2.1b (continued)

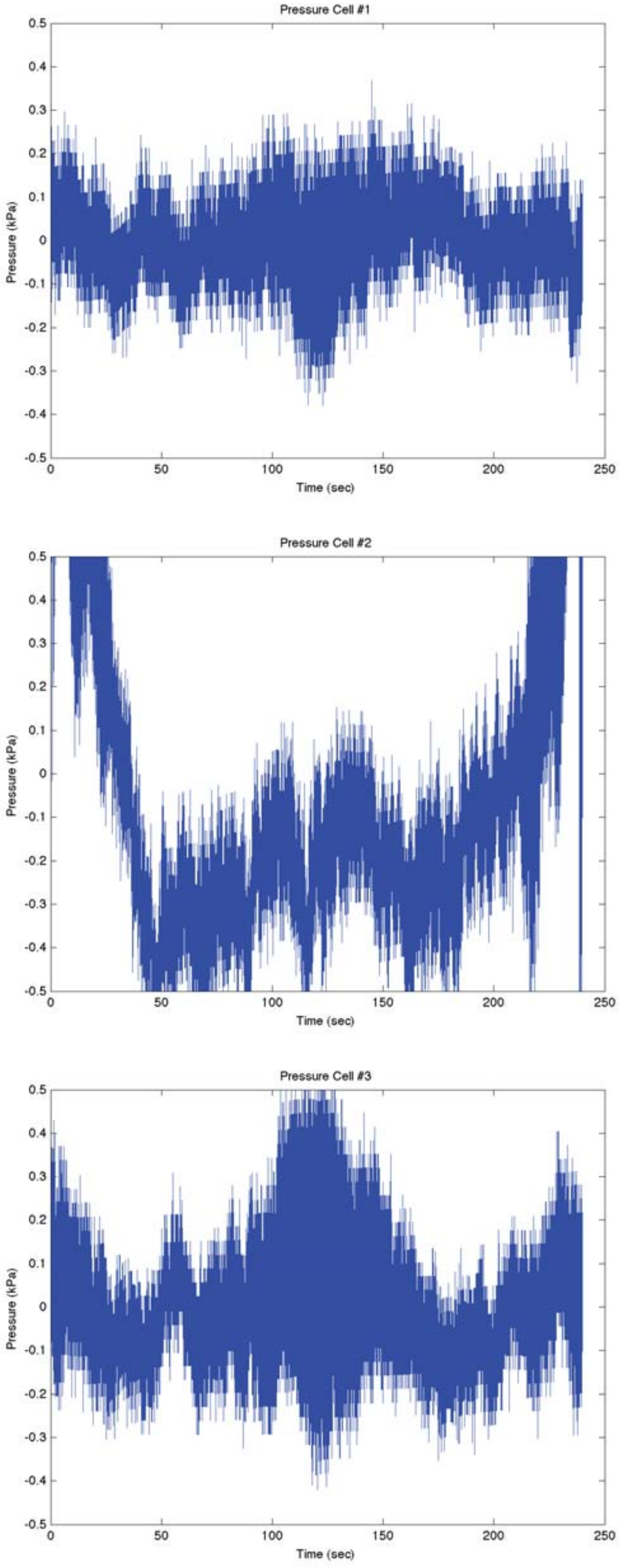

Time domain pressure cell graphs from test 2.2.1b

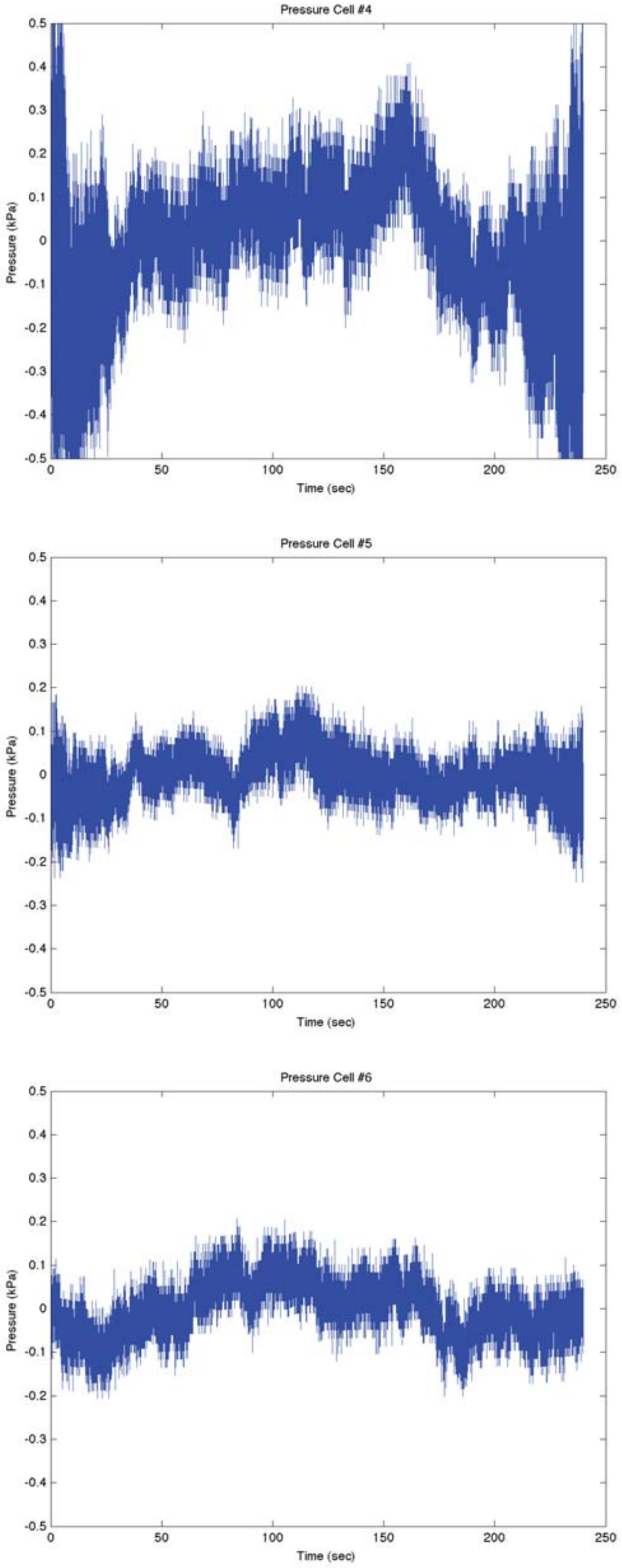

Time domain pressure cell graphs from test 2.2.1b (continued)

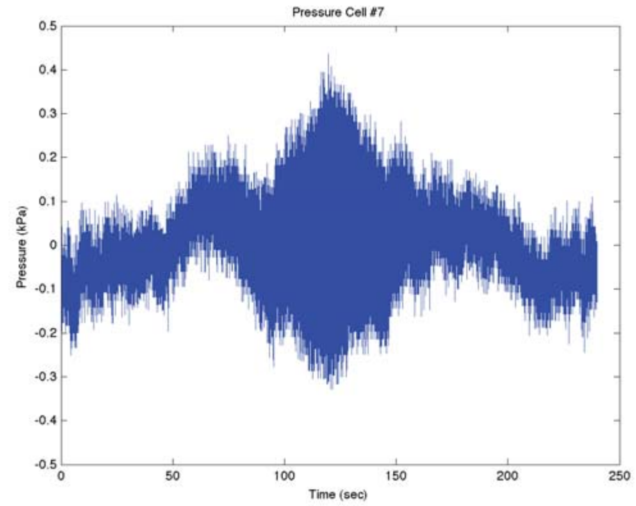

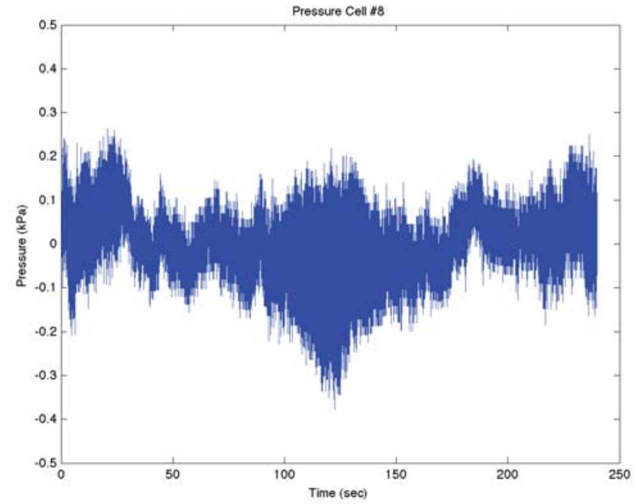

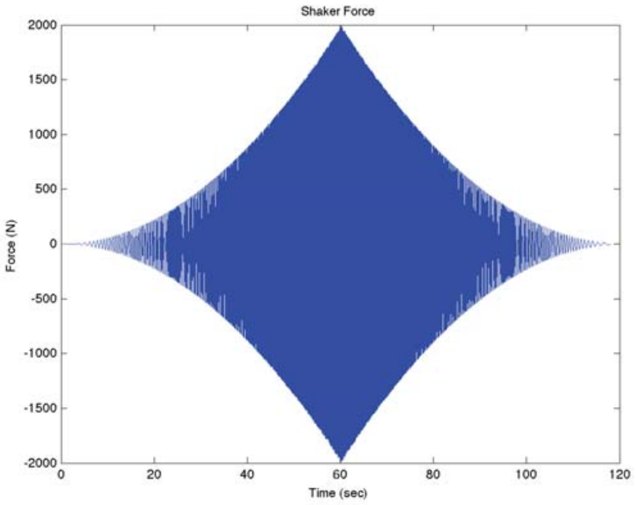

Time domain pressure cell graphs from test 2.2.1b (continued)

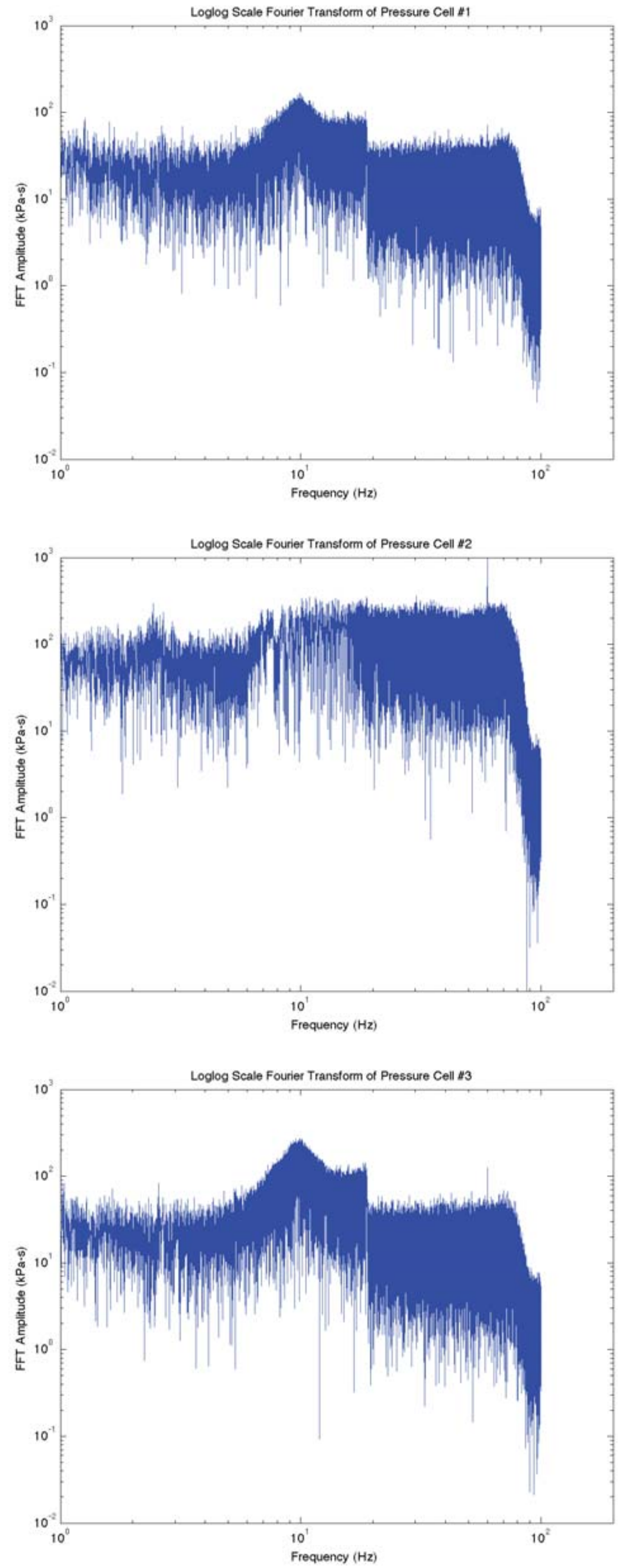

Frequency domain pressure cell graphs from test 2.2.2a

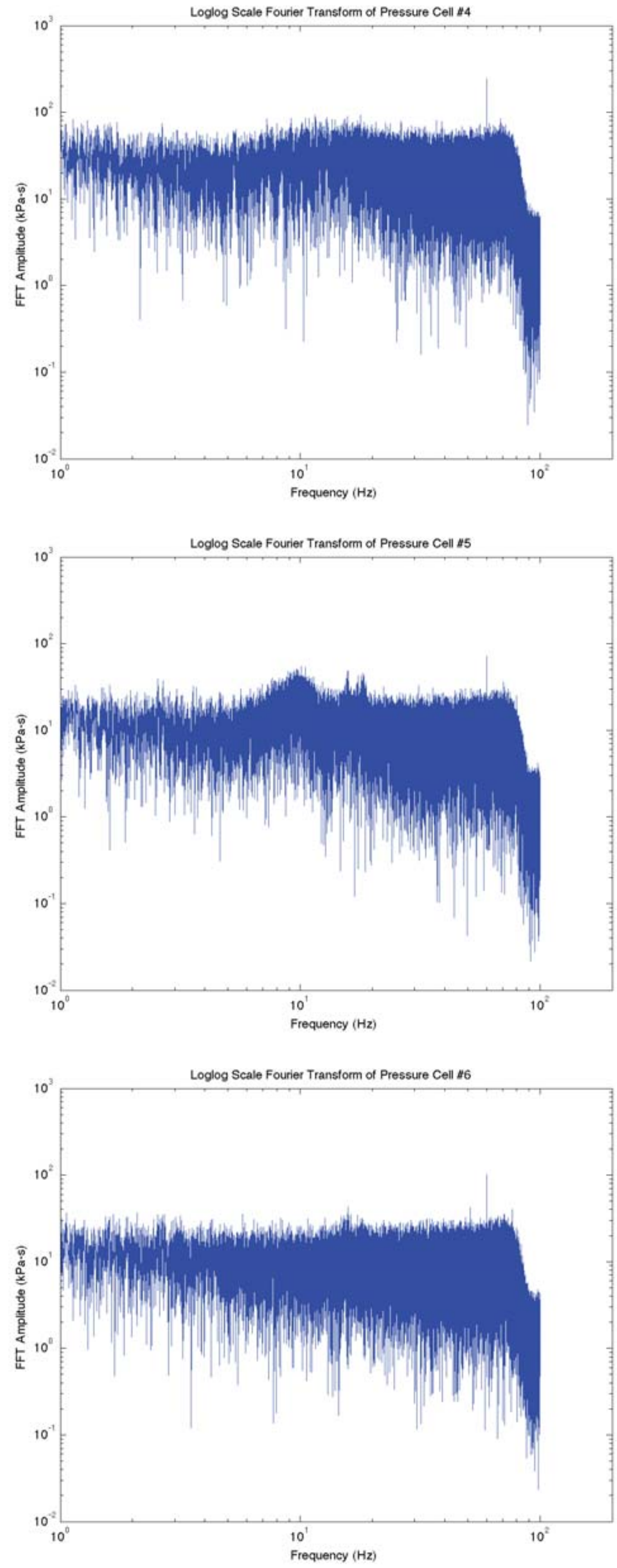

Frequency domain pressure cell graphs from test 2.2.2a (continued)

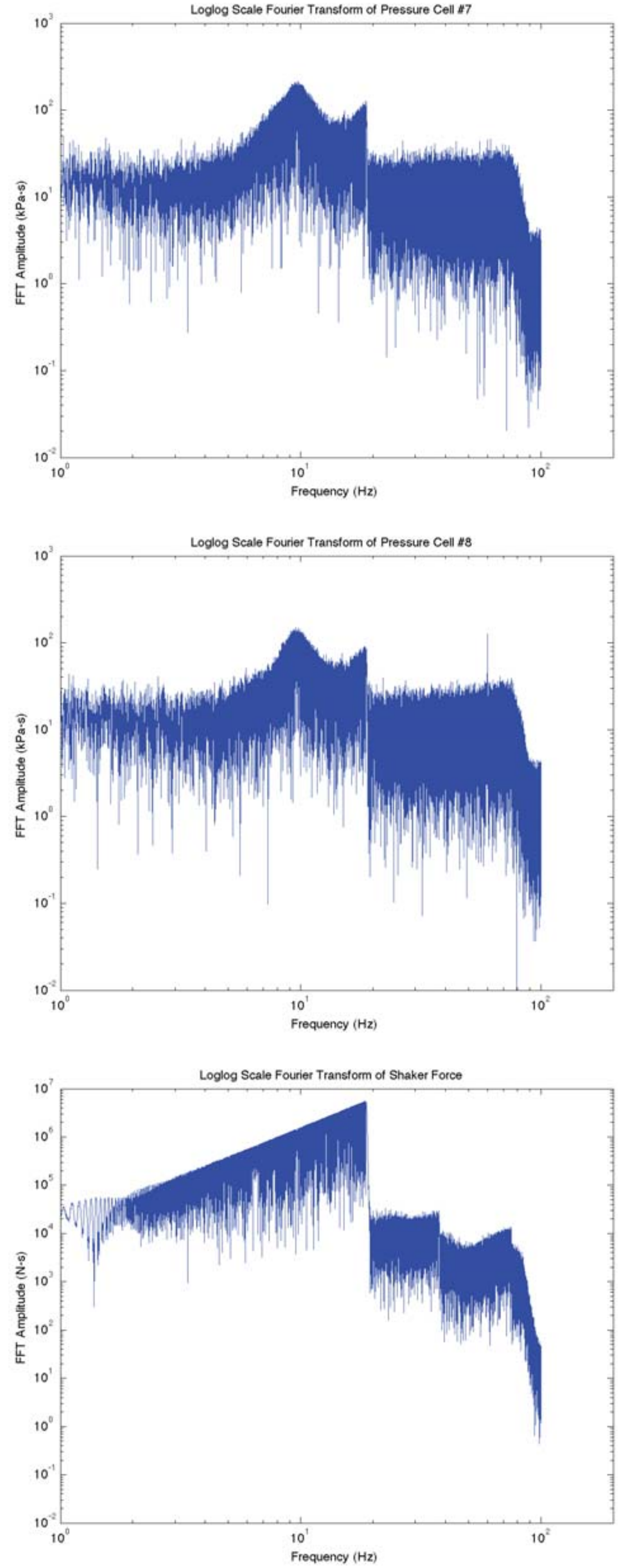

Frequency domain pressure cell graphs from test 2.2.2a (continued)

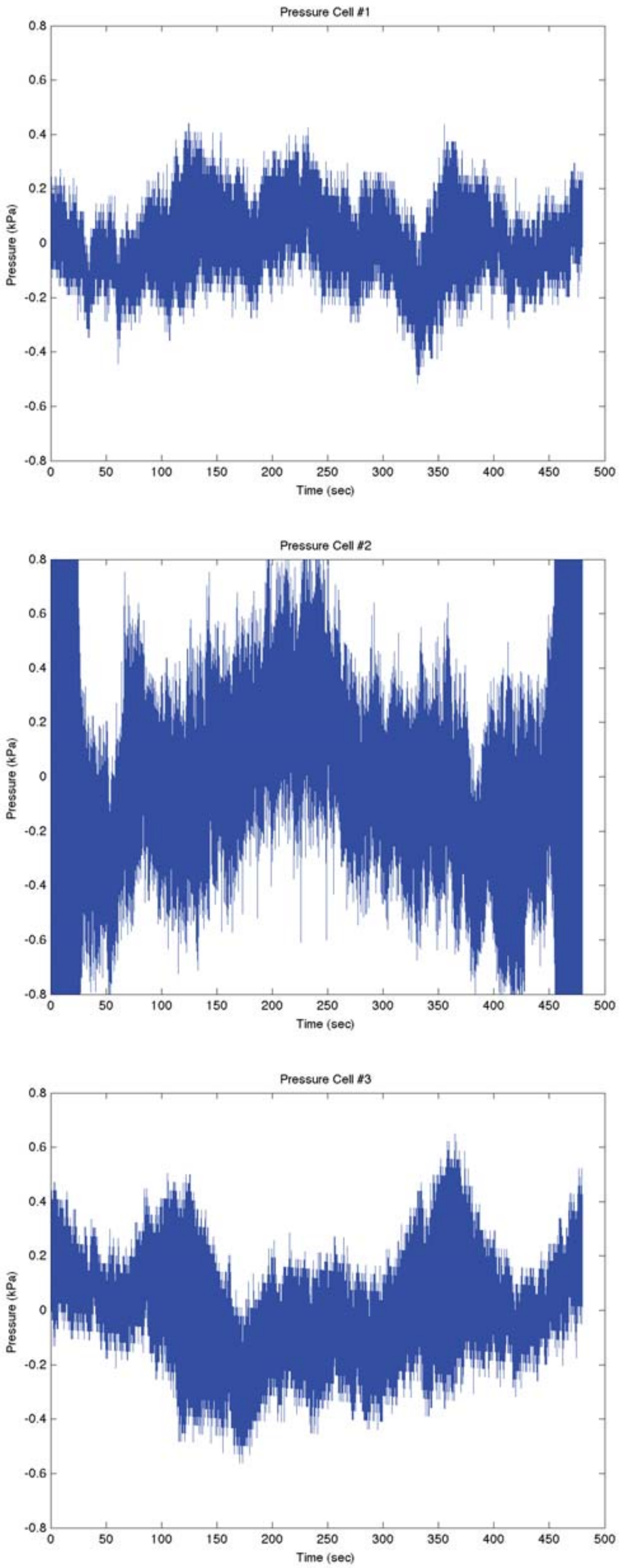

Time domain pressure cell graphs from test 2.2.2a

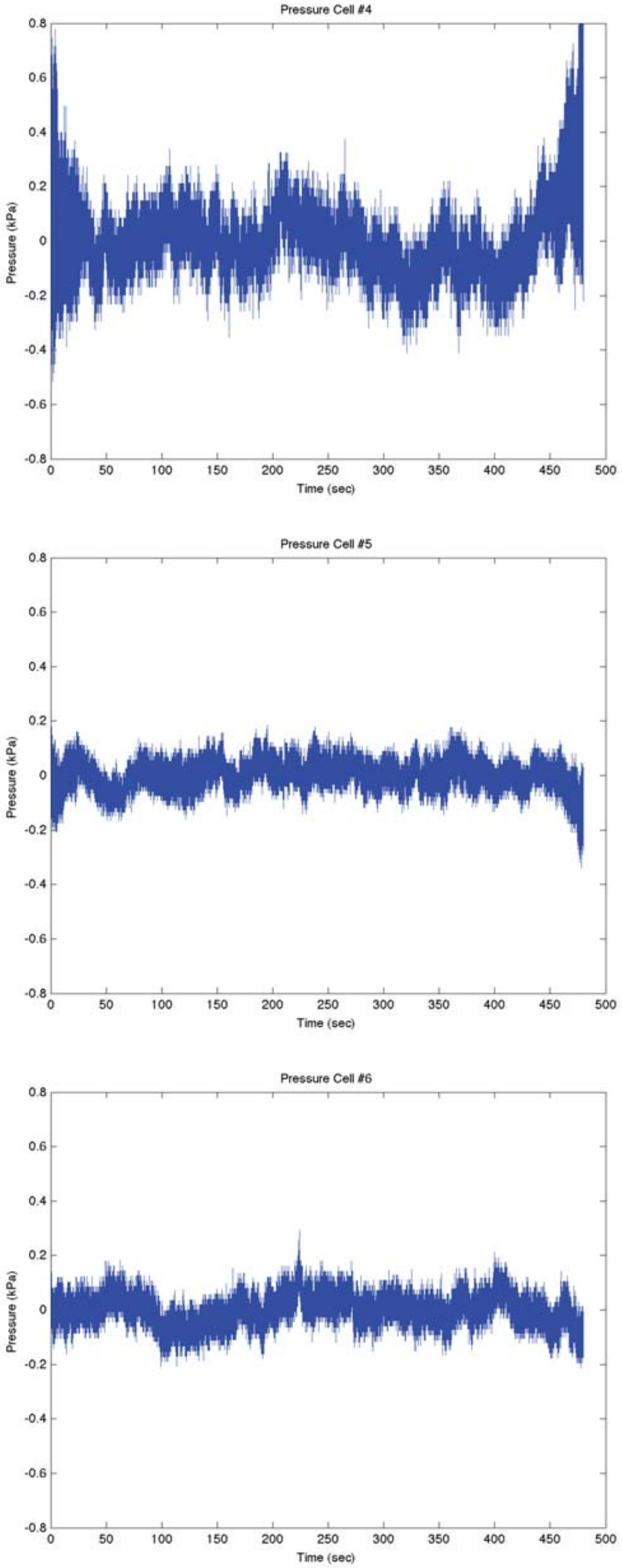

Time domain pressure cell graphs from test 2.2.2a (continued)

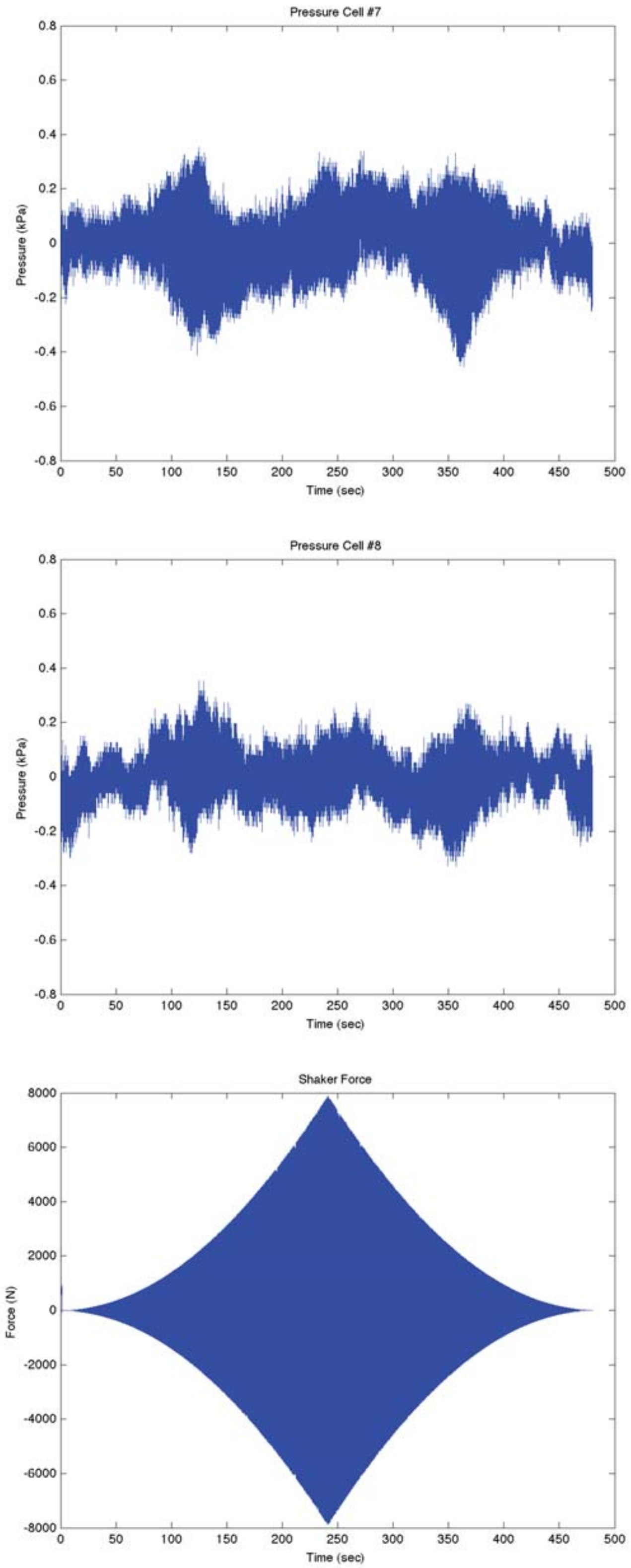

Time domain pressure cell graphs from test 2.2.2a (continued)

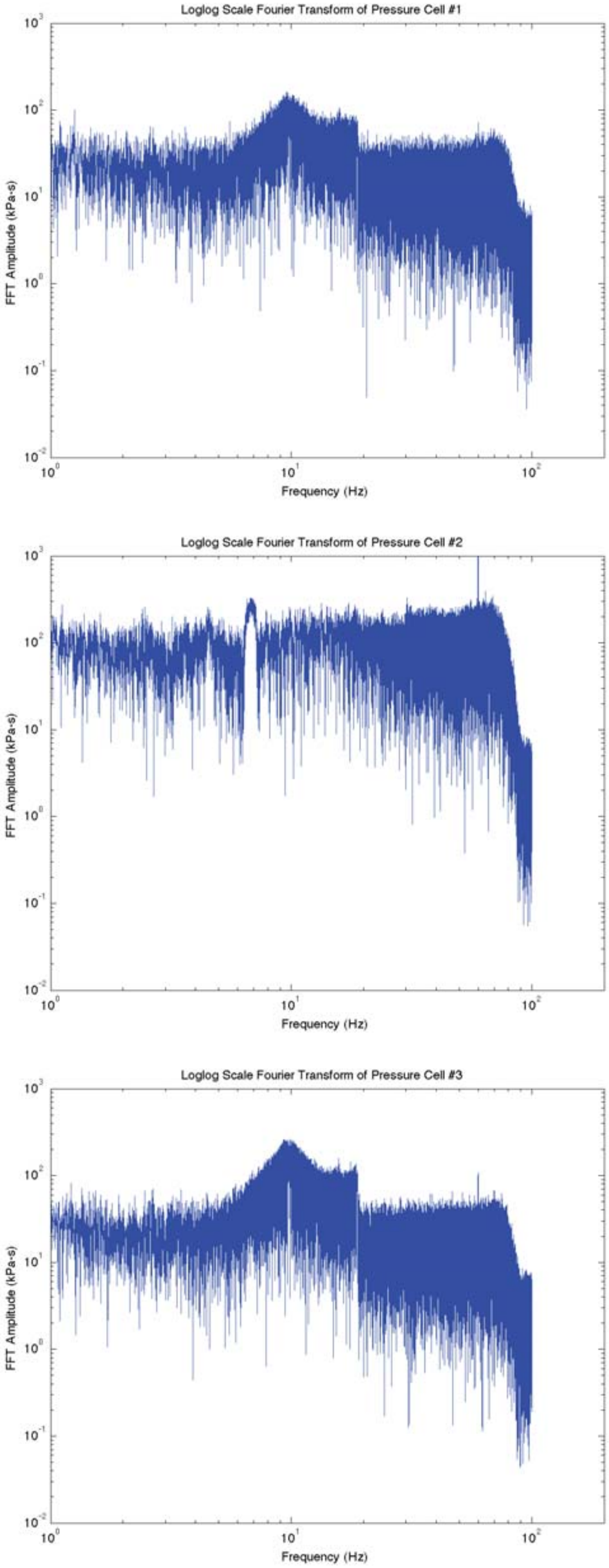

Frequency domain pressure cell graphs from test 2.2.2b

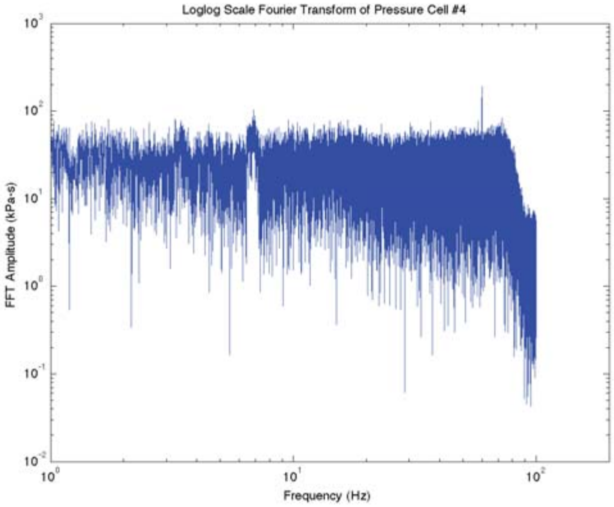

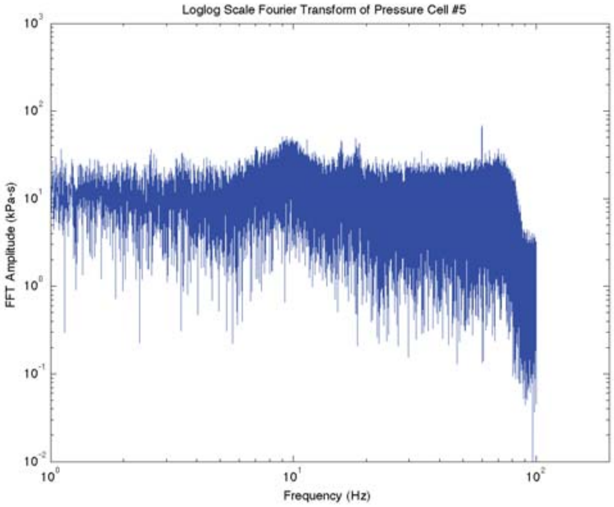

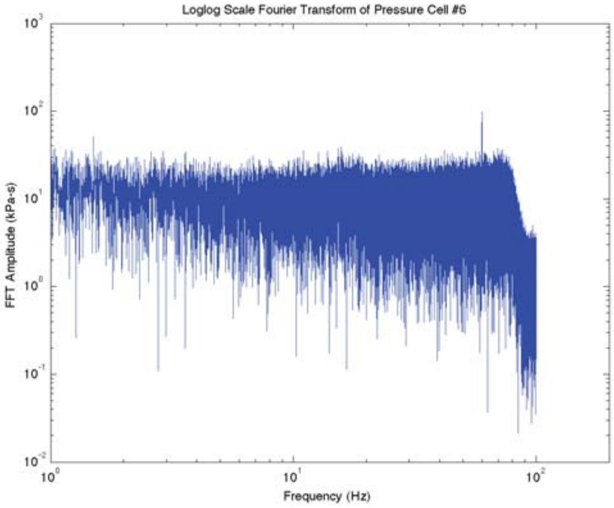

Frequency domain pressure cell graphs from test 2.2.2b (continued)

Loglog Scale Fourier Transform of Pressure Cell #7

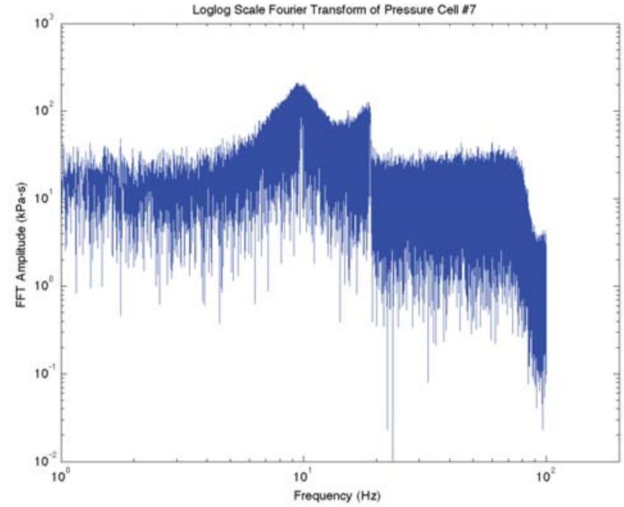

Loglog Scale Fourier Transform of Pressure Cell #8

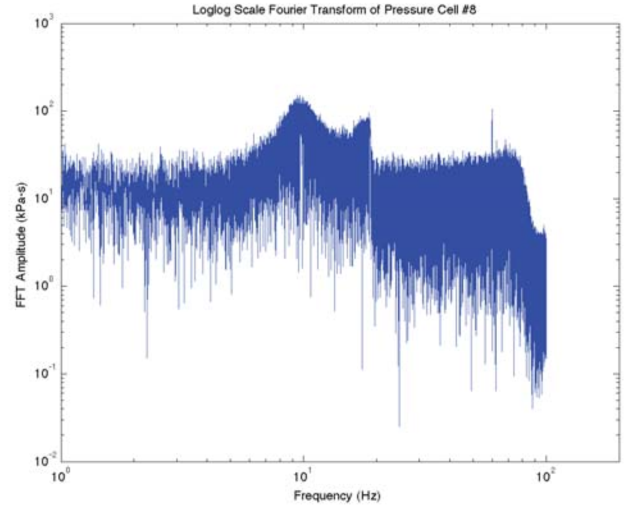

Loglog Scale Fourier Transform of Shaker Force

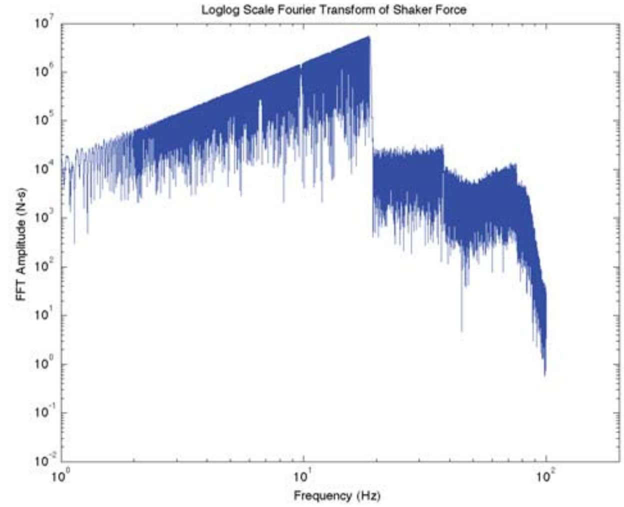

Frequency domain pressure cell graphs from test 2.2.2b (continued)

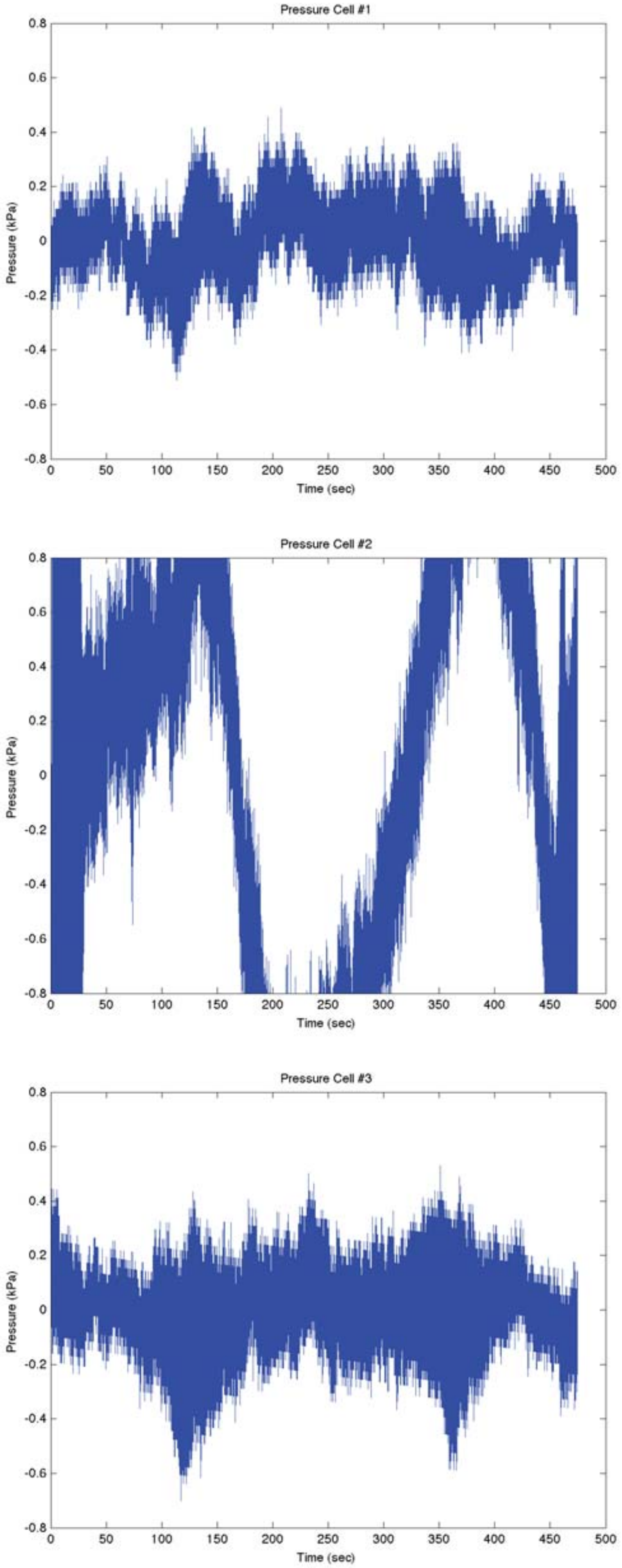

Time domain pressure cell graphs from test 2.2.2b

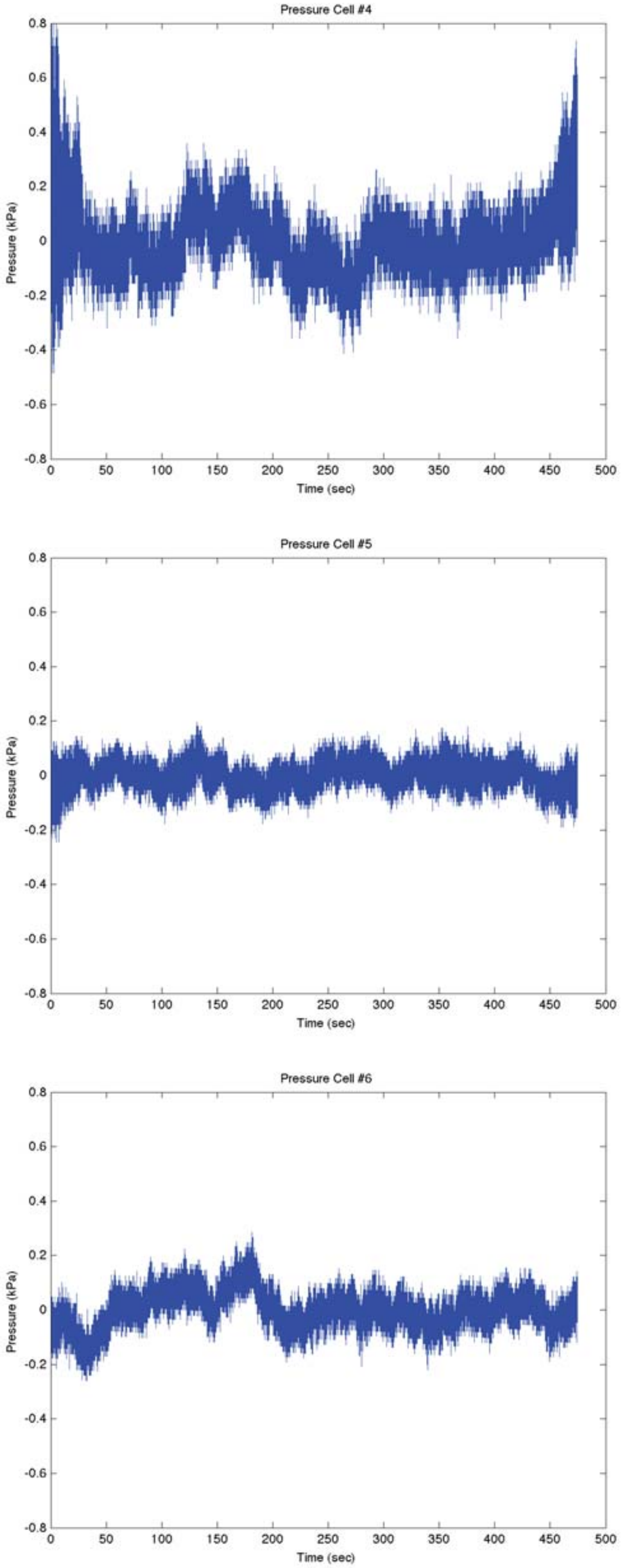

Time domain pressure cell graphs from test 2.2.2b (continued)

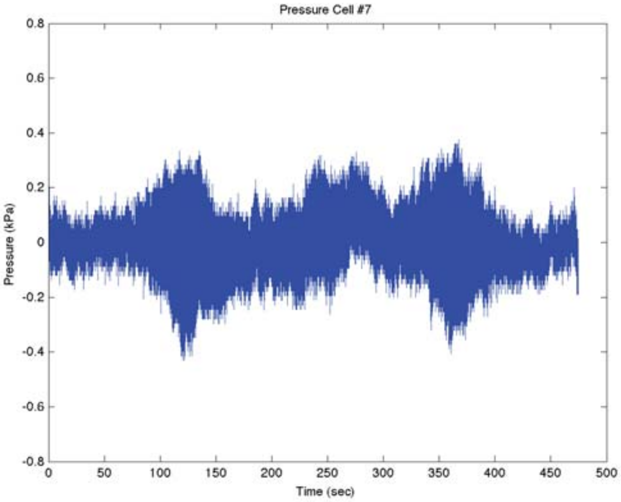

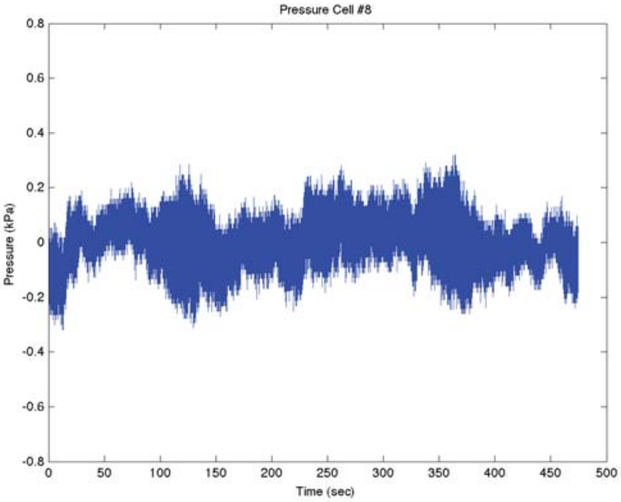

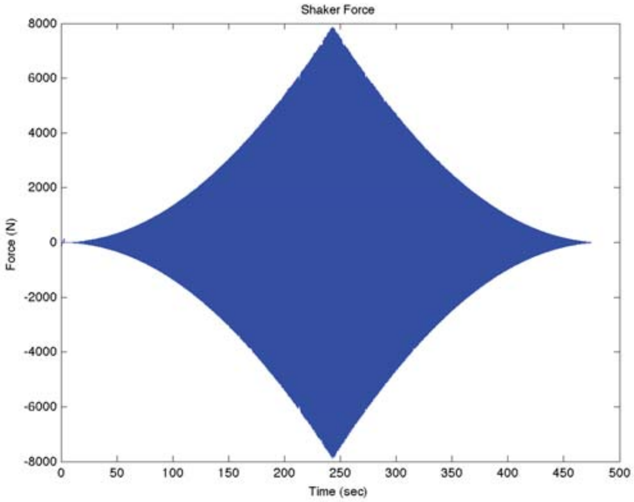

Time domain pressure cell graphs from test 2.2.2b (continued)

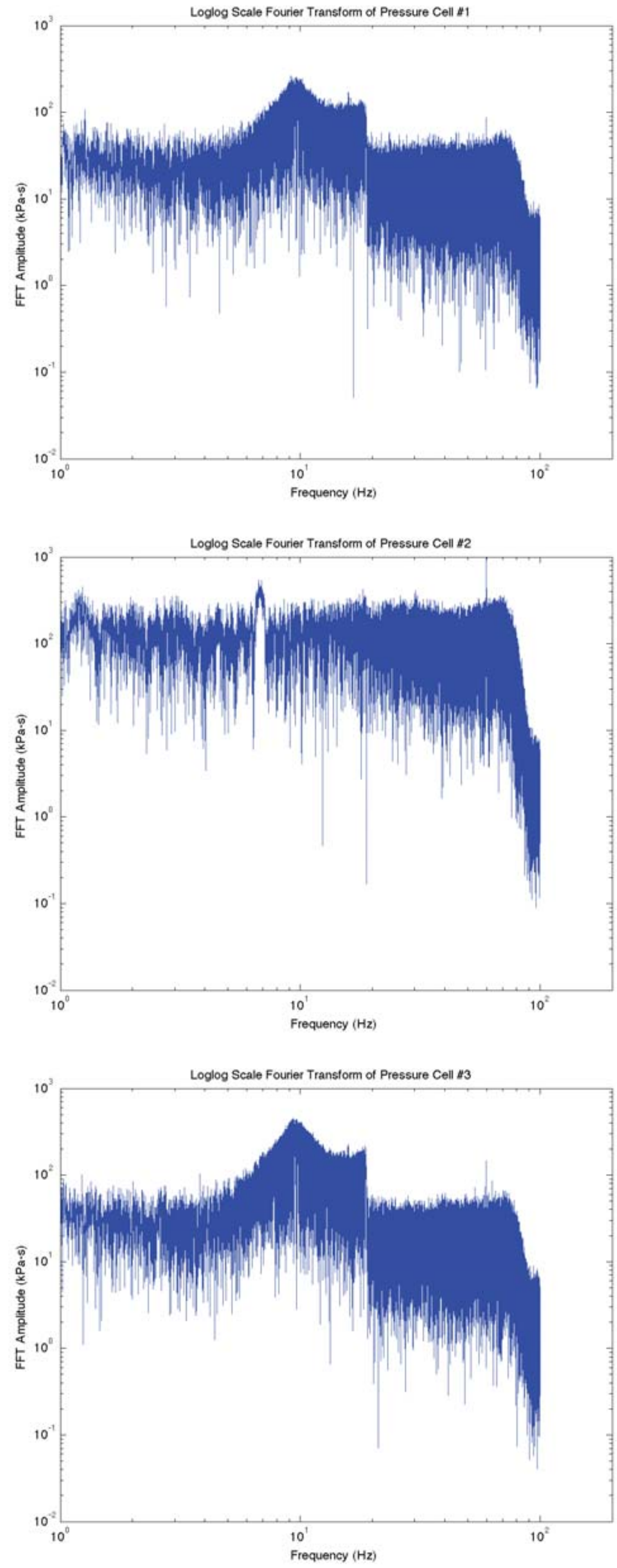

Loglog Scale Fourier Transform of Pressure Cell #1

Loglog Scale Fourier Transform of Pressure Cell #2

Loglog Scale Fourier Transform of Pressure Cell #3

Frequency domain pressure cell graphs from test 2.2.4

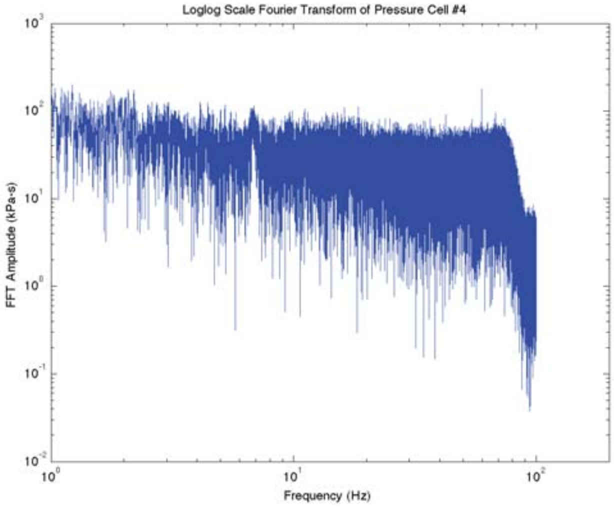

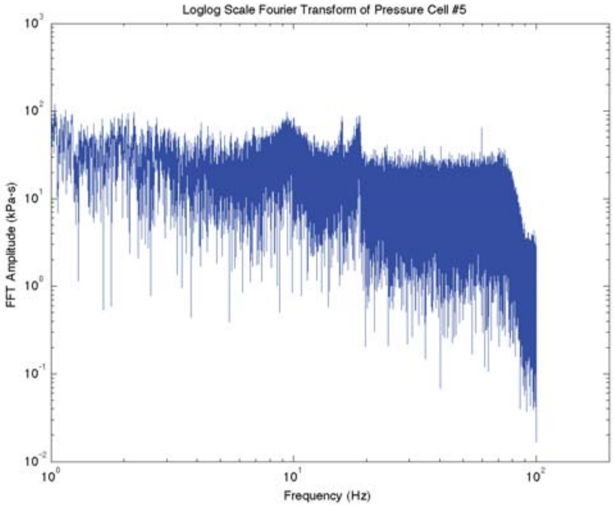

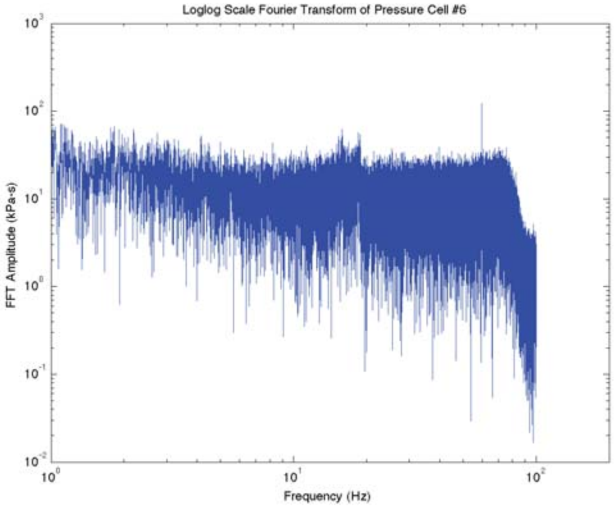

Frequency domain pressure cell graphs from test 2.2.4 (continued)

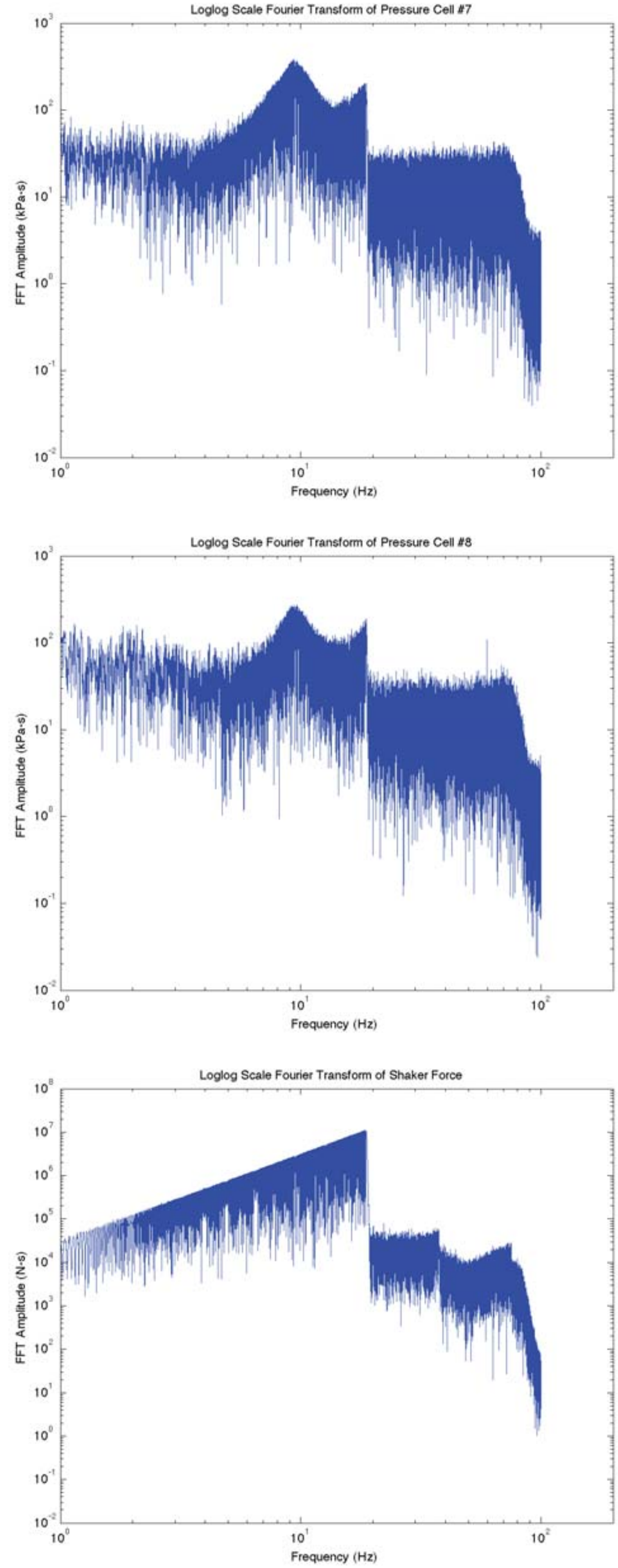

Frequency domain pressure cell graphs from test 2.2.4 (continued)

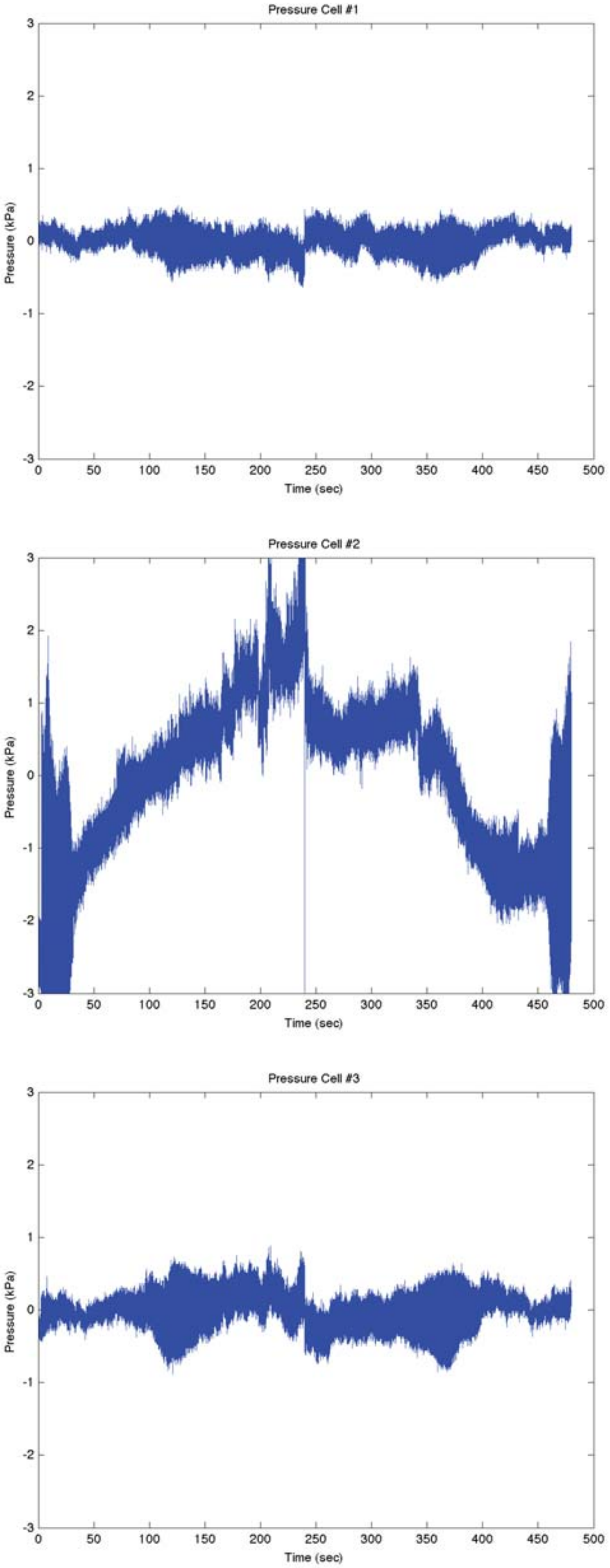

Time domain pressure cell graphs from test 2.2.4

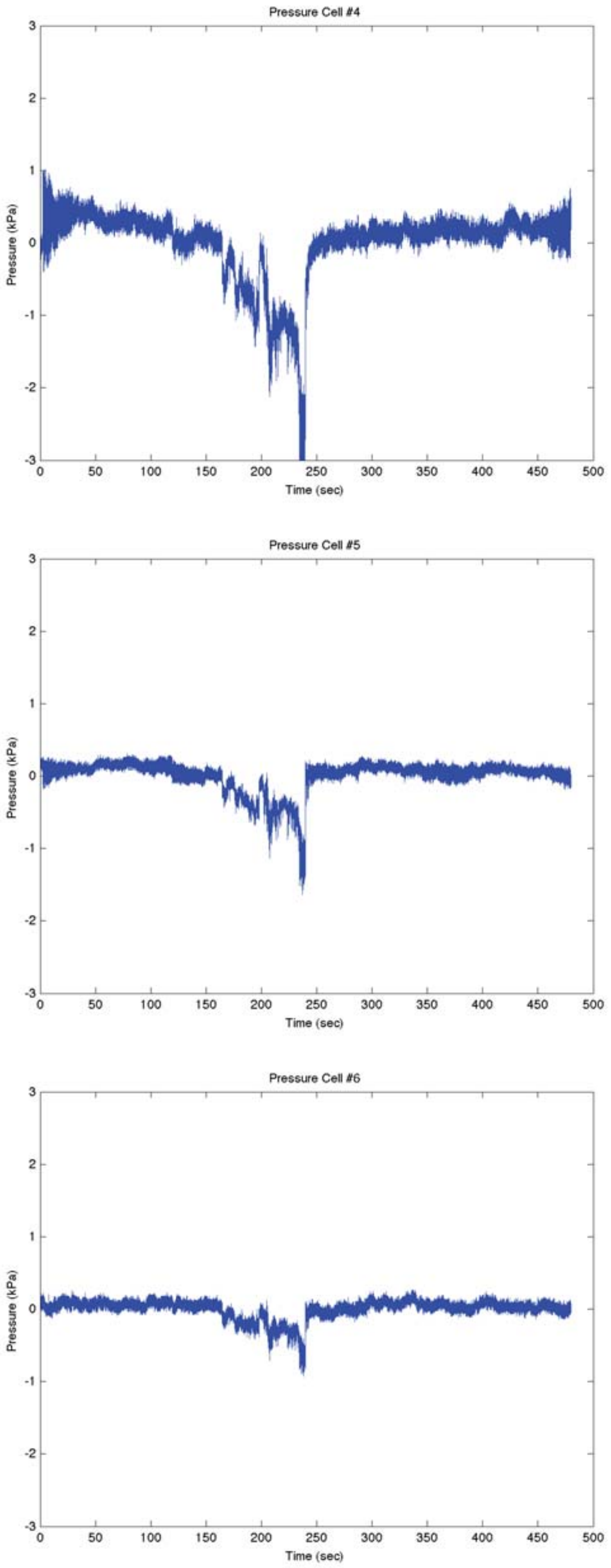

Time domain pressure cell graphs from test 2.2.4 (continued)

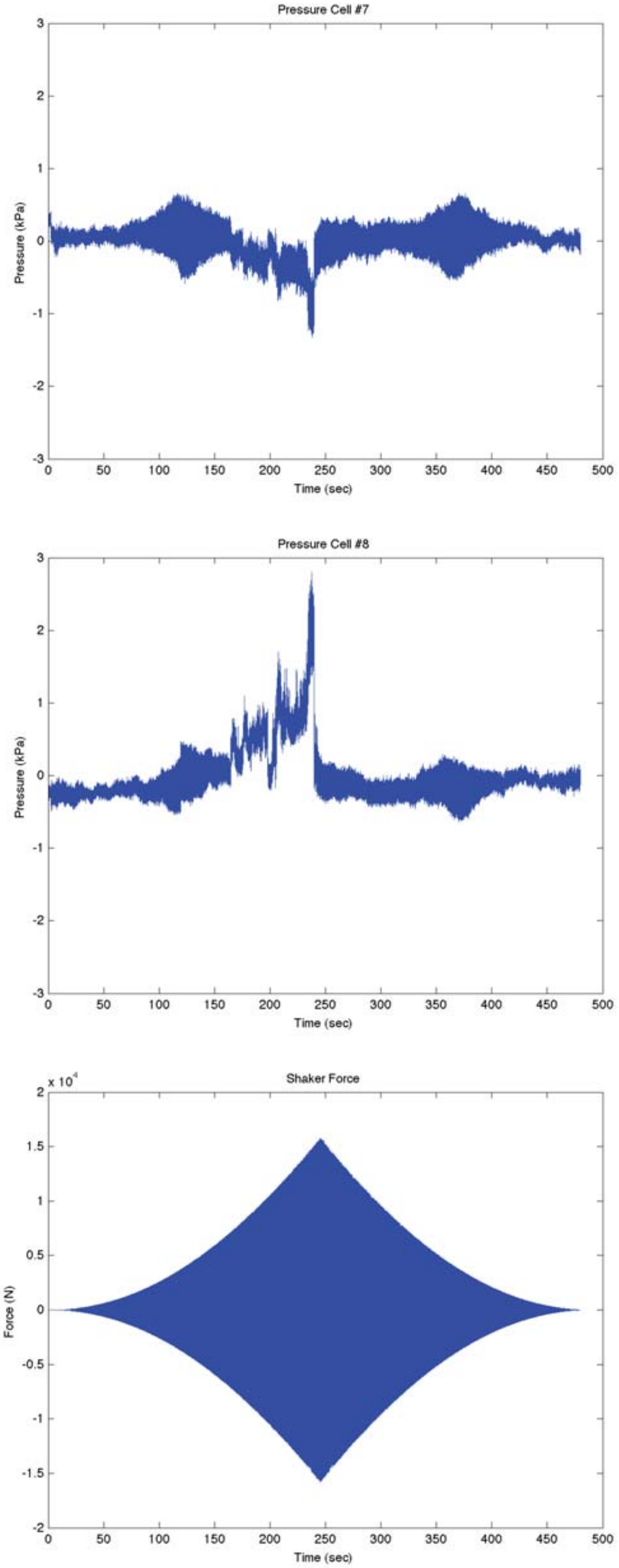

Time domain pressure cell graphs from test 2.2.4 (continued)

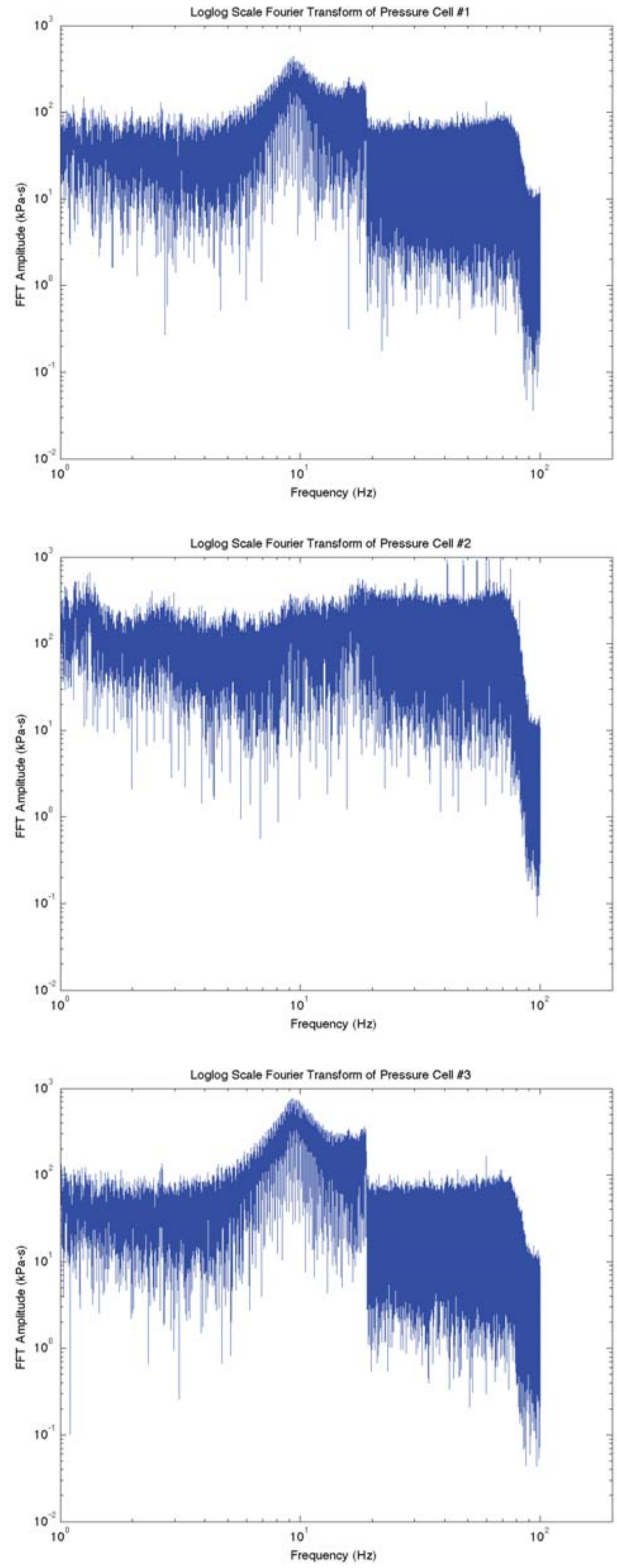

Frequency domain pressure cell graphs from test 2.2.5

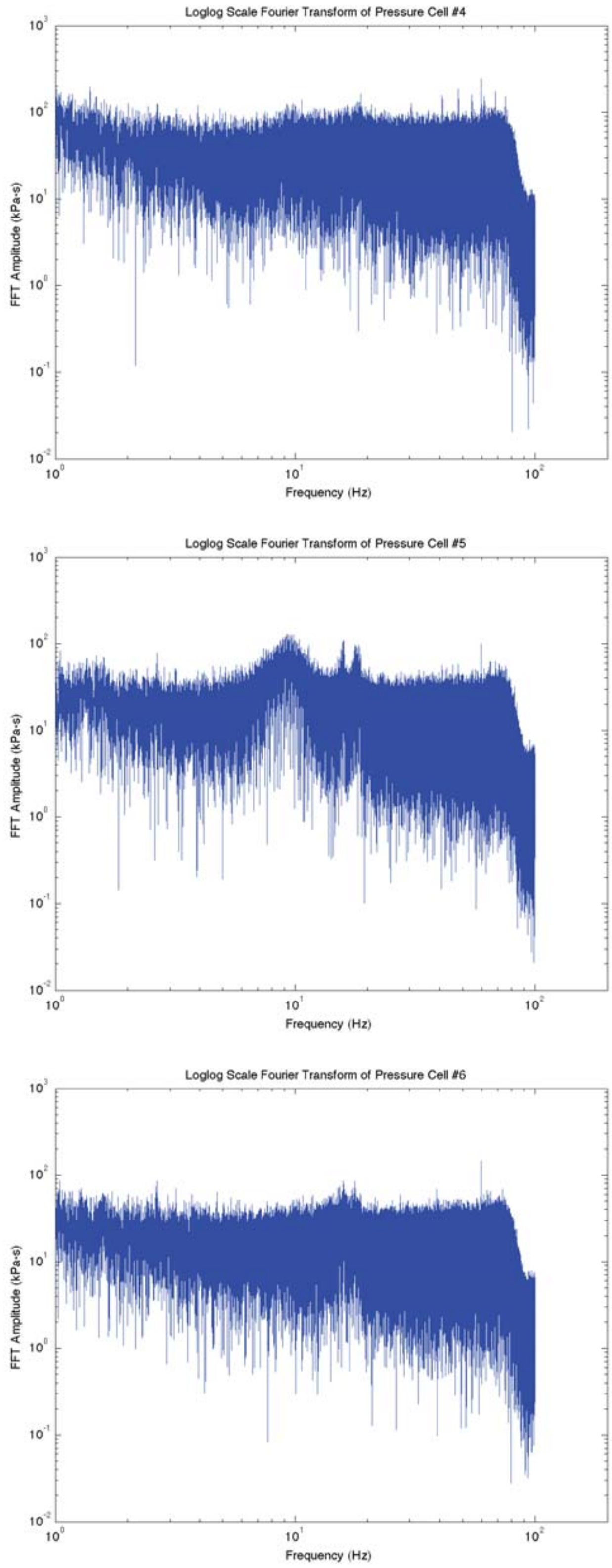

Frequency domain pressure cell graphs from test 2.2.5 (continued)

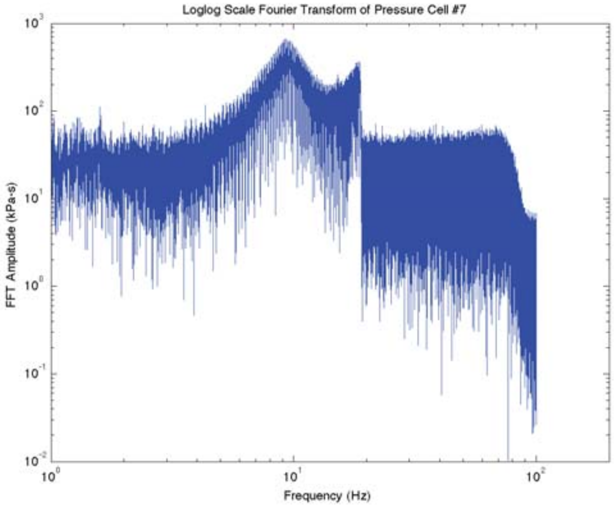

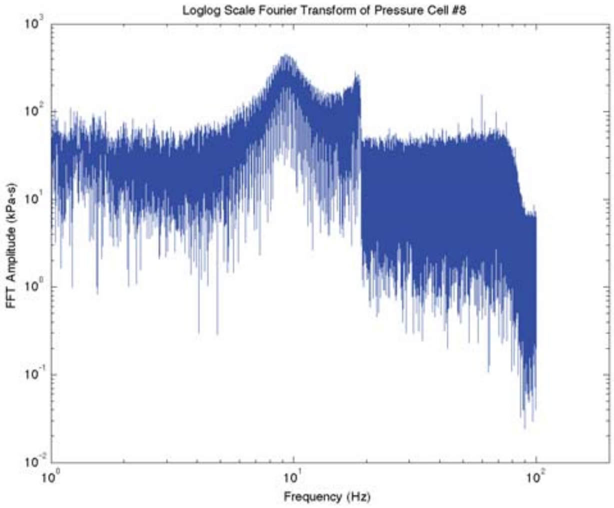

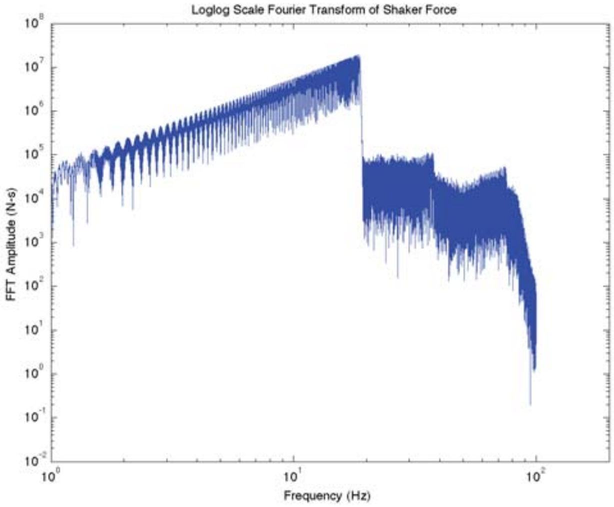

Frequency domain pressure cell graphs from test 2.2.5 (continued)

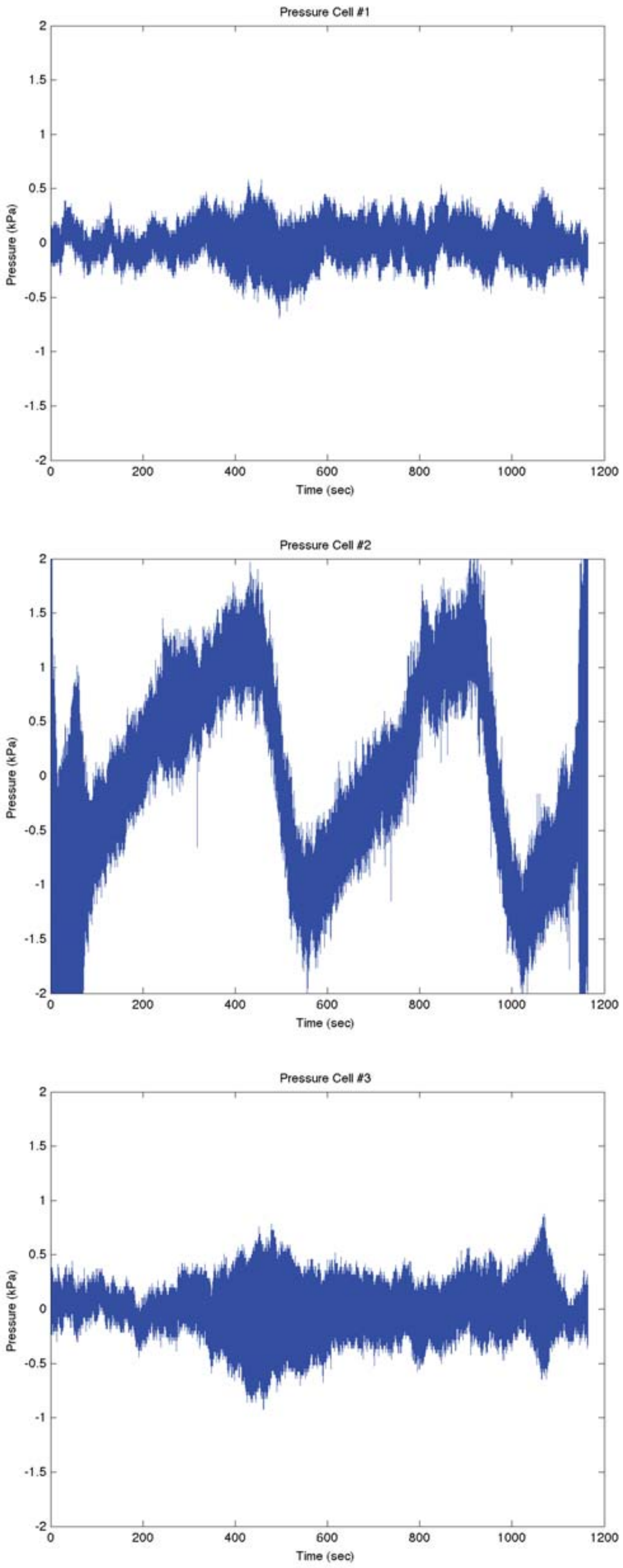

Time domain pressure cell graphs from test 2.2.5

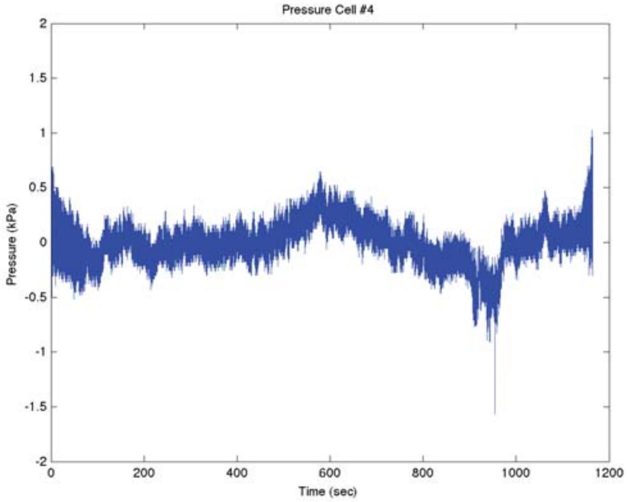

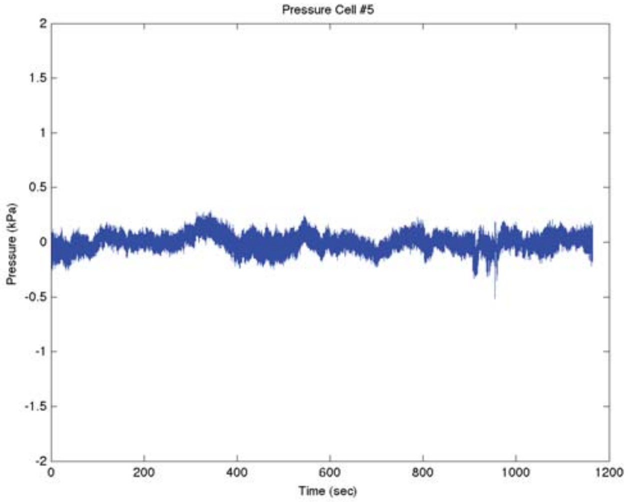

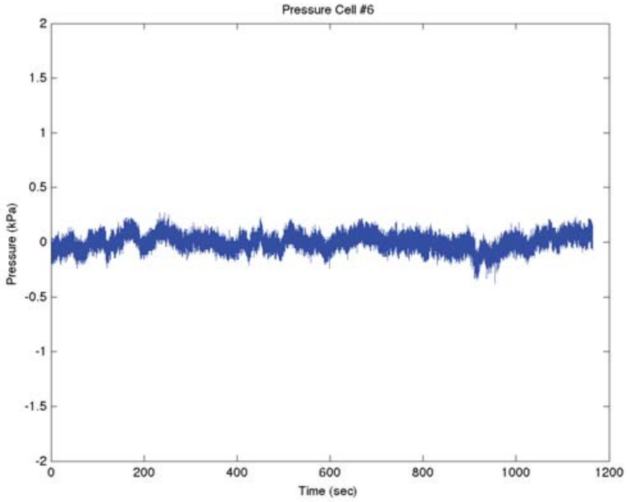

Time domain pressure cell graphs from test 2.2.5 (continued)

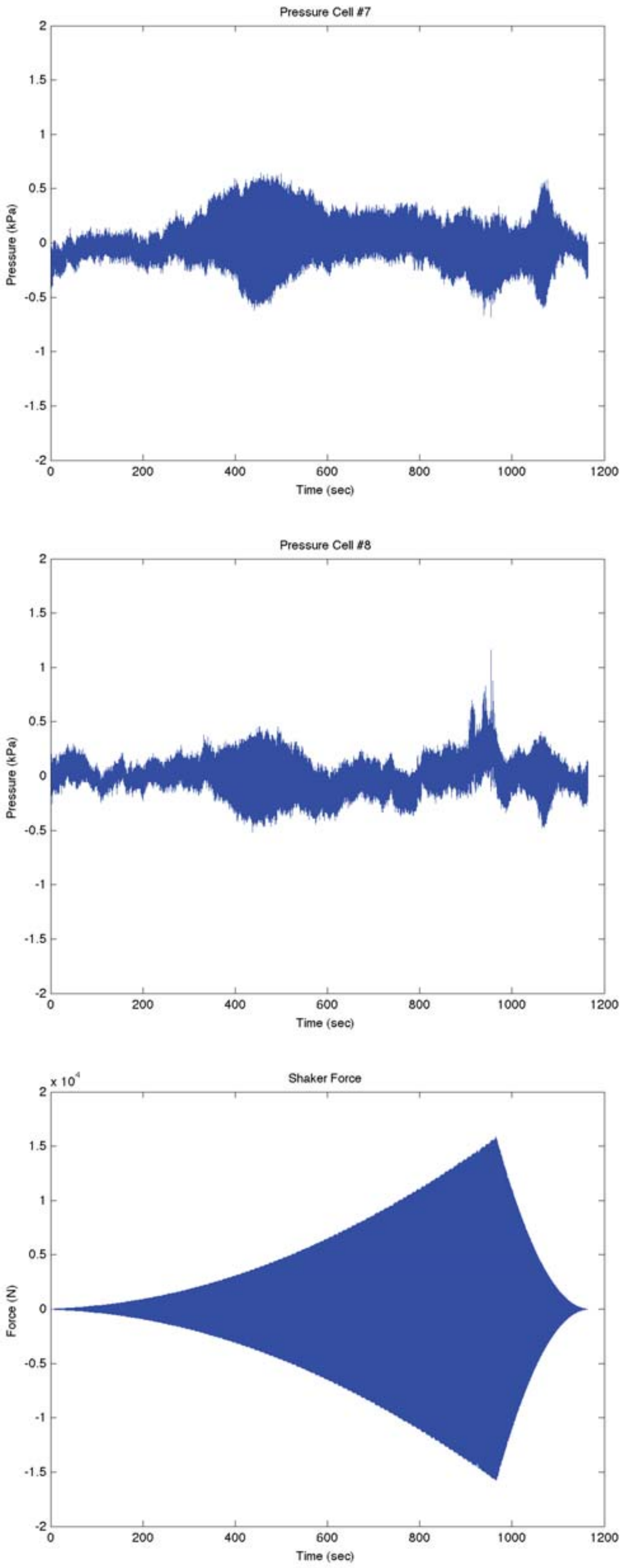

Time domain pressure cell graphs from test 2.2.5 (continued)

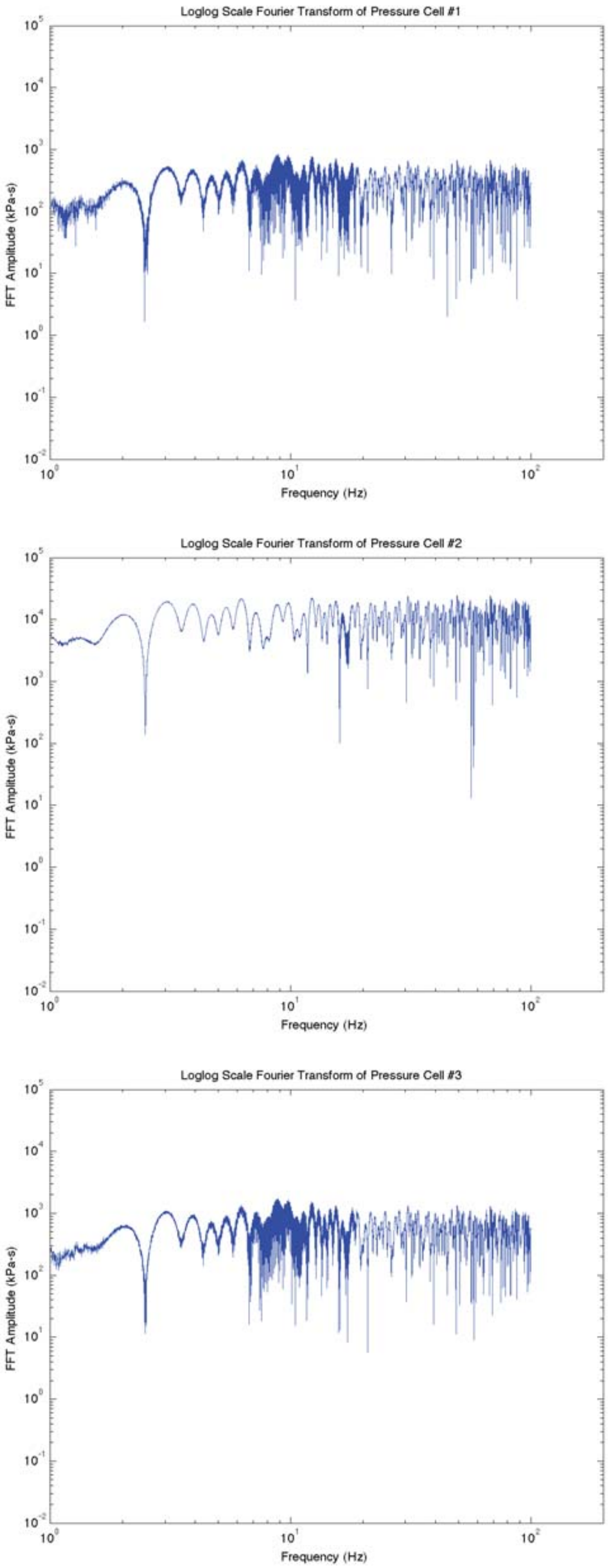

Frequency domain pressure cell graphs from test 2.2.6

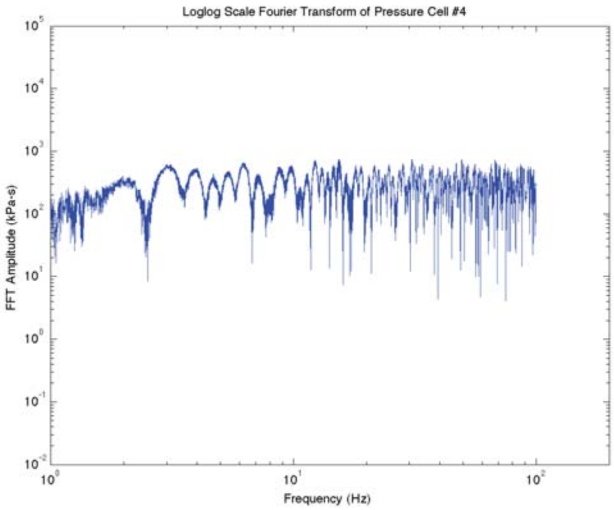

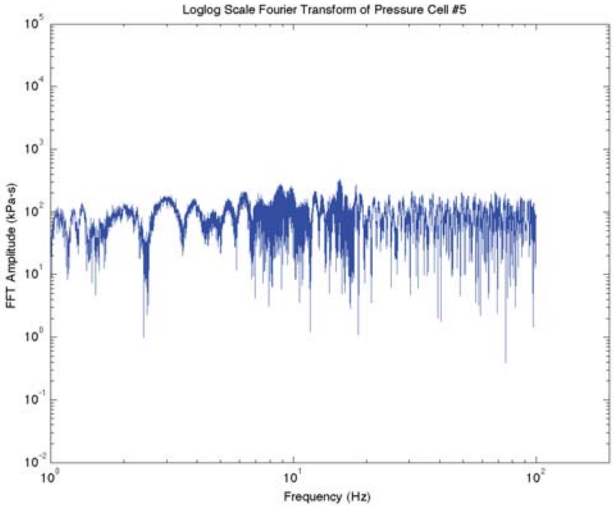

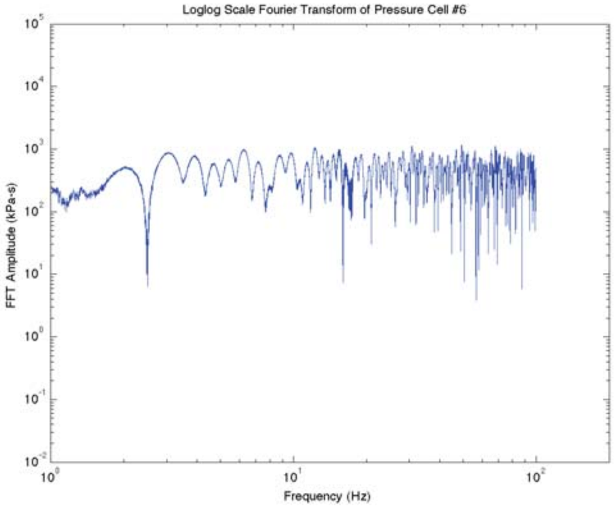

Frequency domain pressure cell graphs from test 2.2.6 (continued)

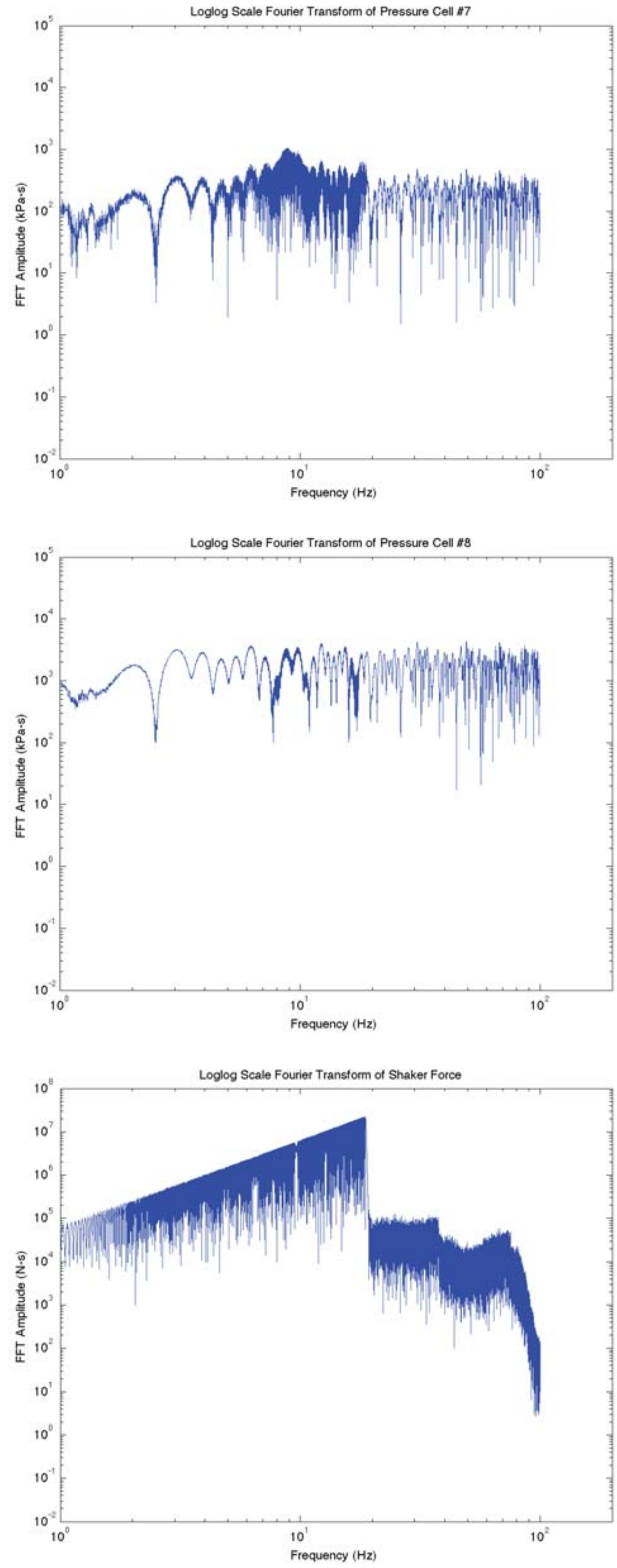

Frequency domain pressure cell graphs from test 2.2.6 (continued)

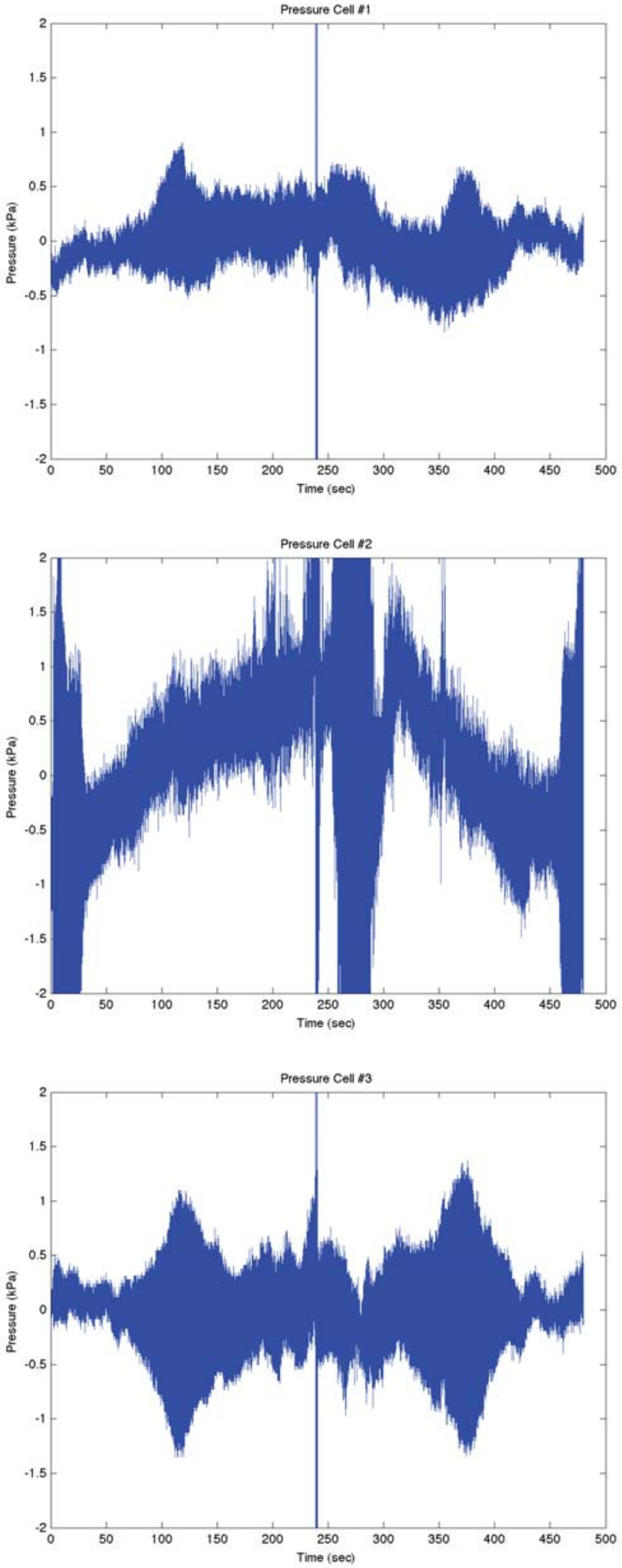

Time domain pressure cell graphs from test 2.2.6

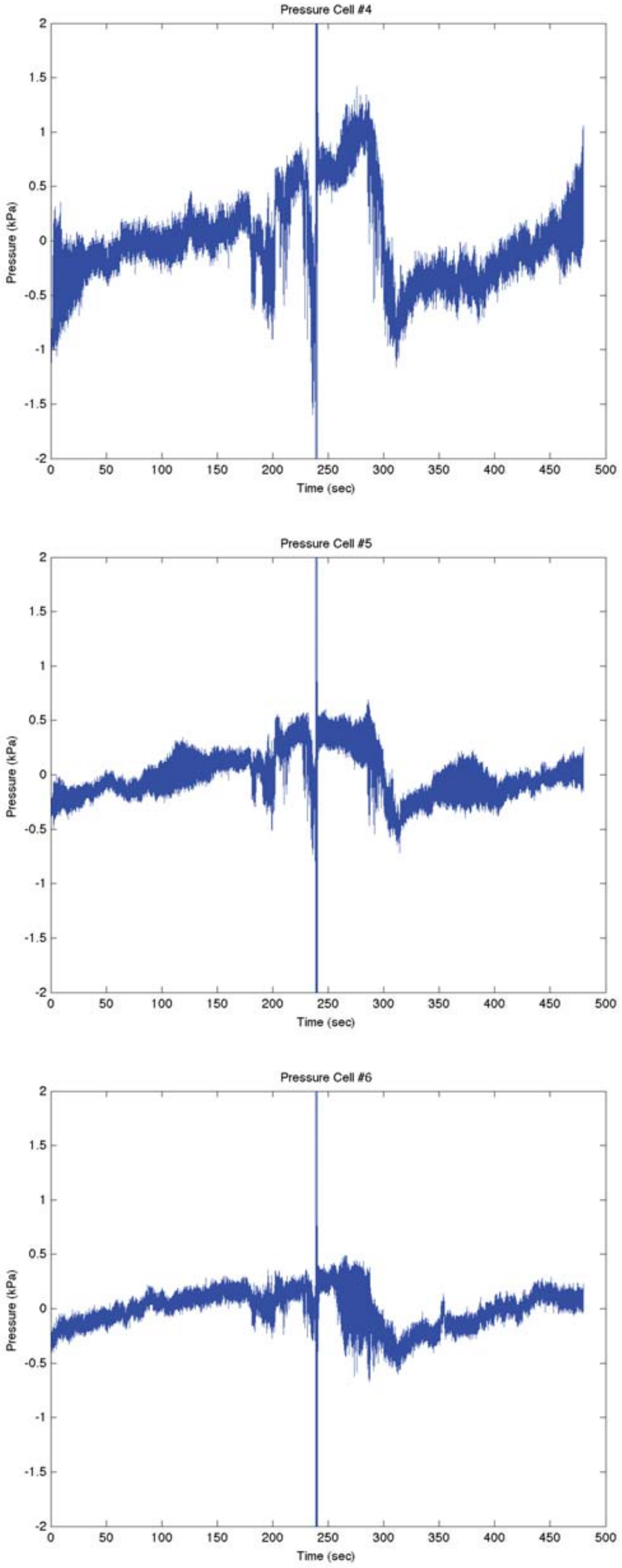

Time domain pressure cell graphs from test 2.2.6 (continued)

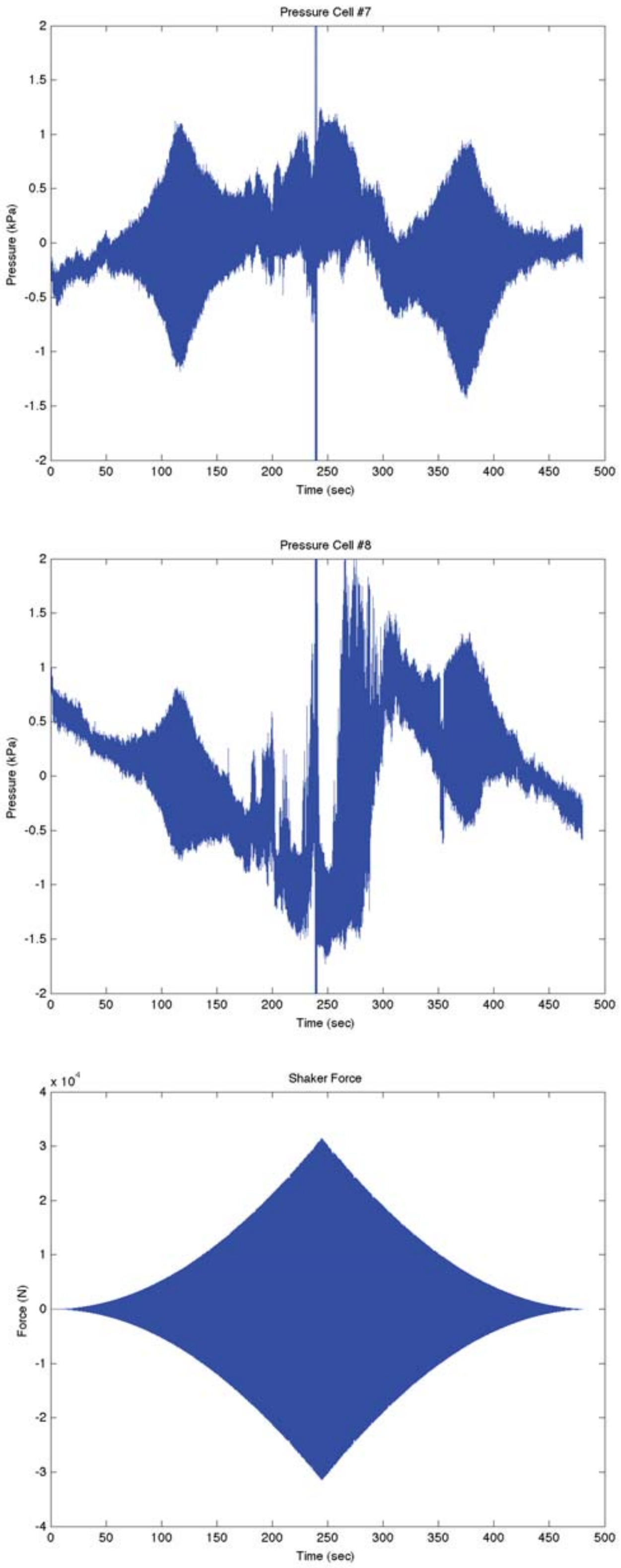

Time domain pressure cell graphs from test 2.2.6 (continued)

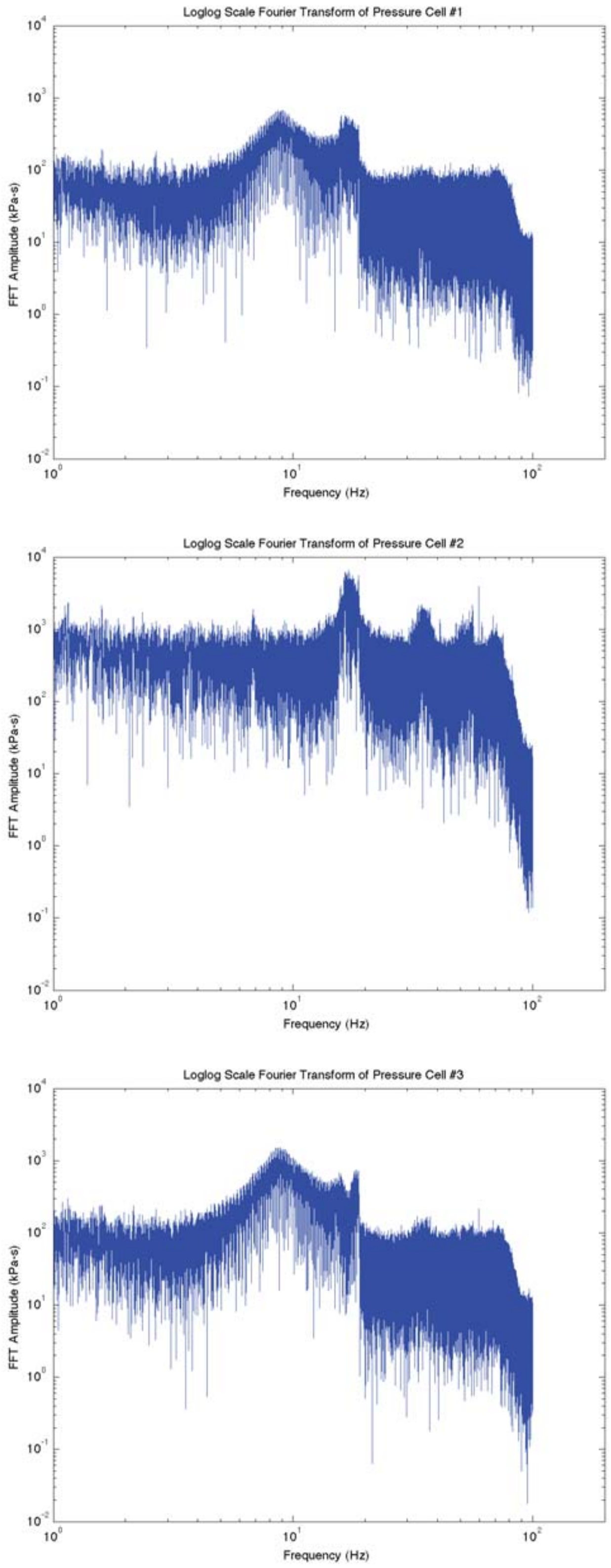

Frequency domain pressure cell graphs from test 2.2.7

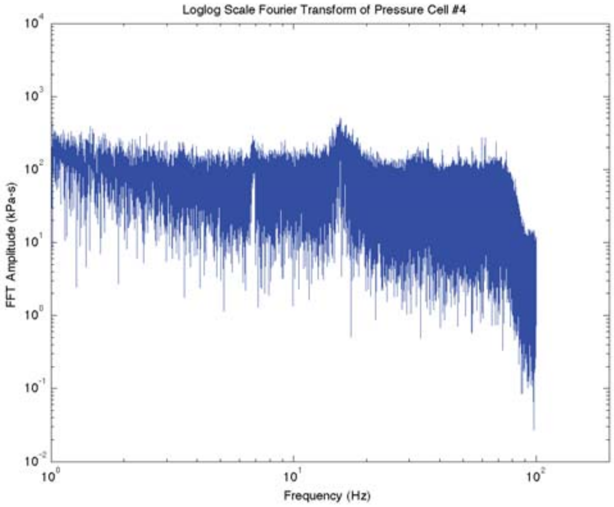

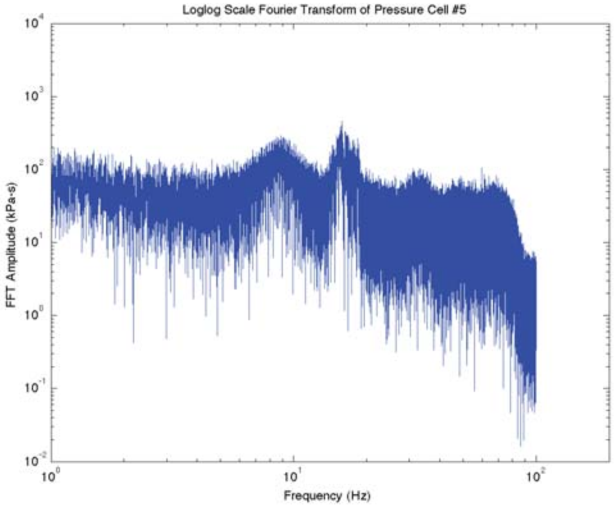

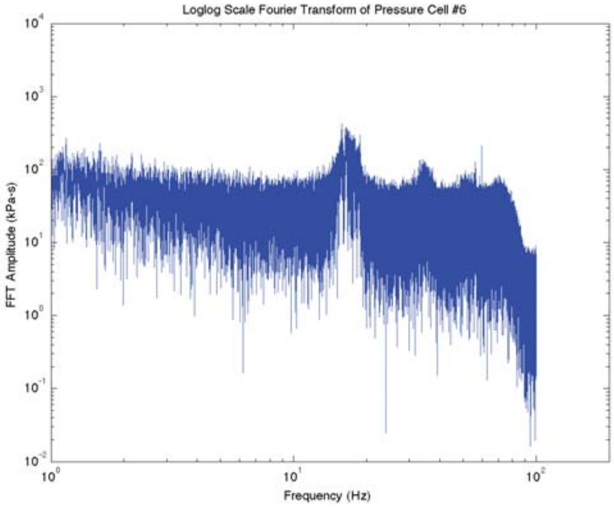

Frequency domain pressure cell graphs from test 2.2.7 (continued)

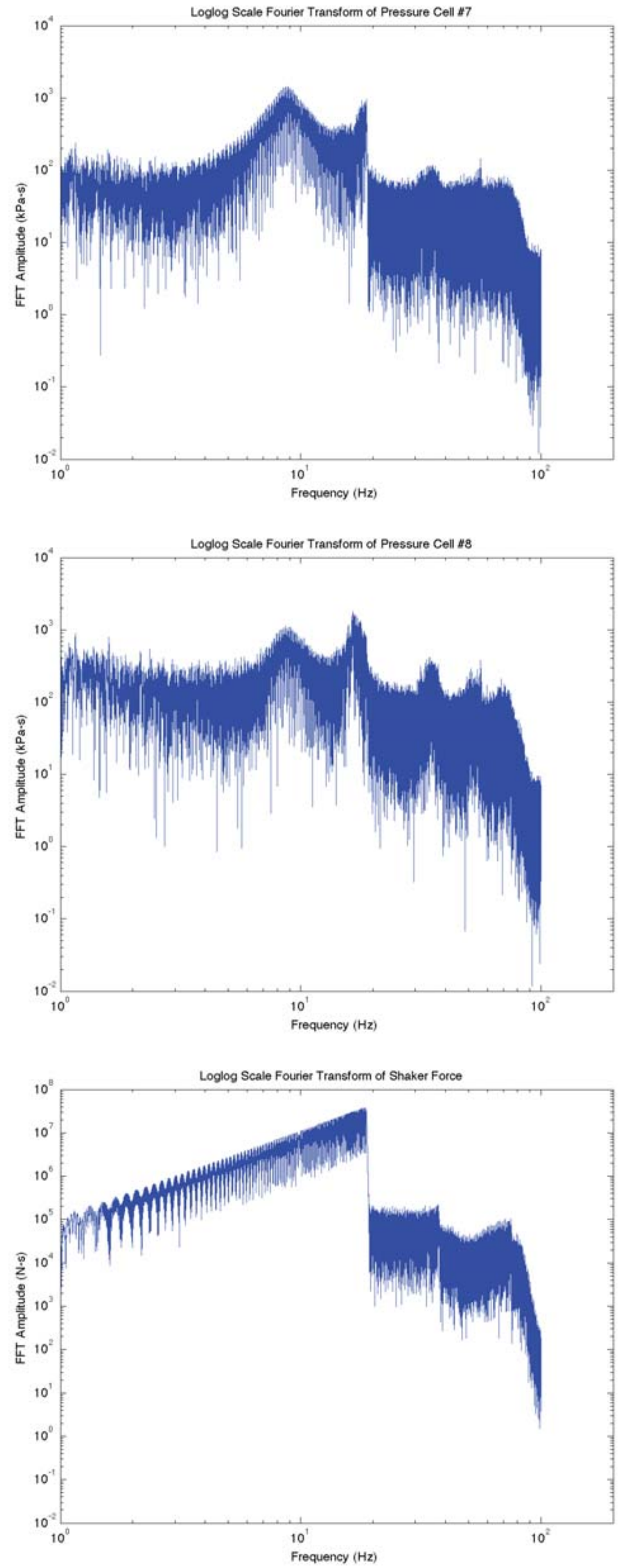

Frequency domain pressure cell graphs from test 2.2.7 (continued)

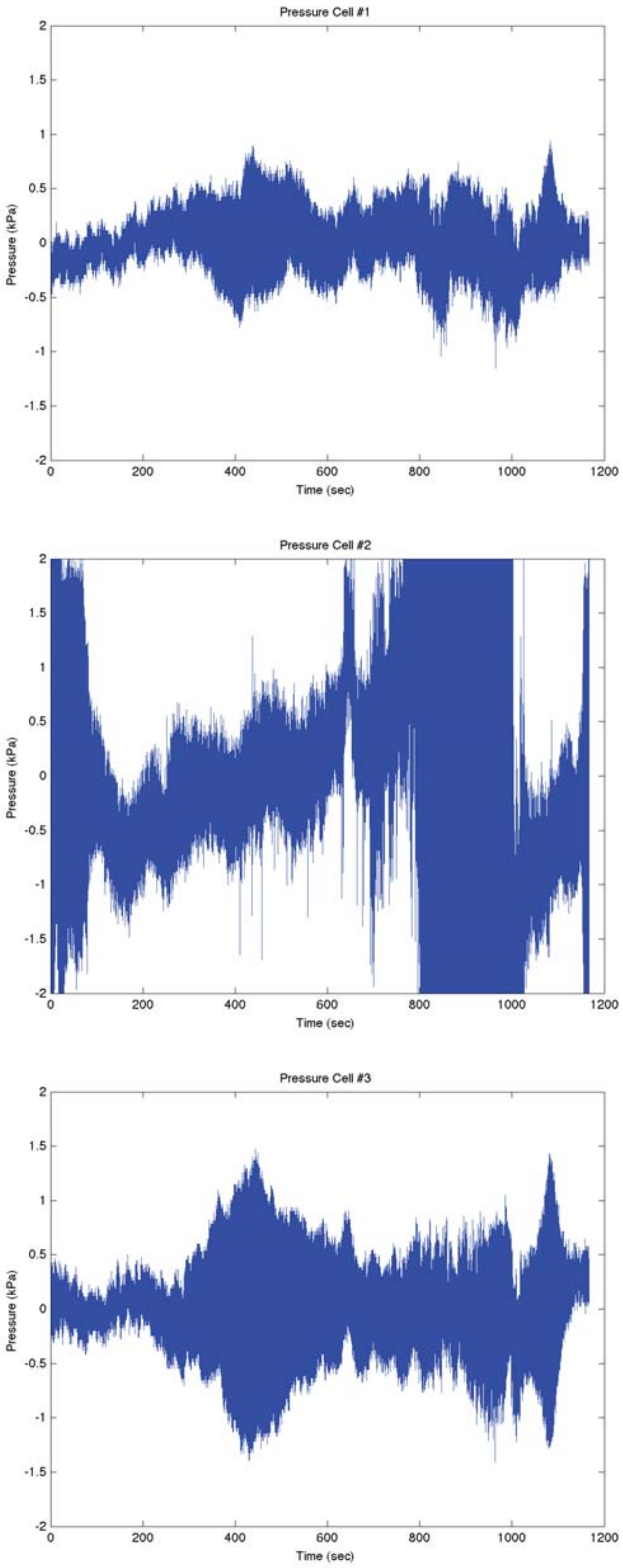

Time domain pressure cell graphs from test 2.2.7

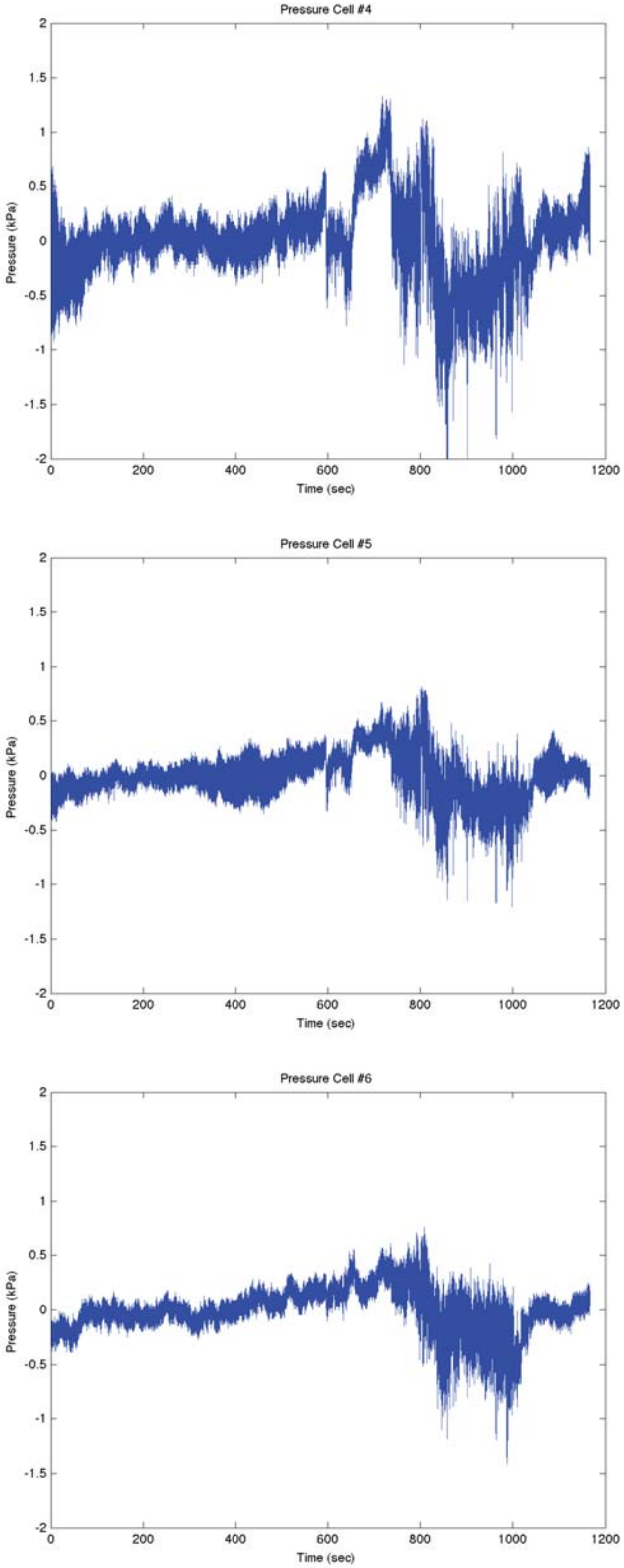

Time domain pressure cell graphs from test 2.2.7 (continued)

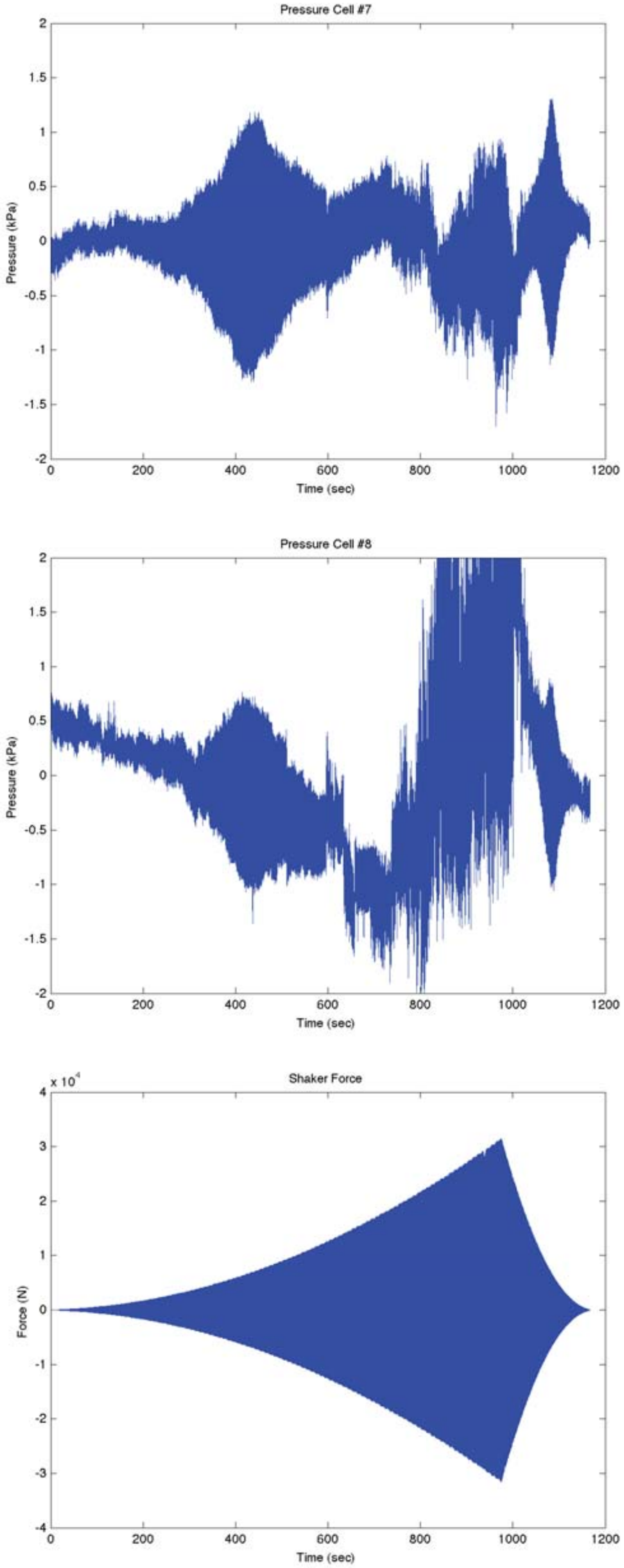

Time domain pressure cell graphs from test 2.2.7 (continued)

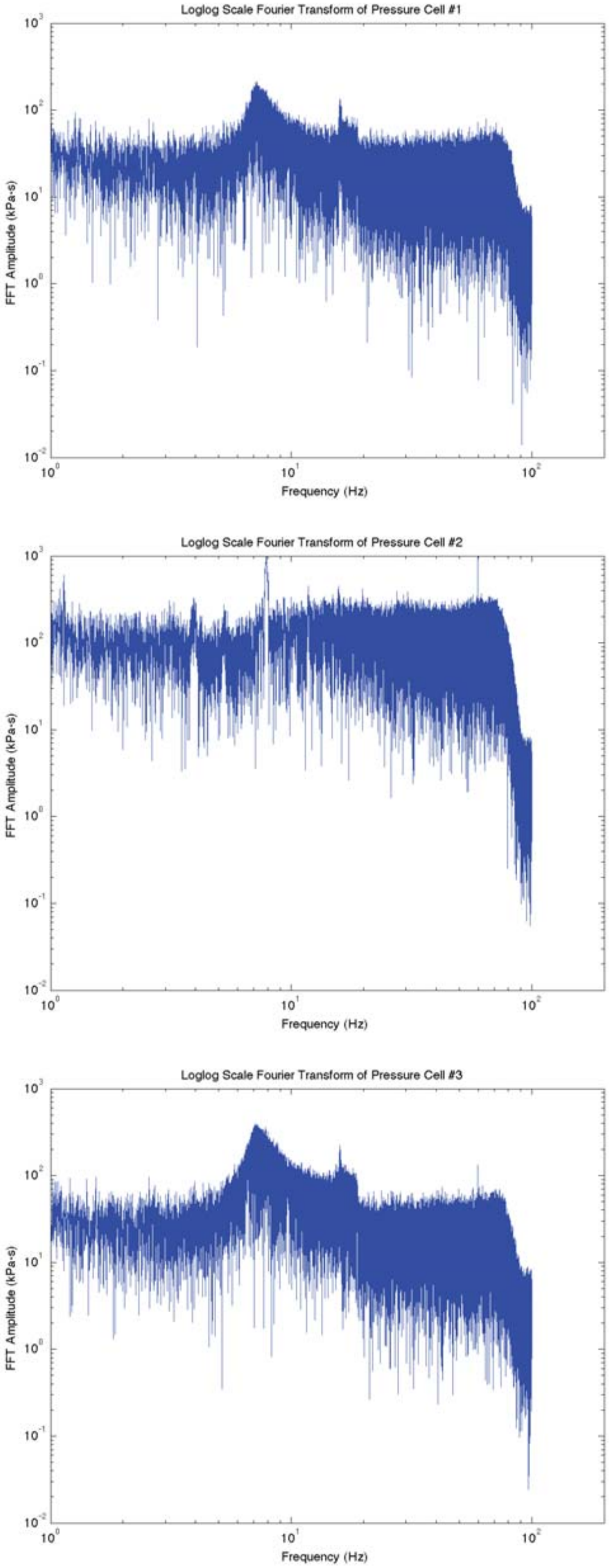

Frequency domain pressure cell graphs from test 2.2.8

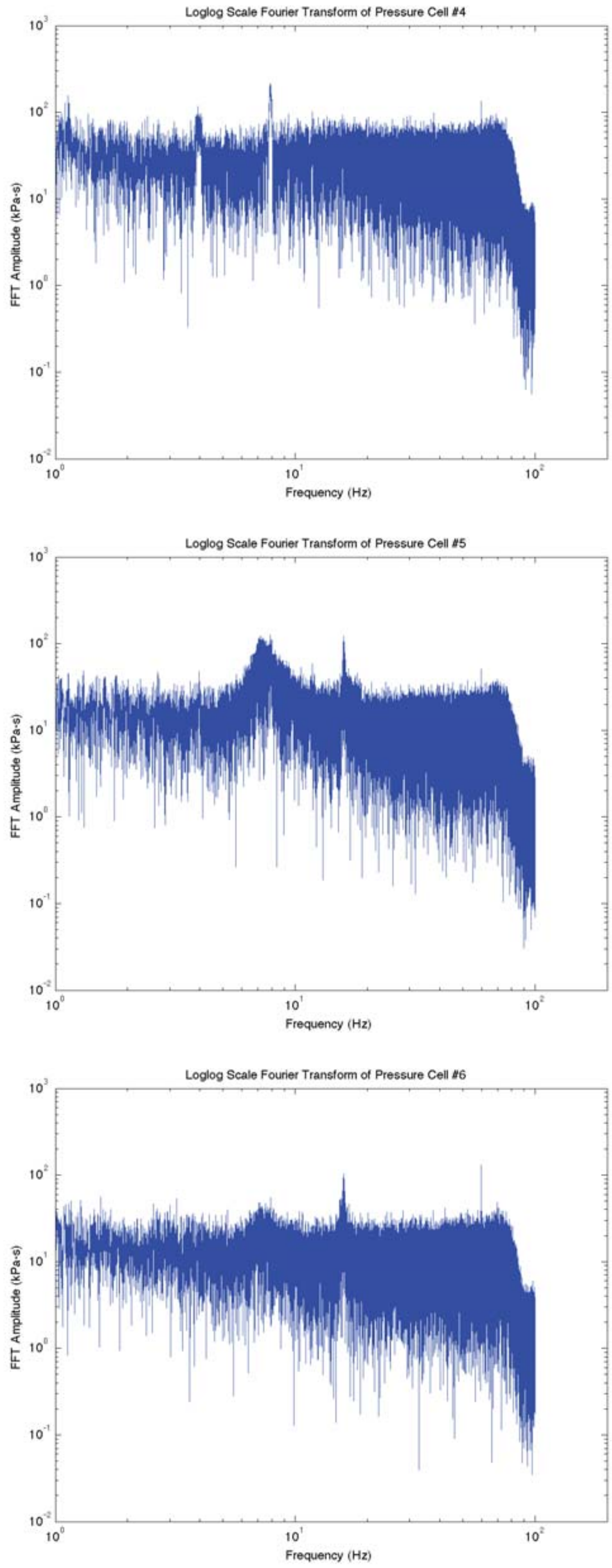

Frequency domain pressure cell graphs from test 2.2.8 (continued)

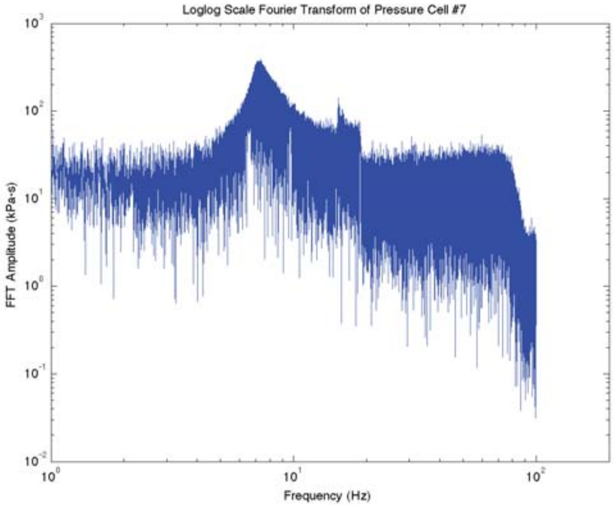

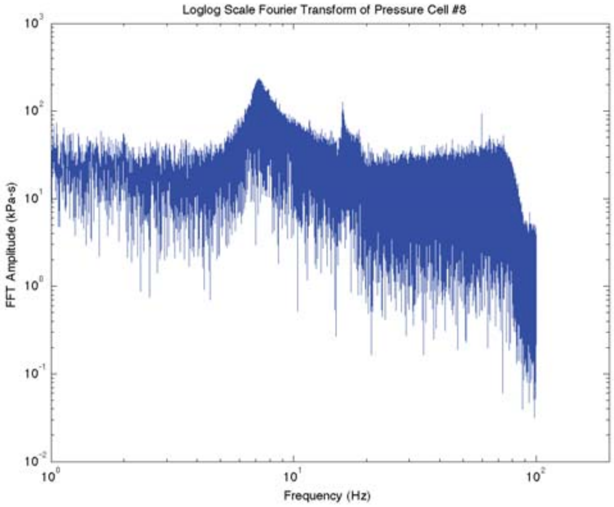

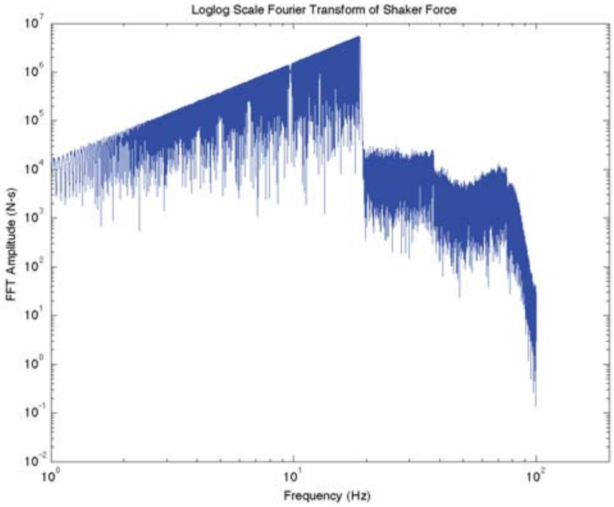

Frequency domain pressure cell graphs from test 2.2.8 (continued)

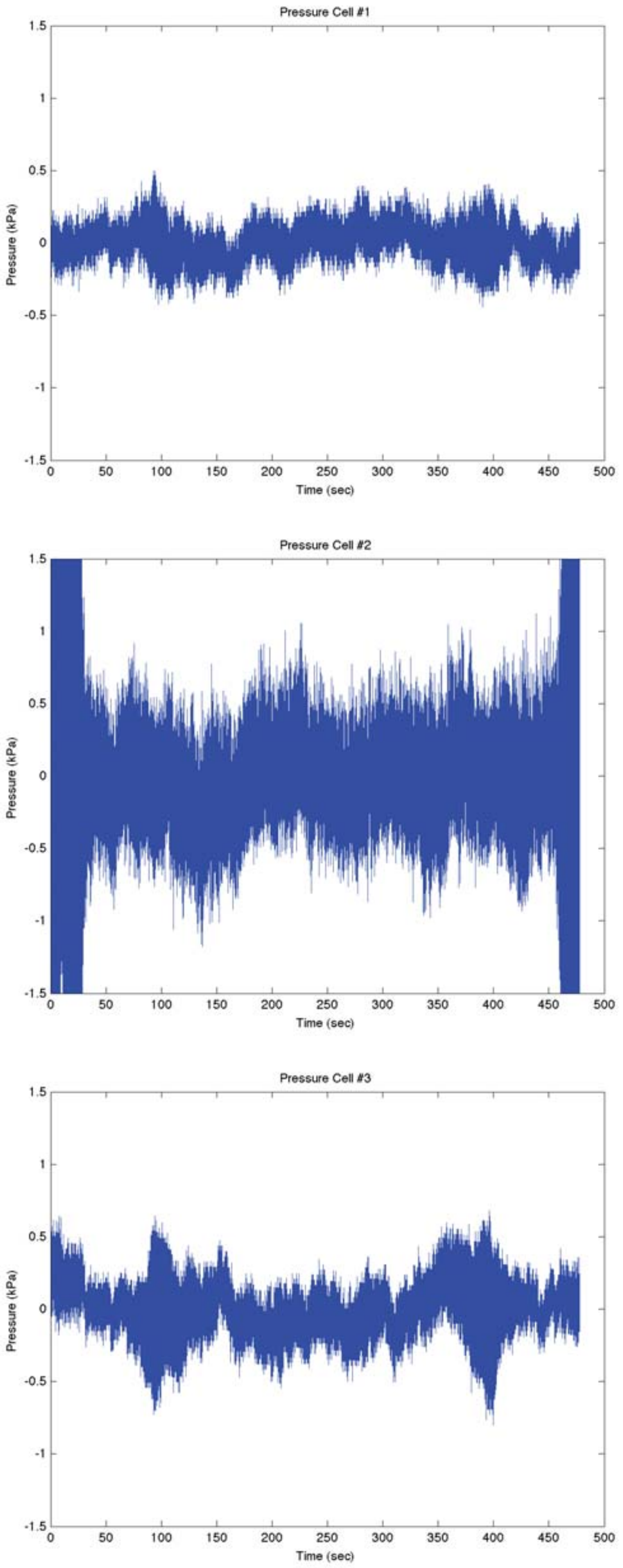

Time domain pressure cell graphs from test 2.2.8

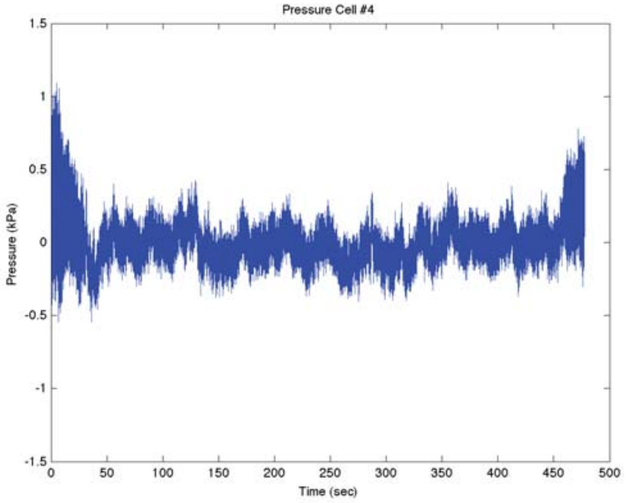

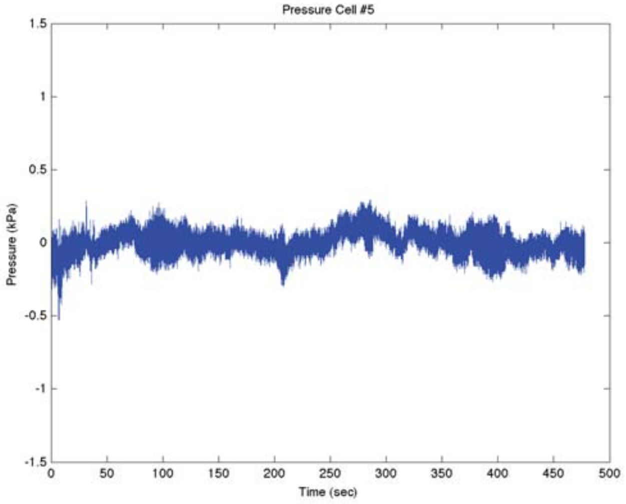

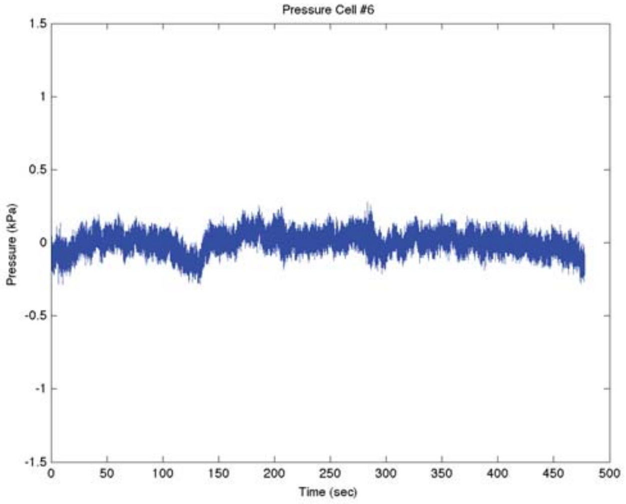

Time domain pressure cell graphs from test 2.2.8 (continued)

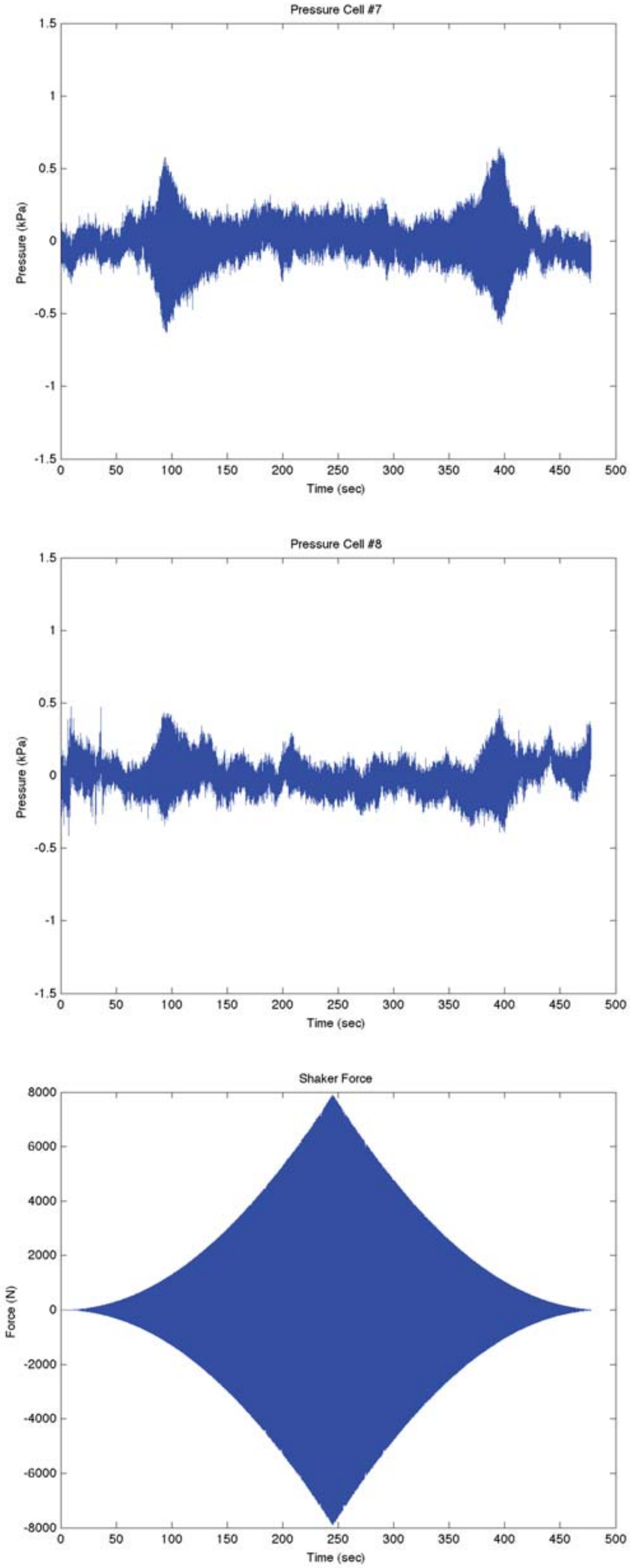

Time domain pressure cell graphs from test 2.2.8 (continued)

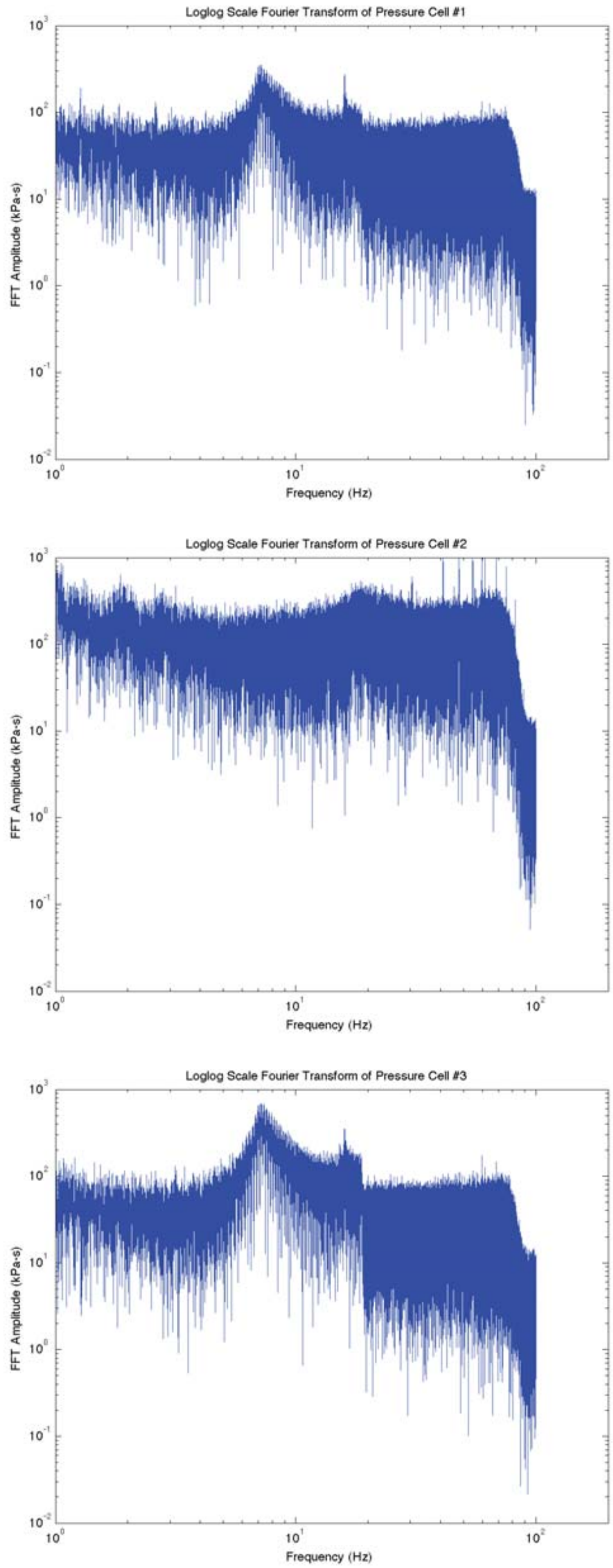

Frequency domain pressure cell graphs from test 2.2.9

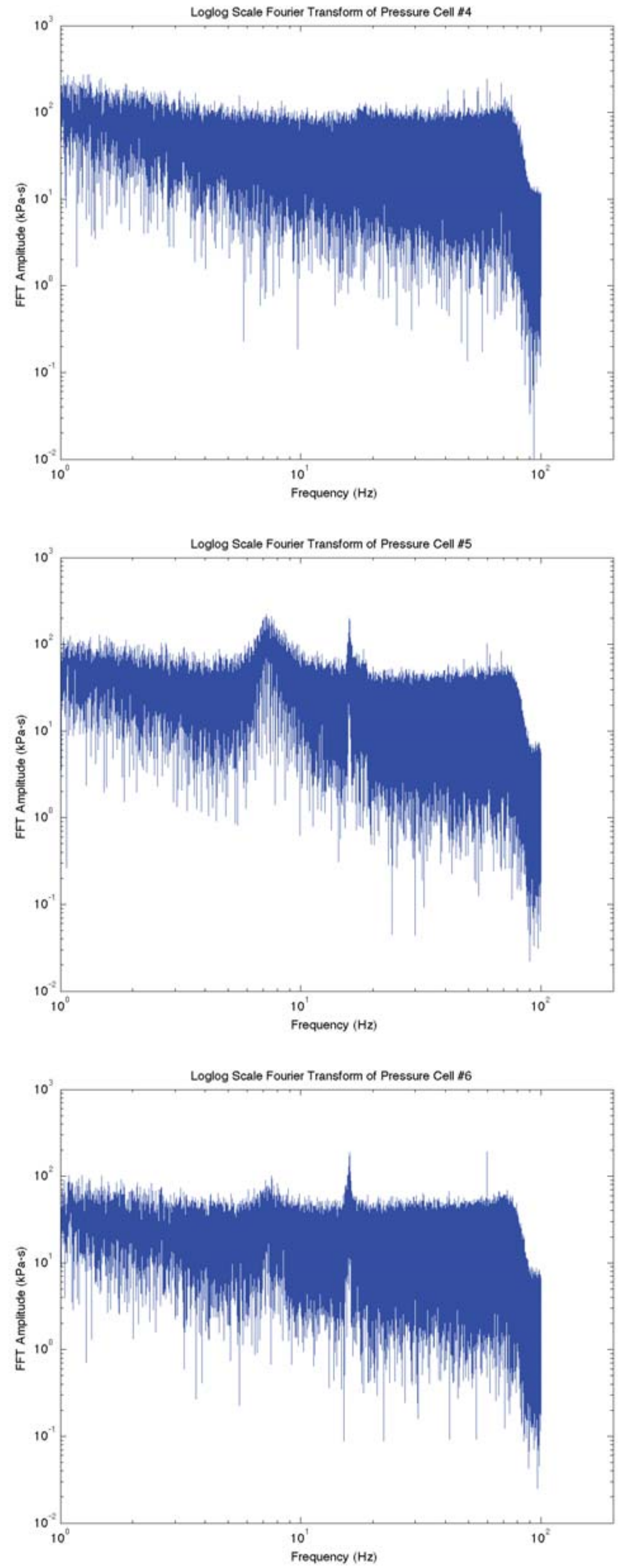

Frequency domain pressure cell graphs from test 2.2.9 (continued)

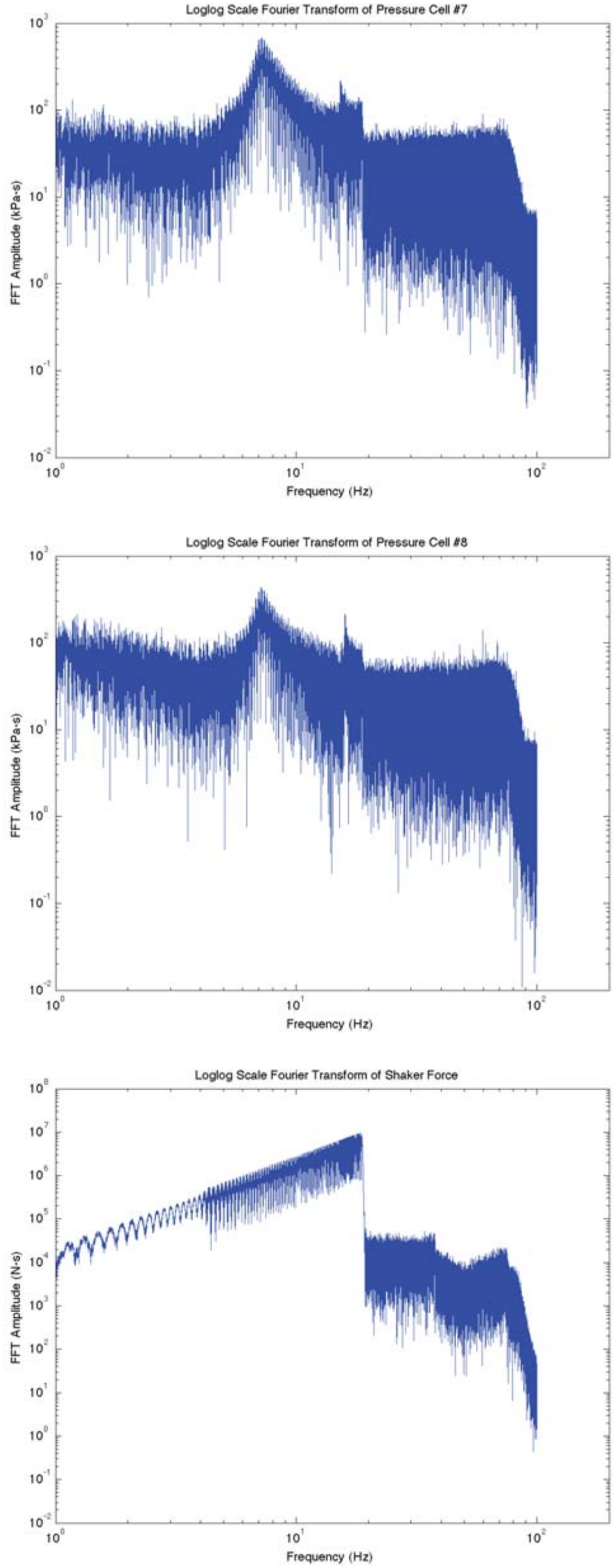

Frequency domain pressure cell graphs from test 2.2.9 (continued)

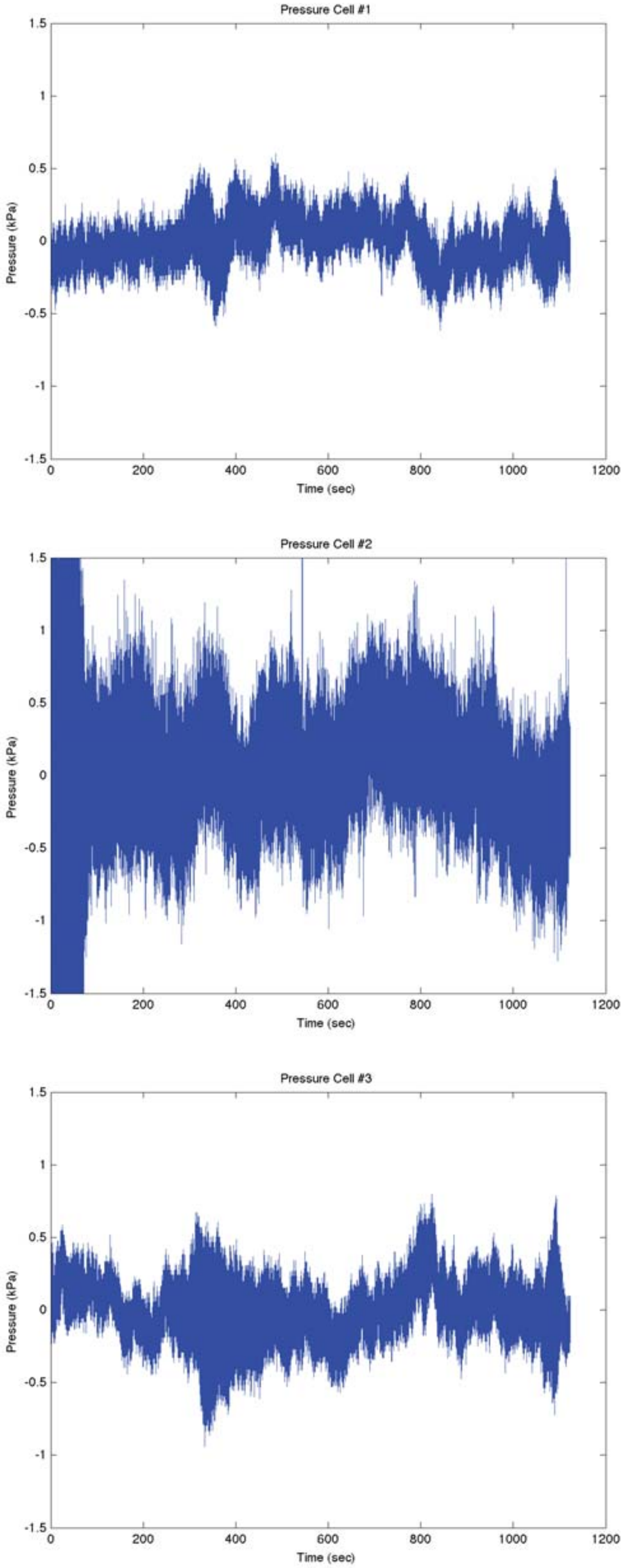

Time domain pressure cell graphs from test 2.2.9

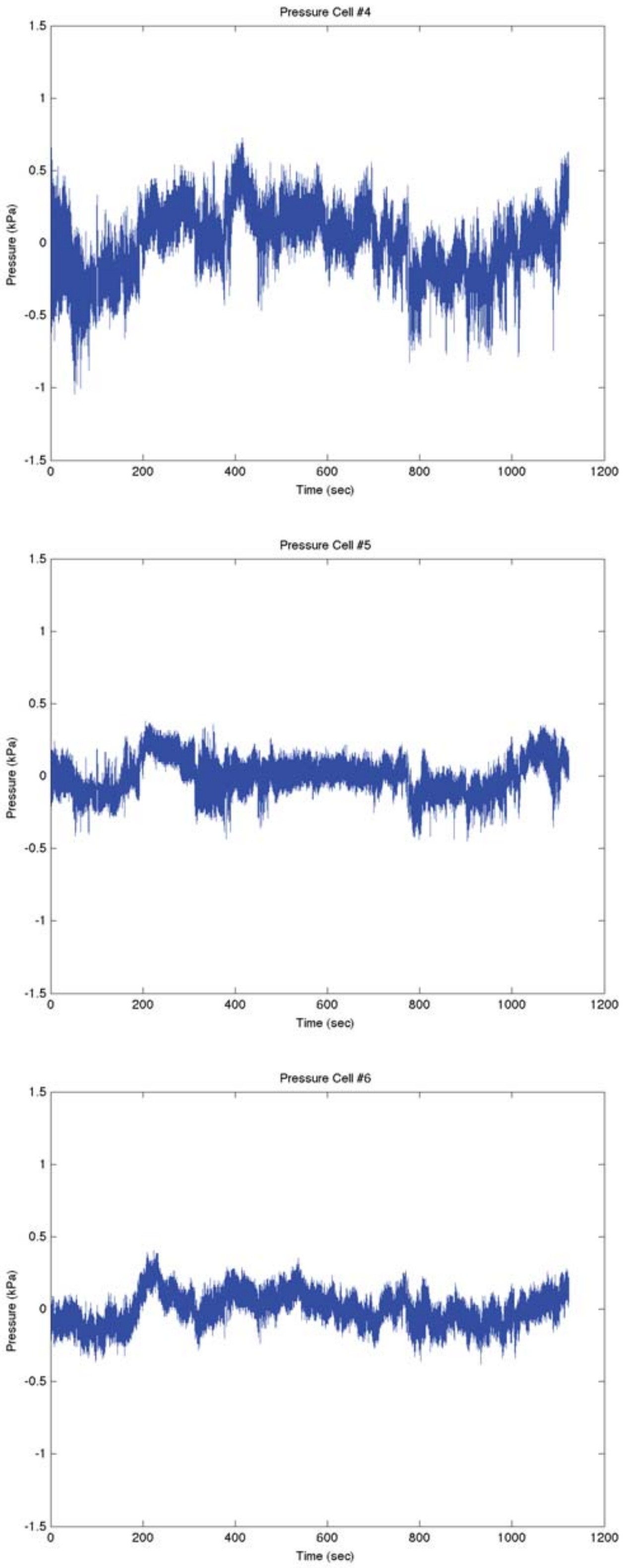

Time domain pressure cell graphs from test 2.2.9 (continued)

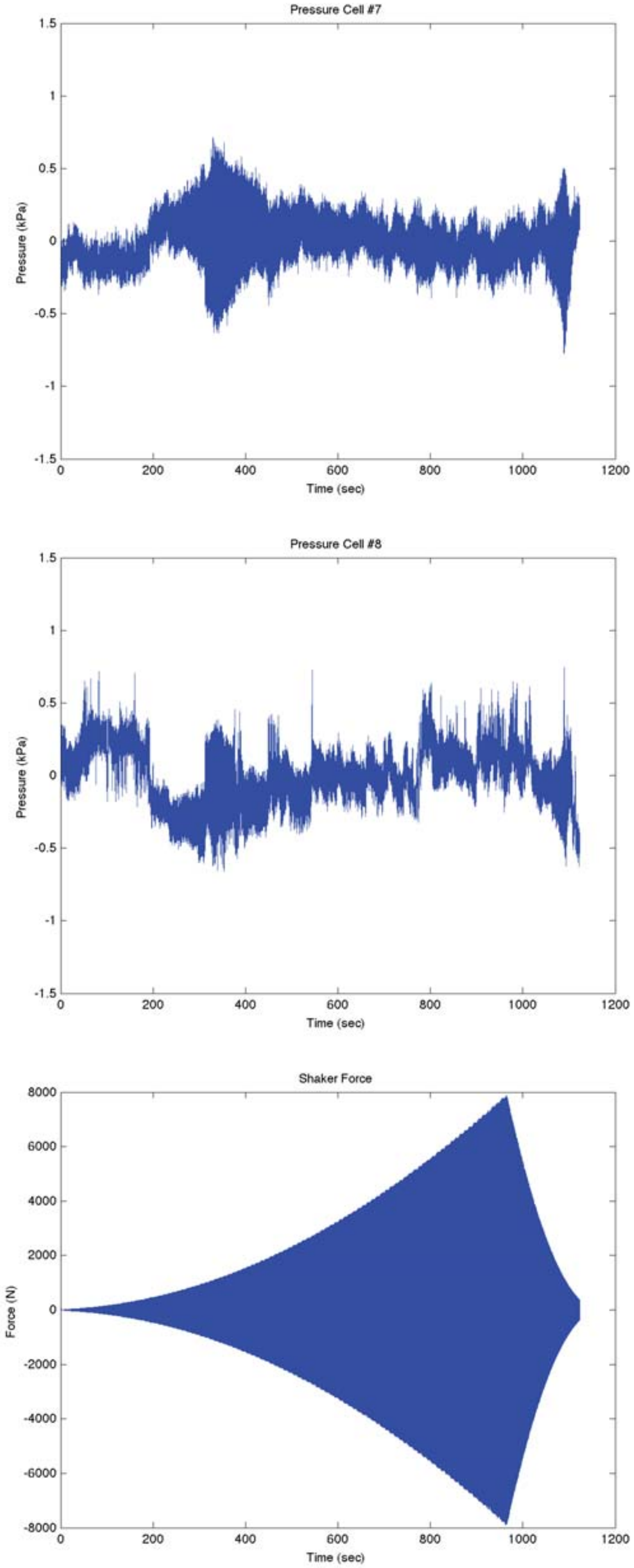

Time domain pressure cell graphs from test 2.2.9 (continued)

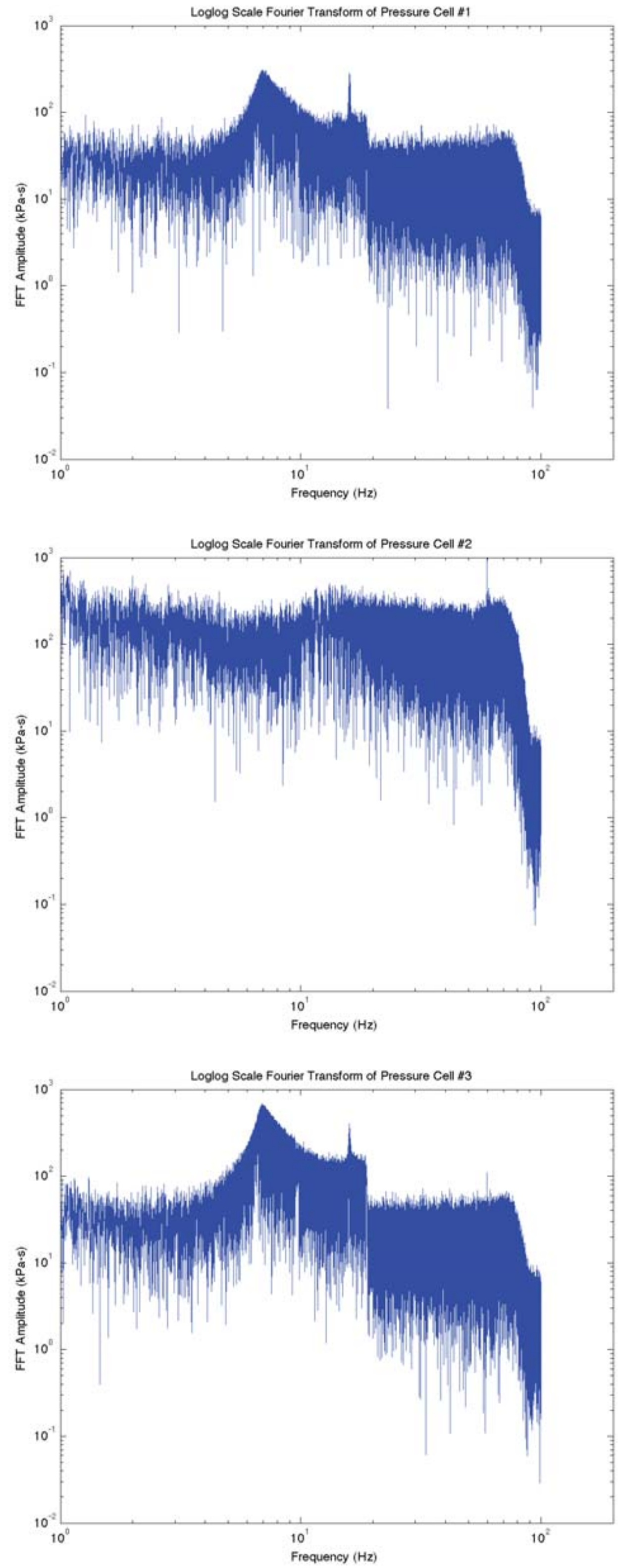

Frequency domain pressure cell graphs from test 2.2.10

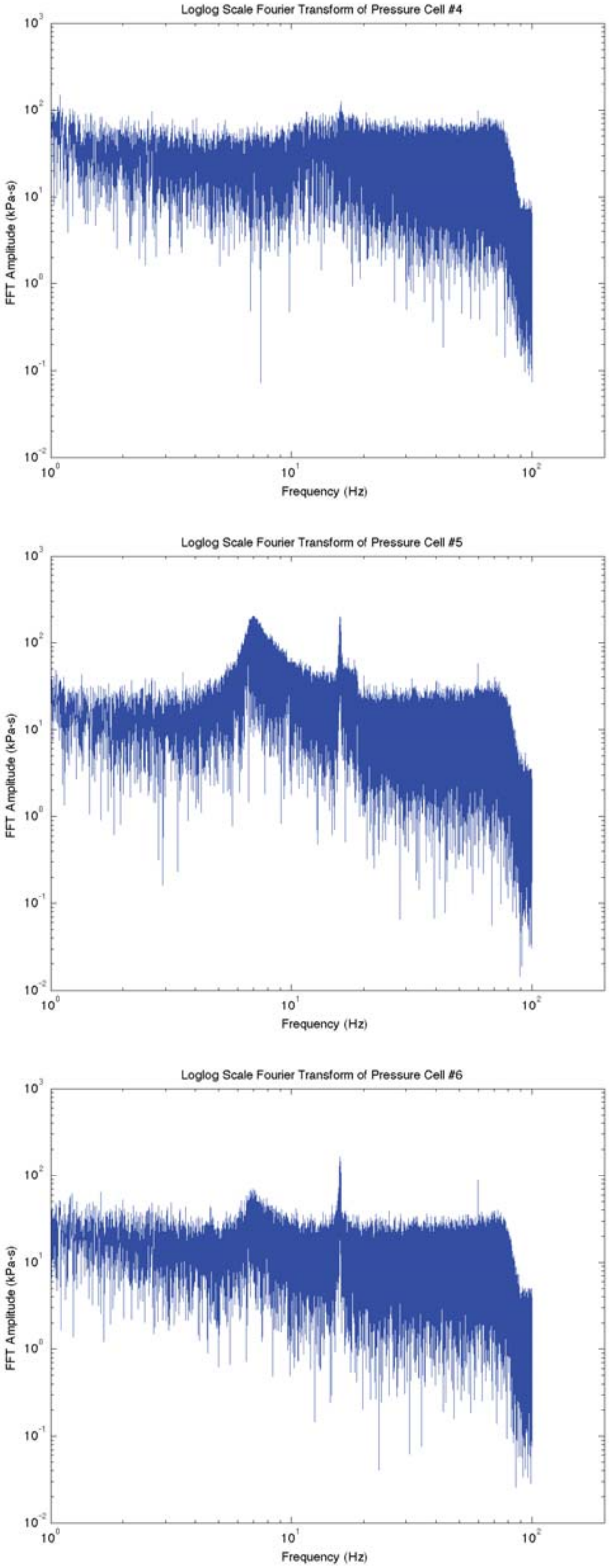

Frequency domain pressure cell graphs from test 2.2.10 (continued)

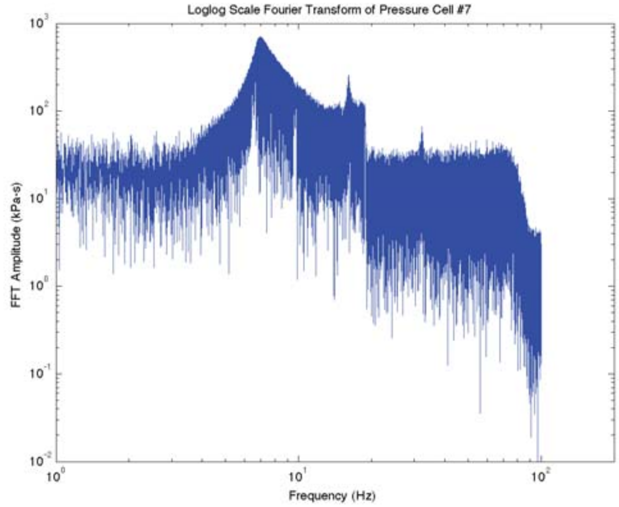

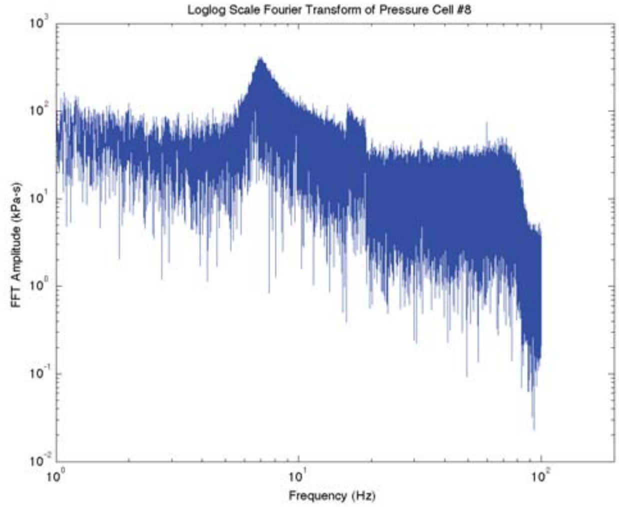

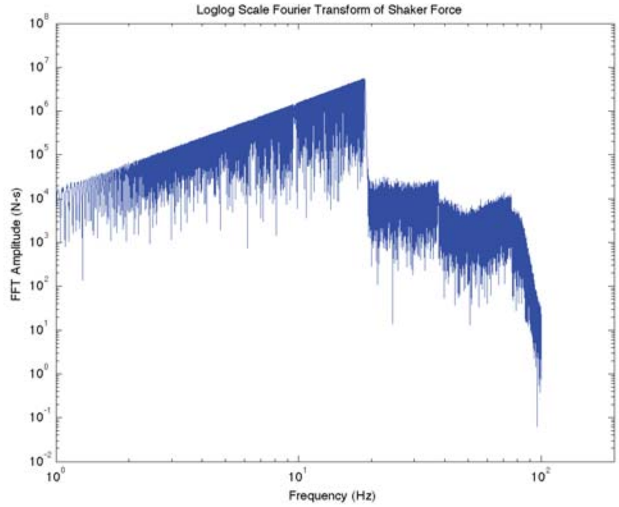

Frequency domain pressure cell graphs from test 2.2.10 (continued)

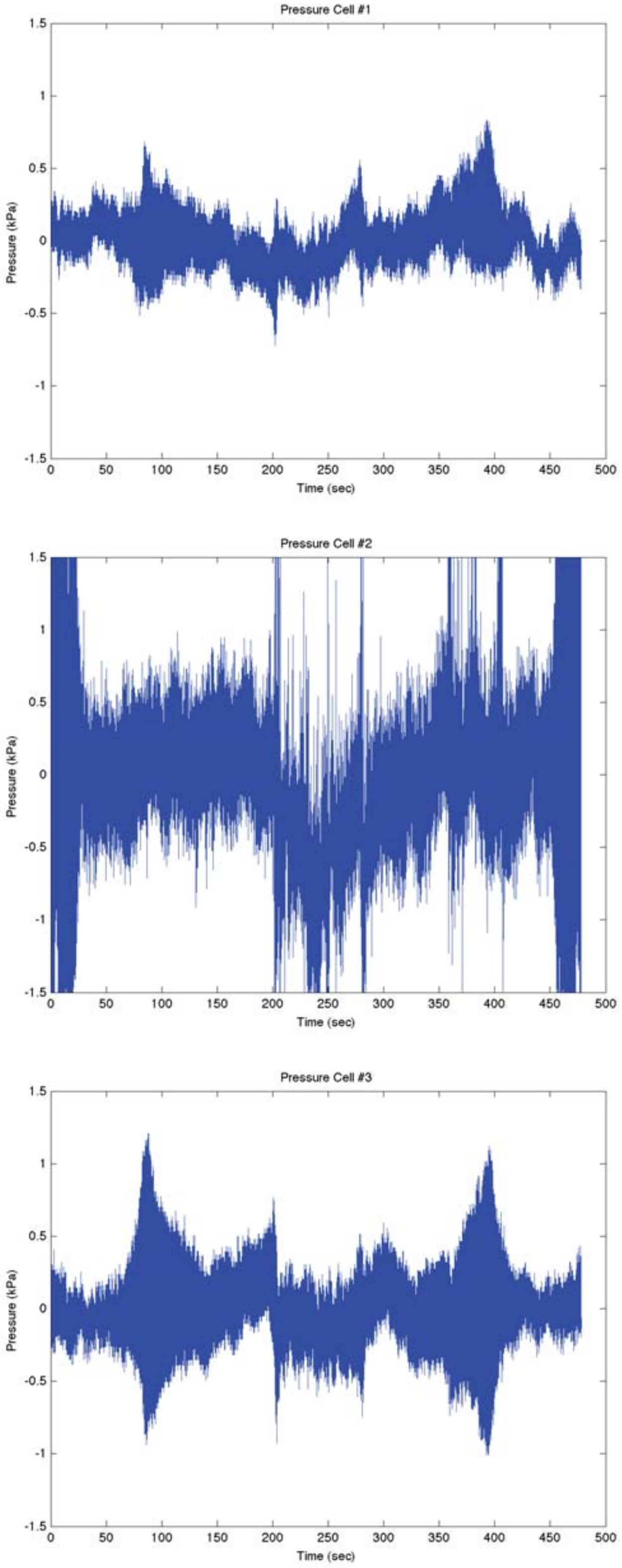

Time domain pressure cell graphs from test 2.2.10

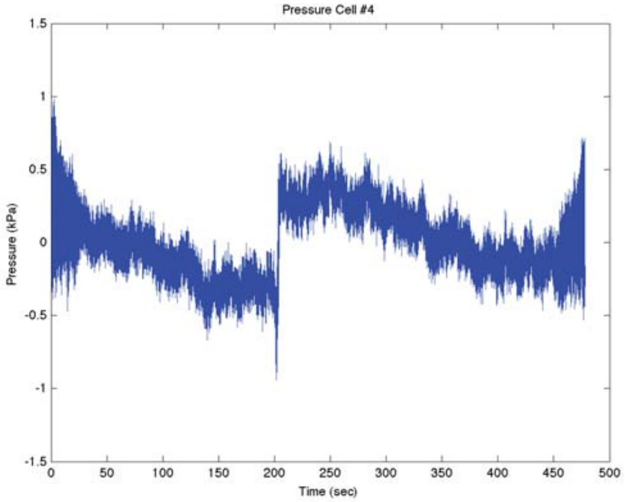

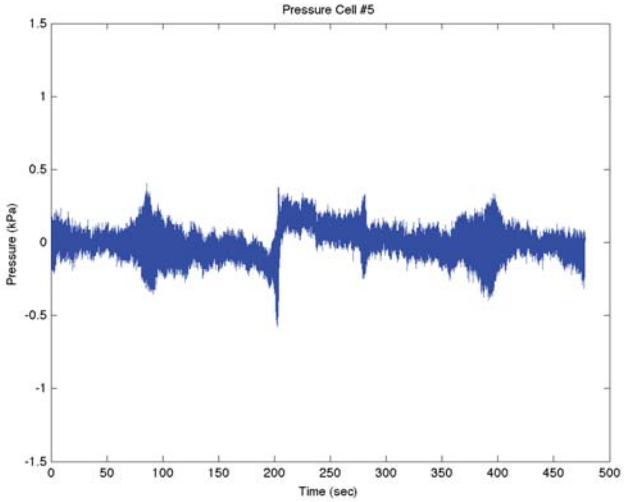

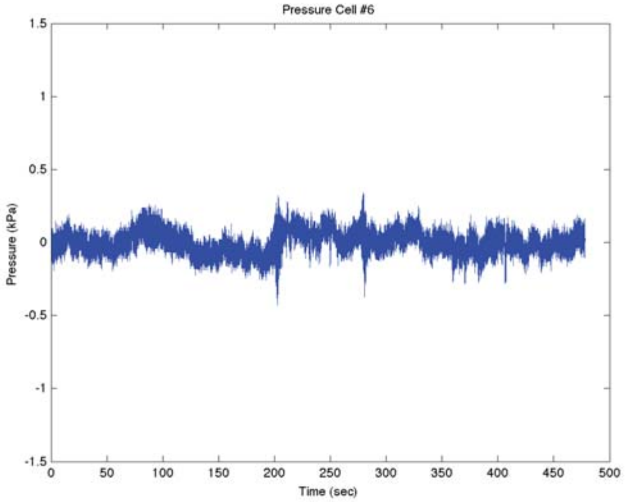

Time domain pressure cell graphs from test 2.2.10 (continued)

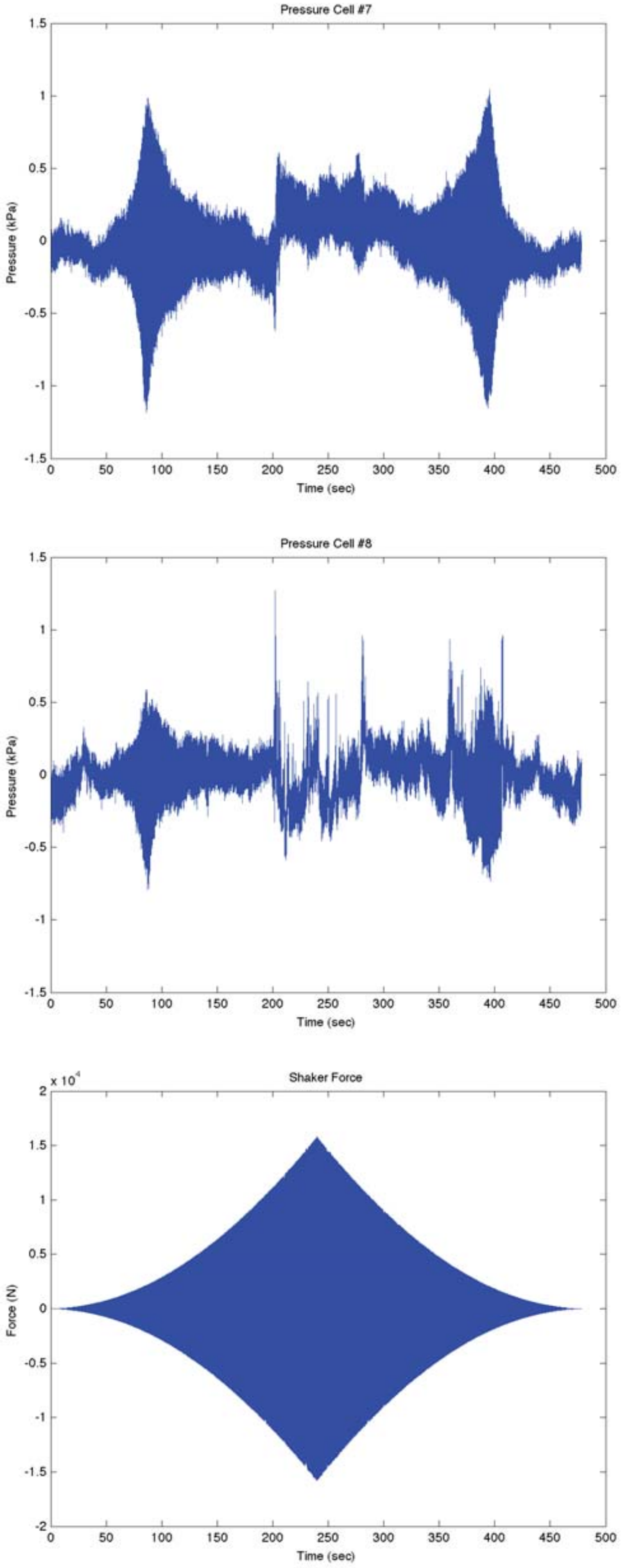

Time domain pressure cell graphs from test 2.2.10 (continued)

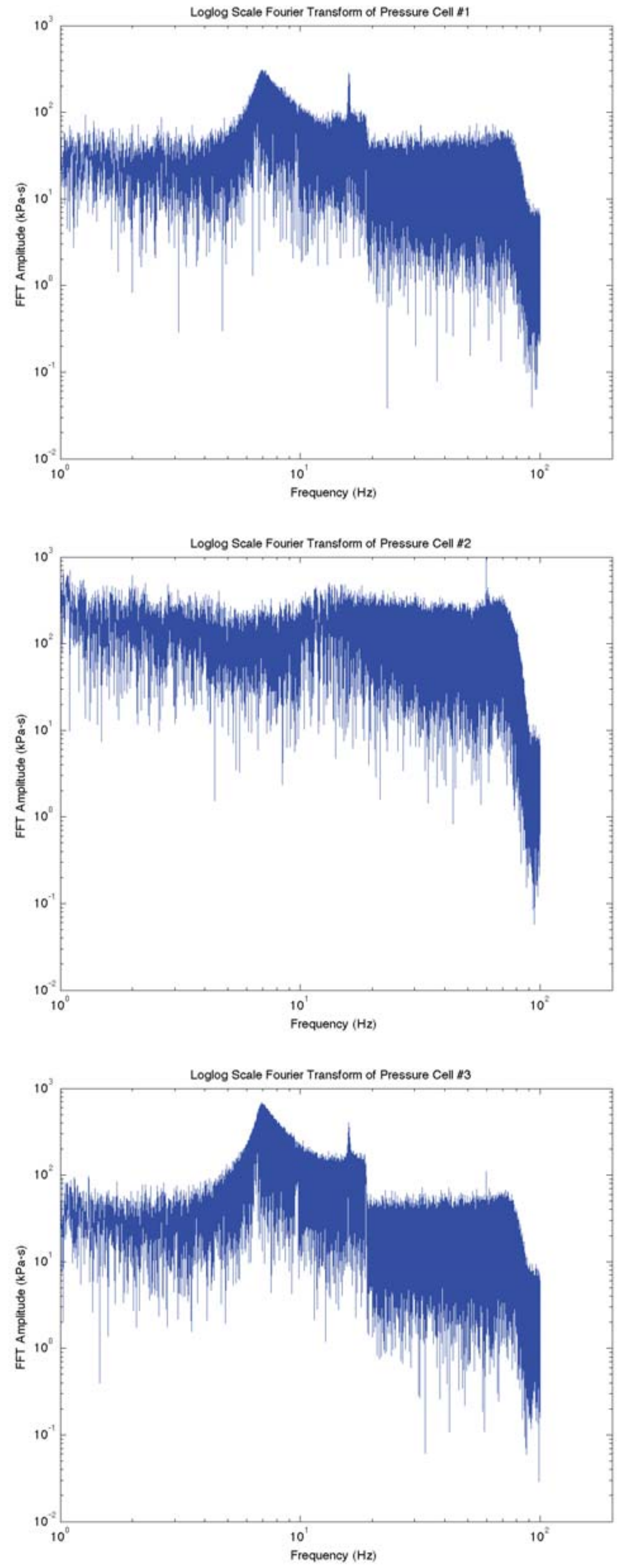

Frequency domain pressure cell graphs from test 2.2.11

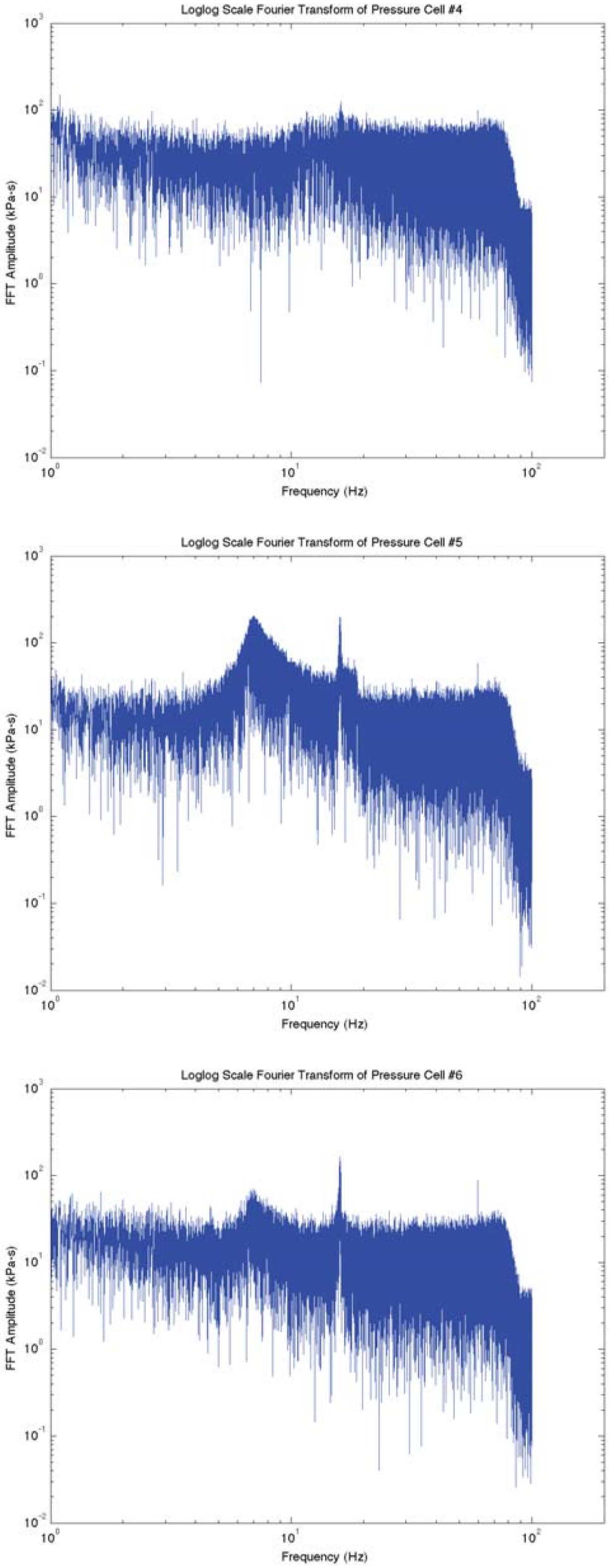

Frequency domain pressure cell graphs from test 2.2.11 (continued)

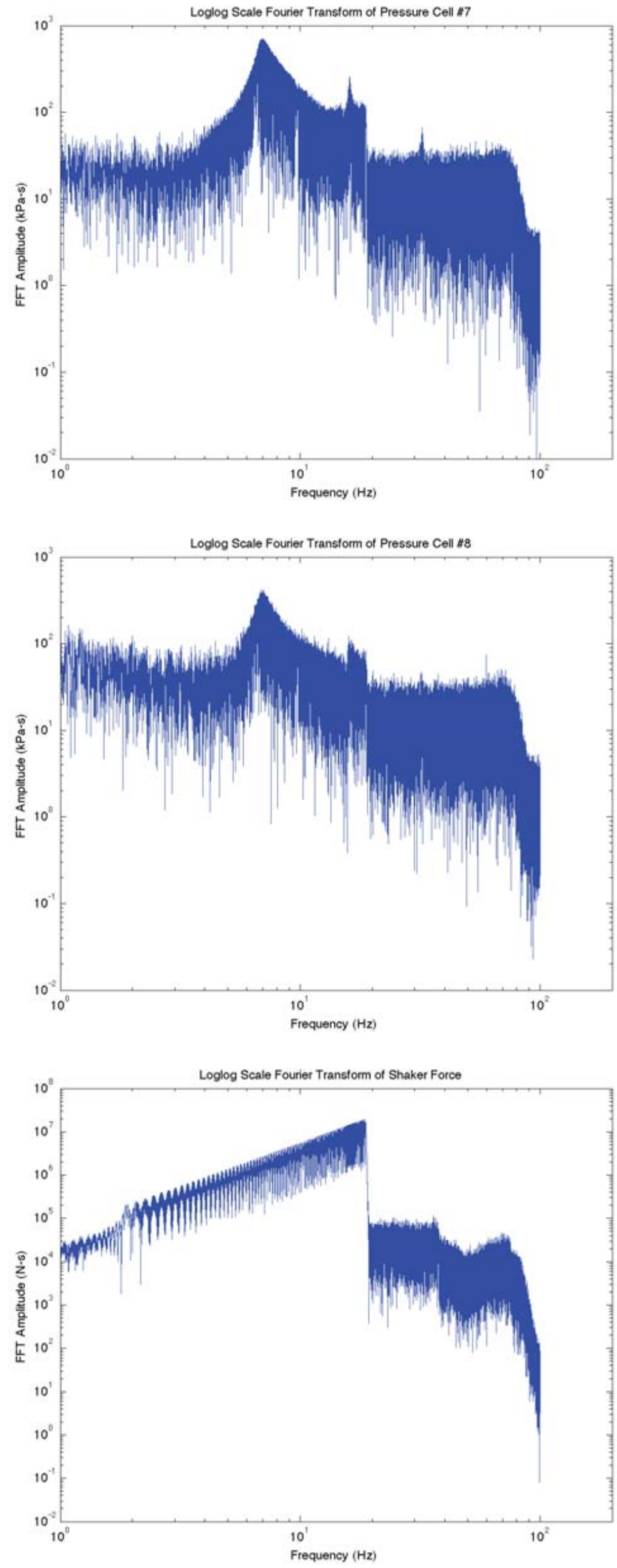

Frequency domain pressure cell graphs from test 2.2.11 (continued)

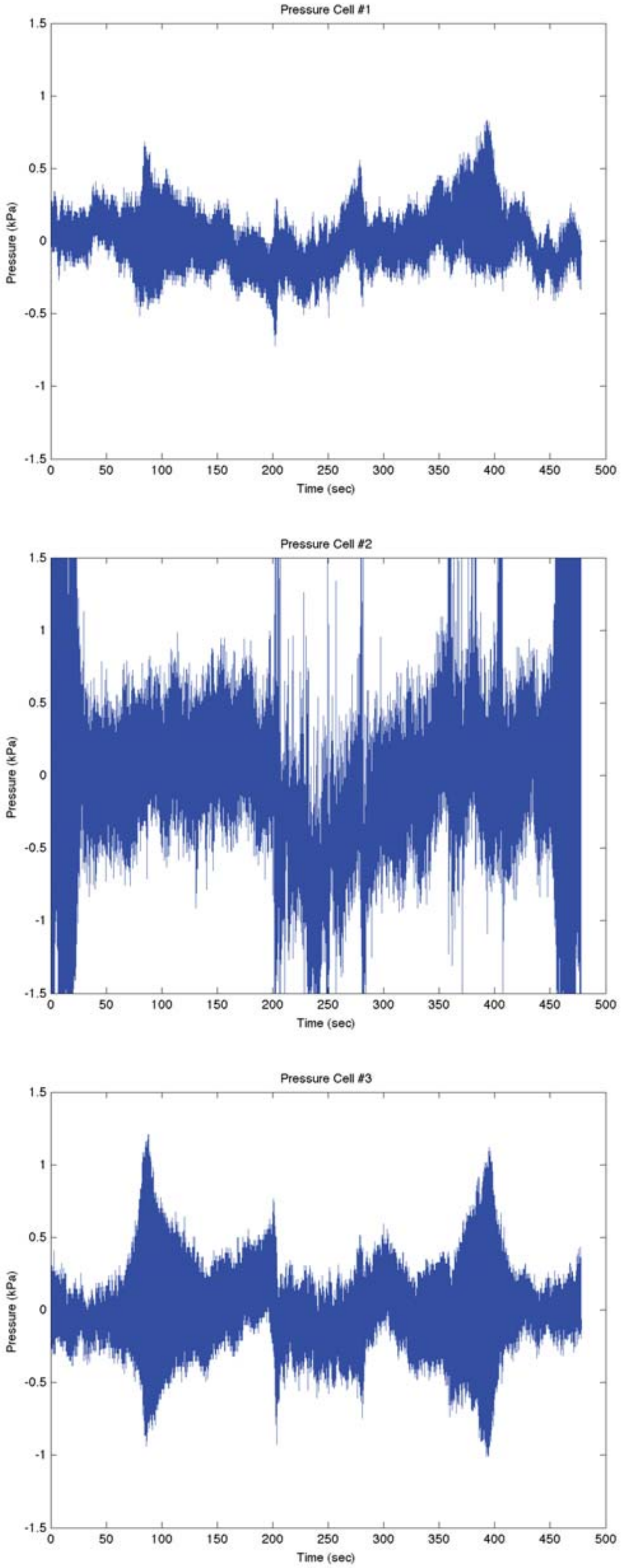

Time domain pressure cell graphs from test 2.2.11

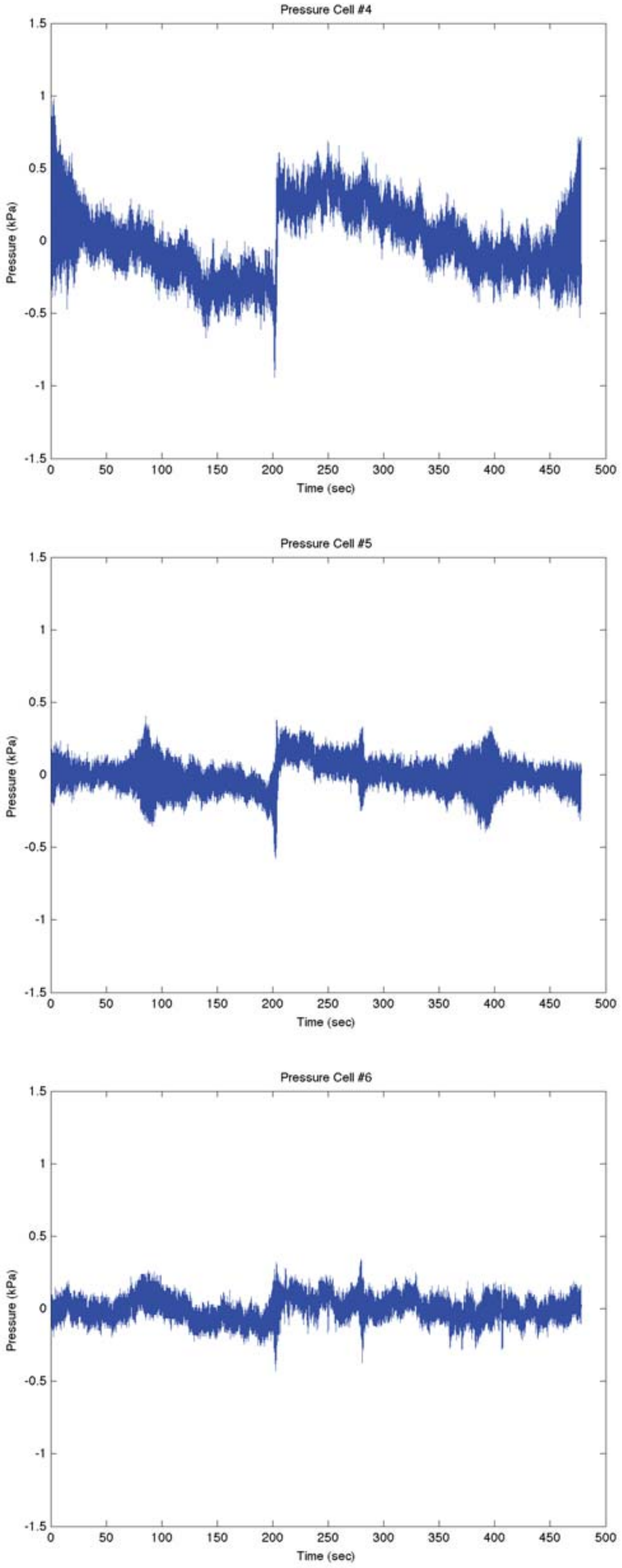

Time domain pressure cell graphs from test 2.2.11 (continued)

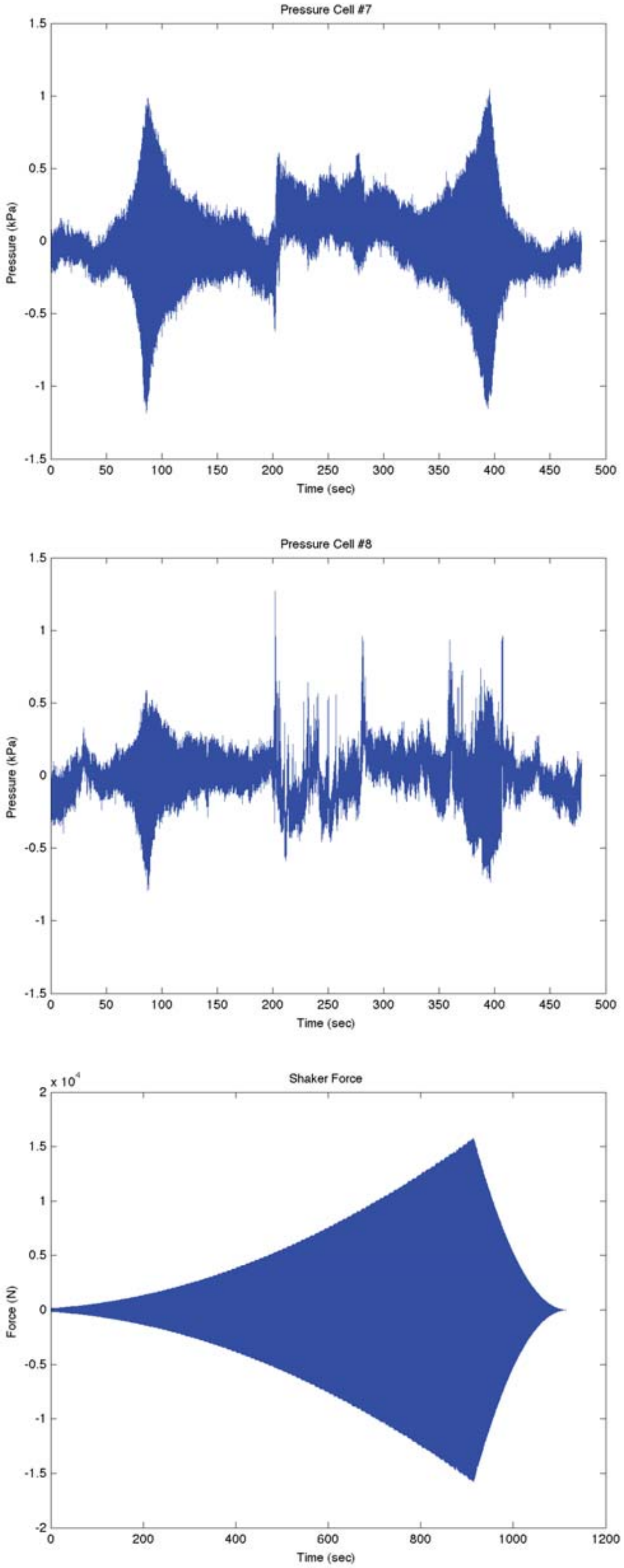

Time domain pressure cell graphs from test 2.2.11 (continued)

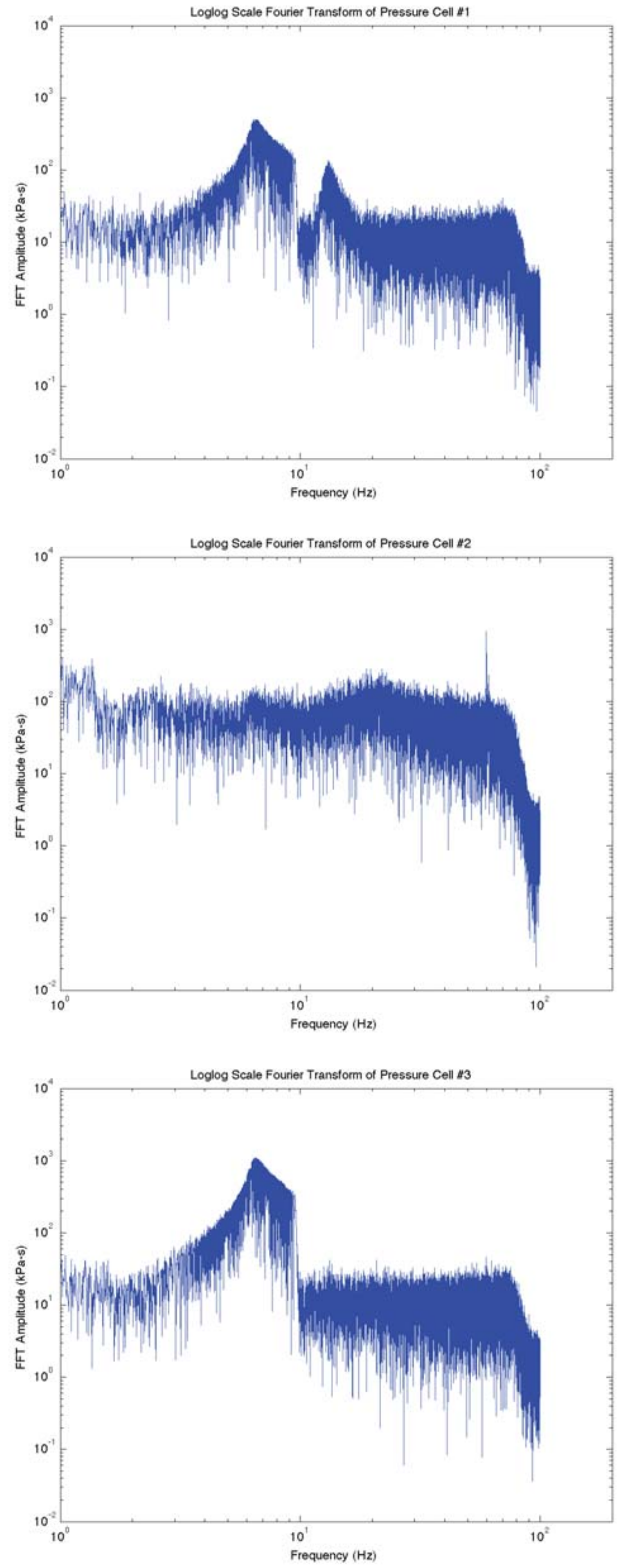

Frequency domain pressure cell graphs from test 2.2.12

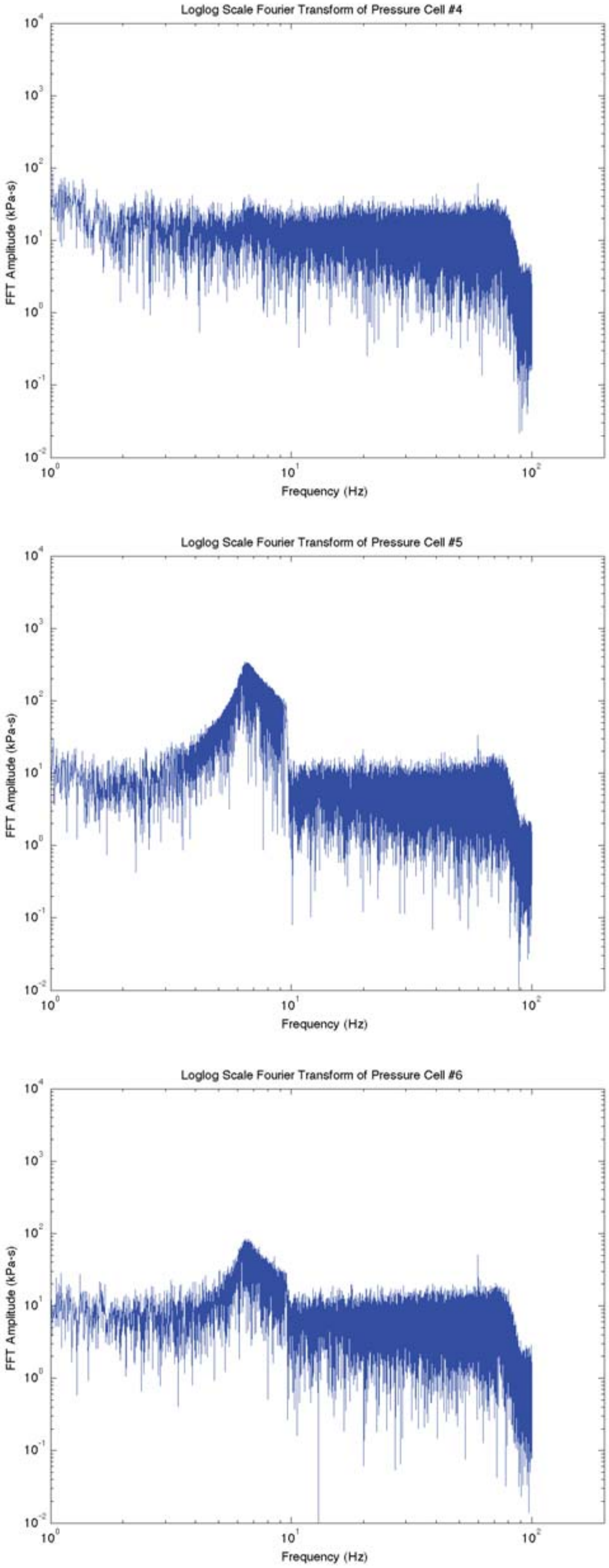

Frequency domain pressure cell graphs from test 2.2.12 (continued)

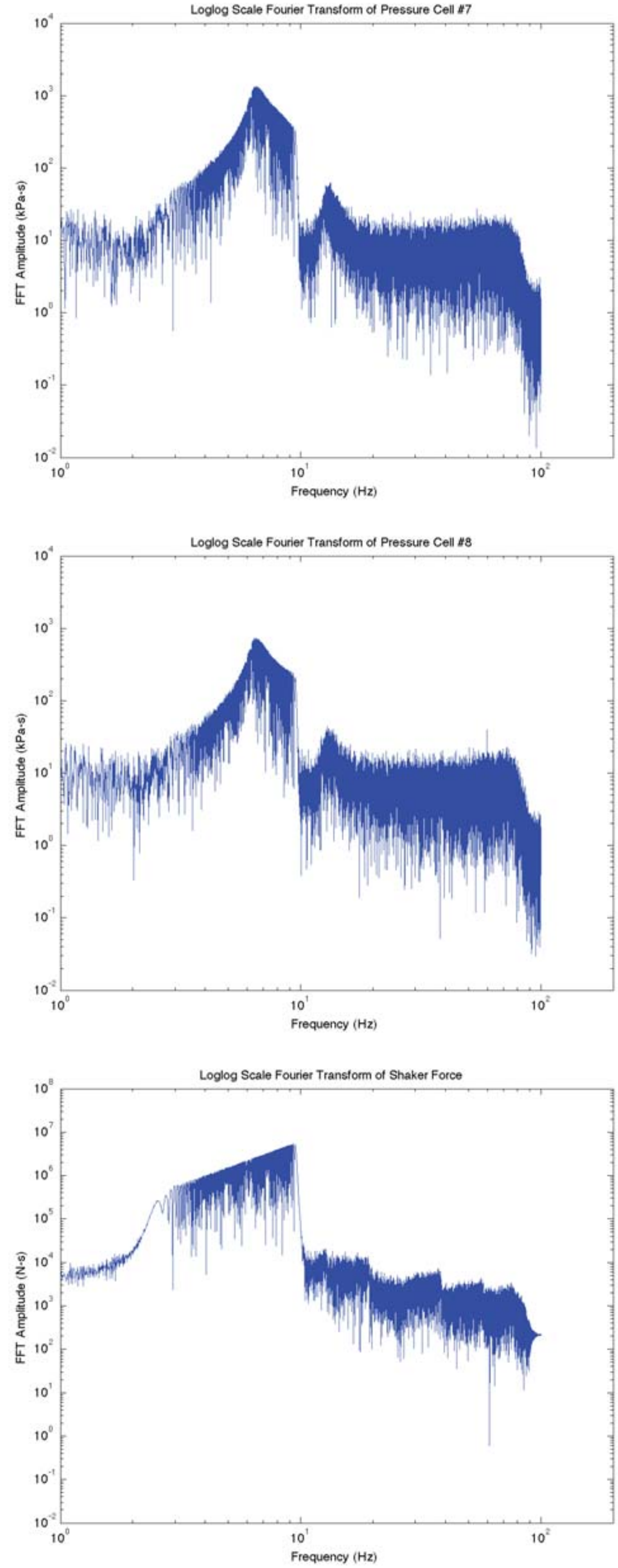

Frequency domain pressure cell graphs from test 2.2.12 (continued)

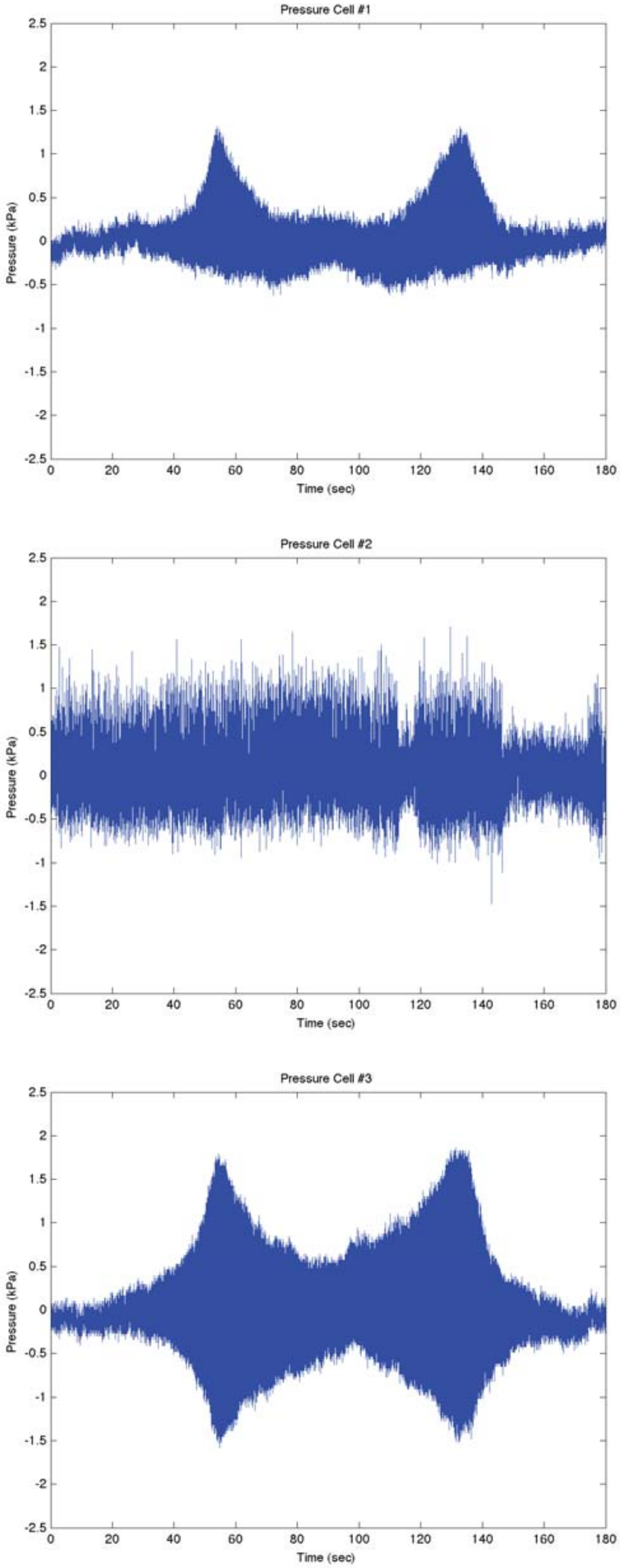

Time domain pressure cell graphs from test 2.2.12

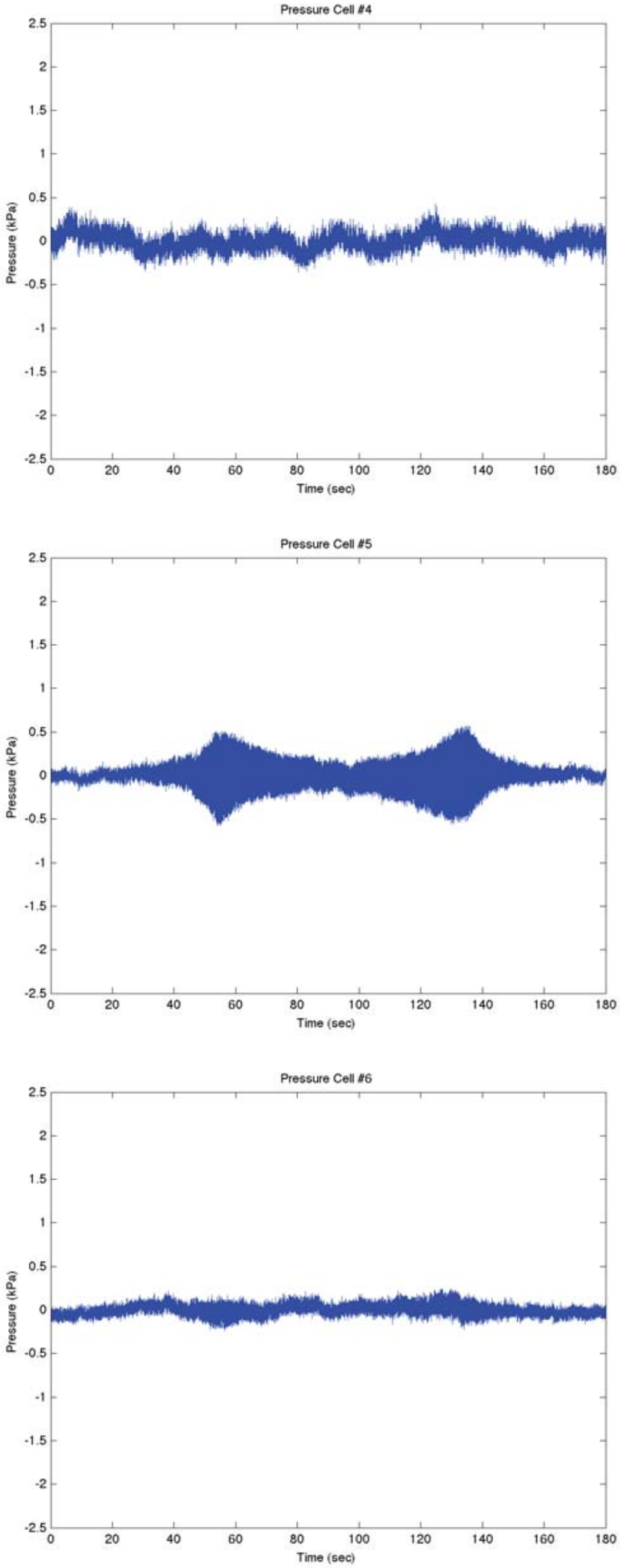

Time domain pressure cell graphs from test 2.2.12 (continued)

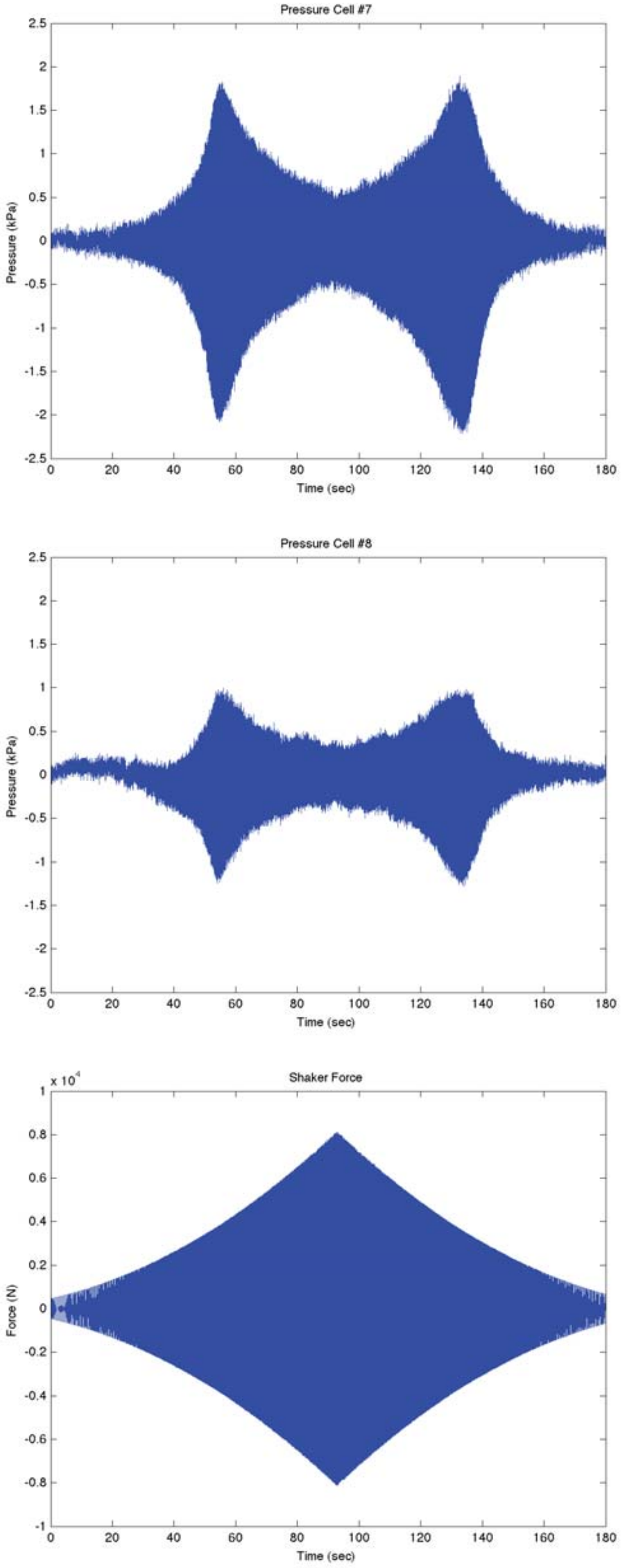

Time domain pressure cell graphs from test 2.2.12 (continued)

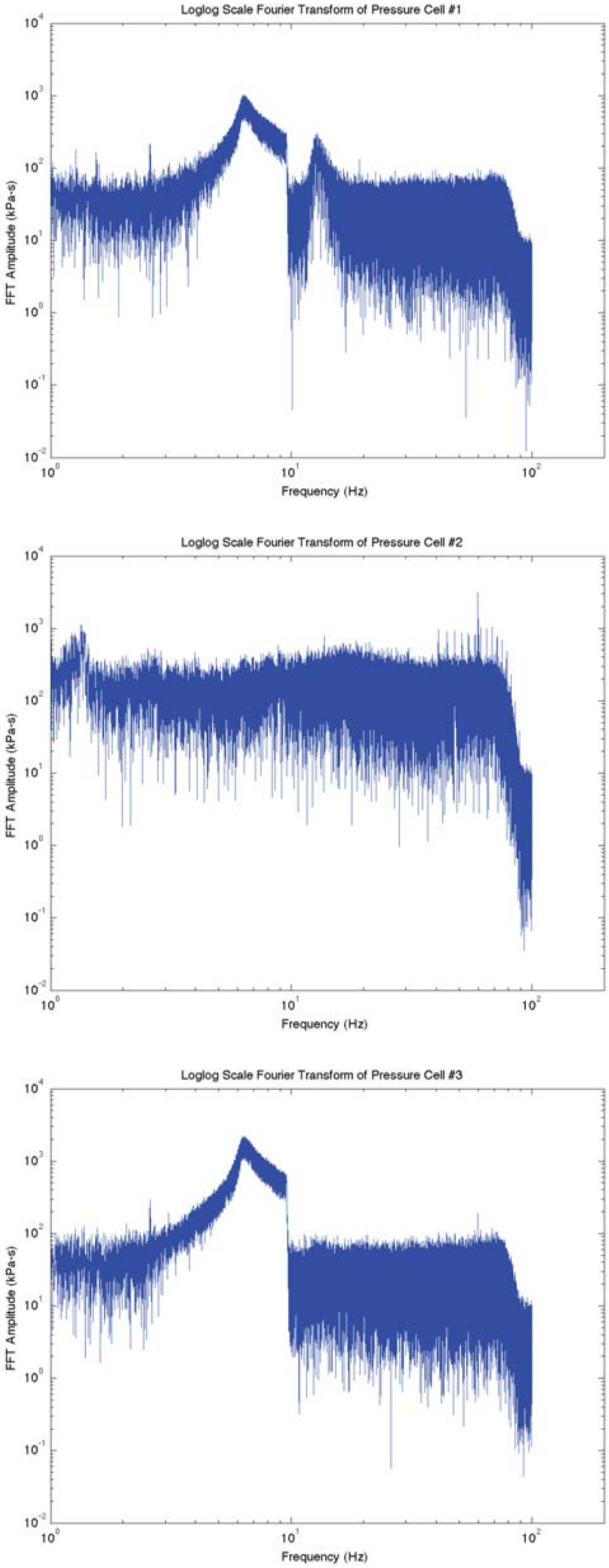

Frequency domain pressure cell graphs from test 2.2.13

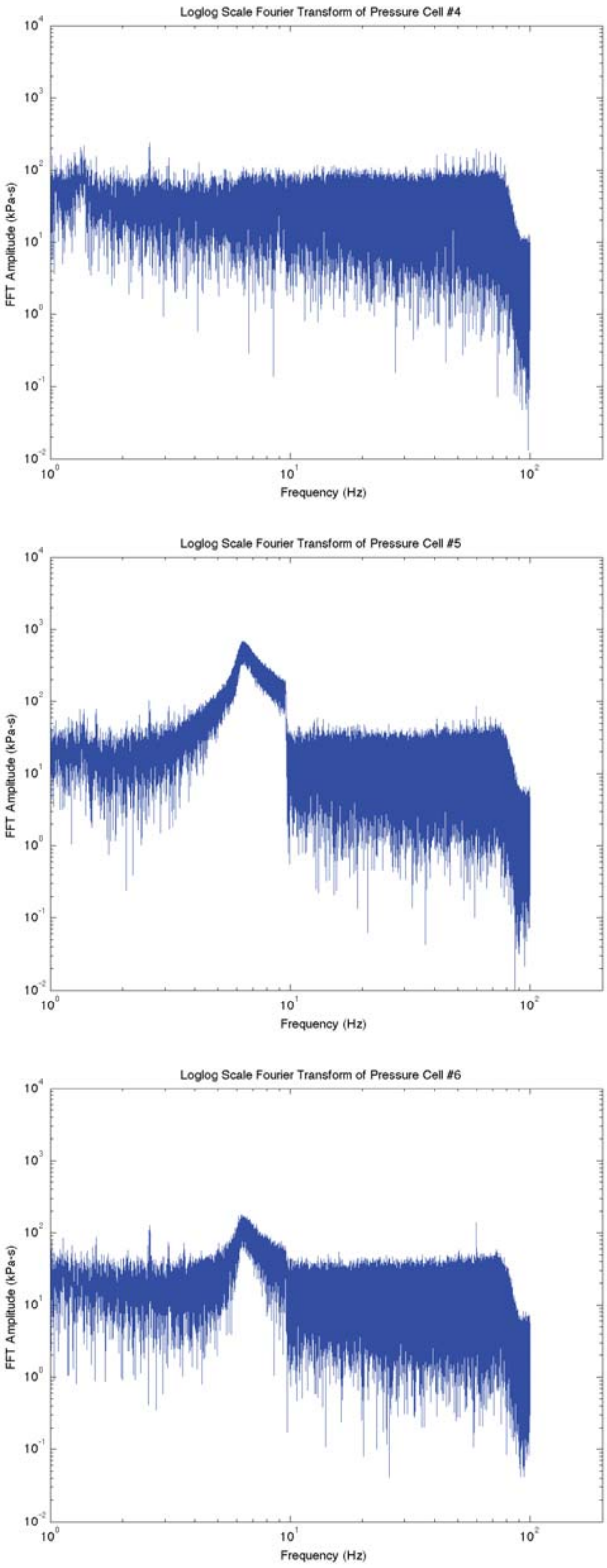

Frequency domain pressure cell graphs from test 2.2.13 (continued)

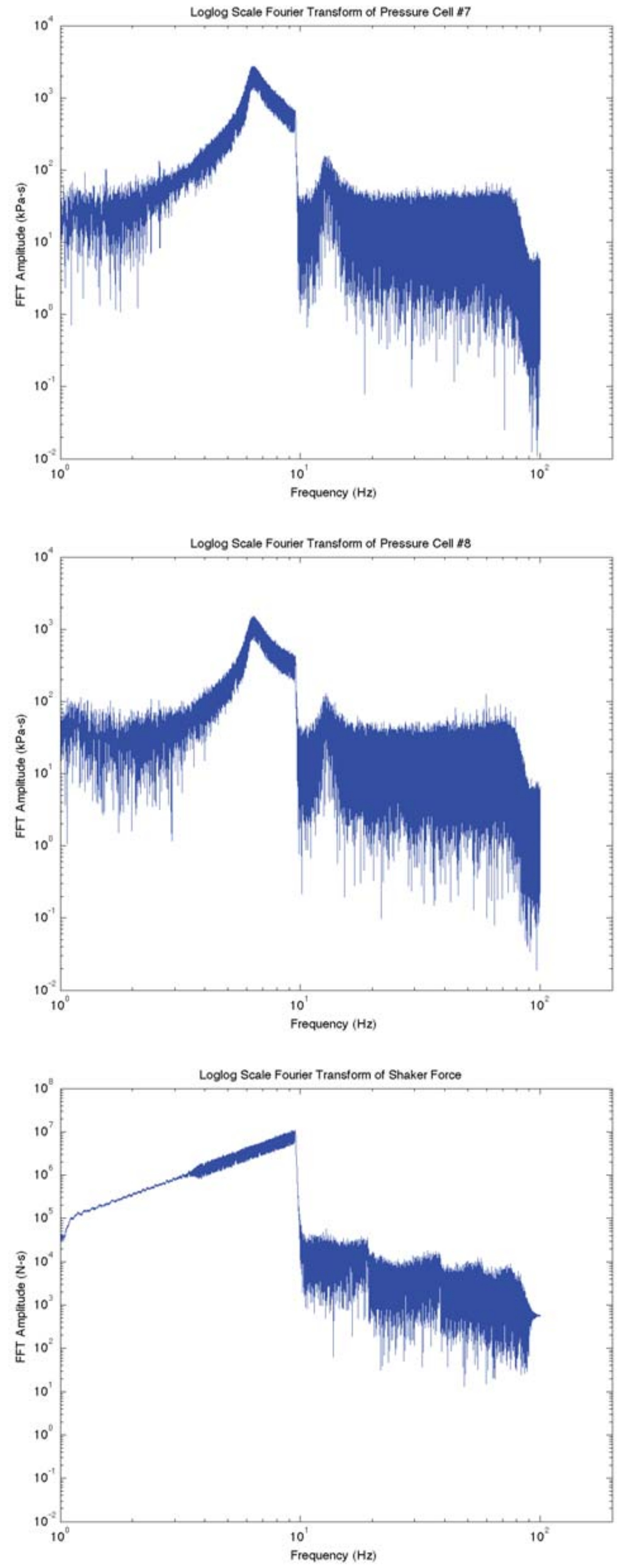

Frequency domain pressure cell graphs from test 2.2.13 (continued)

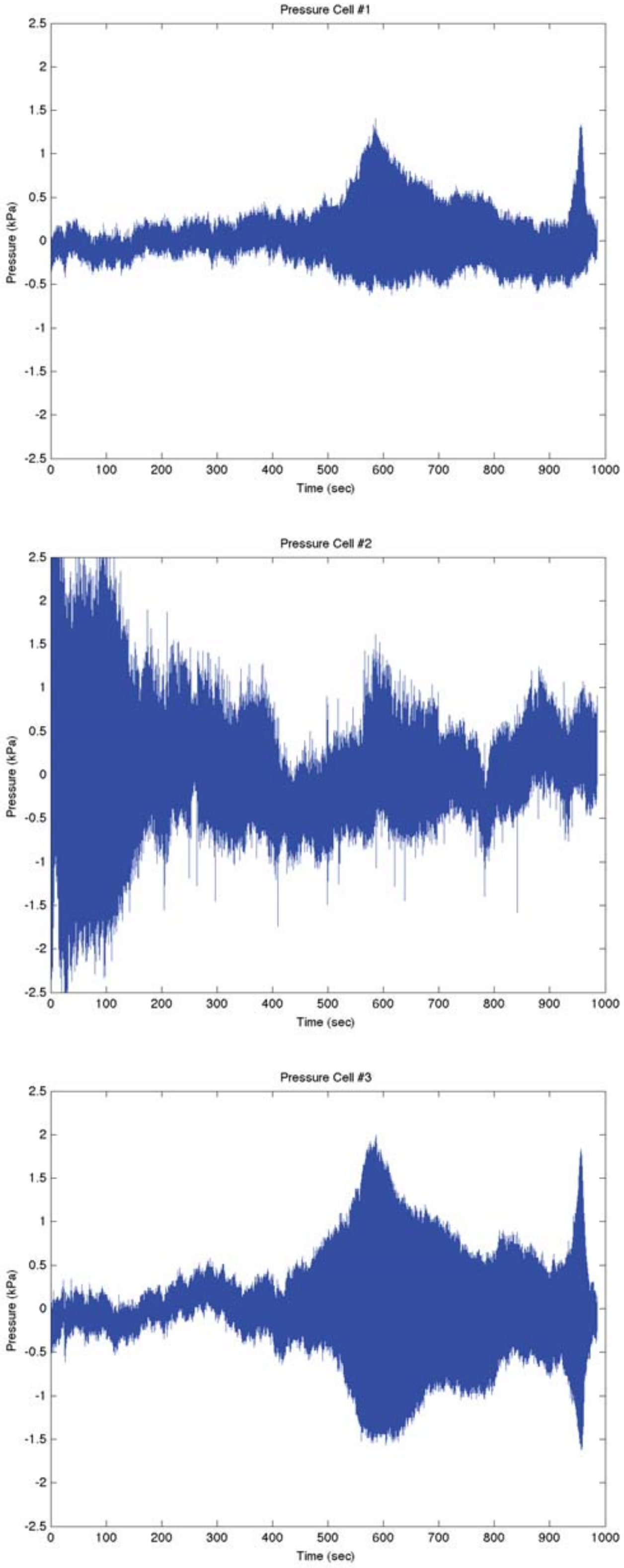

Time domain pressure cell graphs from test 2.2.13

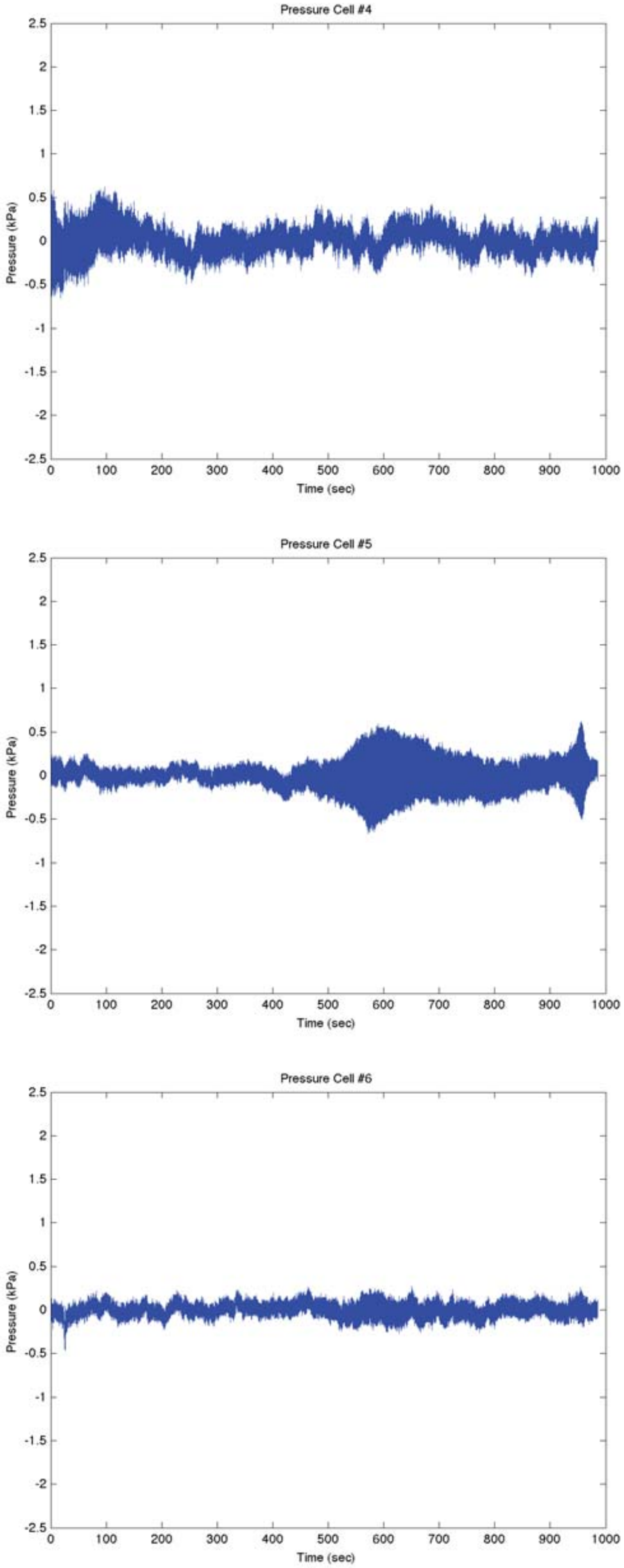

Time domain pressure cell graphs from test 2.2.13 (continued)

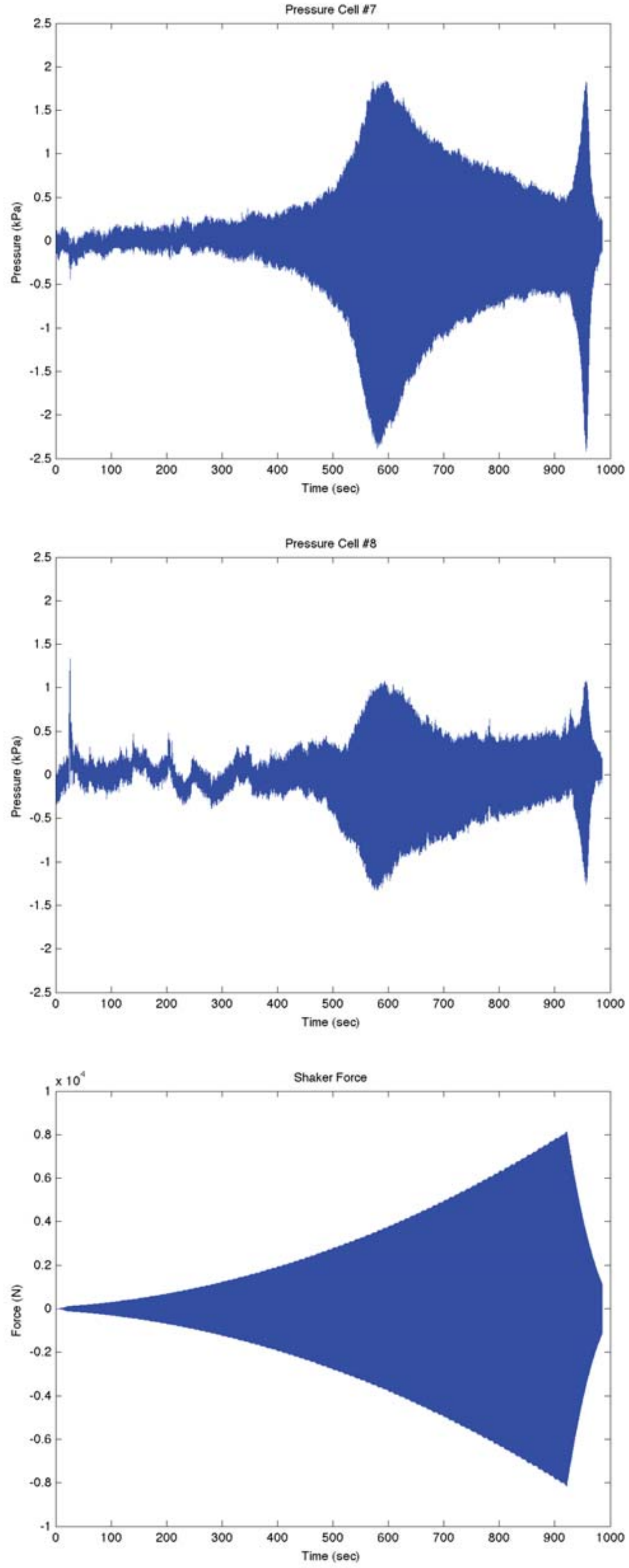

Time domain pressure cell graphs from test 2.2.13 (continued)

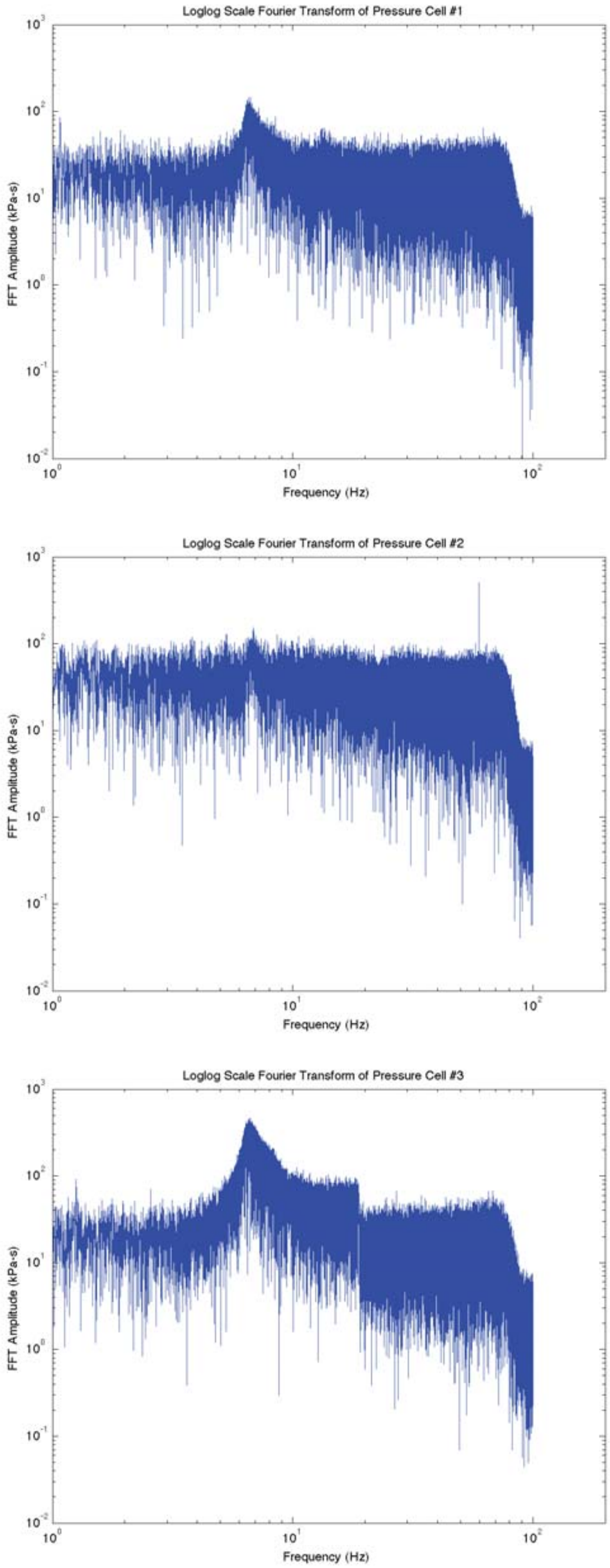

Frequency domain pressure cell graphs from test 2.2.14

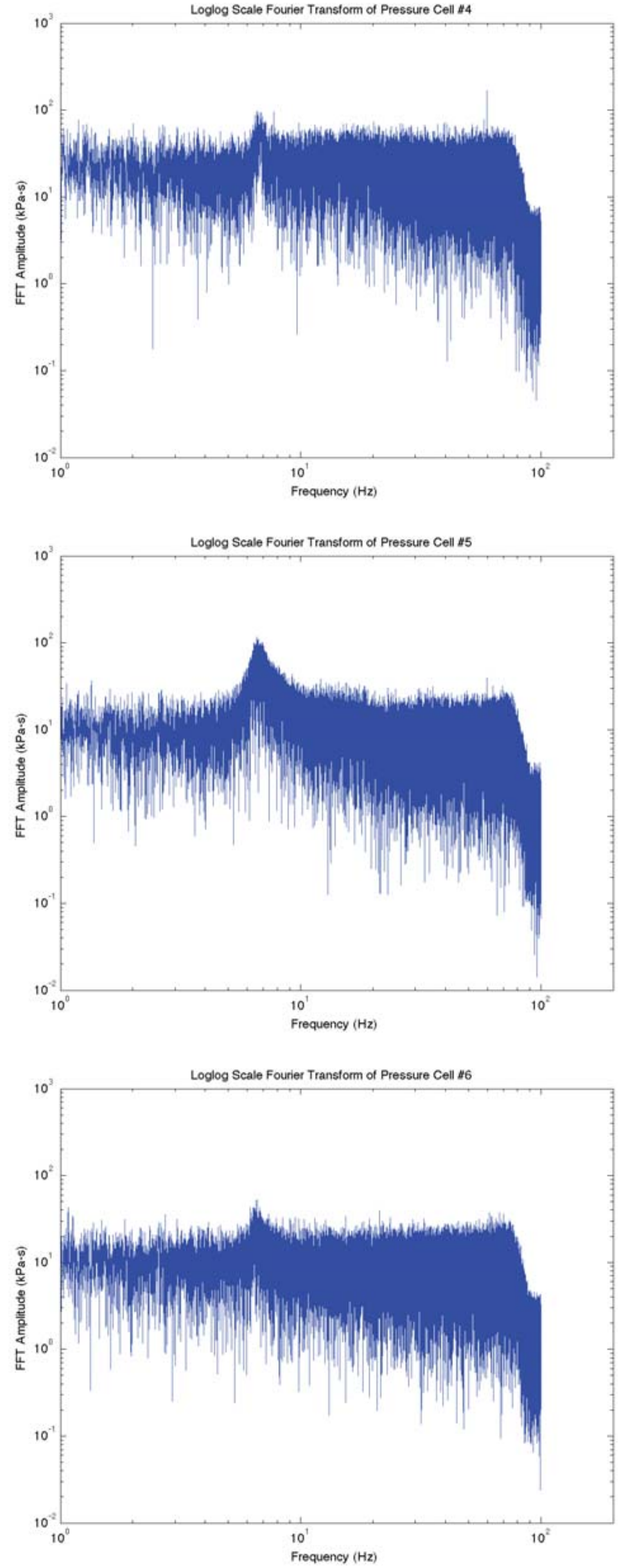

Frequency domain pressure cell graphs from test 2.2.14 (continued)

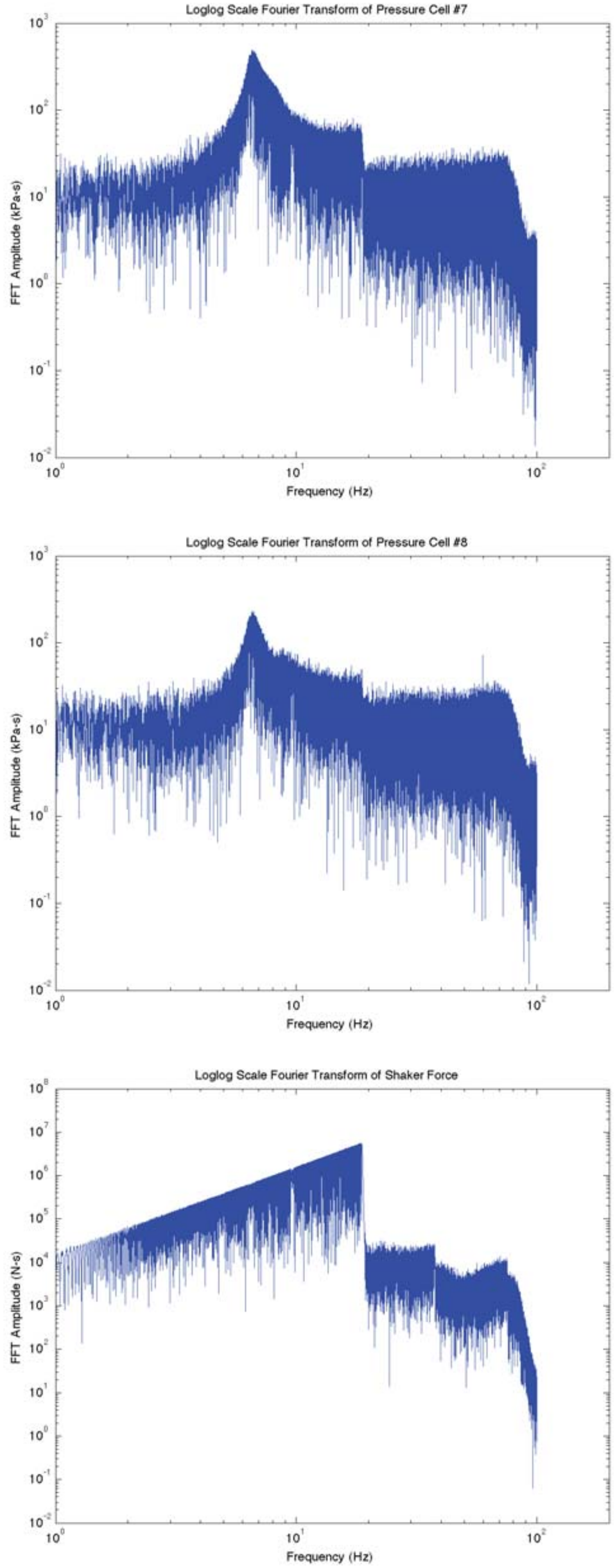

Frequency domain pressure cell graphs from test 2.2.14 (continued)

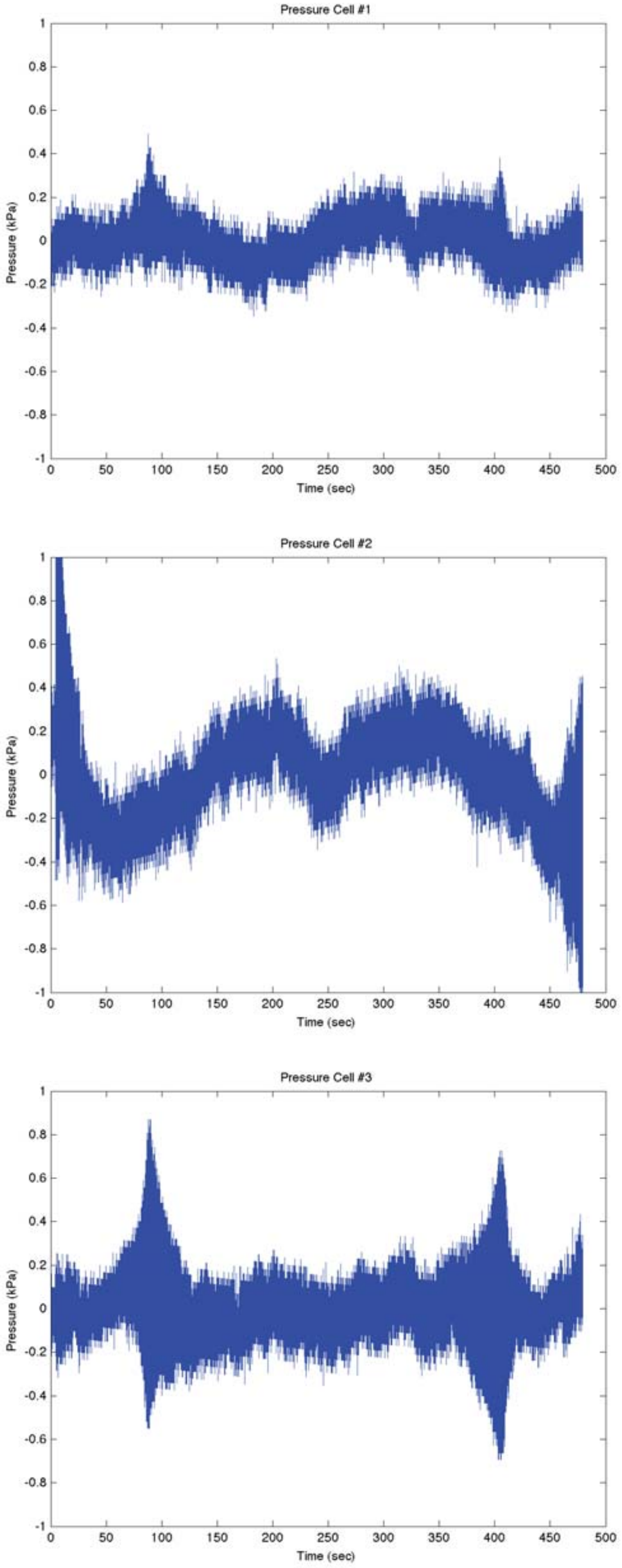

Time domain pressure cell graphs from test 2.2.14

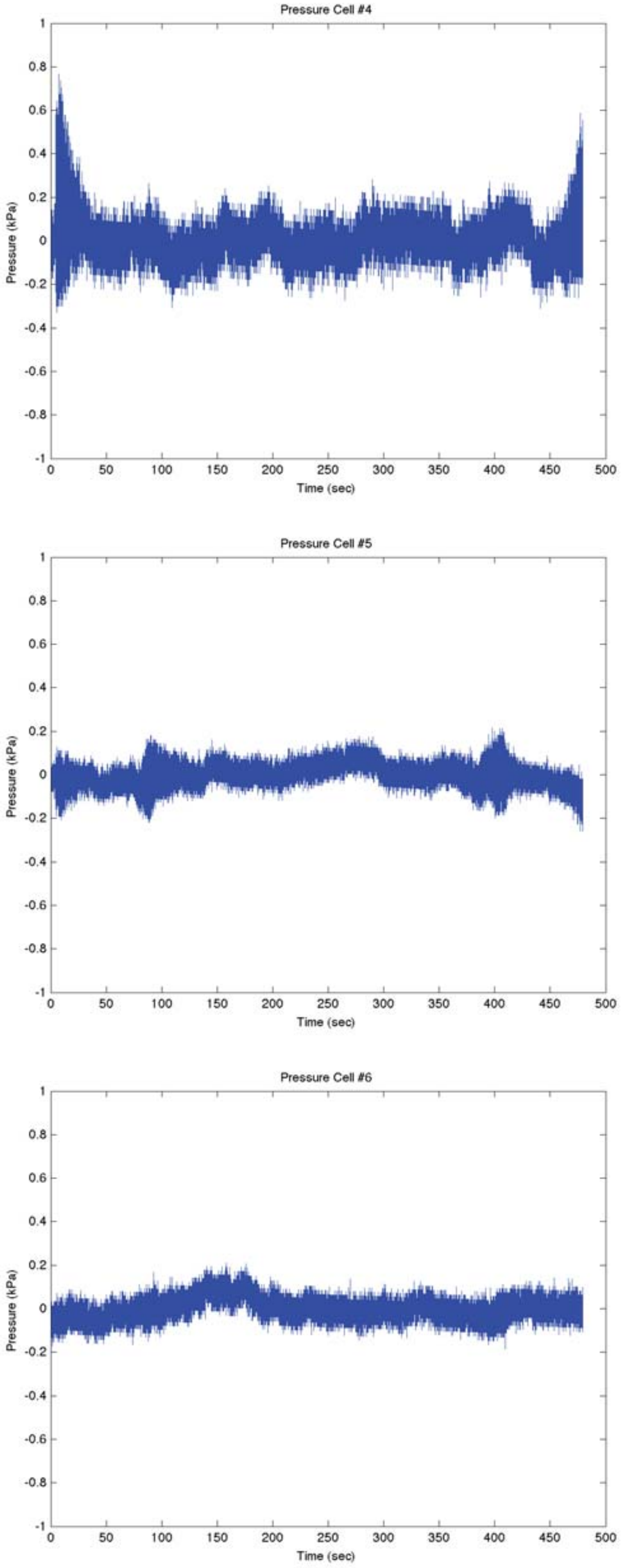

Time domain pressure cell graphs from test 2.2.14 (continued)

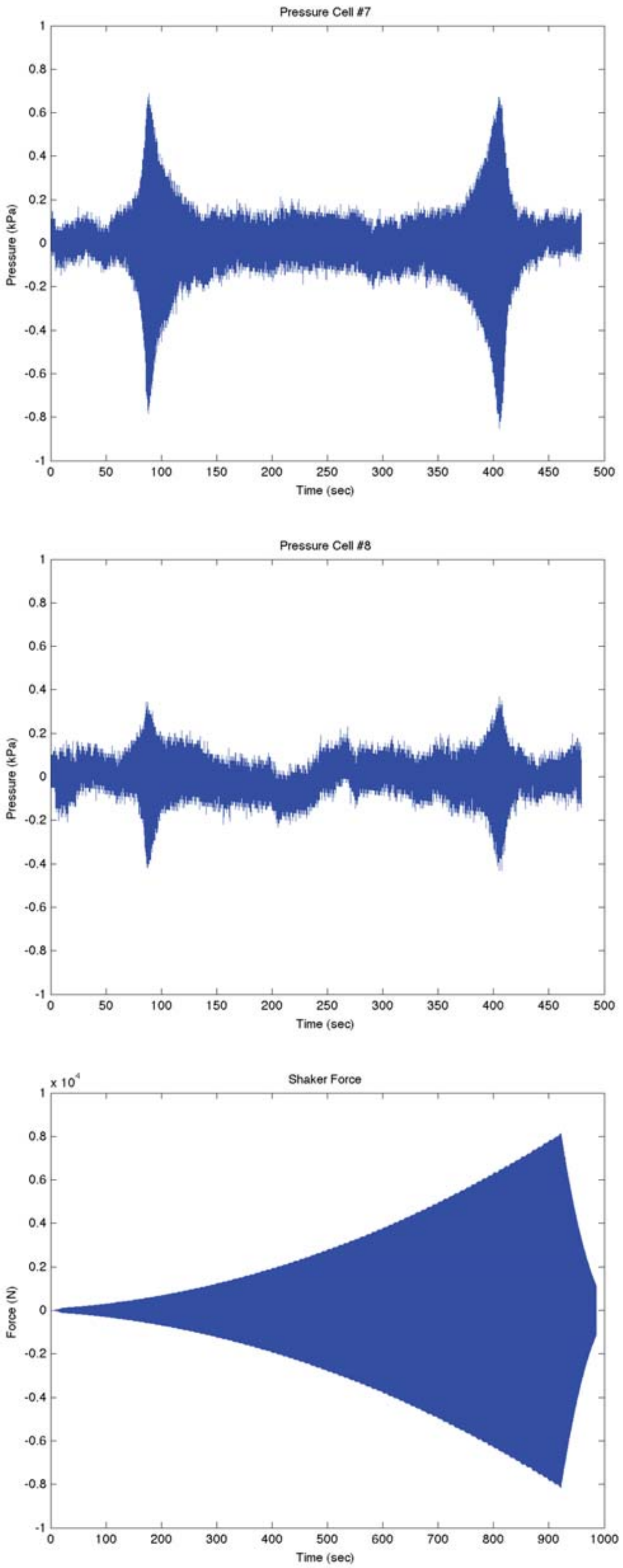

Time domain pressure cell graphs from test 2.2.14 (continued)

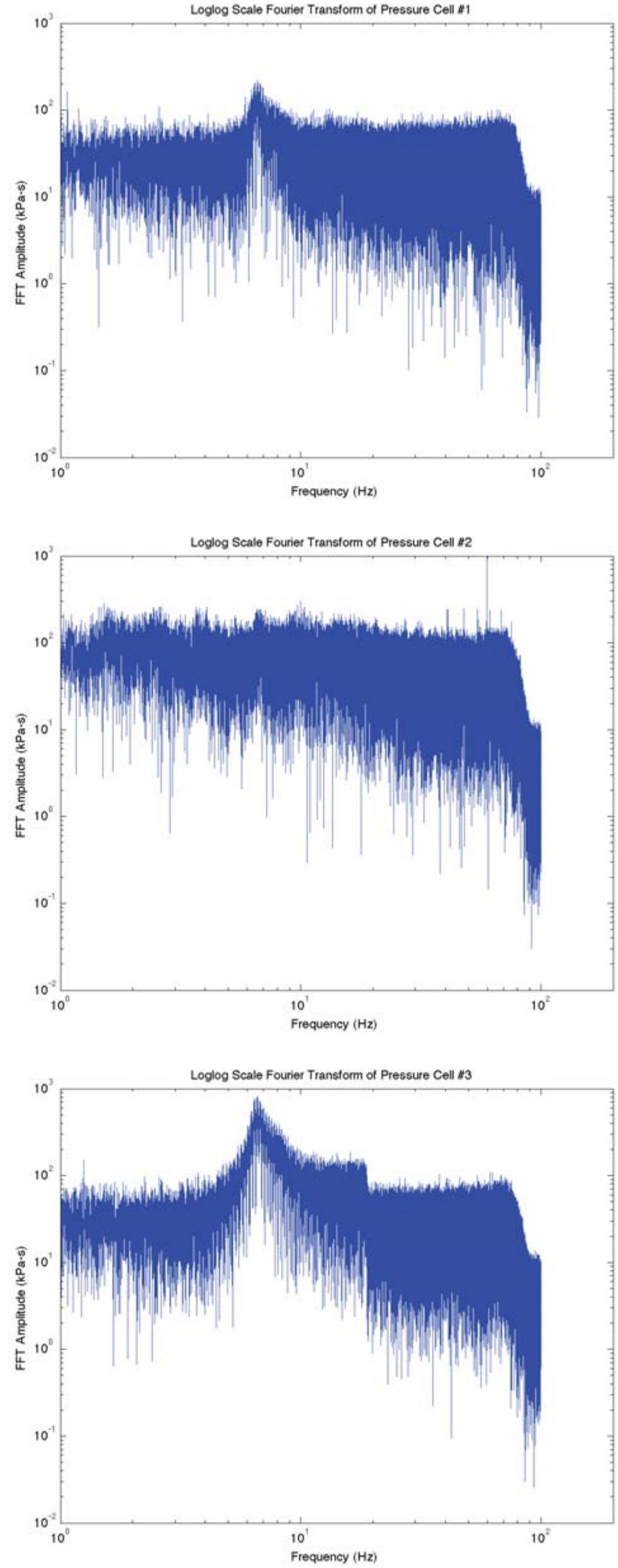

Frequency domain pressure cell graphs from test 2.2.15

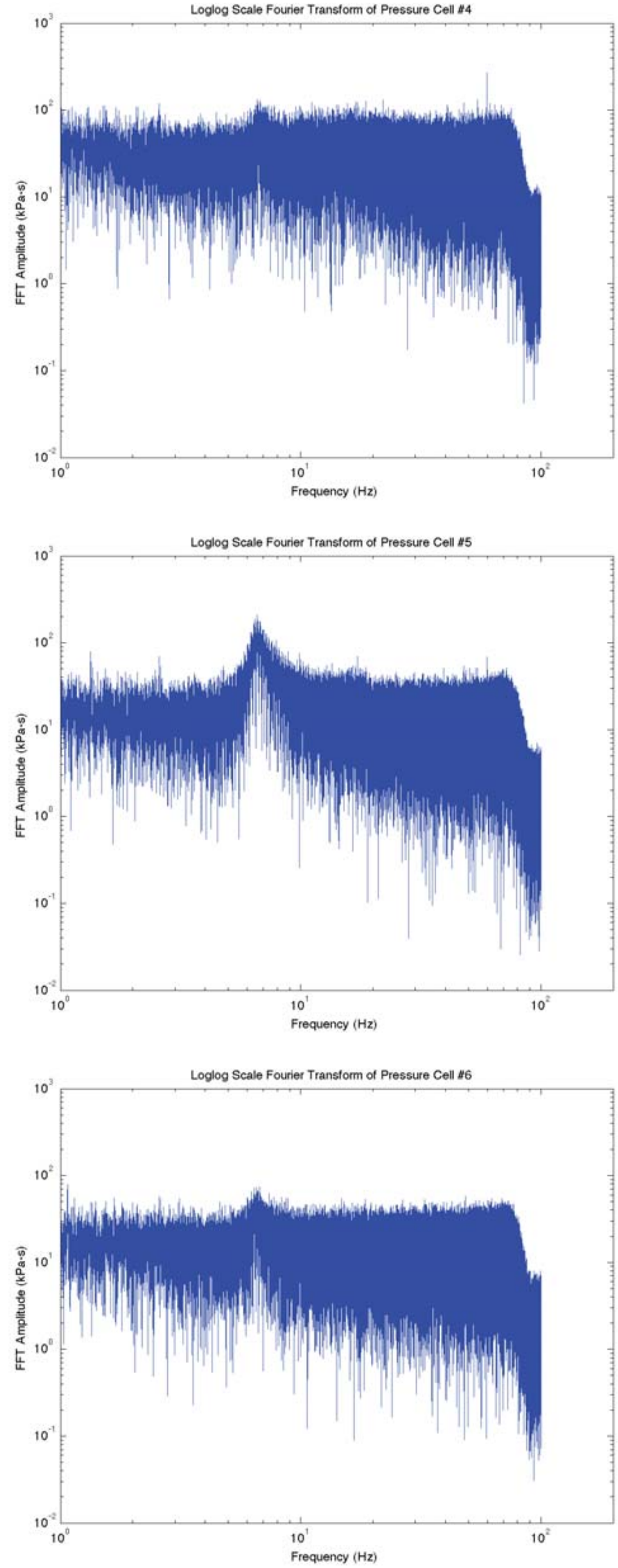

Frequency domain pressure cell graphs from test 2.2.15 (continued)

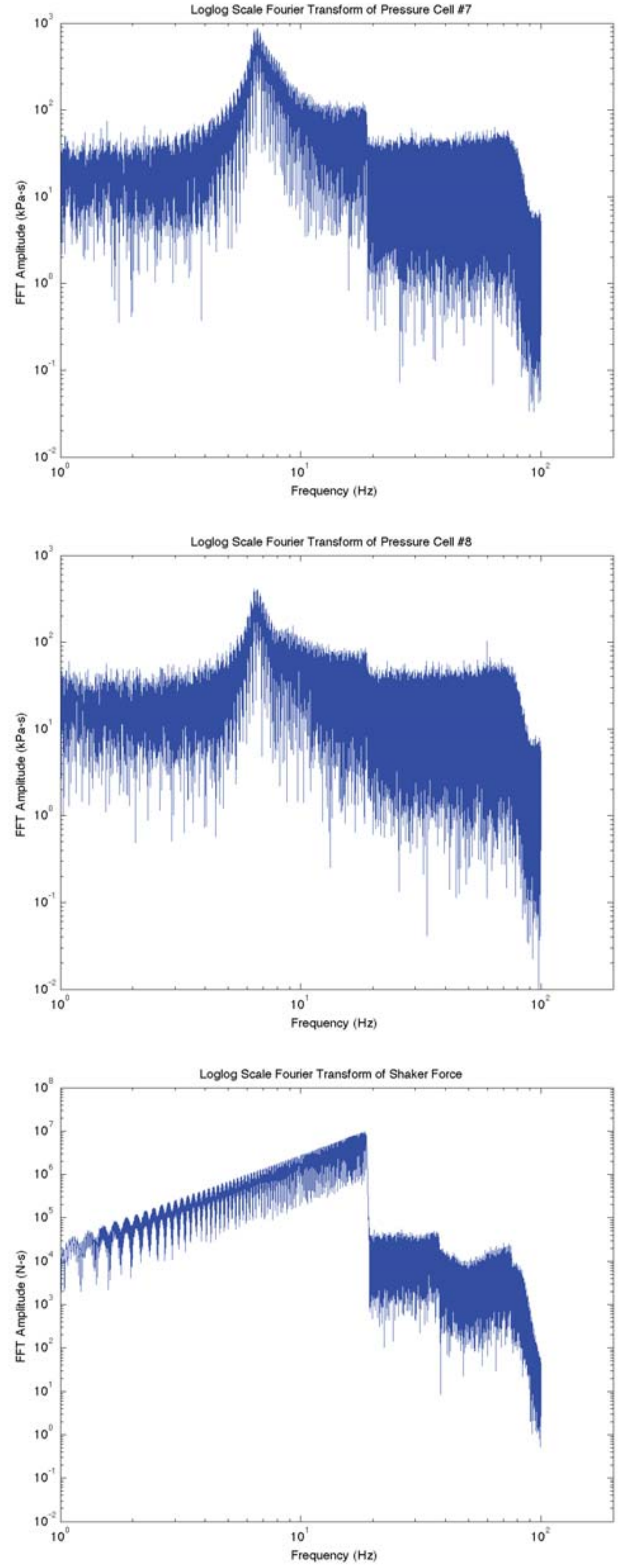

Frequency domain pressure cell graphs from test 2.2.15 (continued)

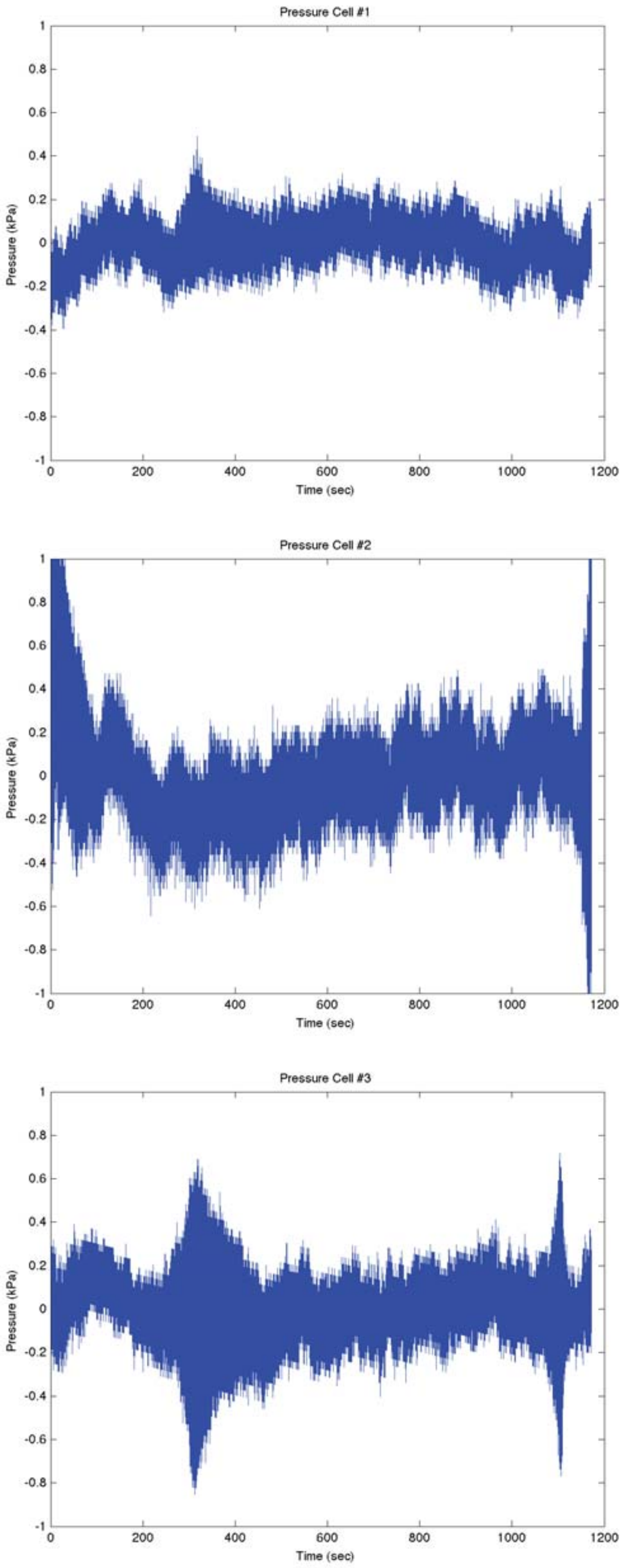

Time domain pressure cell graphs from test 2.2.15

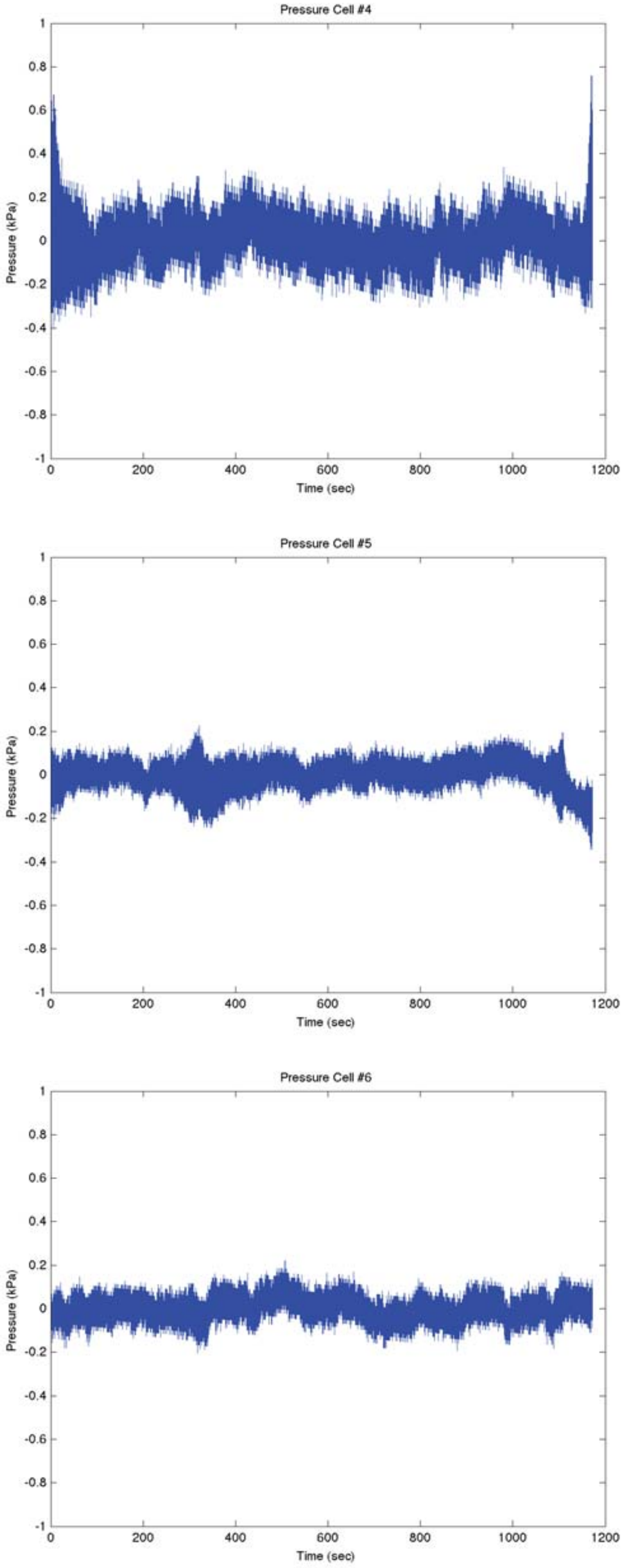

Time domain pressure cell graphs from test 2.2.15 (continued)

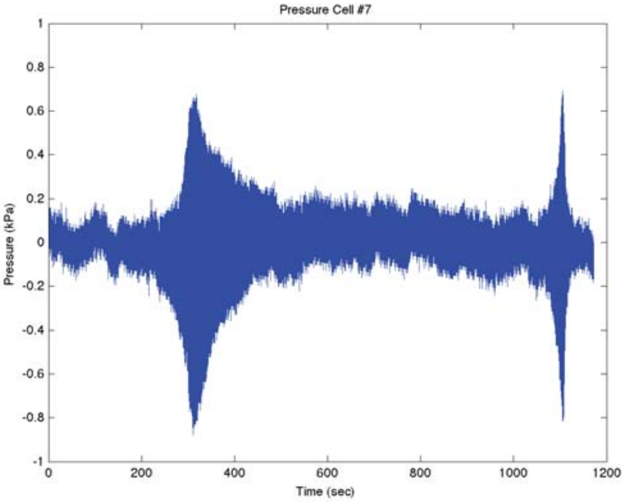

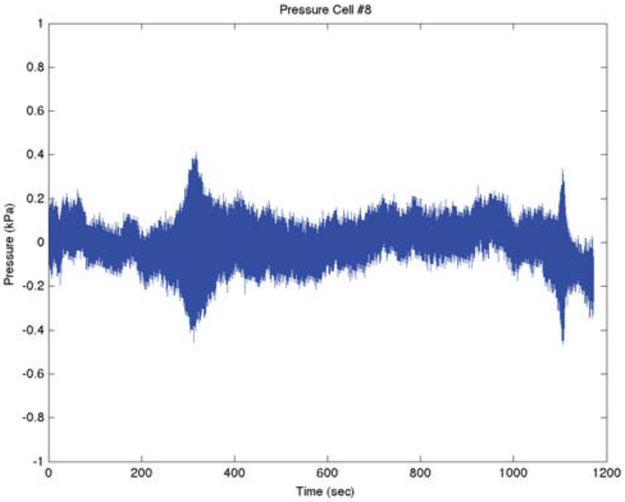

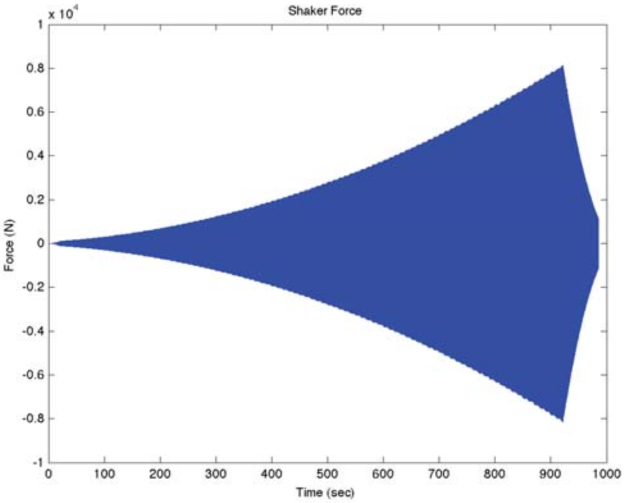

Time domain pressure cell graphs from test 2.2.15 (continued)

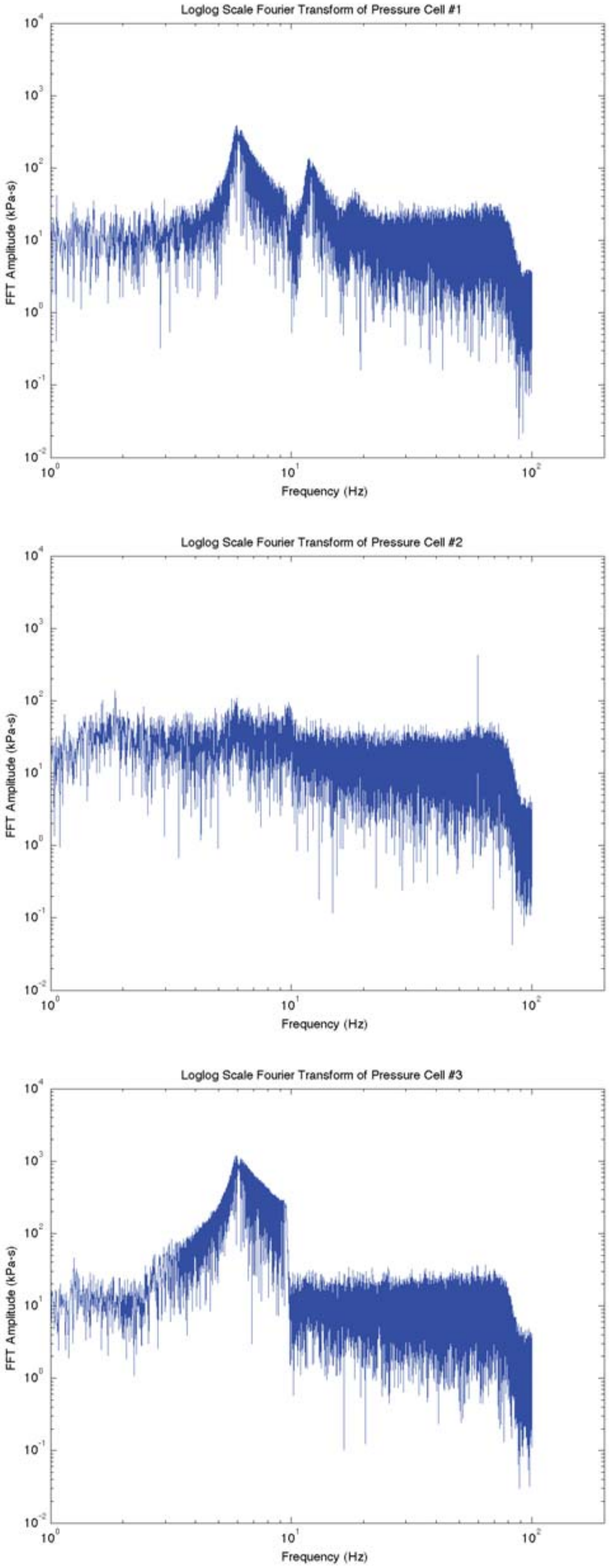

Frequency domain pressure cell graphs from test 2.2.16

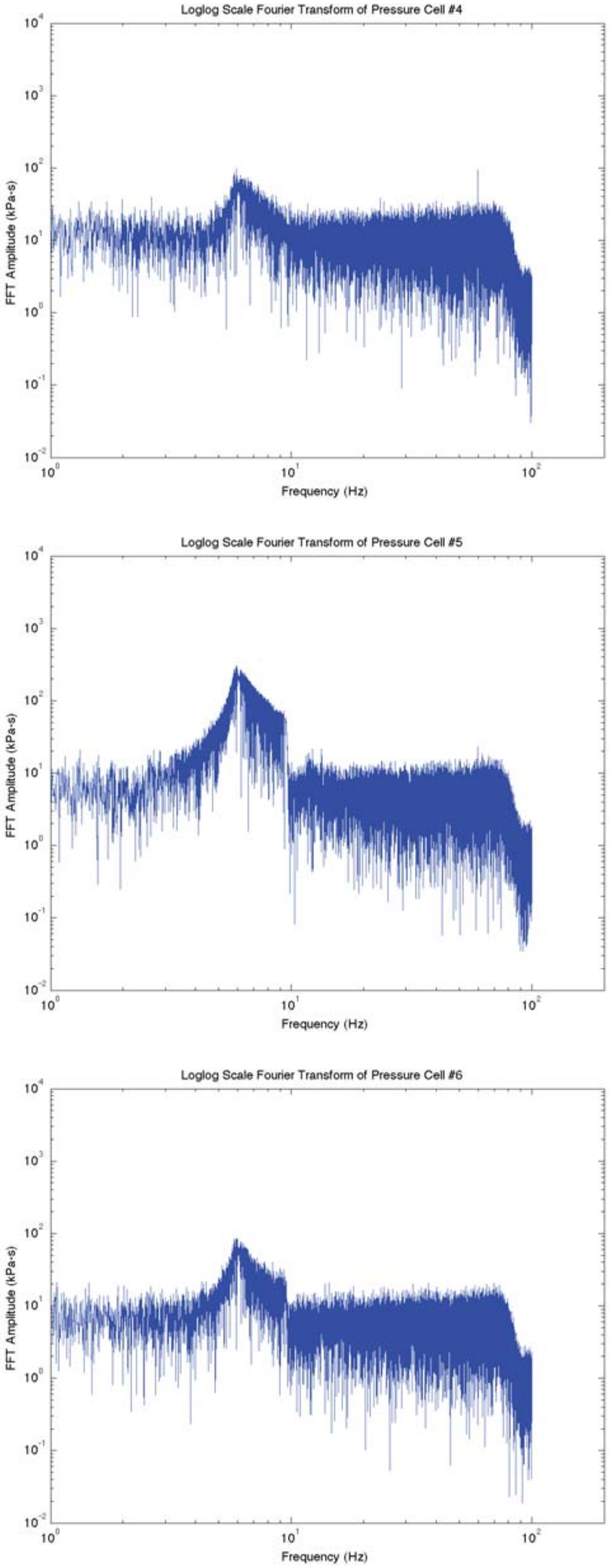

Frequency domain pressure cell graphs from test 2.2.16 (continued)

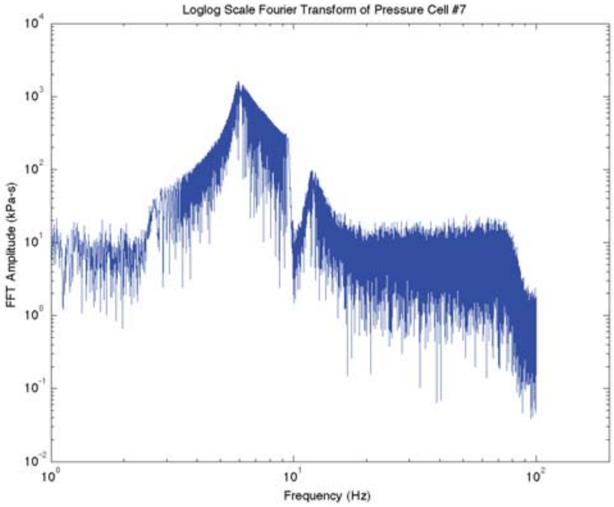

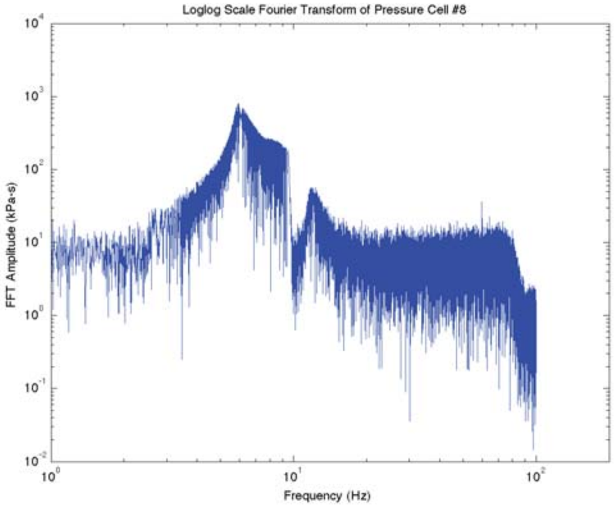

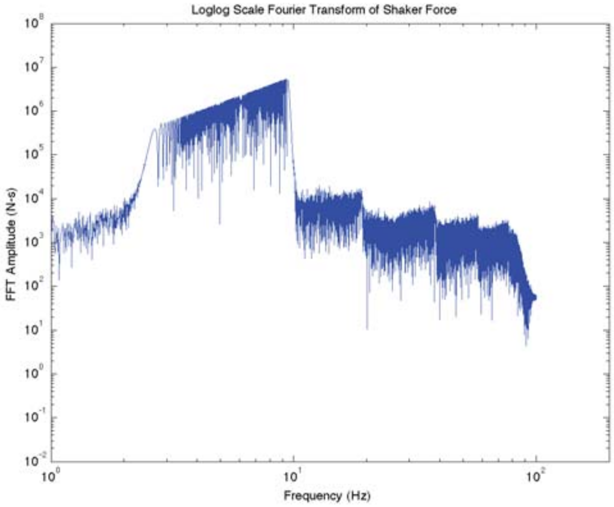

Frequency domain pressure cell graphs from test 2.2.16 (continued)

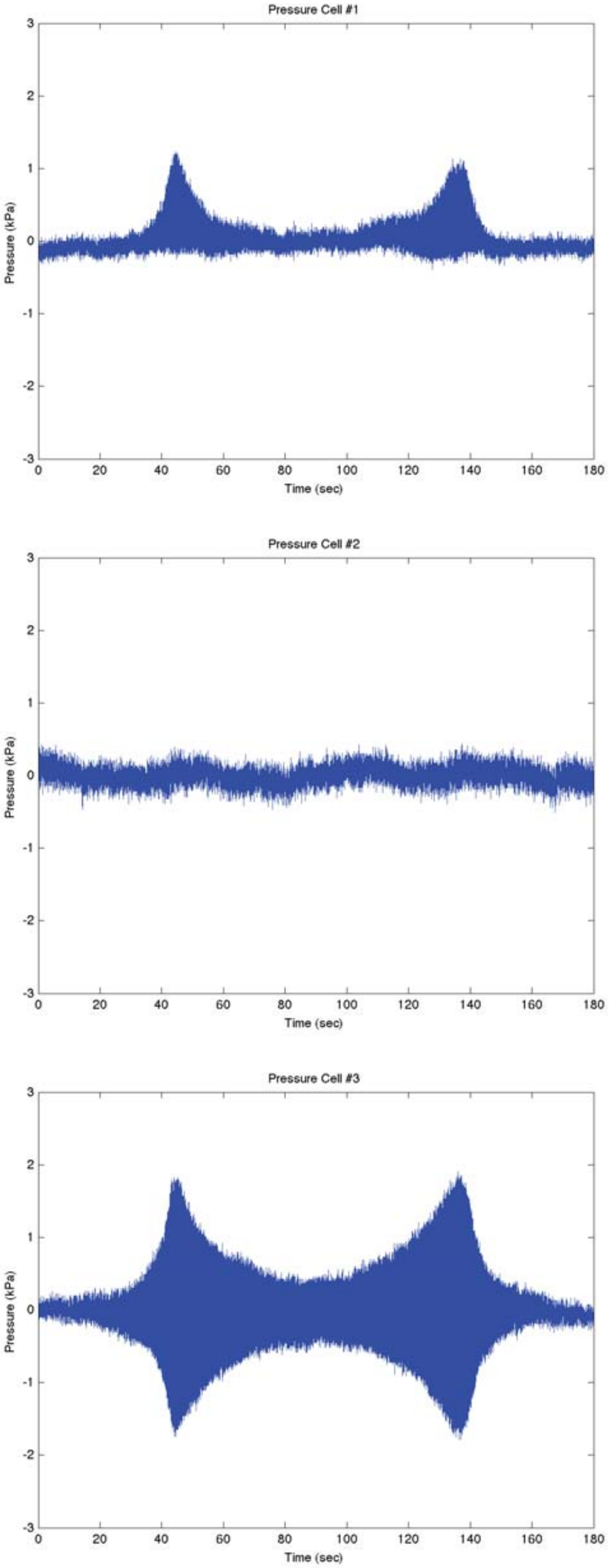

Time domain pressure cell graphs from test 2.2.16

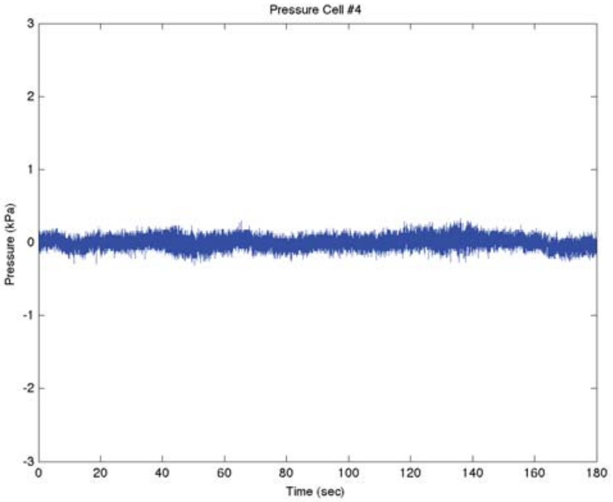

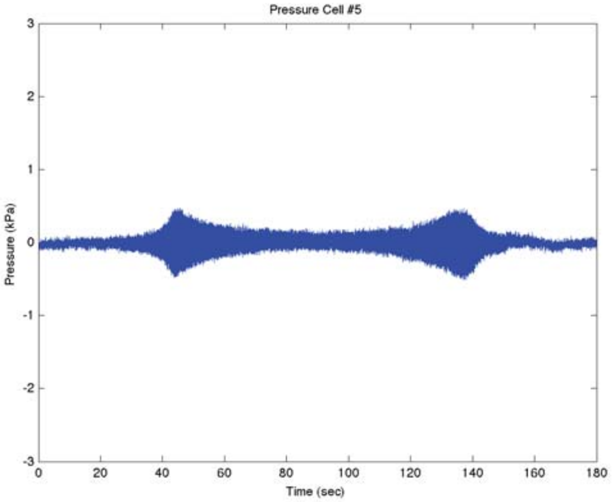

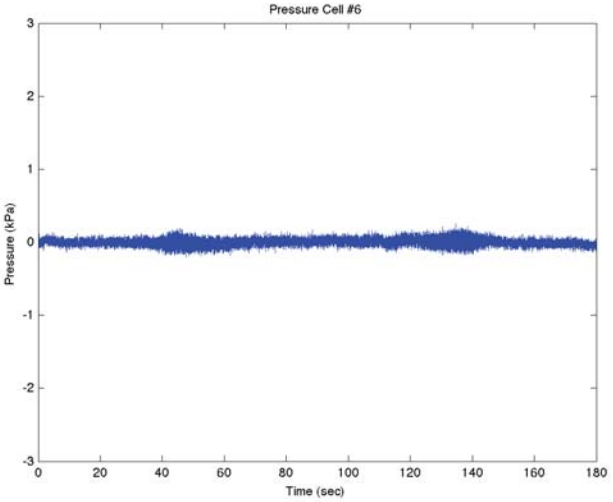

Time domain pressure cell graphs from test 2.2.16 (continued)

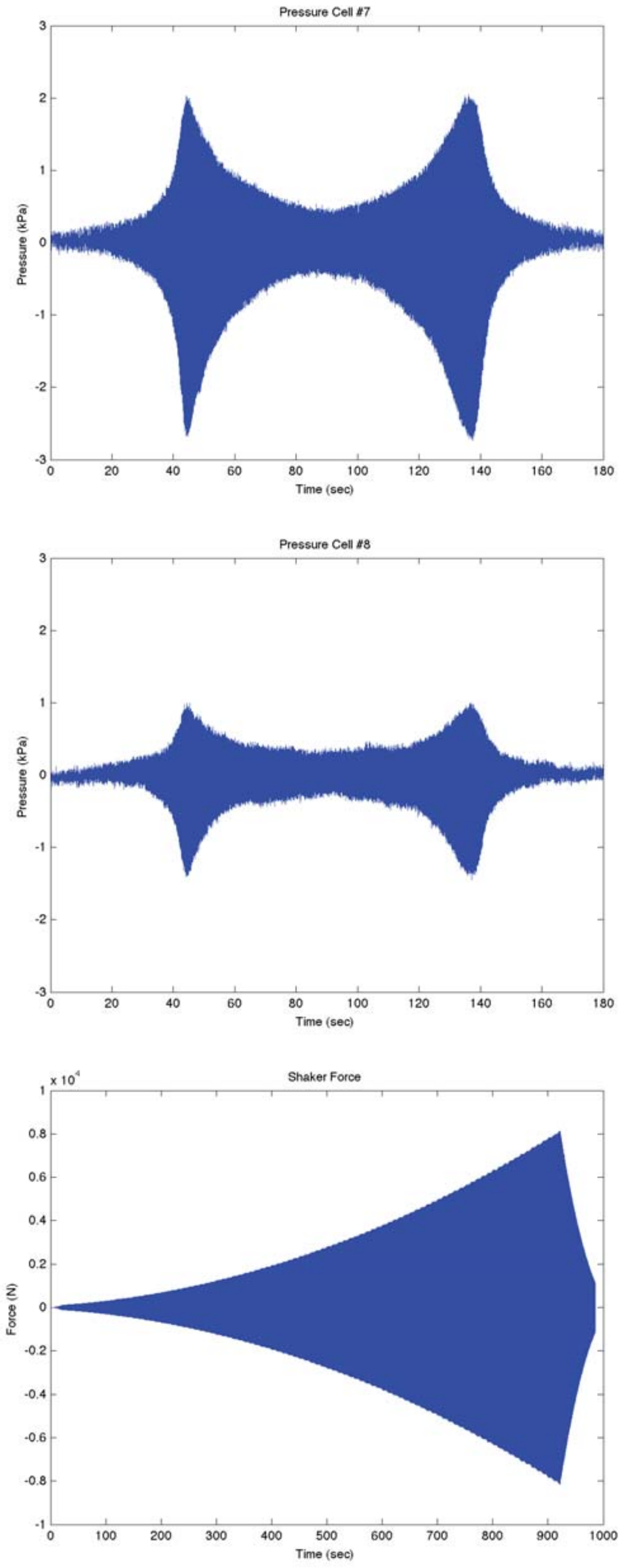

Time domain pressure cell graphs from test 2.2.16 (continued)

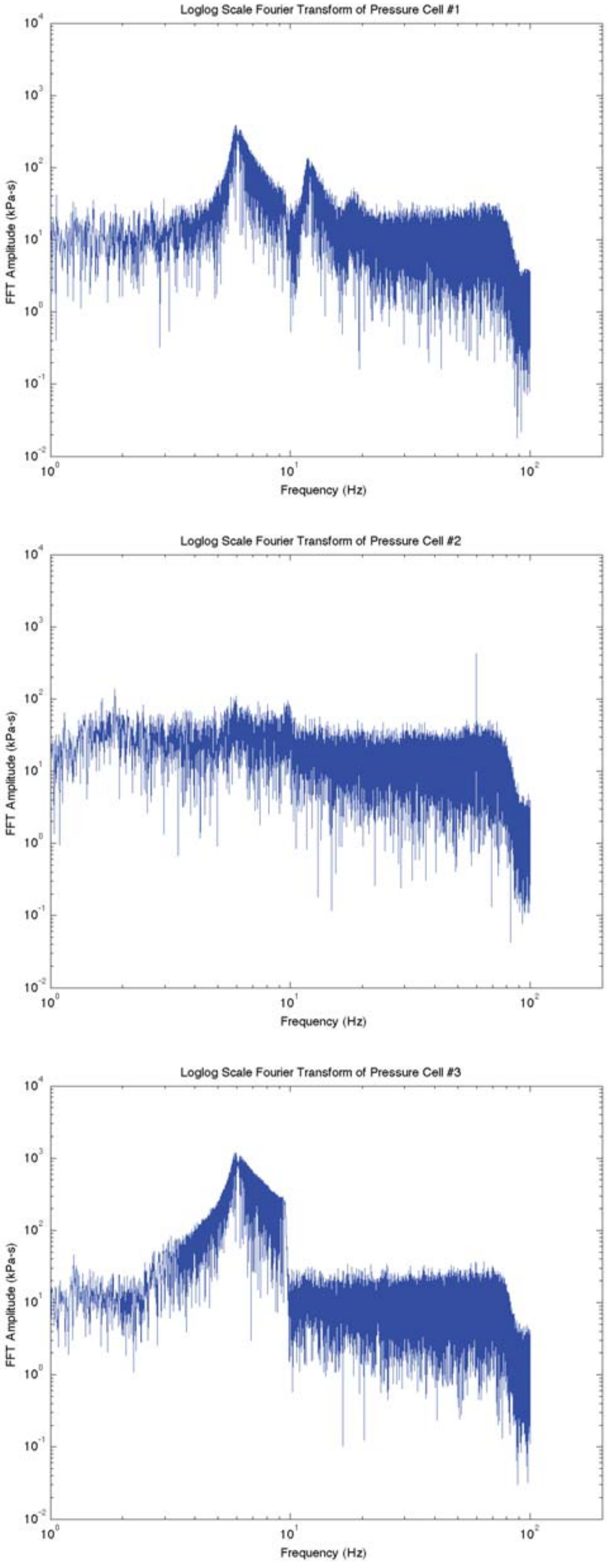

Frequency domain pressure cell graphs from test 2.2.19

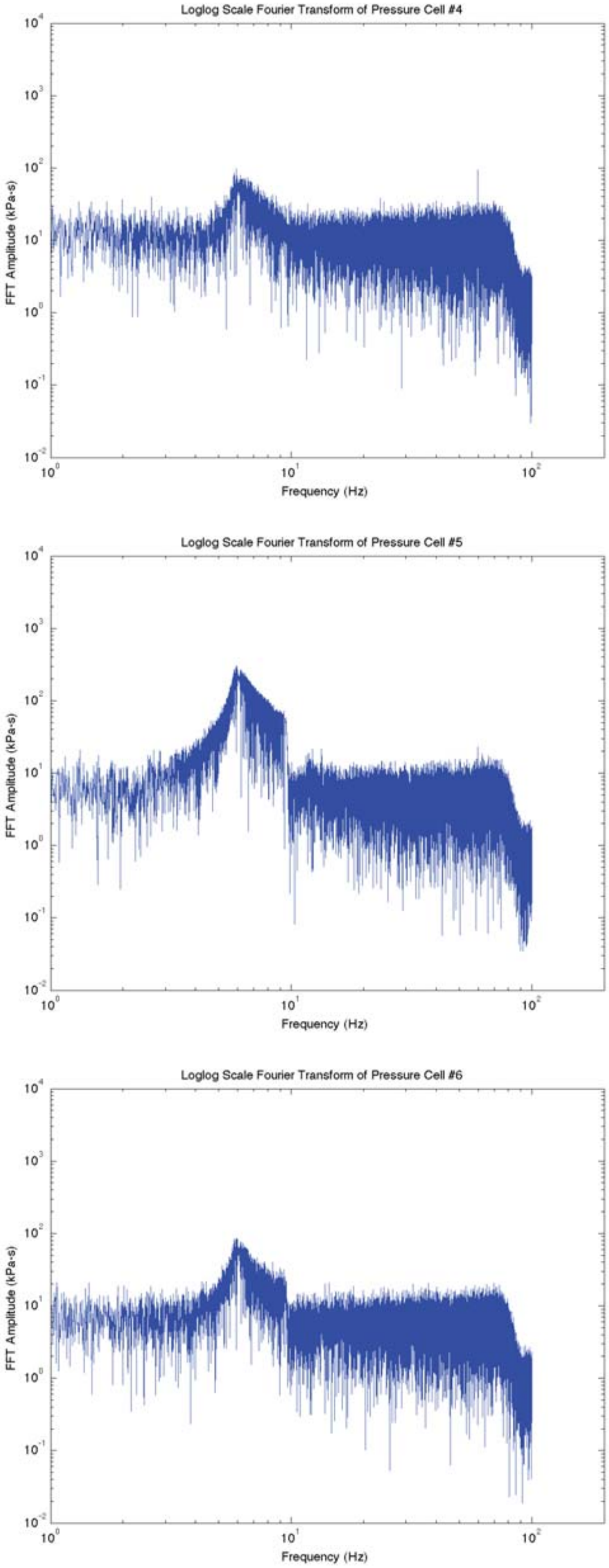
Loglog Scale Fourier Transform of Pressure Cell #4

Loglog Scale Fourier Transform of Pressure Cell #5

Loglog Scale Fourier Transform of Pressure Cell #6

Frequency domain pressure cell graphs from test 2.2.19 (continued)

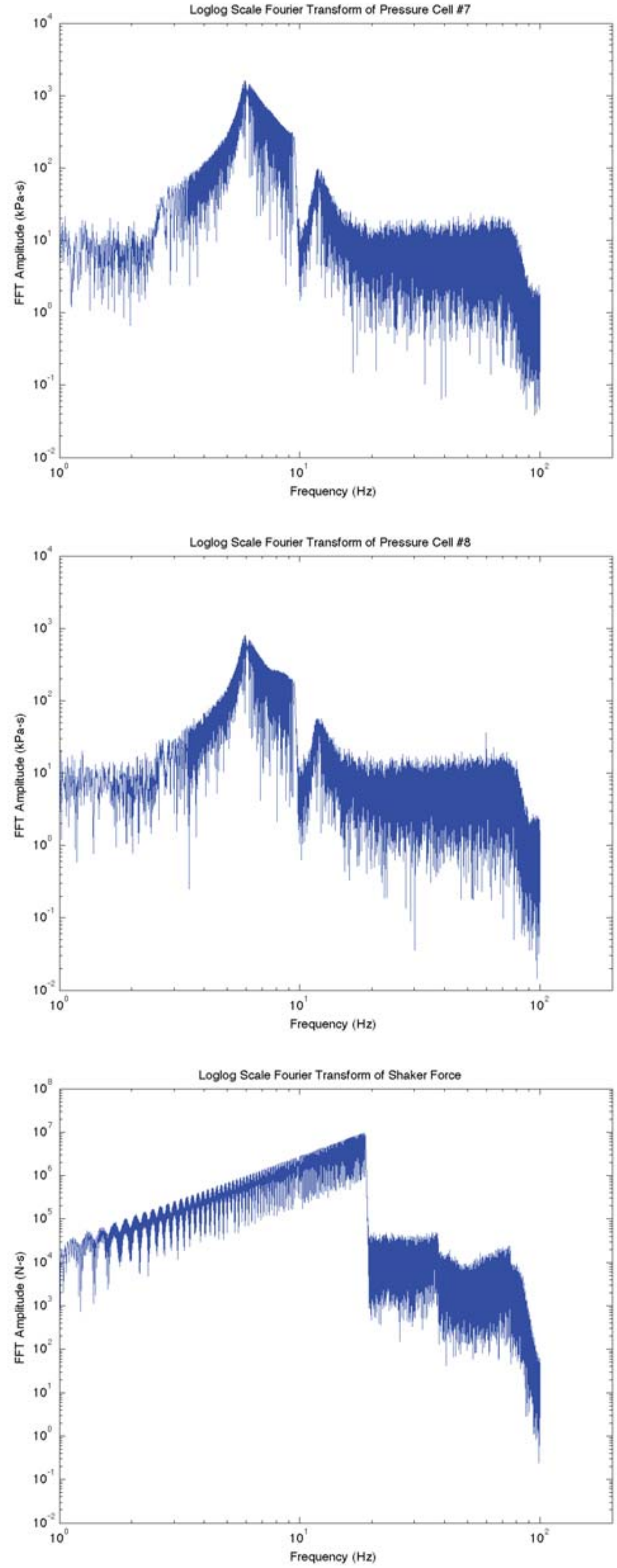

Frequency domain pressure cell graphs from test 2.2.19 (continued)

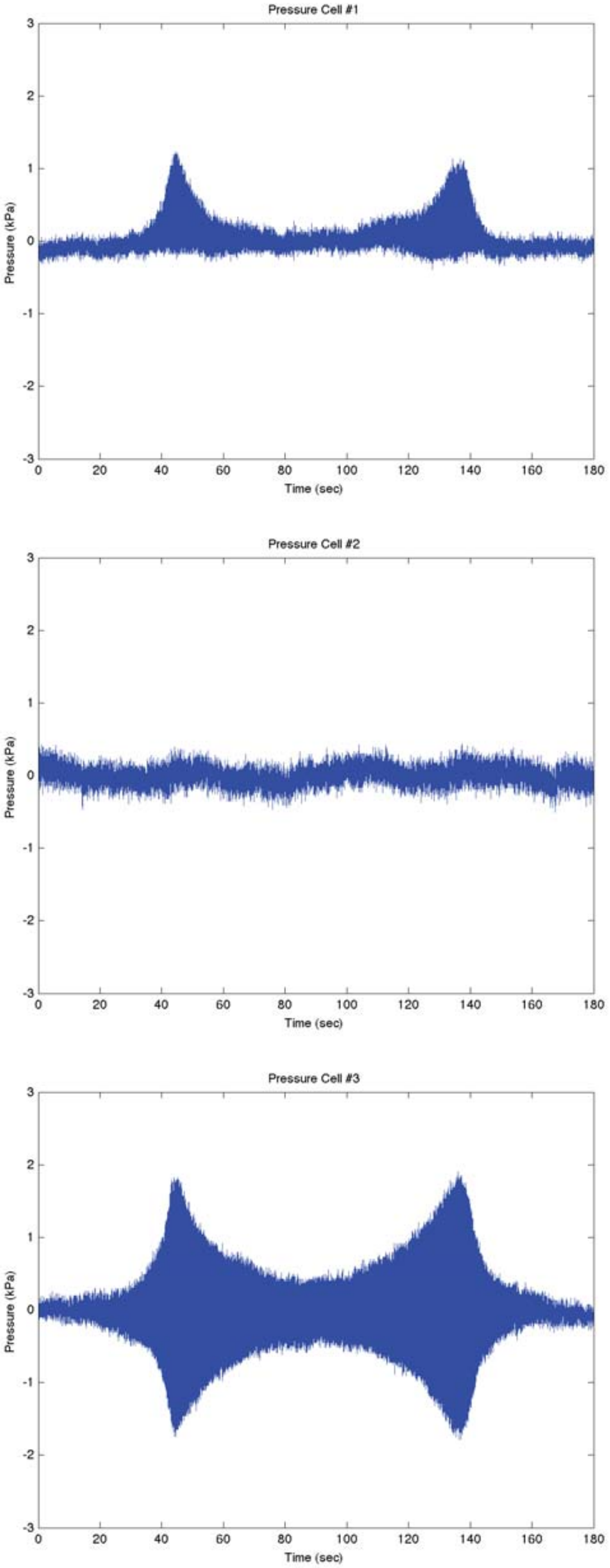

Time domain pressure cell graphs from test 2.2.19

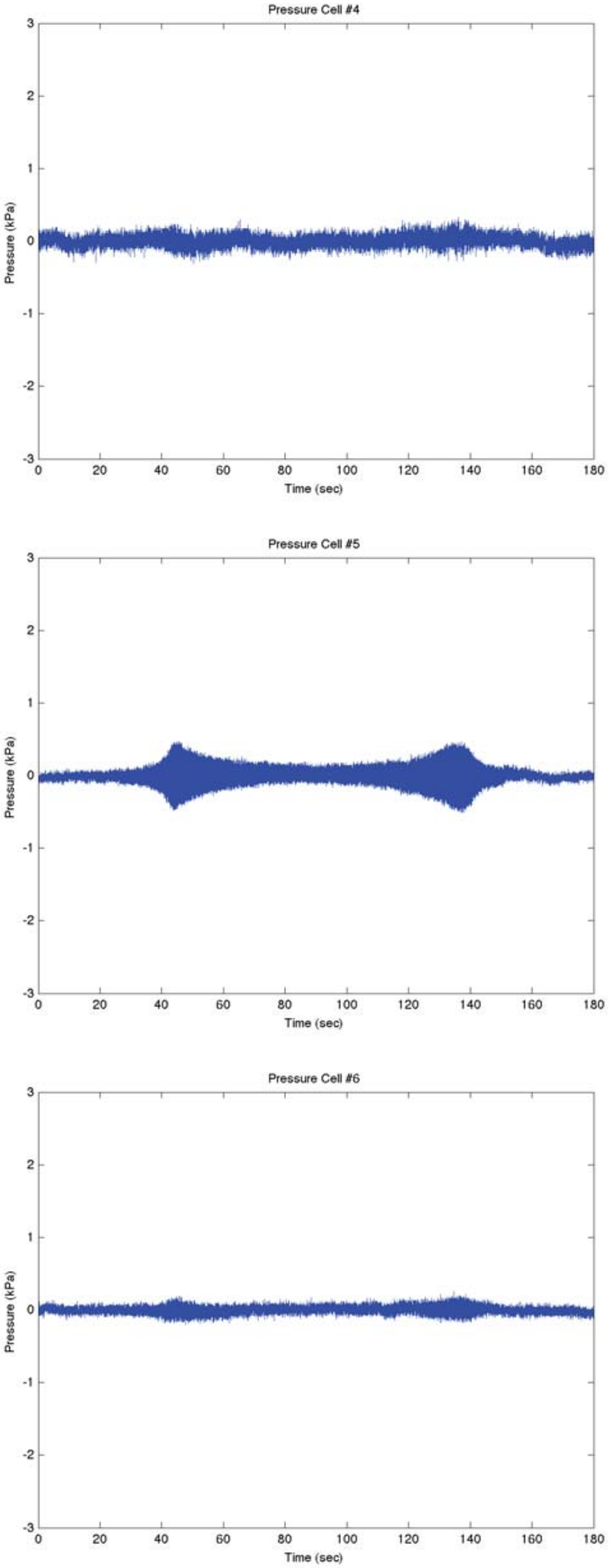

Time domain pressure cell graphs from test 2.2.19 (continued)

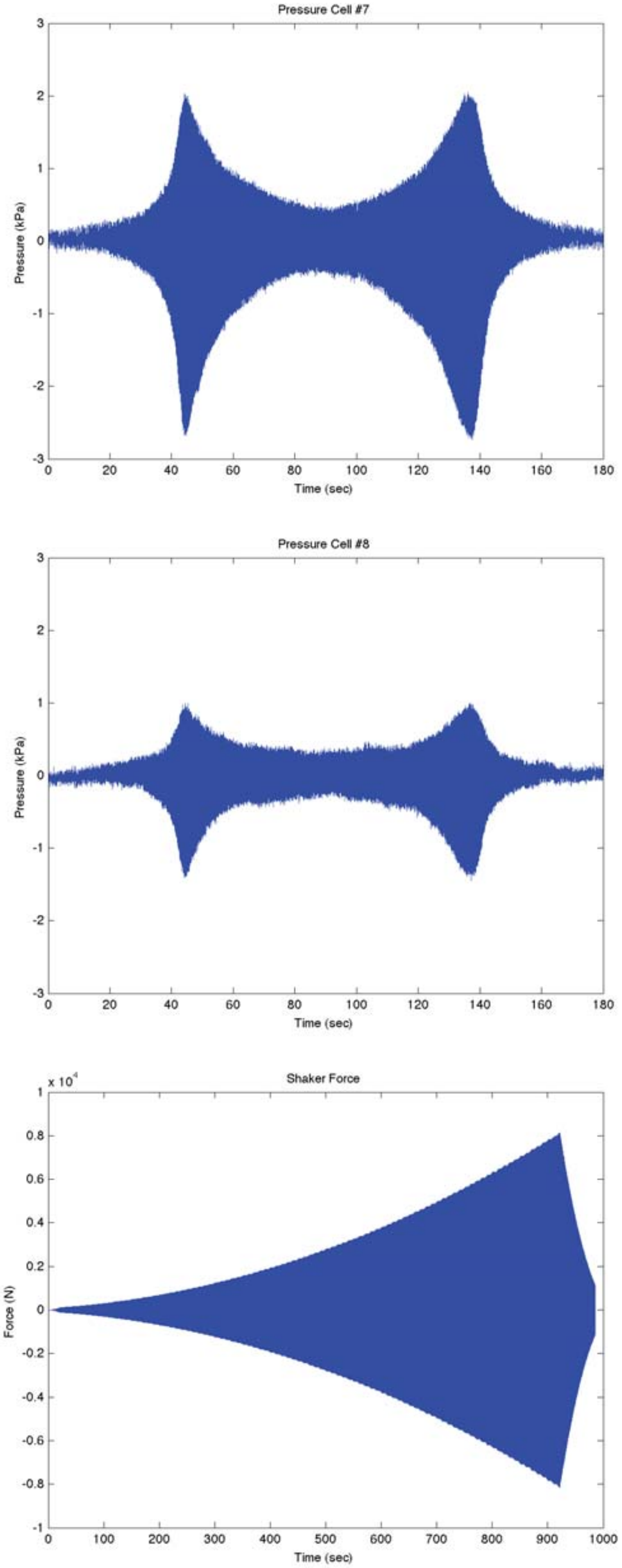

Time domain pressure cell graphs from test 2.2.19 (continued)

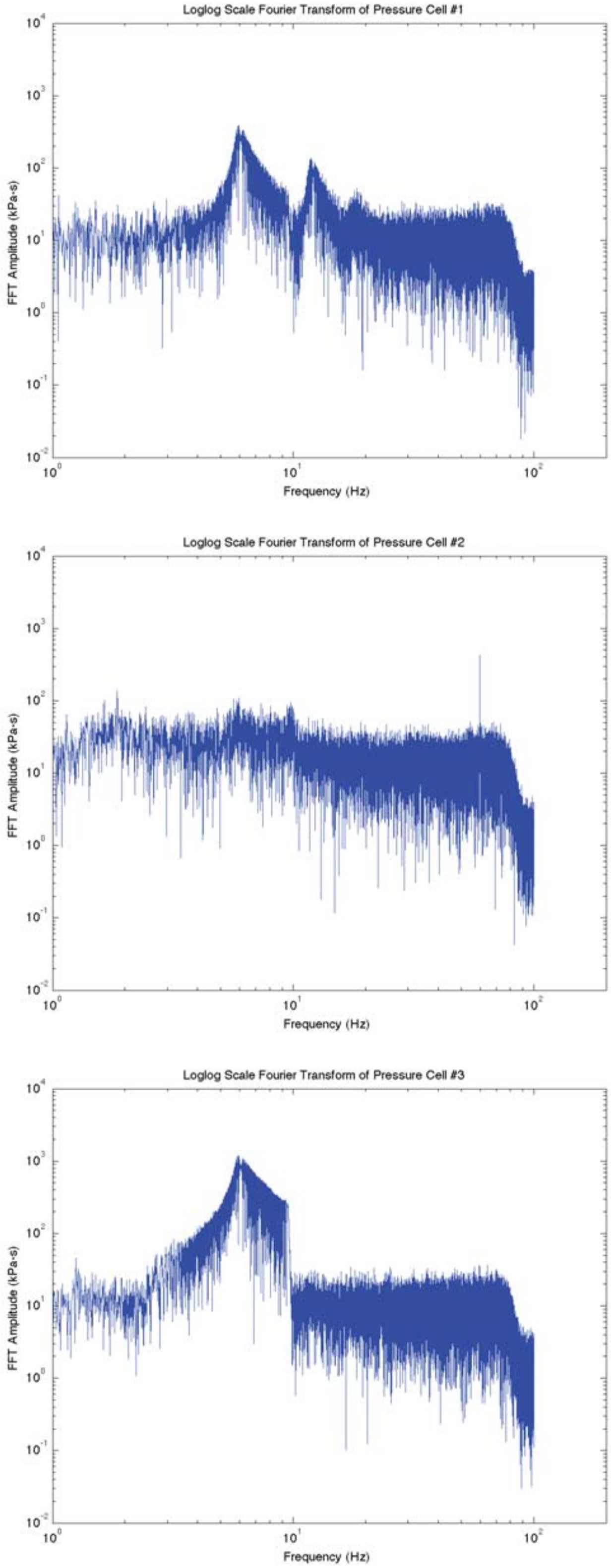

Frequency domain pressure cell graphs from test 2.2.20

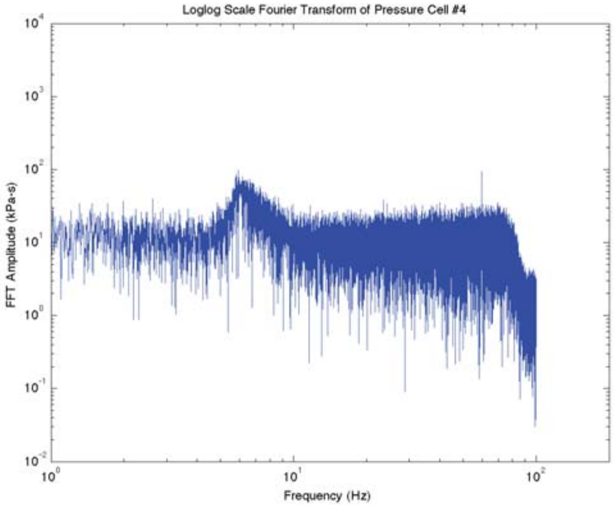

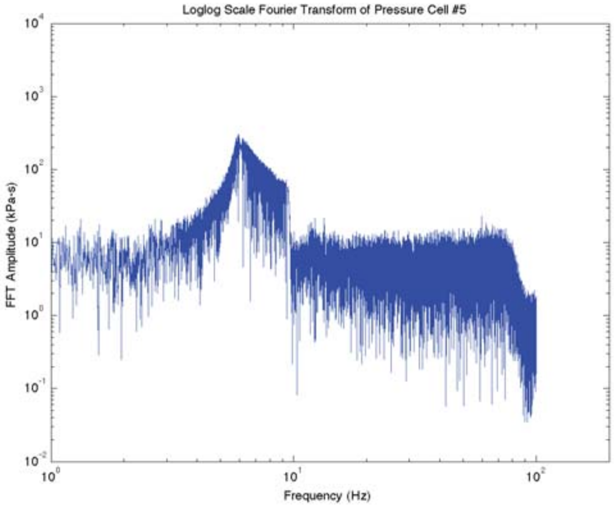

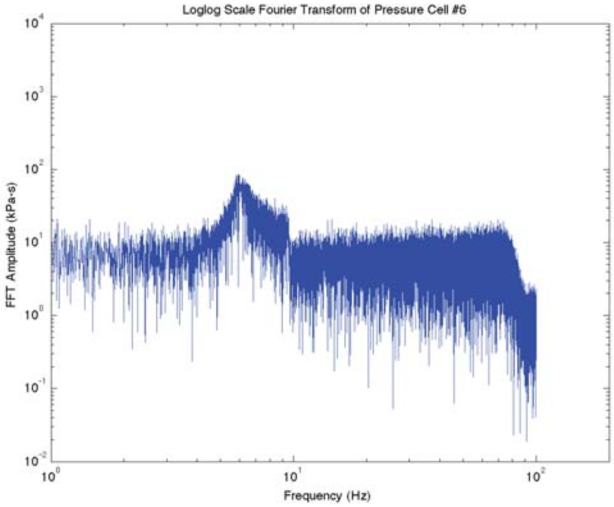

Frequency domain pressure cell graphs from test 2.2.20 (continued)

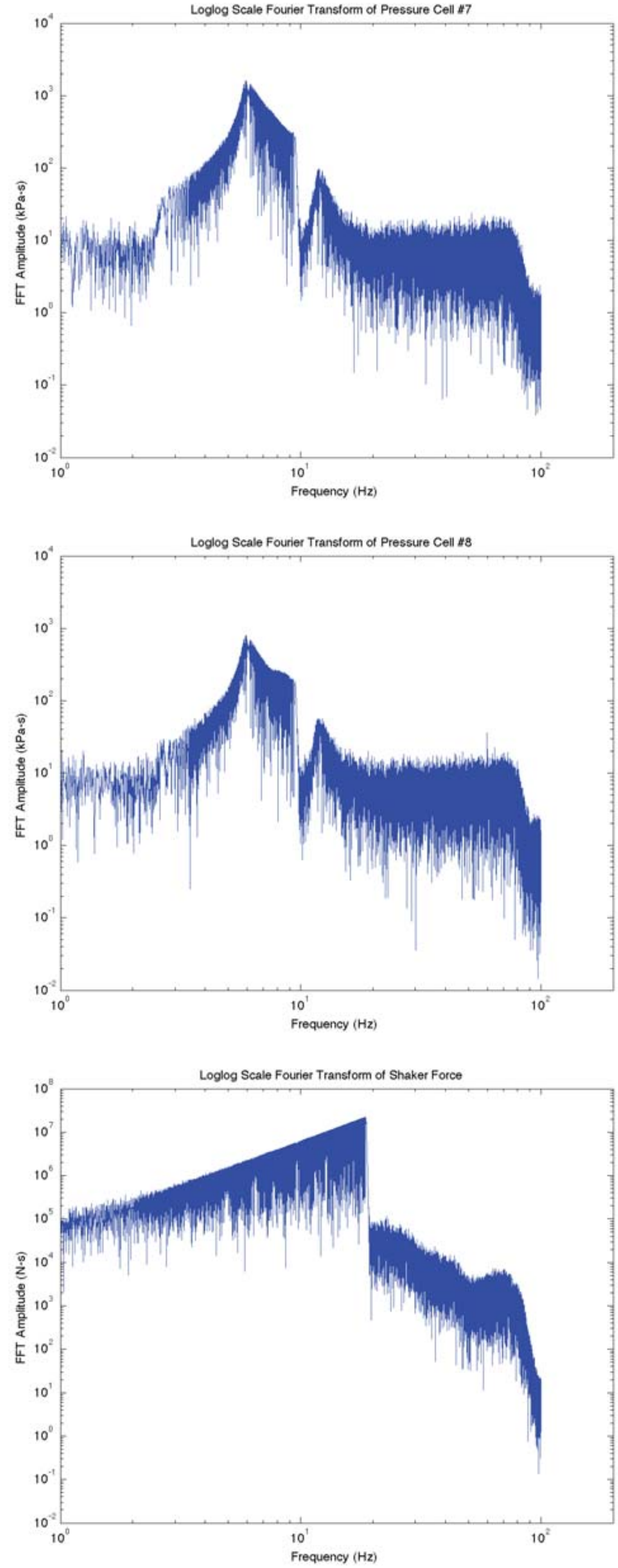

Frequency domain pressure cell graphs from test 2.2.20 (continued)

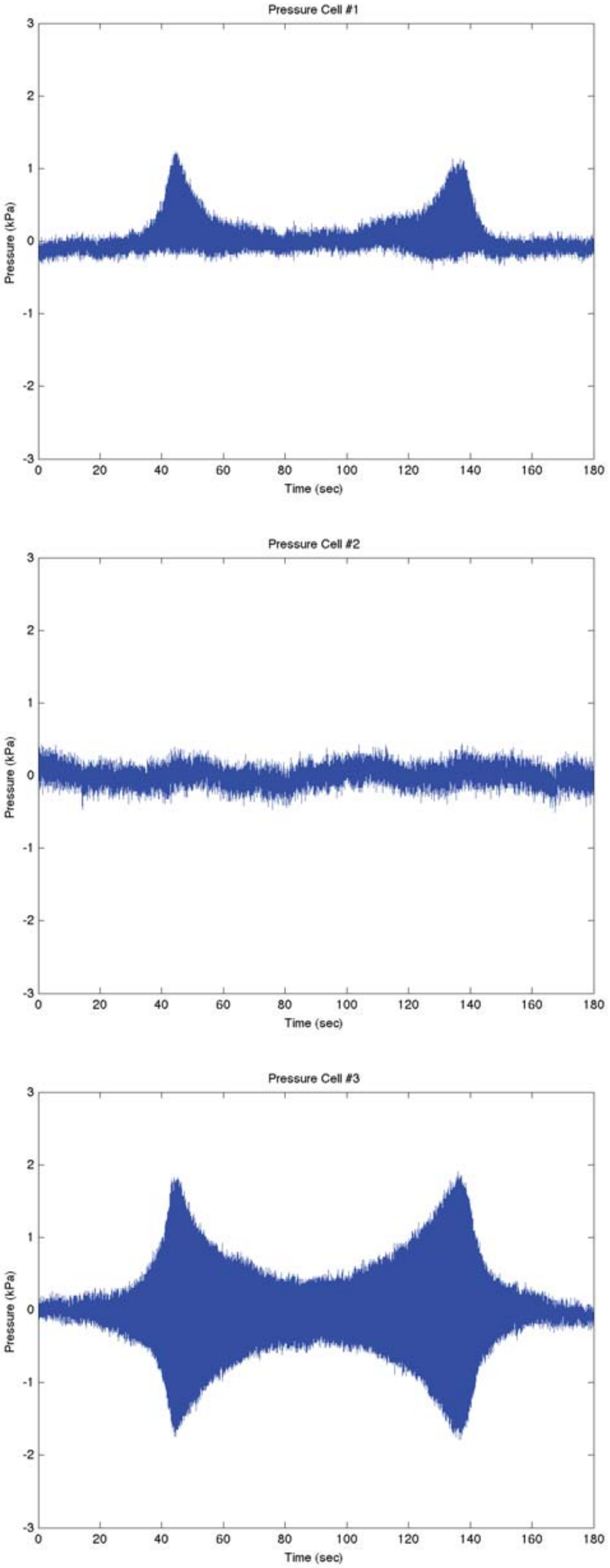

Time domain pressure cell graphs from test 2.2.20

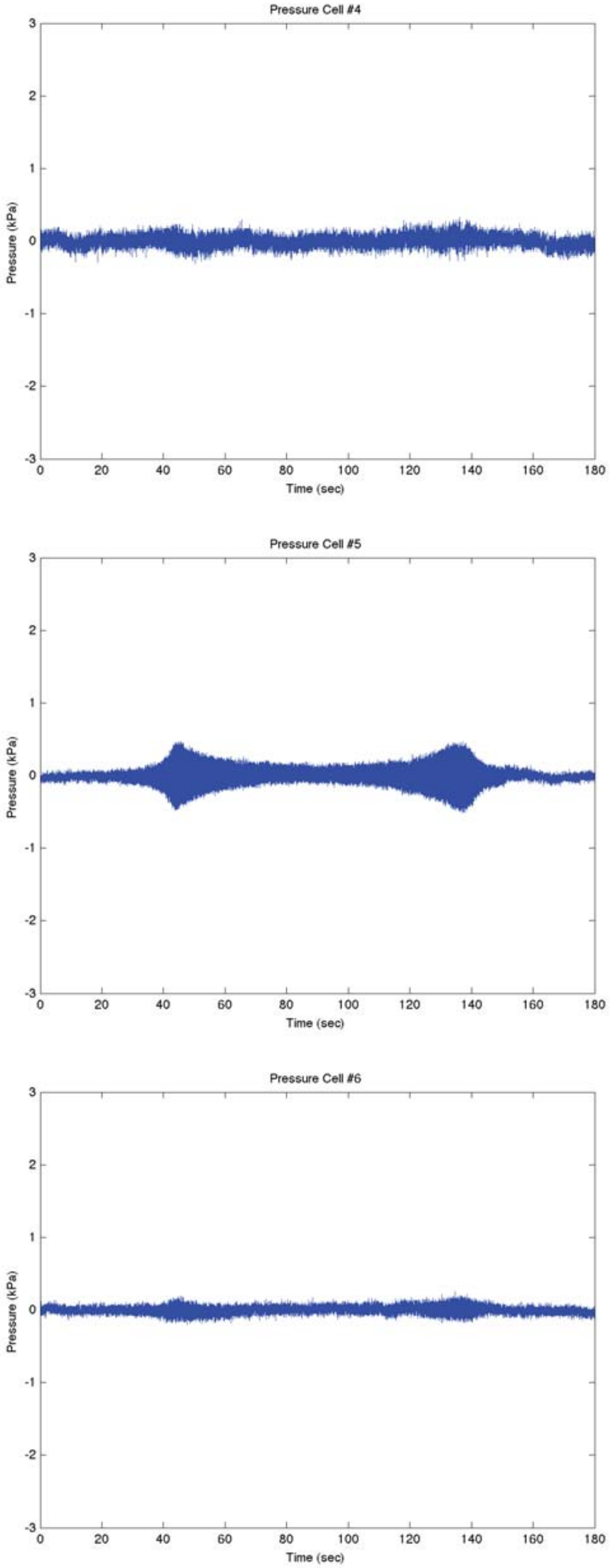

Time domain pressure cell graphs from test 2.2.20 (continued)

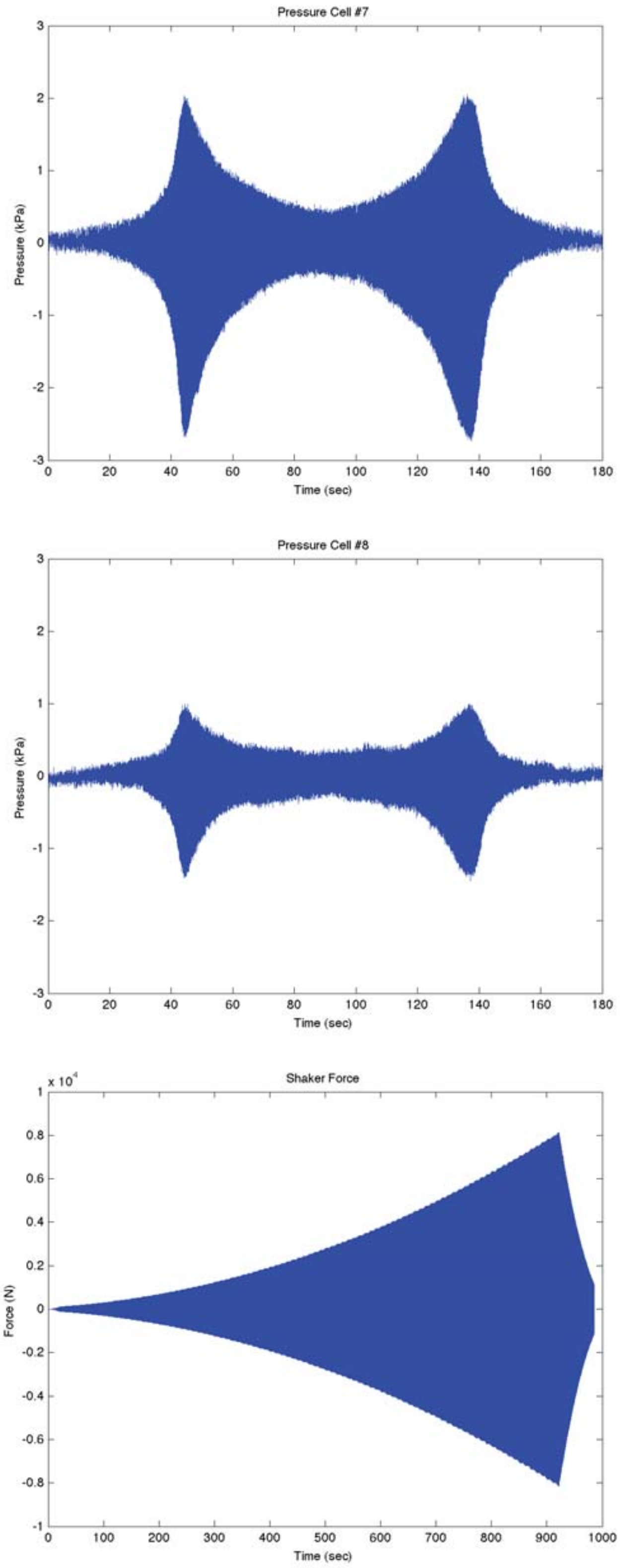

Time domain pressure cell graphs from test 2.2.20 (continued)

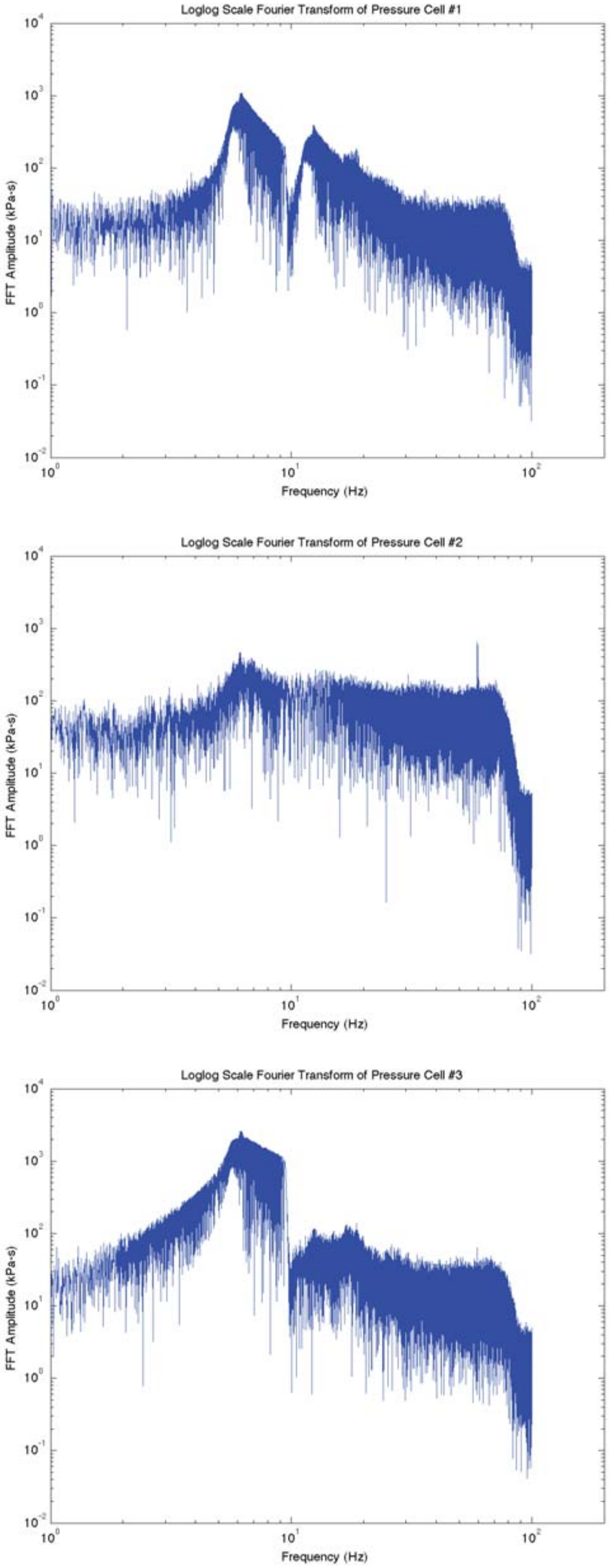

Frequency domain pressure cell graphs from test 2.2.22

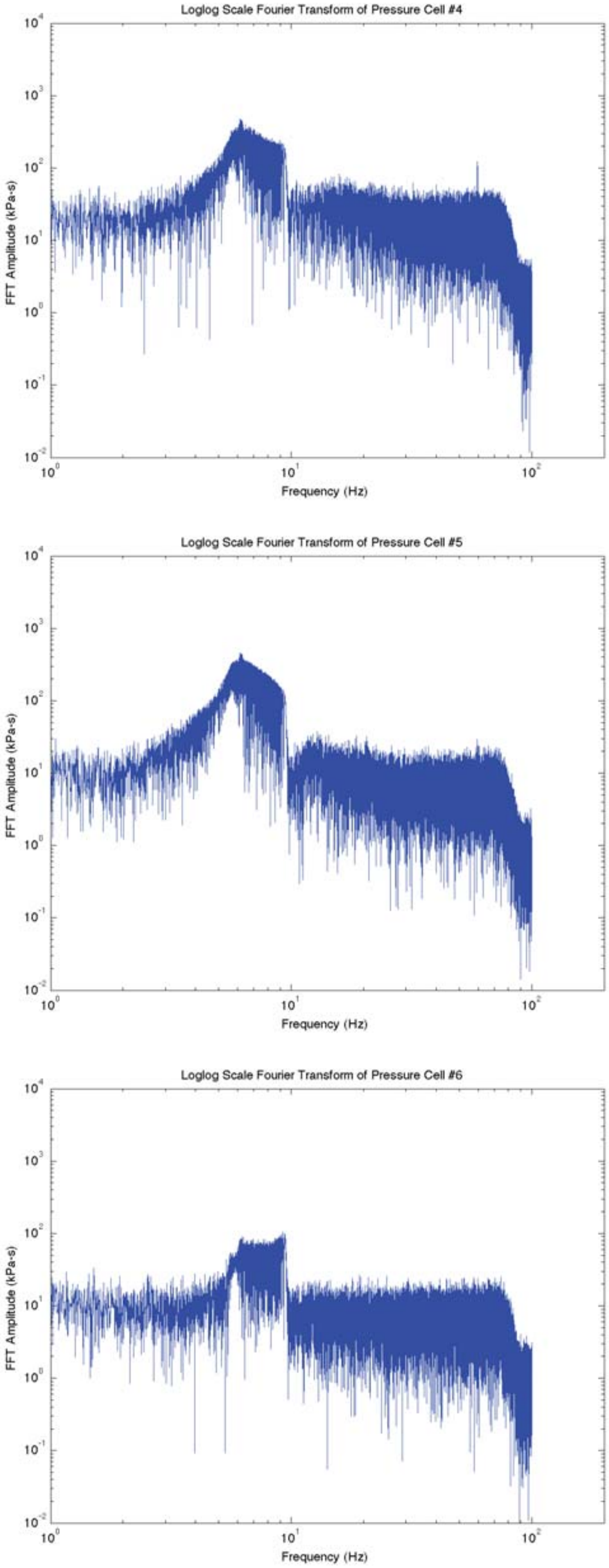

Frequency domain pressure cell graphs from test 2.2.22 (continued)

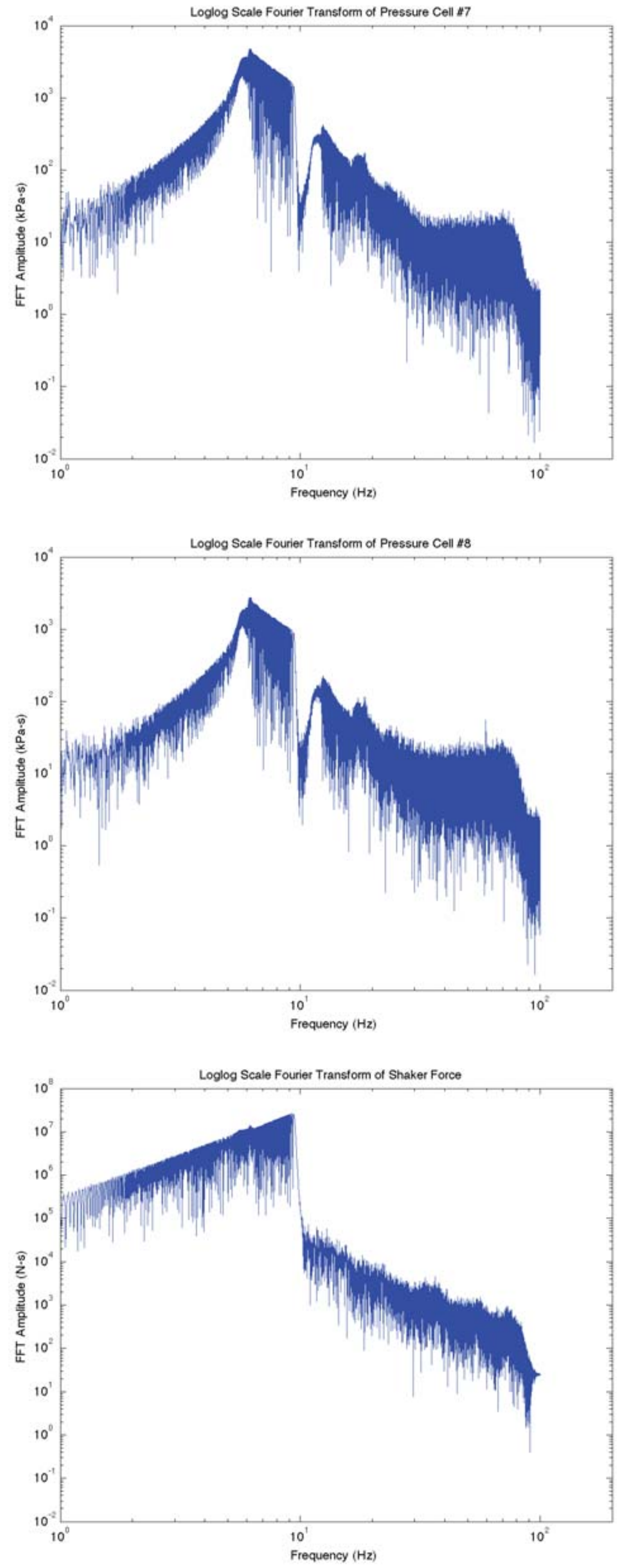

Frequency domain pressure cell graphs from test 2.2.22 (continued)

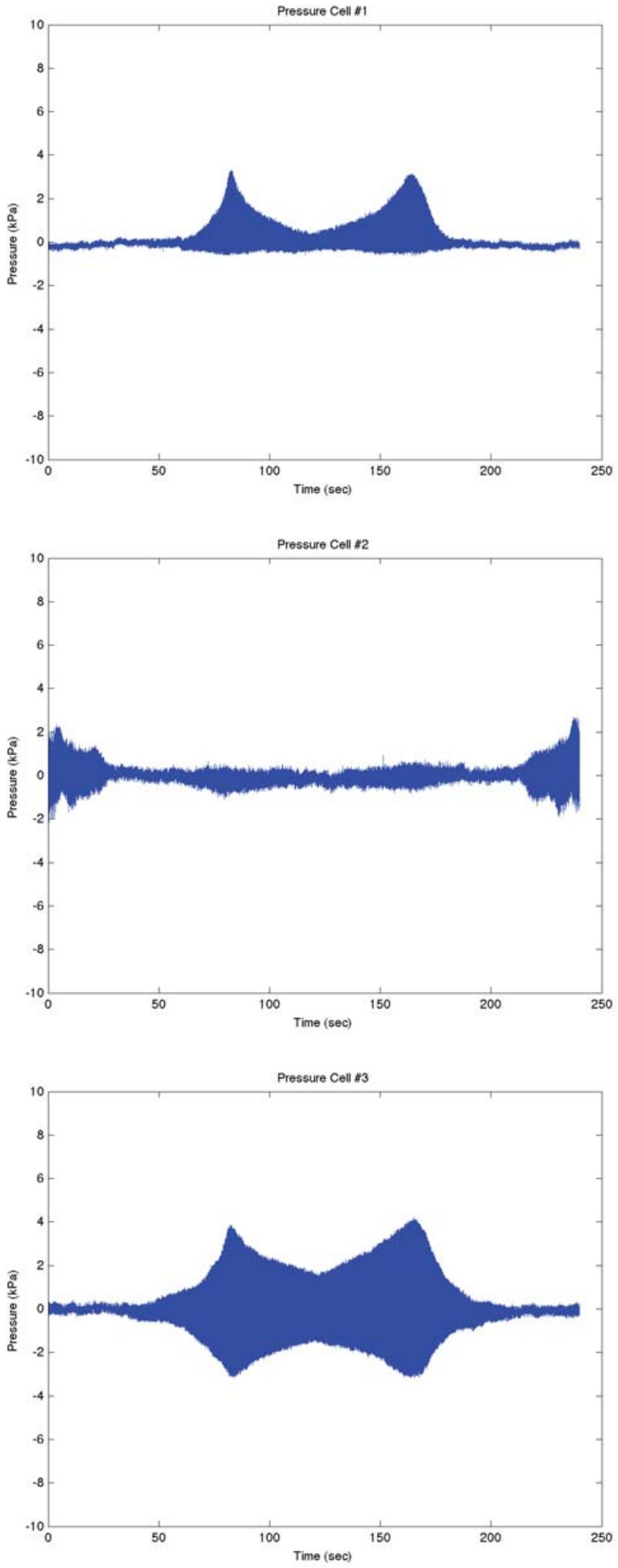

Time domain pressure cell graphs from test 2.2.22

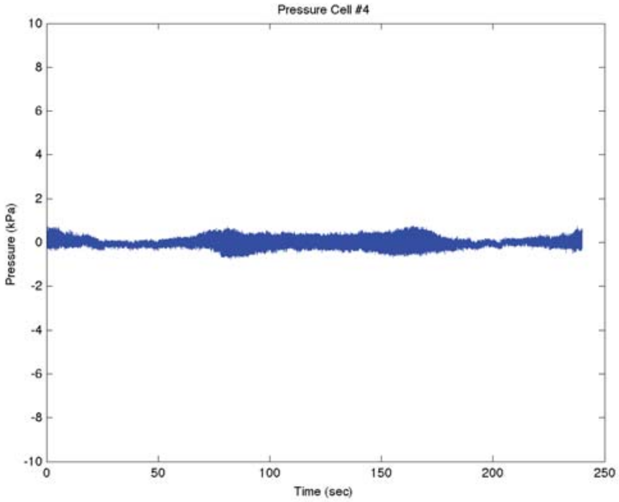

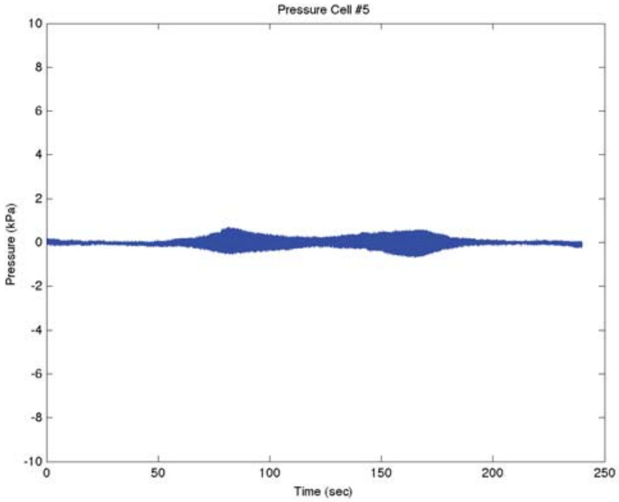

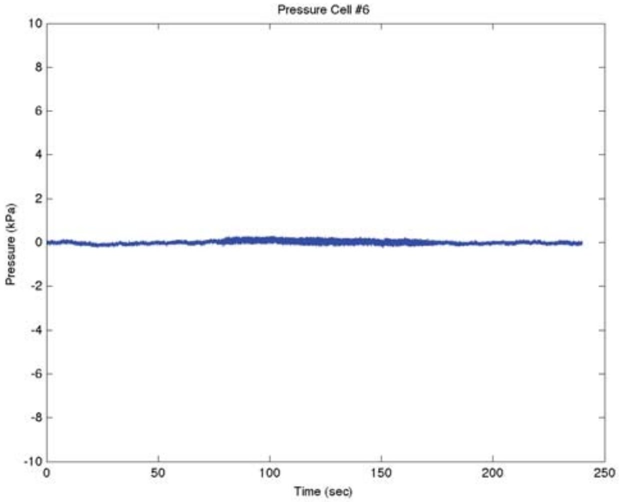

Time domain pressure cell graphs from test 2.2.22 (continued)

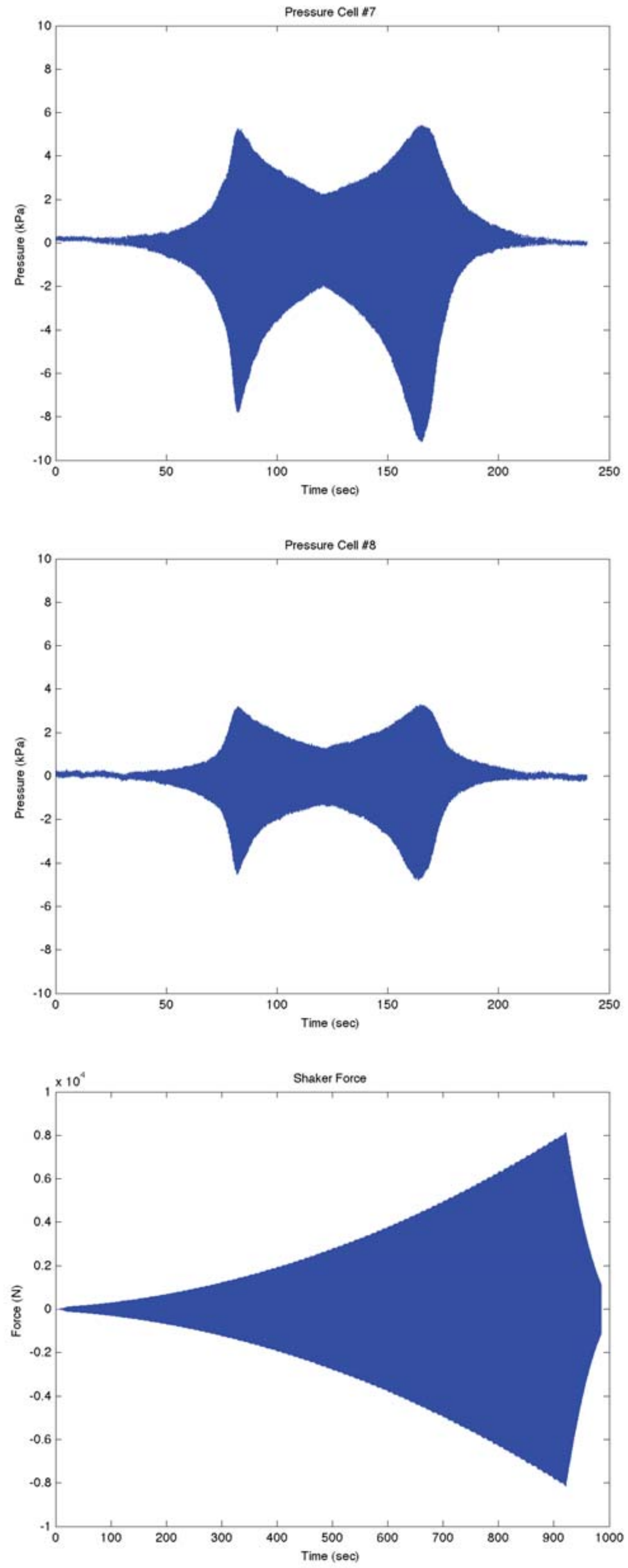

Time domain pressure cell graphs from test 2.2.22 (continued)

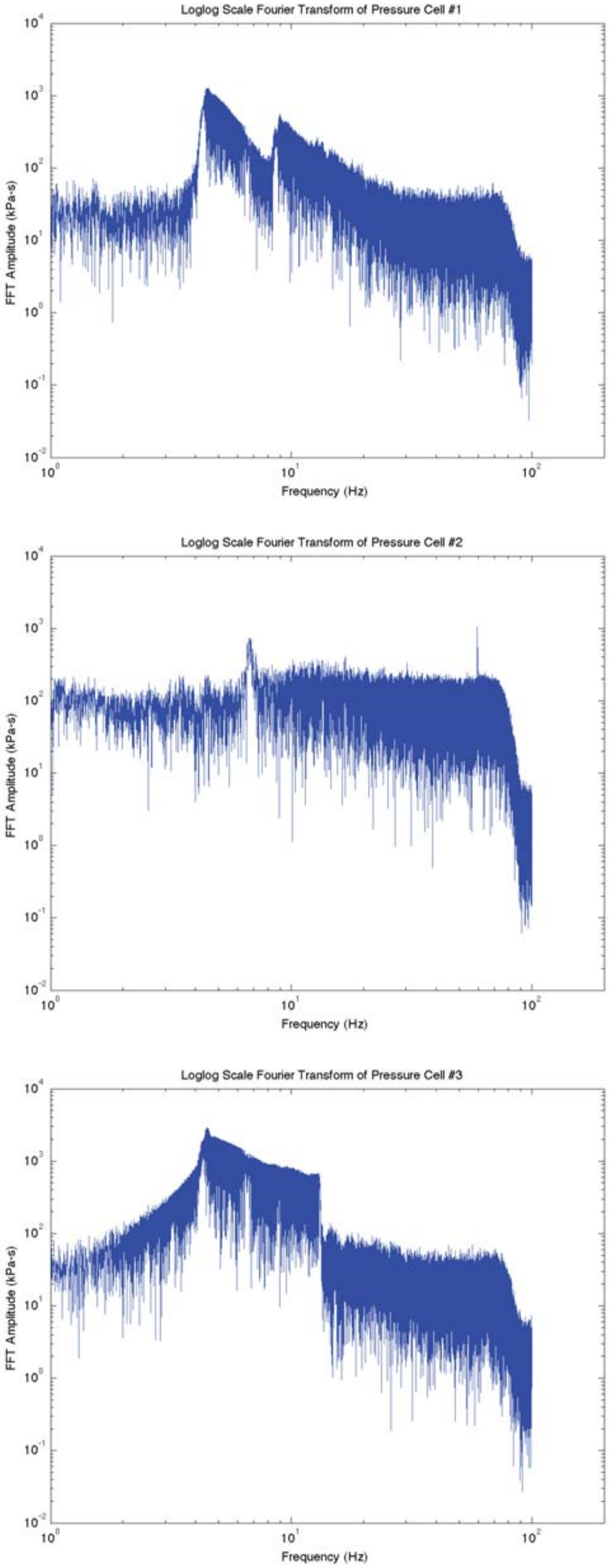

Frequency domain pressure cell graphs from test 2.2.24b

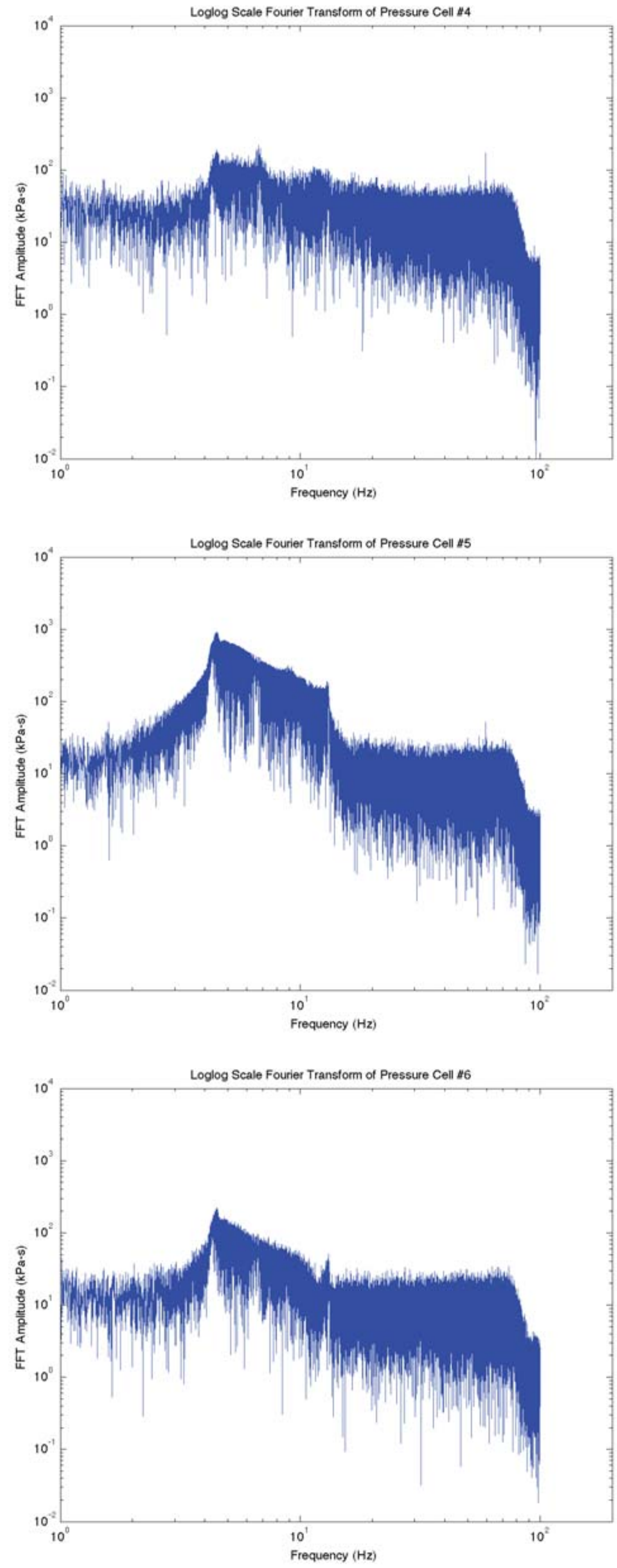

Frequency domain pressure cell graphs from test 2.2.24b (continued)

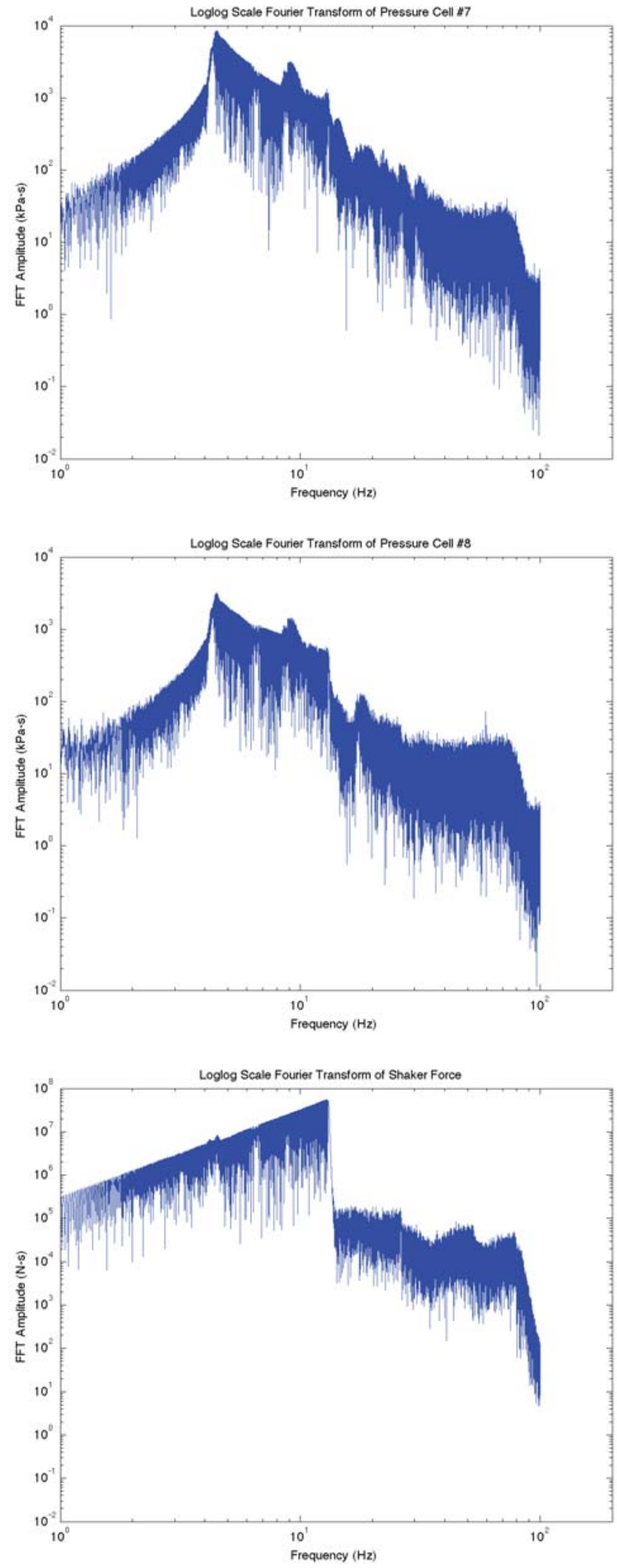

Frequency domain pressure cell graphs from test 2.2.24b (continued)

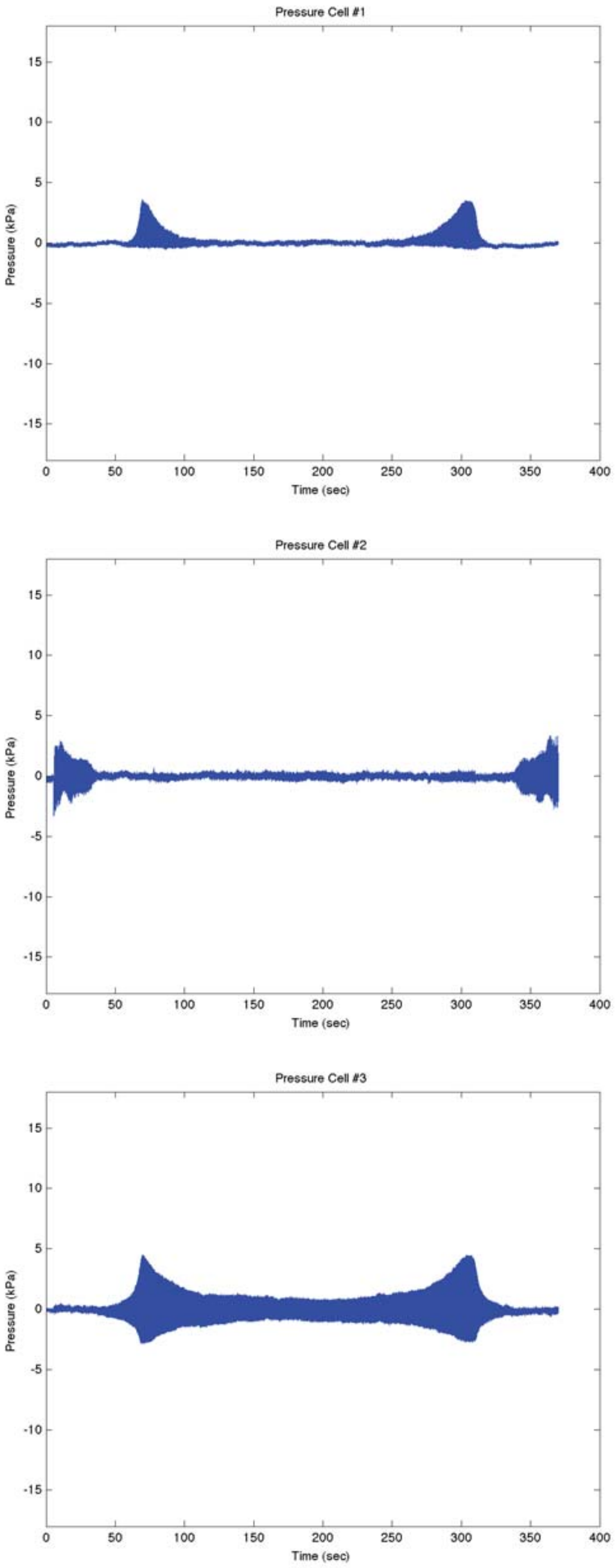

Time domain pressure cell graphs from test 2.2.24b

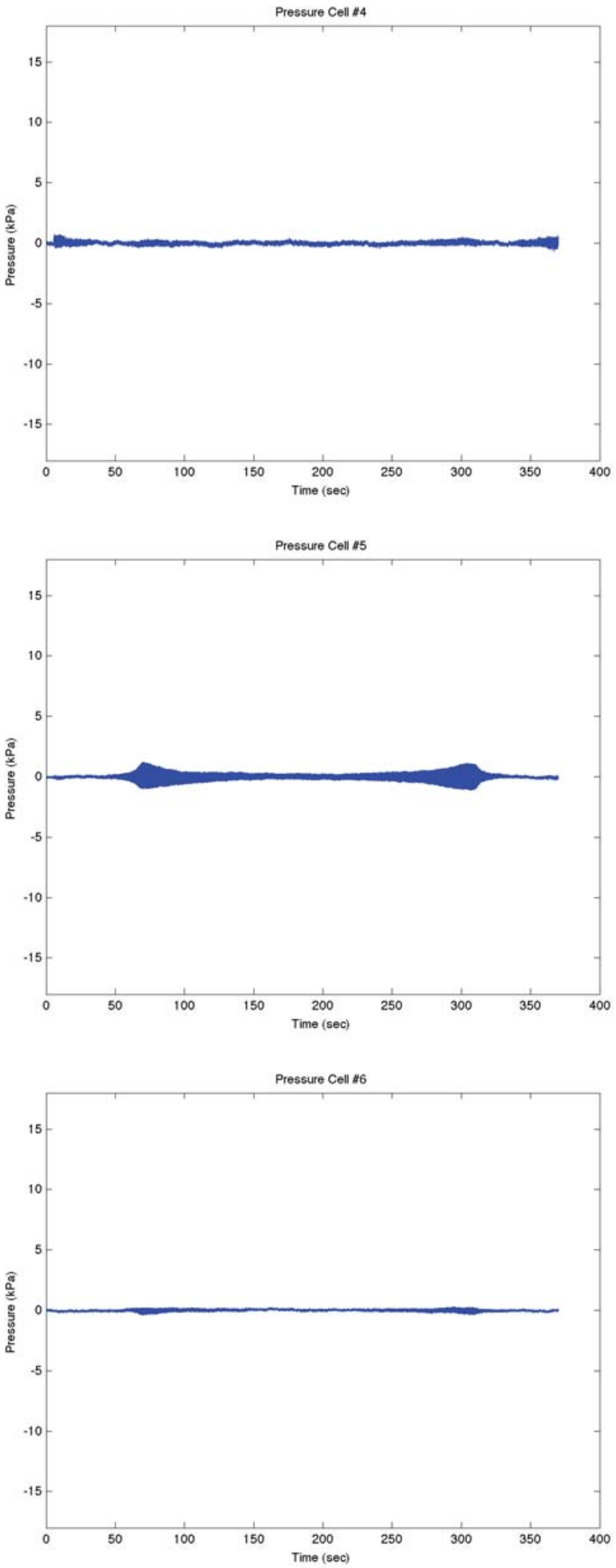

Time domain pressure cell graphs from test 2.2.24b (continued)

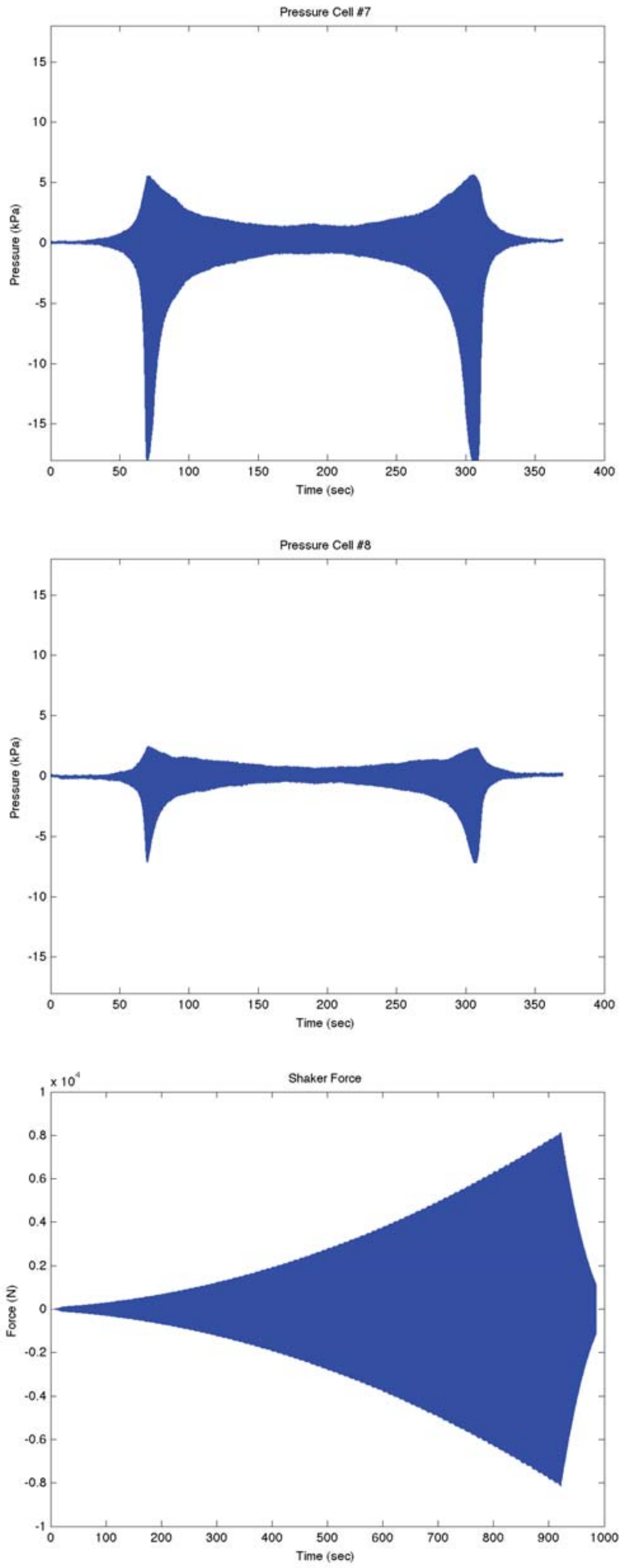

Time domain pressure cell graphs from test 2.2.24b (continued)

APPENDIX B

MATLAB CODES

```
clear all, close all, clc

load('FFT 2.2.1a 0.05MM.mat')
%Evaluate Pressure Cell Data (log-log)
z=10000
x= VarName26;

%Create Time Vector
dt=0.005;   %time step in seconds
l=length(x);
Time=[0:dt:(l*dt-dt)];
x=detrend(x);

%Plot FFT
Fnyq=1/(2*dt);              %calculate nyqqest frequency
freq=linspace(-Fnyq,Fnyq,l+1)'; %Create Frequency Vector
freq=freq(1:l);

FFTx=fft(x);               %fourier transform
X=fftshift(FFTx);              %changes the order of the vector
ACH=abs(X);                %find fourier magnitude
pCH=angle(X);              %find fourier phase

figure(1)
loglog(freq,ACH)
title('Loglog Scale Fourier Transform of Pressure Cell #1')
xlabel('Frequency (Hz)')
xlim([1,max(200)])     %change the x-axes limits here
ylabel('FFT Amplitude (kPa-s)')
ylim([min(.01),max(z)])      %change the x-axes limits here

h=gcf
saveas(h,'ll1.png')

x= VarName27;

%Create Time Vector
dt=0.005   %time step in seconds
l=length(x);
Time=[0:dt:(l*dt-dt)];
x=detrend(x);


%Plot FFT
Fnyq=1/(2*dt);              %calculate nyqqest frequency
```

```
freq=linspace(-Fnyq,Fnyq,l+1)'; %Create Frequency Vector
freq=freq(1:l);

FFTx=fft(x);               %fourier transform
X=fftshift(FFTx);              %changes the order of the vector
ACH=abs(X);                %find fourier magnitude
pCH=angle(X);              %find fourier phase

figure(2)
loglog(freq,ACH)
title('Loglog Scale Fourier Transform of Pressure Cell #2')
xlabel('Frequency (Hz)')
xlim([1,max(200)])      %change the x-axes limits here
ylabel('FFT Amplitude (kPa-s)')
ylim([min(.01),max(z)])      %change the x-axes limits here

h=gcf
saveas(h,'ll2.png')

x= VarName28;

%Create Time Vector
dt=0.005   %time step in seconds
l=length(x);
Time=[0:dt:(l*dt-dt)];
x=detrend(x);

%Plot FFT
Fnyq=1/(2*dt);              %calculate nyqqest frequency
freq=linspace(-Fnyq,Fnyq,l+1)'; %Create Frequency Vector
freq=freq(1:l);

FFTx=fft(x);               %fourier transform
X=fftshift(FFTx);              %changes the order of the vector
ACH=abs(X);                %find fourier magnitude
pCH=angle(X);              %find fourier phase

figure(3)
loglog(freq,ACH)
title('Loglog Scale Fourier Transform of Pressure Cell #3')
xlabel('Frequency (Hz)')
xlim([1,max(200)])      %change the x-axes limits here
ylabel('FFT Amplitude (kPa-s)')
ylim([min(.01),max(z)])      %change the x-axes limits here
```

```
h=gcf
saveas(h,'ll3.png')

x= VarName29;

%Create Time Vector
dt=0.005   %time step in seconds
l=length(x);
Time=[0:dt:(l*dt-dt)];
x=detrend(x);

%Plot FFT
Fnyq=1/(2*dt);             %calculate nyqqest frequency
freq=linspace(-Fnyq,Fnyq,l+1)'; %Create Frequency Vector
freq=freq(1:l);

FFTx=fft(x);               %fourier transform
X=fftshift(FFTx);              %changes the order of the vector
ACH=abs(X);                %find fourier magnitude
pCH=angle(X);              %find fourier phase

figure(4)
loglog(freq,ACH)
title('Loglog Scale Fourier Transform of Pressure Cell #4')
xlabel('Frequency (Hz)')
xlim([1,max(200)])     %change the x-axes limits here
ylabel('FFT Amplitude (kPa-s)')
ylim([min(.01),max(z)])     %change the x-axes limits here

h=gcf
saveas(h,'ll4.png')

x= VarName30;

%Create Time Vector
dt=0.005   %time step in seconds
l=length(x);
Time=[0:dt:(l*dt-dt)];
x=detrend(x);

%Plot FFT
Fnyq=1/(2*dt);             %calculate nyqqest frequency
freq=linspace(-Fnyq,Fnyq,l+1)'; %Create Frequency Vector
freq=freq(1:l);
```

```
FFTx=fft(x);              %fourier transform
X=fftshift(FFTx);             %changes the order of the vector
ACH=abs(X);               %find fourier magnitude
pCH=angle(X);             %find fourier phase

figure(5)
loglog(freq,ACH)
title('Loglog Scale Fourier Transform of Pressure Cell #5')
xlabel('Frequency (Hz)')
xlim([1,max(200)])     %change the x-axes limits here
ylabel('FFT Amplitude (kPa-s)')
ylim([min(.01),max(z)])     %change the x-axes limits here

h=gcf
saveas(h,'ll5.png')

x= VarName31;

%Create Time Vector
dt=0.005   %time step in seconds
l=length(x);
Time=[0:dt:(l*dt-dt)];
x=detrend(x);

%Plot FFT
Fnyq=1/(2*dt);            %calculate nyqqest frequency
freq=linspace(-Fnyq,Fnyq,l+1)'; %Create Frequency Vector
freq=freq(1:l);

FFTx=fft(x);              %fourier transform
X=fftshift(FFTx);             %changes the order of the vector
ACH=abs(X);               %find fourier magnitude
pCH=angle(X);             %find fourier phase

figure(6)
loglog(freq,ACH)
title('Loglog Scale Fourier Transform of Pressure Cell #6')
xlabel('Frequency (Hz)')
xlim([1,max(200)])     %change the x-axes limits here
ylabel('FFT Amplitude (kPa-s)')
ylim([min(.01),max(z)])     %change the x-axes limits here

h=gcf
saveas(h,'ll6.png')
```

```
x= VarName32;

%Create Time Vector
dt=0.005   %time step in seconds
l=length(x);
Time=[0:dt:(l*dt-dt)];
x=detrend(x);

%Plot FFT
Fnyq=1/(2*dt);             %calculate nyqqest frequency
freq=linspace(-Fnyq,Fnyq,l+1)'; %Create Frequency Vector
freq=freq(1:l);

FFTx=fft(x);               %fourier transform
X=fftshift(FFTx);              %changes the order of the vector
ACH=abs(X);                %find fourier magnitude
pCH=angle(X);              %find fourier phase

figure(7)
loglog(freq,ACH)
title('Loglog Scale Fourier Transform of Pressure Cell #7')
xlabel('Frequency (Hz)')
xlim([1,max(200)])      %change the x-axes limits here
ylabel('FFT Amplitude (kPa-s)')
ylim([min(.01),max(z)])      %change the x-axes limits here

h=gcf
saveas(h,'ll7.png')

x= VarName33;

%Create Time Vector
dt=0.005   %time step in seconds
l=length(x);
Time=[0:dt:(l*dt-dt)];
x=detrend(x);


%Plot FFT
Fnyq=1/(2*dt);             %calculate nyqqest frequency
freq=linspace(-Fnyq,Fnyq,l+1)'; %Create Frequency Vector
freq=freq(1:l);

FFTx=fft(x);               %fourier transform
X=fftshift(FFTx);              %changes the order of the vector
```

```
ACH=abs(X);              %find fourier magnitude
pCH=angle(X);             %find fourier phase

figure(8)
loglog(freq,ACH)
title('Loglog Scale Fourier Transform of Pressure Cell #8')
xlabel('Frequency (Hz)')
xlim([1,max(200)])     %change the x-axes limits here
ylabel('FFT Amplitude (kPa-s)')
ylim([min(.01),max(z)])  %change the x-axes limits here

h=gcf
saveas(h,'ll8.png')

x= VarName34;

%Create Time Vector
dt=0.005   %time step in seconds
l=length(x);
Time=[0:dt:(l*dt-dt)];
x=detrend(x);


%Plot FFT
Fnyq=1/(2*dt);             %calculate nyqqest frequency
freq=linspace(-Fnyq,Fnyq,l+1)'; %Create Frequency Vector
freq=freq(1:l);

FFTx=fft(x);              %fourier transform
X=fftshift(FFTx);              %changes the order of the vector
ACH=abs(X);              %find fourier magnitude
pCH=angle(X);             %find fourier phase

figure(9)
loglog(freq,ACH)
title('Loglog Scale Fourier Transform of Shaker Force')
xlabel('Frequency (Hz)')
xlim([1,max(200)])     %change the x-axes limits here
ylabel('FFT Amplitude (N-s)')
ylim([min(.01),max(z)])     %change the x-axes limits here

h=gcf
saveas(h,'llsh.png')
```

```
clear all, close all, clc

load('FFT 2.2.1a 0.05MM.mat')
%Evaluate Pressure Cell Data (Pressure vs. Time)
w= -10                    %min value for y-limit
y= 10                     %max value for y-limit
x= VarName26;

%Create Time Vector
dt=0.005   %time step in seconds
l=length(x);
Time=[0:dt:(l*dt-dt)];
x=detrend(x);

%Plot Pressure Cell versus Time
figure(1)
plot(Time,x)
title('Pressure Cell #1')
xlabel('Time (sec)')
%xlim([0,max(100)])      %change the x-axes limits here
ylabel('Pressure (kPa)')
ylim([min(w),max(y)])      %change the y-axes limits here

h=gcf
saveas(h,'pc1.png')

x= VarName27;

%Create Time Vector
dt=0.005   %time step in seconds
l=length(x);
Time=[0:dt:(l*dt-dt)];
x=detrend(x);

%Plot Pressure Cell versus Time
figure(2)
plot(Time,x)
title('Pressure Cell #2')
xlabel('Time (sec)')
%xlim([0,max(100)])      %change the x-axes limits here
ylabel('Pressure (kPa)')
ylim([min(w),max(y)])      %change the y-axes limits here

h=gcf
saveas(h,'pc2.png')
```

```
x= VarName28;

%Create Time Vector
dt=0.005   %time step in seconds
l=length(x);
Time=[0:dt:(l*dt-dt)];
x=detrend(x);

%Plot Pressure Cell versus Time
figure(3)
plot(Time,x)
title('Pressure Cell #3')
xlabel('Time (sec)')
%xlim([0,max(100)])      %change the x-axes limits here
ylabel('Pressure (kPa)')
ylim([min(w),max(y)])       %change the y-axes limits here

h=gcf
saveas(h,'pc3.png')

x= VarName29;

%Create Time Vector
dt=0.005   %time step in seconds
l=length(x);
Time=[0:dt:(l*dt-dt)];
x=detrend(x);

%Plot Pressure Cell versus Time
figure(4)
plot(Time,x)
title('Pressure Cell #4')
xlabel('Time (sec)')
%xlim([0,max(100)])      %change the x-axes limits here
ylabel('Pressure (kPa)')
ylim([min(w),max(y)])      %change the y-axes limits here

h=gcf
saveas(h,'pc4.png')

x= VarName30;

%Create Time Vector
dt=0.005   %time step in seconds
```

```
l=length(x);
Time=[0:dt:(l*dt-dt)];
x=detrend(x);

%Plot Pressure Cell versus Time
figure(5)
plot(Time,x)
title('Pressure Cell #5')
xlabel('Time (sec)')
%xlim([0,max(100)])     %change the x-axes limits here
ylabel('Pressure (kPa)')
ylim([min(w),max(y)])      %change the y-axes limits here

h=gcf
saveas(h,'pc5.png')

x= VarName31;

%Create Time Vector
dt=0.005   %time step in seconds
l=length(x);
Time=[0:dt:(l*dt-dt)];
x=detrend(x);

%Plot Pressure Cell versus Time
figure(6)
plot(Time,x)
title('Pressure Cell #6')
xlabel('Time (sec)')
%xlim([0,max(100)])     %change the x-axes limits here
ylabel('Pressure (kPa)')
ylim([min(w),max(y)])    %change the y-axes limits here

h=gcf
saveas(h,'pc6.png')

x= VarName32;

%Create Time Vector
dt=0.005   %time step in seconds
l=length(x);
Time=[0:dt:(l*dt-dt)];
x=detrend(x);

%Plot Pressure Cell versus Time
```

```
figure(7)
plot(Time,x)
title('Pressure Cell #7')
xlabel('Time (sec)')
%xlim([0,max(100)])     %change the x-axes limits here
ylabel('Pressure (kPa)')
ylim([min(w),max(y)])      %change the y-axes limits here

h=gcf
saveas(h,'pc7.png')

x= VarName33;

%Create Time Vector
dt=0.005   %time step in seconds
l=length(x);
Time=[0:dt:(l*dt-dt)];
x=detrend(x);

%Plot Pressure Cell versus Time
figure(8)
plot(Time,x)
title('Pressure Cell #8')
xlabel('Time (sec)')
%xlim([0,max(100)])     %change the x-axes limits here
ylabel('Pressure (kPa)')
ylim([min(w),max(y)])    %change the y-axes limits here

h=gcf
saveas(h,'pc8.png')

x= VarName34;

%Create Time Vector
dt=0.005   %time step in seconds
l=length(x);
Time=[0:dt:(l*dt-dt)];
x=detrend(x);

%Plot Pressure Cell versus Time
figure(9)
plot(Time,x)
title('Shaker Force')
xlabel('Time (sec)')
%xlim([0,max(Time)])     %change the x-axes limits here
```

```
ylabel('Force (N)')
%ylim([min(x),max(x)])      %change the y-axes limits here

h=gcf
saveas(h,'pcsh.png')
```

REFERENCES

REFERENCES

ASCE. (2010). *Minimum design loads for buildings and other structures,* ASCE/SEI 7-10, American Society of Civil Engineers, Reston, Virginia.

Crouse, C. B. & McGuire, J. (2001). “Energy dissipation in soil structure interaction.” *Earthquake Spectra*, 17(2), 235-259.

Chopra, A. (1995). *Dynamics of structures: Theory and applications to earthquake engineering,* 3rd Ed., Prentice Hall, Englewood Cliffs, N.J.

Clough, R.W., & Penzien, J. (1993). *Dynamics of structures*, McGraw Hill, New York.

Dobry, R., & O'rourke, M. J. (1983). “Discussion of ‘Seismic response of end-bearing piles’ by Raul Flores-Berrones and Robert V. Whitman (April, 1982).” *Journal of Geotechnical Engineering*, 109(5), 778-781.

Gazetas, G. (1991). “Foundation vibrations,” *Foundation engineering handbook*, 2nd Ed., Chapter 15, H.-Y. Fang, ed., Chapman and Hall, New York.

Holtz, R. D., & Kovacs, W. D. (2011). *An introduction to geotechnical engineering,* 2nd Ed., Pearson, Upper Saddle River, NJ.

Kausel, E. (2010). “Early history of soil-structure interaction.” *Soil Dynamics and Earthquake Engineering*, 30(9), 822-832.

Kramer, S. (1996). *Geotechnical earthquake engineering*, Prentice Hall, Upper Saddle River, N.J.

Kurtulus, A. (2006). “Field measurement of the linear and nonlinear shear moduli of soils using drilled shafts as dynamic cylindrical sources.” Ph.D. Dissertation, The University of Texas at Austin, U.S.A.

Luco, J.E., & Westmann, R.A. (1971). “Dynamic response of circular footings.” *Journal of Engineering Mechanics*, 97(5), 1381-1395.

Mikami, A., Stewart, J.P., Ostadan, F., & Crouse, C.B. (2006). “Representation of ground motion incoherence for the analysis of kinematic soil-structure interaction,” *Proc., 8th U.S. National Conference on Earthquake Engineering, Paper No. 1071.*

Mylonakis, G., Nikolaou, S., & Gazetas, G. (2006). “Footings under seismic loading: Analysis and design issues with emphasis on bridge foundations.” *Soil Dynamics and Earthquake Engineering*, 26, 824-853.

Mylonakis, G. (2009). “Seismic analysis of coupled soil-pile-structure systems leading to the definition of a pseudo-natural SSI frequency.” *Soil Dynamics and Earthquake Engineering*, *29*, 1005-1015.

NIST. (2012). *Soil-structure interaction for building structures, report No. NIST GCR 12- 917-21*, National Institute of Standards and Technology, U.S. Department of Commerce, Washington D.C.

Pais, A., & Kausel, E. (1988). “Approximate formulas for dynamic stiffnesses of rigid foundations.” *Soil Dynamics and Earthquake Engineering*, 7(4), 213-227.

Reinert, E. T., Brandenberg, S. J., Stewart, J. P., & Moss, R. E. S. (2012). “Dynamic field test of a model levee founded on peaty organic soil using an eccentric mass shaker.” *15th World Conf. on E.Q. Eng.*

Saitoh, M. (2007). “Simple model of frequency-dependent impedance functions in soil-structure interaction using frequency-independent elements.” *Journal of Engineering Mechanics*, 133, 1101-1114.

Shi, J. (2011). “A response-based simplified model for vertical vibrations of embedded foundations.” *Soil Dynamics and Earthquake Engineering*, 31, 773-784.

Star, L. M. (2011). “Seismic vulnerability of structures: Demand characteristics and field testing to evaluated soil-structure interaction effects.” Ph.D. Dissertation, University of California, Los Angeles, Los Angeles, CA.

Stewart, J. P., Kim, S., Bielak, J., Dobry, R., & Power, M. (2003). “Revisions to soil structure interaction procedures in NEHRP design provisions.” *Earthquake Spectra*, 19(3), 677-696.

Tileylioglu S., Stewart J. P. & Nigbor R. L. (2011). “Dynamic stiffness and damping of shallow foundation from forced vibration of a field test structure.” *Journal of Geotechnical & Geoenvironmental Engineering*, 137, 344-353.

Veletsos, A.S., & Meek, J.W. (1974). “Dynamic behavior of building-foundation systems.” *Earthquake Engineering and Structural Dynamics*, 3, 121-138.

Veletsos, A.S., & Wei, Y. T. (1971). “Lateral and rocking vibrations of footings.” *Journal of Soil Mechanics and Foundation Division*, 97(9), 1227–1248.